UNIVERSITÄT BONN
Physikalisches Institut

Energy-loss measurement with the ZEUS Central Tracking Detector

von

Detlef Bartsch

The measurement of the specific energy loss due to ionisation, dE/dx, in a drift chamber is a very important tool for particle identification in final states of reactions between high energetic particles. Such identification requires a well understood dE/dx measurement including a precise knowledge of its uncertainties. Exploiting for the first time the full set of ZEUS data from the HERA operation between 1996 and 2005 twelve detector-related influences affecting the dE/dx measurement of the ZEUS Central Tracking Detector have been identified, separately studied and parameterised. A sophisticated iterative procedure has been developed to correct for these twelve effects, which takes into account the correlations between them. A universal parameterisation of the detector-specific Bethe-Bloch curve valid for all particle species has been extracted. In addition, the various contributions to the measurement uncertainty have been disentangled and determined. This yields the best achievable prediction for the single-track dE/dx resolution. For both the analysis of the measured data and the simulation of detector performance, the detailed understanding of the measurement and resolution of dE/dx gained in this work provides a tool with optimum power for particle identification in a physics studies.

Post address:
Nussallee 12
D-53115 Bonn
Germany

Bonn University
May 2007

UNIVERSITÄT BONN
Physikalisches Institut

Energy-loss measurement with the ZEUS Central Tracking Detector

von
Detlef Bartsch

Dieser Forschungsbericht wurde als Dissertation von der Mathematisch-Naturwissenschaftlichen Fakultät der Universität Bonn angenommen und ist auf dem Hochschulschriftenserver der ULB Bonn http://hss.ulb.uni-bonn.de/diss_online elektronisch publiziert.

Erscheinungsjahr: 2007

Referent: Prof. Dr. Erwin Hilger
Korreferent: Prof. Dr. Klaus Desch

Tag der Promotion: 24.05.2007

Contents

List of Figures

List of Tables

Chapter 1

Introduction

More than twenty years ago, in the 1980s, the electron-proton collider HERA[1] at the particle physics research centre DESY[2] in Hamburg and the multi-purpose detectors H1 and ZEUS were designed in order to extend the famous deep-inelastic scattering experiments of the seventies at SLAC[3] into hithero unexplored kinematic regions. Consequently, the physics emphasis was dominantly on inclusive measurements and on the exploration of the proton structure down to extremely small distances of the order of 10^{-18} m or 1/1000 of the diameter of a nucleon. The detectors were optimised for the measurement of jet energies based on calorimetry and high-resolution tracking, while the identification of individual particles in the hadronic final state of the collision events was given lower priority.

Over the years of operation of HERA and of its detectors the physics topics investigated widened considerably. Generally, with increasing collected luminosity and correspondingly increasing numbers of events, measurements of semi-inclusive and rare exclusive reaction channels became the focus of the experimenters.

This concerned especially the physics of heavy flavours, which on the one hand is characterised by small cross sections, on the other hand offers particularly reliable theoretical predictions since pertubative Quantum ChromoDynamics (pQCD), the theory of strong interactions, benefits from the large masses of heavy quarks. In order to achieve high signal-to-background ratios for such channels, new experimental tools of event selection by means of event topology and particle separation were required. A large fraction of heavy flavoured mesons decay semileptonically, which requires the capability to identify leptons. The early analyses in this field concentrated on the muonic channels, because the properties of muons allow their easy identification [1]. In order to test the theoretical predictions in independent measurements there is a high interest in measuring also the electron channels. It turned out, that the most powerful method for electron identification in the typical momentum range of these decays is the measurement of the mean specific energy loss by ionisation, dE/dx, of the corresponding tracks.

In recent years another topic for analyses at HERA became popular, the search for the exotic baryon species of pentaquarks. A characteristic method for such searches is the identification of a(n) (anti-)proton in the decay chain of the pentaquark. In the low mo-

[1] **H**adron **E**lectron **R**ing **A**nlage
[2] **D**eutsches **E**lektron **Sy**nchrotron
[3] **S**tanford **L**inear **A**ccelerator **C**enter

mentum regime the measured dE/dx separates protons very efficiently from other particle types. An early stage of the necessary corrections of the dE/dx measurement with the ZEUS Central Tracking Detector (CTD), as also described in this thesis, was used in these analyses [2] as well as for the identification of Λ_c-decays [3].

A long shutdown in the years 2000 and 2001, followed by a year of re-commissioning, separates HERA and detector operation in two periods called HERA I and HERA II. The present ZEUS detector contains two components that may be used for dE/dx measurements: the CTD, available for the whole ZEUS data-taking and the MVD, available for HERA II.

In order to measure rare events one needs to collect and investigate as many events as accessible, leading to the requirement to combine data from HERA I and HERA II in the same analyses. As the MVD did not exist during HERA I, such dE/dx-based analyses can only exploit the CTD for this issue. Therefore, during recent years, a proper and well validated measurement of dE/dx with the CTD became more and more crucial.

In the early 1990s, after the first data had been taken by ZEUS, several corrections on the dE/dx measurement with the CTD were developed. Based on the small amount of data then available, these corrections yielded the best results achievable at that time for the dE/dx measurements. Nevertheless, large systematic errors were left in the measurement prohibiting most of its applications. After these first approaches, for almost a decade, the dE/dx corrections remained untouched at that level. Nowadays by far more data are available, enabling much more sophisticated methods for correcting the dE/dx measurement. In this thesis, such an approach will be described, discussed and demonstrated. The result of this work represents a major improvement of the dE/dx measurement with the ZEUS CTD.

An essential tool for a physics analysis is the full Monte-Carlo simulation (MC) of events generated according to the theoretical prediction and measured with the detector components. In many cases, such simulations are used to extract the efficiency and the purity of the employed event selection. In particular, these values are mandatory to transform the collected amount of events into a measured cross section for the respective physics process. In ZEUS, the MC simulation of the dE/dx measurement was for a long time not good enough. For example, it was not possible to use MC data for the calculation of the corresponding efficiency.

Without a proper comprehension of the idiosyncrasies of the dE/dx measurement its exploitation was rather limited. Typical applications were:

- Cut out only clearly identified particles:
  Selecting data only in momentum ranges where the dE/dx of the particle species under investigation is very different from that of other particle species. In such a case a rather pure sample can be selected with sufficiently high efficiency.

  The disadvantage of this method is its limited applicability. It will only work in the low momentum range for heavy – and thus more strongly ionising – particles like protons or kaons. This approach has been chosen for proton identification [4].

- Statistical subtraction of background:
  A signal-enriched sample and a background-enriched sample is generated. The background sample is normalised to the signal sample in a range of dE/dx which is purely

background. The statistical subtraction of the two distributions in the signal range then yields the number of signal events [5].

This approach is quite sensitive to systematical differences in the dE/dx measurement of tracks in the two samples. The selection of the two samples introduces differences in several parameters (like track kinematics) which the dE/dx measurement depends on. This can cause systematic differences between the background sample in the signal region and the true background in the signal sample. If the background in the signal sample is high (very often the signal is the small difference of two large numbers) this systematic error penetrates dramatically scaled-up into the determined signal.

A well-understood measurement of dE/dx solves these problems. Corrections for effects which influence and deteriorate the dE/dx measurement improve its resolution and therefore the separation power of a dE/dx-based particle identification. Furthermore, systematic differences between data samples are strongly reduced by these corrections. This is the prime impact of proper corrections, because systematic differences are the main source for the previously mentioned large uncertainties in analysis results based on dE/dx measurements. Detailed investigations of differently selected data samples furthermore give access to quantitative estimates for the systematic uncertainties of the dE/dx measurements; in the past this kind of uncertainty was quantitatively not known at all. Finally, a detailed knowledge of the uncertainties of the dE/dx measurement allows for a realistic Monte-Carlo generation of dE/dx values, enabling the usage of dE/dx in Monte-Carlo simulations for the first time in ZEUS.

The improvements resulting from this work are already being used in a few ZEUS analyses, especially for the electron identification in semileptonic decays of heavy-flavoured mesons [6, 7, 8].

As the ZEUS CTD has not been designed for a high dE/dx resolution one cannot ever expect to achieve a very high resolution with this detector. A particle identification like for example achieved with the OPAL jet-chamber (3% resolution of dE/dx)[4], which allowed a 2σ-separation between kaons and pions in the momentum range $1.5\,\mathrm{GeV} < p < 100\,\mathrm{GeV}$ based on dE/dx measurements, is technically impossible with the ZEUS CTD. The separation power of the dE/dx measurement has to be combined with measurements of other detector components in order to achieve a maximal separation power.

The calculation of likelihood values for different particle hypotheses is the best way to succeed in this task: likelihoods from different sources can easily be combined to a global likelihood value. The work presented in this thesis delivers properly measured dE/dx values and their uncertainty as well as likelihood values for all particle hypotheses.

This thesis is organised as follows. In Chapter 2 the HERA collider and the detector components of ZEUS relevant for this analysis will be introduced as well as the software for the reconstruction of tracks and for their specific energy loss in the CTD. A brief overview of the theory for the ionisation energy loss in matter will be given in Chapter 3. The main body of this thesis is comprised in Chapter 4; following a description of the data samples used for this analysis and an introduction to the identified effects influencing the dE/dx measurements, one finds a detailed description of the correction methods as well

[4] A nice overview of the dE/dx resolution of several drift chambers can be found in [9].

as the algorithm to optimise and de-correlate these partial corrections. The chapter closes with the method applied to measure correctly the dependence of the specific ionisation on the particle speed (BETHE-BLOCH curve). The results of the dE/dx corrections will be shown and extensively discussed in Chapter 5. A summary of the thesis is given in Chapter 6. Several rather technical issues are collected in the appendices.

Chapter 2

Storage ring, detector components, track reconstruction

In this chapter, the experimental facilities which provide the environment for this analysis work will be presented. The first section describes the accelerator facility HERA. The ZEUS detector will be described in the second section, focussing on its capabilities for particle identification. The goal of this analysis work are corrections to the dE/dx measurement with the ZEUS CTD. Due to the pre-eminent importance of this detector component for this work, the description of the ZEUS detector will focus on the CTD. The potential of different detector components for particle identification will be exposed in Sect. 2.3. In the fourth section the reconstruction of tracks from hit patterns in the CTD will be introduced and Sect. 2.5 describes the so called Phase I dE/dx reconstruction from CTD hits.

2.1 The HERA collider

The **H**adron **E**lektron **R**ing **A**nlage [10], located at DESY in Hamburg, is the only electron (positron)[1] - proton collider on earth. The storage ring with a circumference of $\approx 6.3\,\mathrm{km}$ is separated into two rings mounted on top of each other, one for the electrons, the other one for the protons. The electron ring consists of normal-conducting dipole-magnets at $0.3\,T$ and super-conducting cavities to accelerate the electron beam up to an energy of 27.5 GeV. The proton machine consists of super-conducting magnets with a magnetic field of $4.7\,T$ and normal-conducting cavities, delivering a beam with the energy of 920 GeV (820 GeV until 1997). For colliding beams this results in a centre-of-mass energy of 300 GeV until 1997 and 318 GeV after increasing the proton energy.

There are four interaction regions at HERA, shown in Fig. 2.1. At two of them, ep-collisions are delivered for the detectors H1 and ZEUS. The HERMES detector uses only the longitudinally polarised electron beam with a fixed polarised or unpolarised gas target to investigate the spin structure of electron-proton or electron-deuteron interactions. Until the end of 2000 HERA-B was using the proton beam together with a fixed wire target. HERA-B was designed to investigate $\mathcal{CP}$-violation in the $B^0\bar{B}^0$-system.

The HERA I data-taking ended in the year 2000. During the shutdown 2000/2001 HERA

[1] In the following, the term 'electron' will denote both, the electron (e^-) and the positron (e^+).

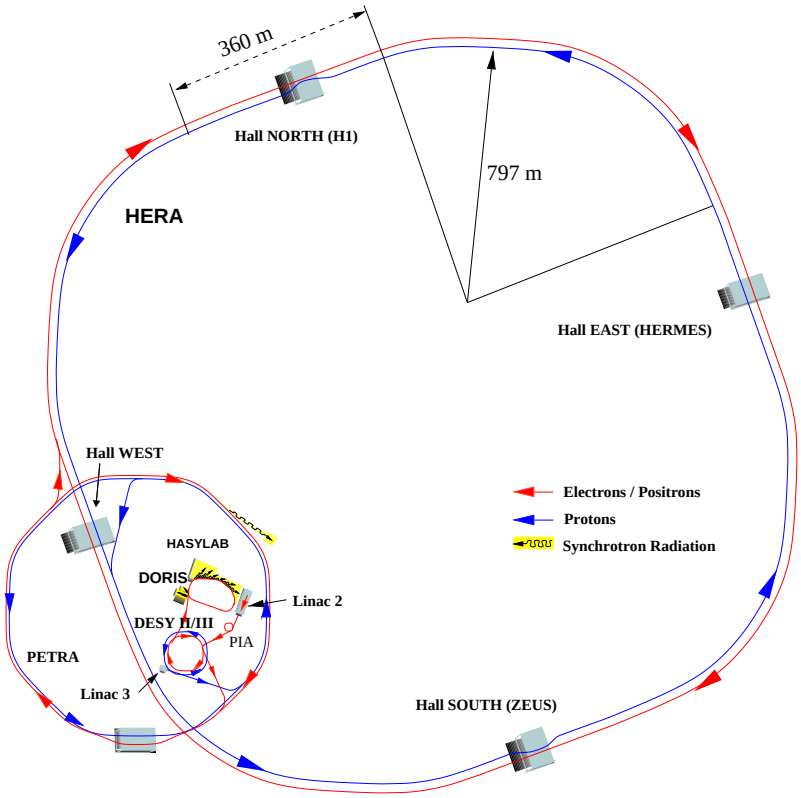

Figure 2.1: HERA and its pre-accelerators. At each straight section detectors are located.

was upgraded to deliver longitudinally polarised lepton beams at all interaction regions and to achieve an increased specific luminosity [11]. Until the mid of 2003 HERA and the experiments had to cope with severe background problems [12]. Since October 2003 stable beam operation has been achieved again. Presently the HERA II data-taking is still ongoing and will end in June 2007.

2.2 The ZEUS detector

The ZEUS detector [13] is designed to measure the final states of ep reactions as precisely as possible. Due to the much higher energy of the proton beam compared to the lepton beam the ep-centre-of-mass system (cms) is boosted in proton flight direction. To properly cope with this boost, the ZEUS detector is equipped asymmetrically.

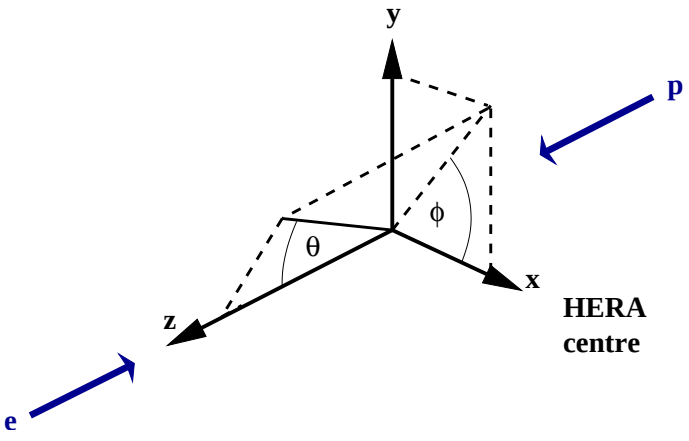

Figure 2.2: The ZEUS coordinate system.

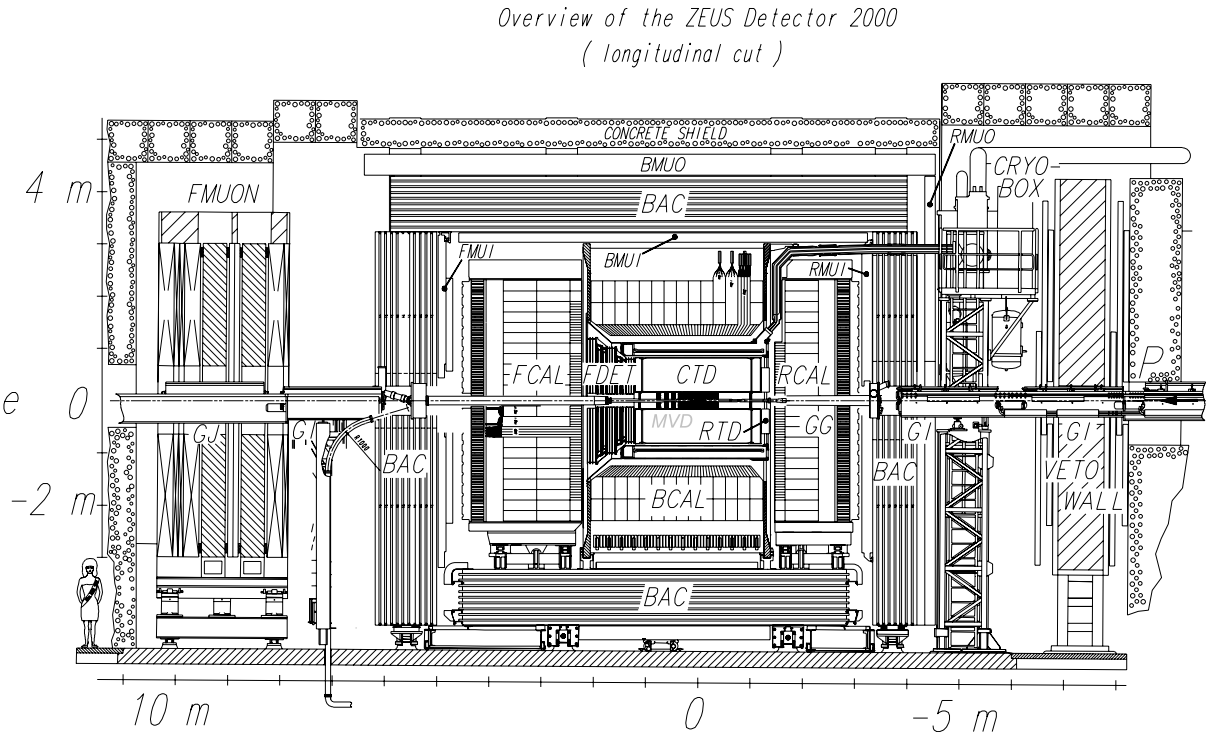

Figure 2.3: Longitudinal cut of the ZEUS detector after HERA II upgrade.

The ZEUS coordinate system [14] as shown in Fig. 2.2 is a right-handed orthogonal system with the origin at the nominal interaction point (IP); the z-axis is pointing in proton flight direction (also referred to as the forward direction), the x-axis points towards the centre of HERA and the y-axis is pointing upward.

A cross section of the ZEUS detector is shown in Fig. 2.3. The main detector is approximately 19 m long, 12 m wide and 11 m high with a weight of around 3600 t. It is composed of several sub-detectors surrounding the interaction point concentrically. The primary purpose of the inner detectors is the measurement of the charged particle tracks. The inner detectors are surrounded by a super-conducting coil, producing a solenoidal magnetic field of 1.43 T. The particle trajectory bends within this magnetic field offering the opportunity to reconstruct the momentum of the particle. Furthermore, the combination of the trajectories of all tracks of an event is used to reconstruct the production vertex.

Since HERA II the innermost detector is the micro-vertex detector (MVD), a silicon strip detector designed for high resolution to reconstruct secondary vertices. The central tracking detector (CTD) is the main tracking drift chamber of ZEUS. In the forward direction it is supplemented by a set of 3 planar drift chambers, the forward tracking detector (FTD). Since HERA II the 2 gaps between the FTD chambers are filled with the straw tube tracker (STT). In Fig. 2.3 these detectors are labelled together as the forward detector (FDET). In the rear direction there is the rear tracking detector (RTD) similar to one of the FTDs. For very small scattering angles the small angle rear tracking detector (SRTD) covers a rectangular area of $70 \times 70\,\mathrm{cm}^2$ around the beam pipe just in front of the rear uranium calorimeter.

The inner detectors are surrounded by calorimeters to measure the energy of the particles.

The uranium-scintillator calorimeter (UCAL) covers most of the 4π solid angle (except for small regions around the beam pipe).

The front face of the calorimeter is covered by the presampler [15], a scintillation detector that produces almost similar amounts of signal for each charged particle passing through. Therefore this detector measures the multiplicity of a particle shower, which is generated when the primary particle passes through the dead material in front of this detector. The energy loss due to such showers in the dead material in front of the calorimeter cannot be taken into account by the energy measurement of the UCAL. The main goal of the presampler is to estimate this energy loss exploiting the shower multiplicity and to apply an energy correction to the UCAL measurement. As the free pathlength between interactions for electromagnetically and hadronically interacting particles differs significantly (about a factor of 20), their multiplicities in the presampler also differ. Therefore one can use the presampler for the separation of these two particle classes. The separation power is rather limited, as the thickness of the dead material in front of the presampler is only of the order of 1-2.5 electromagnetic radiation lengths.

The Hadron Electron Separator (HES) [16] is a single layer of silicon diodes located within the forward calorimeter (FCAL) and the rear calorimeter (RCAL) at a depth of 3 radiation lengths, where the highest multiplicity in electromagnetic showers is found. The principle of the hadron-electron separation is the same as described for the presampler.

The calorimeter is surrounded by the backing calorimeter (BAC), designed to measure the energy deposited by jets leaking out of the UCAL and serving as the return yoke for the solenoid. The BAC is also a useful device for muon identification, as most of the signals measured within the BAC are caused by muons. The layout of the BAC, measuring the passage of particles in 8 layers, furthermore allow to reconstruct the direction of the muon passing through. The muon chambers (F/B/RMUON) surround the BAC. In electron direction one finds the veto-wall (VETO). Interaction products of the proton beam with remaining gas molecules in the beam pipe are registered by this detector. This information is used as a veto against beam-induced background.

With about 250000 readout channels and bunch crossings every 96 ns, the theoretical maximum data volume produced by the ZEUS detector is enormous. A reduction factor of 10^6 has to be achieved to limit the data flow to a manageable size. This task is carried out by the trigger system in 3 steps. The first level trigger (FLT) is a pure hardware device, realized for each detector component separately. All data collected by the ZEUS detector is buffered in analogue pipelines as long as the FLT works to find a decision. Only if the FLT takes a positive decision, the data is read out from the pipeline and submitted to further readout electronics to be digitised and setup for the next trigger state. The second level trigger (SLT) combines information from all sub-detectors. Several quantities already available at FLT-level are recalculated with higher precision, which allows a more stringent selection. At this level also physics filters are applied. The third level trigger (TLT) is a pure software trigger in a computer farm. The code for this trigger is written in high-level programming languages which allows easy maintenance and upgrades. Over the years several TLT chains were modified to react on the developing aims in the physics program and on the increasing specific luminosity[2]. Most of the TLT trigger chains are

[2]Over the years the focus changed from high-statistics channels which allow to collect sufficient data for interesting physics results already within a short data taking time to rare channels which need a lot of collected luminosity. As there are upper limits for the manageable trigger rate, with increasing specific luminosity high-rate channels had to be pre-scaled or even removed from the TLT.

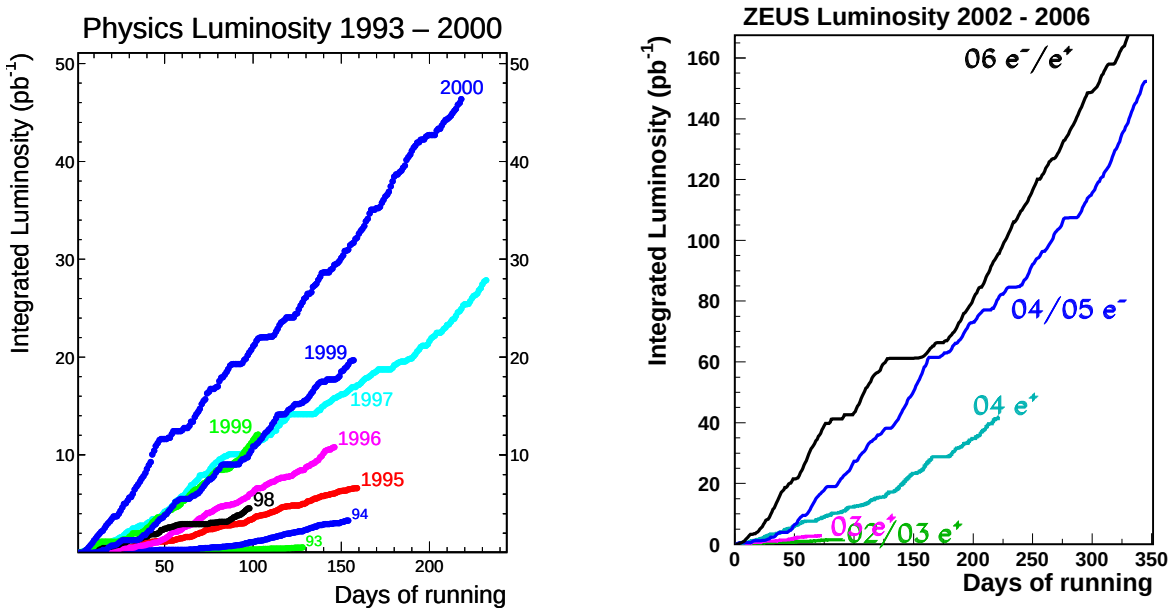

Figure 2.4: The luminosity gated by ZEUS.

dedicated for special physics channels. For an easy and fast data handling some trigger bits are saved in Data Summary Tapes (DST).

For this work data from the years 1996 to 2005 were used. The registered luminosity in the HERA I period was 121 pb^{-1} (174 pb^{-1} delivered by HERA) and for HERA II 176 pb^{-1} (289 pb^{-1} delivered). Figure 2.4 displays the physics luminosity growth separated by years.

2.2.1 Central Tracking Detector

The central tracking detector (CTD) [17, 18] is the most important detector for measuring the charge and the momentum of charged particles. It is a cylindrical drift chamber of 241 cm overall length, the active volume covers 205 cm in length shifted relative to the IP by 2.5 cm in the forward direction. Its inner radius is 16.2 cm leaving space for the beam pipe and the MVD; the outer radius is 85 cm. The active volume covers the radial range from 18.2 cm to 79.4 cm.

The outer cylinder is made of a 6 mm thick aluminum alloy sheet formed into a single, complete cylinder. It supports an electrostatic screen to optimise the electrostatic properties of superlayer 9 (see next paragraph). A second electrostatic screen of low-mass construction (Cu/Kapton/foam) is located on the inner cylinder, which is made from two aluminum alloy skins each 0.7 mm thick with a 9 mm gap, filled with polyurethane foam. The inner cylinder is designed to minimise the amount of matter in order to minimise particle scattering. Nevertheless, this cylinder is the main source for electrons from photon conversions (see Sect. 4.1.1.1). The end-plates are made of 20 mm thick 5083-grade aluminum alloy and support the wires in 24192 individual 3 mm feedthroughs.

The signal wires are organised radially in 9 superlayers, each of them covering a sensitive range of 45 mm in radial direction, leading to a total sensitive range of 402 mm in radial direction for the CTD. Each superlayer is separated azimuthally into supercells. The

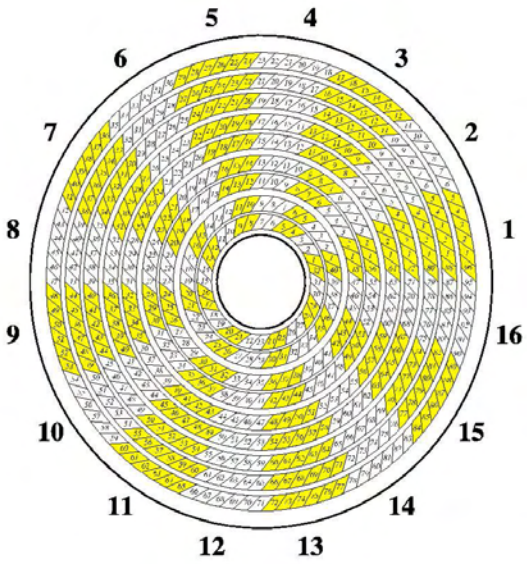

Figure 2.5: Layout of the sectors, superlayers and supercells of the CTD.

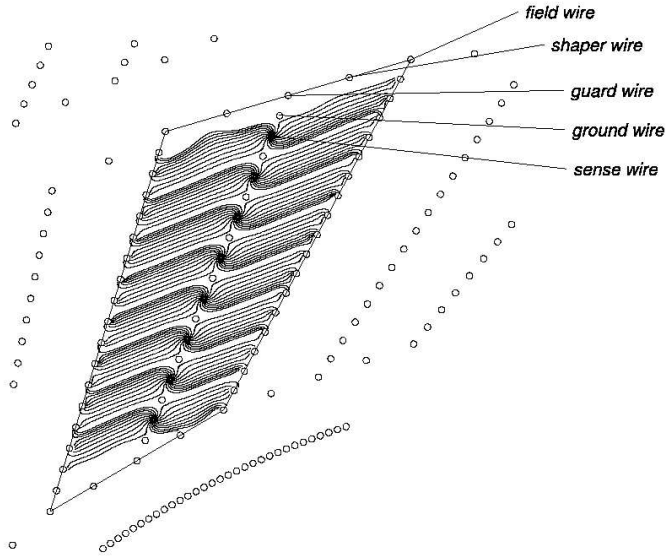

Figure 2.6: Layout of a typical supercell, showing the geometry of the wires and the drift paths. [19]

superlayer	stereo angle [°]			centre radius of supercell [cm]	
	mean	min	max	at $z = 2.5$ cm	at $z = 104$ cm
1	0	0	0	20.95	20.95
2	4.98	4.64	5.32	27.21	28.61
3	0	0	0	34.98	34.98
4	-5.31	-5.06	-5.55	41.28	42.35
5	0	0	0	48.71	48.71
6	-5.51	-5.31	-5.69	55.50	56.36
7	0	0	0	62.72	62.72
8	5.62	5.46	5.77	69.45	70.16
9	0	0	0	76.53	76.53

Table 2.1: Stereo tilt's of wires and radii for the centre of the superlayers. [20]

number of supercells varies from 32 for the innermost superlayer to 96 for the outermost superlayer to provide similar-sized supercells in all superlayers. The layout of the supercells is displayed in Fig. 2.5. Each supercell consists of 8 cells[3] in radial direction which makes up for 72 layers for the whole CTD. The wires in the odd-numbered superlayers are mounted parallel to the beam-line (axial SLs); the remaining 4 even-numbered superlayers are tilted by about $\pm 5\,^\circ$ with respect to the CTD axis in order to provide sensitivity for the measurement of the z-position of tracks (stereo SLs). An overview of the tilt angles and the radial positions of the superlayers is given in Tab. 2.1.

Each supercell contains an array of 8 sense wires with a diameter of 30 µm, made of

[3]The nomenclature differs from some literature, where the name cell is used for the supercell and no special name is given for the sensitive area of a signal wire.

tungsten and operating at $\approx +1.25\,\text{kV}$. The low resistance of tungsten minimises the dispersion of the pulses. The sense wires are surrounded by field wires (Fig. 2.6). The potential of the field wires of a supercell varies from the innermost to the outermost wires in constant steps (from $\approx -2.5\,\text{kV}$ to $\approx -2\,\text{kV}$) such that the field between field wires and signal wires is independent of the width of the supercell. This maintains parallel drift trajectories and a constant drift velocity within most of the supercell. Wires at ground potential are located in the middle between the sense wires to allow the independent adjustment of gain and drift fields. Four shaper and two guard wires are included at the cell ends to provide field uniformity in these regions.

The electric field within the supercells and the magnetic field from the solenoid yields a Lorentz angle of 45 °. The wires of the supercells are also tilted by 45 ° with respect to the radial direction of the CTD, so that the drift of the electrons towards the sense wires is azimuthal in good approximation.

Separate power supplies feed different superlayers and quadrants in azimuthal direction. For each superlayer/quadrant combination 3 different power supplies deliver to the outer end of the field planes, the inner end of the field planes and the sense wires.

The chamber has originally been developed for operation in a solenoidal field of 1.8 T with an argon/ethane mixture of Ar/C_2H_6 : 50/50 bubbled through ethanol. However, ZEUS has never operated with such a field, but instead with a field of 1.43 T. The current gas composition is a mixture of argon, carbon dioxide and ethane bubbled through ethanol with the ratios[4] $Ar/CO_2/C_2H_6$: 86.1/3.2/10.7 [21]. Investigations with a rather similar mixture of 90/9/1 and B = 1.43 T have shown, that the properties of gain, drift velocity and Lorentz angle are very similar to argon/ethane while offering easier safety precautions and protection against whisker growth [22].

Preamplifier cards, each serving the signal wires of one supercell, are mounted directly at the rear end-plate. To permit a proper z-resolution all signal wires in superlayer 1 and half of the signal wires in superlayer 3 and 5 are instrumented with z-by-timing electronics [23] and have preamplifier cards also at the forward end-plate. For the other channels passive terminator boards are connected to the forward side. The pre-amplified signals are sent via $\approx 42\,\text{m}$ long coax cables to the post amplifier cards. The signals from the rear side are digitised and sampled every 9.6 ns in 8-bit Flash Analogue-to-Digital Converters (FADC). A typical pulse train is shown in Fig. 2.7, the pulse height and the arrival time are extracted from the raw hit signals by digital signal processors (DSP) and saved in ADAMO-tables[5] for further usage.

Towards the end of the 2000 data-taking period the CTD high voltage became unstable. These problems were caused by the Malter effect [26], where thin insulating deposits on the cathode wires lead to the accumulation of a positively charged ion layer. These ions cause high electric fields resulting in the emission of electrons from the wire surface. A solution to this problem is the addition of a small amount of water to the gas mixture. However, even a small admixture of 0.15% H_2O to the gas significantly changed the characteristic CTD operating parameters like drift velocity and Lorentz angle, affecting the pulse height spectrum of the chamber, too. This led to a reduced single-hit efficiency and had to be compensated by changes of high voltage and gas mixture. [27]

[4] Status of 10/31/2004

[5] ADAMO provides a system based on the Entity-Relationship model for defining tabular data structures and for manipulating and validating them from FORTRAN, C or other languages. [24]

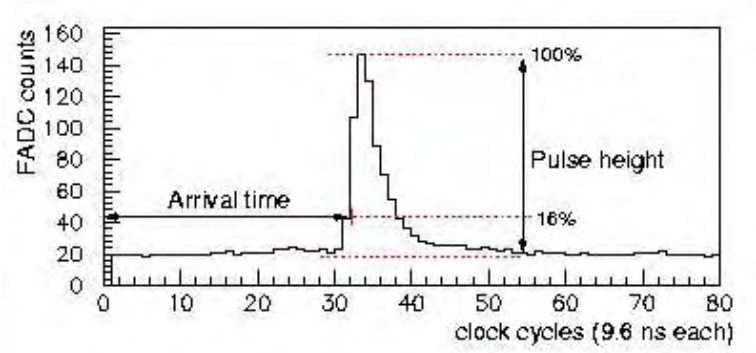

Figure 2.7: Pulse train on a CTD signal wire. [25]

2.2.2 Micro Vertex Detector

The silicon-strip micro vertex detector (MVD) was installed in 2001. Its aim is a significant improvement of the tracking capabilities to permit the reconstruction of impact parameters and secondary vertices.

Figure 2.8 displays the layout of the MVD, which is split into a barrel and a forward region. The sensitive areas are called ladders and contain two layers of orthogonally oriented silicon strips. Details about the detector can be found elsewhere [28].

The MVD measures the charge-deposit on its strips. In combination with the known geometry of the detector and the orientation of the tracks this can be used to measure the ionisation rate. One can use the MVD for particle identification in a similar way as the CTD. As one can observe in Fig. 2.8 a typical track passes 3 ladders, i.e. at most 6 silicon strips. This number is small compared to the number of hits for a typical track in the CTD (see Sect. 2.2.1). Nevertheless, the dE/dx resolution of the MVD is comparable to the resolution of the CTD [29]; the lower number of hits is roughly compensated by a higher signal on each strip due to the higher density of matter.

It is not the task of this thesis to investigate the capability of the MVD for dE/dx measurements.

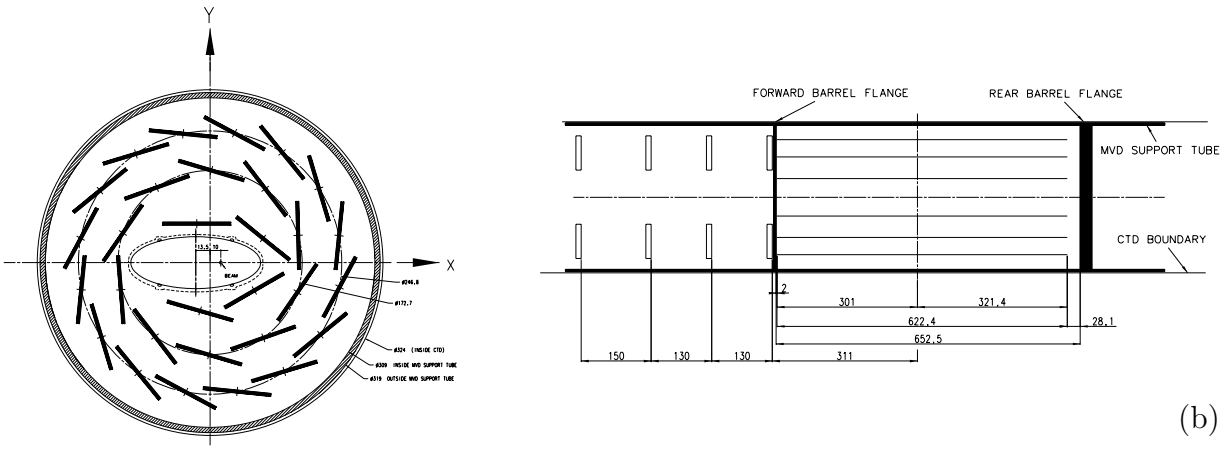

(a) (b)

Figure 2.8: Schematic layout of the barrel-MVD in the xy-plane (a) and the MVD along the beam axis (b), showing only the sensitive areas of the ladders.

2.2.3 Calorimeter

The ZEUS calorimeter [30] (CAL) is a sampling calorimeter, build as a sandwich of depleted uranium and scintillator plates, covering about 99.8% of the solid angle. The plate thicknesses are chosen to get an equal detector response for electromagnetic and hadronic showers (compensating calorimeter). Geometrically the calorimeter consists of 3 parts: the forward (FCAL), barrel (BCAL) and rear calorimeter (RCAL). Each part is subdivided transversally into towers.

Electromagnetically interacting particles (electrons, photons) produce much less deep showers in the calorimeter than hadronically interacting particles. To be sensitive to this difference each tower is separated longitudinally into an electromagnetic section (EMC) with a deepness of 25 radiation lengths ($25\,X_0$) corresponding to one hadronic interaction length ($1\,\lambda_0$) and one (RCAL, $3\,\lambda_0$ deep) or two (BCAL, $2\,\lambda_0$ and FCAL $3\,\lambda_0$ each) hadronic sections (HAC). The energy fraction deposited in the EMC-section is an estimator for the electron identification. For low momentum tracks the separation power of this method is rather small, as low energetic particles do not reach the hadronic section of the calorimeter even if they are hadrons.

In the F/RCAL the towers are quadratic with a cross section of $20 \times 20\,\mathrm{cm}^2$, the BCAL towers are wedge-shaped with a front-area (the side, pointing to the interaction point) of $24 \times 20\,\mathrm{cm}^2$. For high spatial resolution, the EMC-section is split into 4 cells of $5 \times 20\,\mathrm{cm}^2$ (in the RCAL into 2 cells of $10 \times 20\,\mathrm{cm}^2$), whereas the HAC-cells cover the full cross section of the tower. The scintillation light is passed through wavelength shifters to photomultipliers at the back-side of the calorimeters. Each cell is read out at two sides; this allows a position measurement of the energy deposit in one axis within each cell. Neglecting this position measurement, the resulting redundancy permits the measurement of signals in a cell even if one of the two photomultipliers is broken. As an example the design of one FCAL module (the mechanical structure to combine towers) is shown in Fig. 2.9.

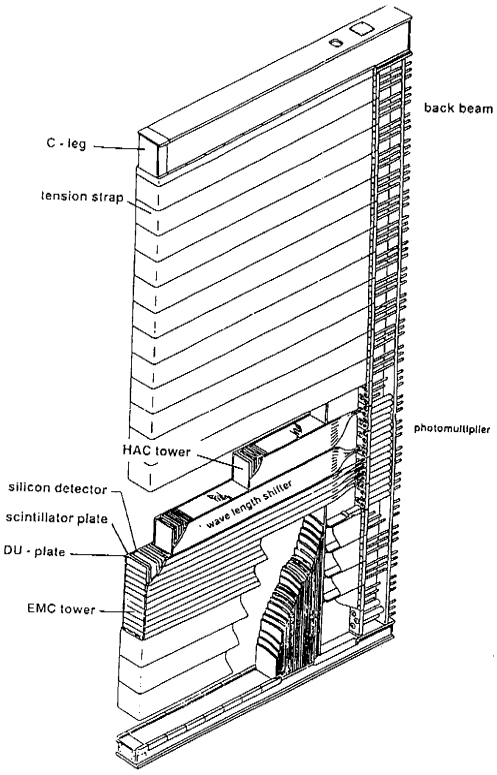

Figure 2.9: View of an FCAL module.

2.3 Detectors for particle identification

Several components of ZEUS allow the separation between different particles. Neutrinos are not measurable at ZEUS; the existence of neutrinos in an event can only be estimated by the lack of measured (transverse) energy [7].

Muons are easily distinguishable from other particles as they traverse much more matter than any other long lived particles. Most of the particles measured by the outer detector components are muons.

Within the calorimeter one can distinguish electromagnetically and hadronically interacting particles by their shower shape. The electromagnetic interaction length is ≈ 20 times smaller than the hadronic one, therefore hadronic showers are much deeper and wider than electromagnetic showers. As already mentioned several detector components make use of the different shower shapes. These approaches allow to separate electrons (and photons) from other particles, but especially if it comes to particles with low momenta the separation power is small; the difference in shower shapes decreases. Especially antiparticles which annihilate in the calorimeter leave a shower very similar to an electromagnetic one. For the particle identification of low momentum tracks, the calorimetric components are helpful devices but their separation power is not high enough; the outcome of their particle identification needs to be combined with the result from other components.

The tracking detectors allow the differential measurement of the energy loss with propagation distance. This is valid for silicon detectors as well as for drift chambers. The energy loss per track length dE/dx is related to the mass of the particle (see Sect. 3.1); this relation can be used for particle identification. Compared to the measurement of shower shapes in the calorimeter this method is much more sensitive to different hadrons; pions, kaons and protons are distinguishable. Furthermore, the differences between particles and antiparticles are negligible.

As the most important tracking device at ZEUS is the CTD, this dissertation focusses on the dE/dx measurement for particle identification with this component. These investigations are based on tracks reconstructed with the CTD. In the next section the method of reconstructing tracks from single-hit information will be introduced.

2.4 CTD track reconstruction

The raw data which is written to tape during data taking has to be processed for further usage. Part of the processing is the Phase I reconstruction which extracts handy data structures from the raw data. In terms of CTD data this means the reconstruction of particle trajectories from hit patterns. The results of the track reconstruction are stored in ADAMO-tables, which are referred to as processed data. These are the data accessible for analysis issues.

The reconstruction of CTD tracks from raw data (time information from single hits) starts with a track seed, consisting of three CTD hits from an axial superlayer in the outer region of the chamber. These track seeds are extrapolated inwards, gathering additional hits. This procedure is applied iteratively to pick up all track candidates. Tracks with too many shared hits are weeded out. Usually, 85% of a candidate's hits must be unique to it. To enhance the acceptance for photon conversions, this rule is somewhat relaxed if

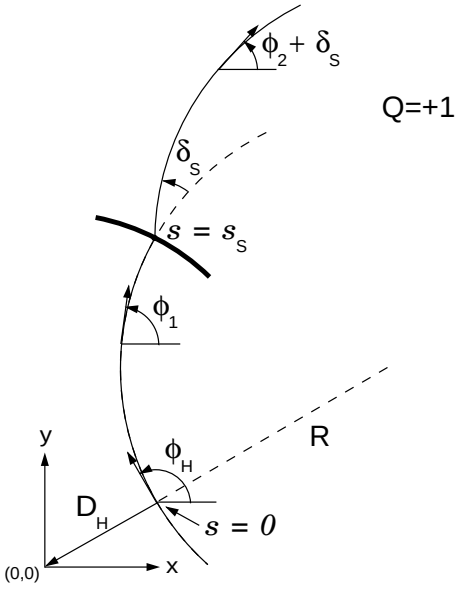

Figure 2.10: A helix for a positively charged track in the xy-plane. [31]

a track candidate spans at least two axial superlayers and shared hits occur only in the innermost of these superlayers.

After picking up all track candidates, each of them is fitted to a 5 parameter helix model. Some hits can be swapped or dropped within this procedure. Consequently most of the track helices end outwards within an axial layer; only less than 1% of all tracks end in stereo layers when all hits in the outermost (axial) layer of these track candidates are rejected during the helix fit procedure.

When the track helices are found, primary and secondary vertices can be determined. Using the vertex as a constraint, the track helices are re-fitted. Track and vertex information is saved in the processed data. The track data saved do not contain information about which wires measured a hit. Only the total number of axial and stereo wire hits as well as the number of the innermost and the outermost superlayer with at least one hit related to the track are saved. Thus working with processed data prevents access to the hit pattern related to a track. A detailed description of the tracking and vertexing algorithms can be found in [31, 32].

As the CTD is located within an almost uniform solenoidal magnetic field, the transversal momentum of charged particles can be extracted from the curvature of the track helix in the xy-plane using

$$p_t[\,\mathrm{GeV}] = 0.3 \cdot B[\,\mathrm{T}] \cdot r[\mathrm{m}] \quad . \tag{2.1}$$

The resolution of p_t for tracks passing all 9 superlayers is parametrised by [33]:

$$\frac{\sigma(p_t)}{p_t} = 0.0067 p_t[\,\mathrm{GeV}] \;\oplus\; 0.0071 \;\oplus\; \frac{0.0011}{p_t[\,\mathrm{GeV}]} \quad . \tag{2.2}$$

This resolution is **not** the same as the mean uncertainty calculated with the covariance matrix of the helix fit. The covariance contains artificial errors build in to improve the efficiency of the tracking algorithm: 'widening' the error for the helix increases the probability to find good hits when extending the initial track seeds to neighbouring superlayers. Therefore the covariance matrix as stored together with the track helix is not the helix covariance in strong mathematical terms. Nevertheless, for some issues used in this thesis the error propagation of the track helix is the best accessible approximation of the error

on helix-related parameters if one needs them track-by-track (in contrast to an expected mean error for all tracks).

The polar angle θ of a track is determined using the z-coordinates of the hits, which are measured by time differences (z-by-timing) and by the stereo superlayers (stereo pattern recognition). The 3-dimensional momentum is obtained by

$$|\boldsymbol{p}| = \frac{p_t}{\sin\theta} \quad . \tag{2.3}$$

The parameters for the track helix as shown in Fig. 2.10 are:

1. θ_H: angle in the xy-plane between the x-axis and the tangent to the helix in its point of closest approach to $(x, y) = (0, 0)$;
2. Q/R: the charge of the particle over the radius of the helix in the xy-plane;
3. QD_H: the charge of the particle times the distance of closest approach to $(0, 0)$ in xy;
4. Z_H: z-coordinate of the point of closest approach;
5. $\cot\theta$: the cotangens of the dip-angle of the helix.

These parameters are accessible in processed data and used in this analysis for reconstructing the track topology [6].

2.5 CTD dE/dx reconstruction

A characteristic distribution of measurement of the ionisation per track length, dE/dx, on a single wire can be seen in Fig. 2.11. The distribution is wide and asymmetric for values below 220 FADC-counts. Due to limitations of the read-out with 8 bits, several hits are measured in saturation, populating a high spike around 230 FADC-counts. Hits with more than 200 FADC-counts are considered saturated.

Within the Phase I reconstruction several corrections are applied to the measured dE/dx of single hits (see Sect. 4.2.1.1). In addition screening cuts remove single hits from the calculation of the mean dE/dx for the tracks. They are supposed to reject hits, if their dE/dx is expected to be badly measured. Hits are ignored if:

- the trajectory has turned nearly parallel to the measurement plane;
- the drift distance is near a cell boundary;
- the pulse height of the hit is distorted by an earlier hit (within 100 ns) on the same sense wire.

[6] Within the last years several different track reconstruction models were delevoped at ZEUS. This analysis is based on the regular tracking, saved in the ADAMO-table VCTRHL. This is convenient because VCTRHL is the only table where dE/dx measurements are saved at ZEUS. Using another tracking algorithm implies to find a proper matching with VCTRHL-tracks in order to access the measured dE/dx.

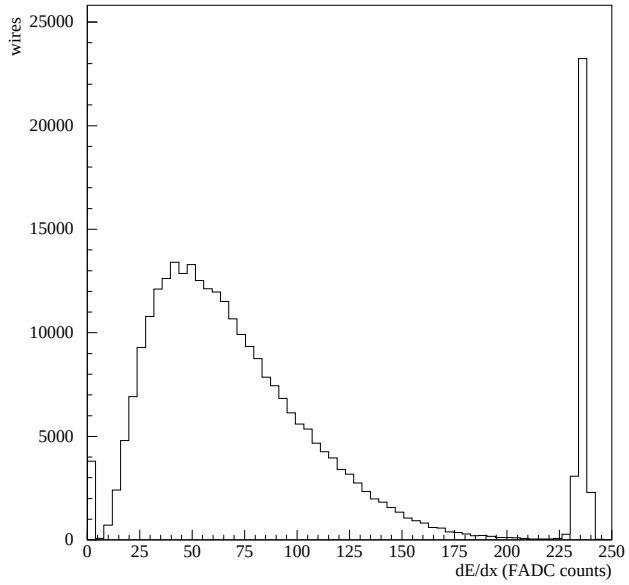

Figure 2.11: Distribution of dE/dx measured on a single wire for a sample of minimum ionising pions. [34]

Finally, the corrected single hit signals are combined into the track dE/dx, using a truncated mean method. The hits which pass the previously mentioned cuts are sorted by their signal size. The measured dE/dx_{FADC} is their mean value after rejecting the lowest 10% and the highest 30% of the measured and corrected dE/dx_{hit}-values. If more than 30% of all hits are saturated, all saturated ones are rejected. For such tracks an additional correction is applied to render their mean value compatible with the 'usual' one. For details see Sect. 4.2.1.4.

The reasons for the truncation are:

- The response of the CTD for very low signals is not well understood. Rejecting the lowest 10% of the measured hits saves the measured dE/dx_{FADC} not to be spoiled by mismeasurements.
- The distribution of dE/dx-measurements for single hits has a long tail to high values. For small samples (at most 72 hits for one track) single hits with very high measurements have a stong influence on the mean value of these samples. Such 'outliers' cause strong fluctuations in the mean value. These fluctuations are strongly reduced by the truncation method.
- The probability density of the signals for single hits is approximatly given by a LANDAU-distribution L_s (see Sect. 3.2), which has an infinite first moment: $\int_{-\infty}^{\infty} \lambda \cdot L_s(\lambda) d\lambda = \infty$. This formula describes the previously mentioned effect of 'outliers' to dominate the mean value of a sample. The upper truncation cancels this problem: integrating L_s to an upper limit, given by a certain area fraction under L_s, leads to a well defined first moment.

Chapter 3

Predictions for the specific energy loss

In this chapter theoretical predictions for the energy loss per path length, dE/dx, of a charged particle passing through matter will be introduced. The first section focuses on the dependence of the mean energy loss on the particle's speed or rather its $\beta\gamma$-value, introducing a functional description of $dE/dx(\beta\gamma)$. This function contains parameters which have to be fixed by a fit to the measured data as shown in the second section. The distribution of the energy loss in a thin medium is spread widely. Whereas the first section deals with the mean energy loss, in the second section LANDAU's calculation of the probability density for a certain energy loss (at fixed $\beta\gamma$) will be introduced.

The nomenclature rules used in this thesis will be declared in the third section.

3.1 The BETHE-BLOCH curve

Based on ERNEST RUTHERFORD's work about the structure of the atom [35], in 1913 NILS BOHR published his calculations about the speed decrease of charged particles passing through matter [36]. The transfer of kinetic energy from the moving particle to the surrounding matter was calculated using classical mechanics, which limits the validity of this calculation to particles with low momenta. In 1930 and 1932 HANS BETHE [37] and CHRISTIAN MØLLER [38] introduced the first calculation for the mean energy loss based on the quantum mechanical principles of the scattering theory [39]. BETHE's calculation is valid for relativistic particles:

$$-\frac{dE}{dX} = \frac{4\pi e^4 N_a \rho \sum Z}{m_e c^2 \sum A} \frac{1}{\beta^2} z^2 \left(\ln \frac{2 m_e c^2 \beta^2 \gamma^2}{I} - \beta^2 \right) \quad ,^{1} \tag{3.1}$$

where z denotes the charge of the travelling particle, N_a the AVOGADRO number, ρ the density of electrons in the matter traversed, $\sum Z$ the sum of the atomic numbers in the molecule of the substance and $\sum A$ the sum of the atomic weights. The symbol I denotes the mean excitation energy of the atom in matter. The calculation of Eqn. 3.1 makes use of a kinematic limit which is valid only for traversing particles much heavier than the

[1] In the following the minus sign in $-dE/dX$ will be skipped; The label dE/dX will represent the (negative) energy loss per path length.

scattered particles (electrons of the gas atoms), therefore this equation is not applicable for electrons.

Felix Bloch calculated the values of I using the Thomas-Fermi theory of the atom, comprising Bohr's and Bethe's results as the non-relativistic and the relativistic limits [40]. The value of I can be calculated for simple atoms, but it has most often been considered as a free parameter to be fitted from measurements. A collection of such determinations calculated by Stephen M. Seltzer and Martin J. Berger is contained in [41].

For small $\beta\gamma$ the β^2-term dominates Eqn. 3.1; dE/dx falls with increasing $\beta\gamma$. The logarithmic term describes the relativistic rise (high $\beta\gamma$). Enrico Fermi stated, that for large γ the polarisation of the medium by the traversing particle shields its field ('density effect') [42], causing a reduction of the relativistic rise. More precise calculations of the correction term $\delta(\gamma)$ for the density effect were carried out by Rudolf M. Sternheimer [43] as well as by Walter H. Barkas and Martin J. Berger [44].

As Eqn. 3.1 shows, the ionisation dE/dX scales with the density of the traversed matter, i.e. with the pressure of the gas in case of a drift chamber. It is customary to substitute for the length X a reduced length $x = \rho X$ measured in $\mathrm{g/cm^2}$ in order to simplify the comparison between different detector materials. The reduced energy loss can be written as

$$\frac{dE}{dx} = \frac{1}{\rho}\frac{dE}{dX} \quad .$$

The ZEUS CTD is operating with atmospheric pressure of the gas. The dependence of the ionisation measurement on the gas pressure will be compensated numerically (see Sect. 4.2.1.2); for simplicity, the pressure-dependence will be ignored in the formulae used in this thesis. The term dE/dx will be used for the specific ionisation energy loss.

The Bethe-Bloch formula describes the energy loss of a particle passing through matter including all high-energy transfers which are kinematically possible. Above a certain transfer energy, electrons are knocked out of a gas atom forming secondary tracks. Such δ-electrons do not contribute to the first track anymore. If their energy is low, the magnetic field of the drift chamber forces them to remain within the sensitive area of the same signal wire, where they were produced. In this case they will loose all their energy by ionisation of the gas, i.e. their energy loss will contribute to the measured signal. In case of a higher energy δ-electron, its track will leave the CTD-cell and the corresponding energy will **not** contribute to the measurement. In order to properly describe the energy loss along a track as measured by a drift chamber, one has to introduce a cut-off E_{max} for the single-interaction energy transfer. The modified Bethe-Bloch formula reads as follows [45]:

$$\left\langle \frac{dE}{dx} \right\rangle_{restricted} = \frac{4\pi e^4 N_a \sum Z}{m_e c^2 \sum A} \frac{1}{\beta^2} z^2 \left(\ln \frac{\sqrt{2 m_e c^2 E_{max}}\beta\gamma}{I} - \frac{\beta^2}{2} - \frac{\delta(\beta)}{2} \right) \quad . \tag{3.2}$$

In contrast to Eqn. 3.1 this equation is also applicable for electrons because the different kinematic limits have been replaced by the common cut-off E_{max}.

In the limit $\beta \to 1$ the γ-dependence cancels and the restricted energy loss reaches the 'Fermi plateau'. This independence of the mean measurable energy loss per path length on $\beta\gamma$ for $\beta\gamma \to \infty$ is characteristic for a thin absorber.

In 1980 Wade W.M. Allison and John H. Cobb published calculations on the $\beta\gamma$-dependence of the energy loss, based on the photo-absorption ionisation model (PAI),

achieving an accuracy of a few percent over 4 orders of magnitude in $\beta\gamma$ [46]. Based on this model, WALTER BLUM and LUIGI ROLANDI give a parametrisation for the description of measured ionisation curves [47]:

$$\frac{dE}{dx} = \frac{p_1}{\beta^{p_4}} \left(p_2 - \beta^{p_4} - \ln \left(p_3 + \frac{1}{(\beta\gamma)^{p_5}} \right) \right) \quad . \tag{3.3}$$

The 5 parameters p_i have to be determined by a fit to the measurements.

3.2 The LANDAU distribution

A charged particle passing through matter looses energy by its interaction with single atoms. These interactions are separable and the energy loss in a single interaction can vary over a wide range. Thus for thin layers of matter the possible energy loss within this layer is widely spread. In a wire chamber like the ZEUS CTD such a layer corresponds to the gas volume from where the signal is collected at one signal wire, i.e the condition 'thin layer' is obviously fulfilled. To describe the signal at a single wire theoretically one has to calculate the probability density for the energy loss Δ within such a layer. This calculation was done by LEV D. LANDAU [48]:

$$f(x,\Delta) = \frac{1}{2\pi\imath} \int_{+\imath\infty+\sigma}^{-\imath\infty+\sigma} \exp \left[p\Delta - x \int_0^\infty w(E) \left(1 - e^{-pE}\right) dE \right] dp \quad ,$$

where $f(x,\Delta)$ denotes the probability density for an energy loss Δ in a layer of thickness x and $w(E)$ is the probability of an energy loss E in the medium. Up to this point the equation is an exact calculation of the ionisation energy loss, but in order to solve it one has to know the function $w(E)$, which describes the ionisation probability at atomic level. Refering to MILTON STANLEY LIVINGSTON and HANS BETHE [49] the function

$$w(E) = \frac{2\pi e^4 N_a \rho \sum Z}{m_e c^2 \sum A} \frac{1}{\beta^2} \frac{1}{E^2}$$

(using the same nomenclature as for Eqn. 3.1) was inserted, finding a generalised form for the energy loss probability

$$f(x,\Delta) =: f(\lambda) = \frac{1}{\sqrt{2\pi}} e^{-\frac{1}{2}\left(\lambda + e^{-\lambda}\right)} \tag{3.4}$$

with

$$\begin{aligned} \lambda &= \frac{\Delta - \Delta_0}{\xi} \quad , \\ \xi &= x \frac{2\pi e^4 c^2 N_a \rho \sum Z}{m_e \sum A} \frac{1}{\beta^2} \quad , \end{aligned}$$

where Δ_0 denotes the most probable energy loss. It is remarkable, that λ scales with β^2, i.e. the width of the density distribution $f(\lambda)$ scales with β^2, too.

The shape of $f(\lambda)$ will be used in this thesis to represent the probability distribution of the signal height for single hits. The (truncated) mean value (corresponding to Δ_0) is determined by the BETHE-BLOCH prediction as introduced in Sect. 4.4; the width (proportional to ξ^{-1}) will be extracted from data.

3.3 Nomenclature rules

Some concepts are used for a uniform nomenclature within this thesis. These nomenclature rules are introduced here.

Investigating the dependence of a statistically distributed measurement on a certain parameter leads to two-dimensional plots. For example, the dependence of the measured dE/dx on the momentum p can be displayed in a scatter plot of dE/dx versus p. In many cases one does not want to focus on this two-dimensional distribution, but on the p-dependence of the mean measured dE/dx. This corresponds to a one-dimensional graph of $\langle dE/dx \rangle$ in bins of p; each bin of the histogram shows the mean value of all measured dE/dx values of tracks in the corresponding p-bin and the error of the entry in the histogram represents the uncertainty of this mean value. In this thesis such a kind of plot will be called a 'profile plot'.

As long as not explicitly declared differently in the text, the symbol dE/dx always represents the specific energy loss for the whole track (truncated mean of dE/dx_{hit} values of participating hits). The symbol dE/dx_{mips} is applied to denote the measured dE/dx_{meas} divided by the run-by-run factor f_r (see Sect. 4.2.1.2). The term dE/dx_{norm} stands for the normalised dE/dx, which is the measured dE/dx_{meas} over the expected dE/dx_{exp} according to the Bethe-Bloch shaped dependence on $\beta\gamma$. Therefore, in dE/dx_{norm} the momentum dependence of dE/dx is removed and its value should be 1.

Very often one has to deal with hit related variables, e.g. the hit position z. The corrections which will be introduced in the next chapters are not working at hit- but at track-level. This implies, that representatives for hit variables at track-level are needed. They are built up by using the track helix to calculate hit parameters at the position of the signal wires (possible hits) and taking their average value. The nomenclature for this is to use a bar over the variable, e.g. $\bar{z}$ stands for the average value of the z-positions of all possible hits along the wire.

To find systematic dependencies between variables one has to look at distributions containing many tracks. The investigated information is given in the mean value of the distribution of one variable in bins of the other one. This kind of mean value of a profile is indicated with angle brackets, e.g. $\langle \bar{z} \rangle$ stands for the mean value of $\bar{z}$ of a sample of tracks.

For simplicity the angle brackets are dropped as long as the context clearly shows, that the mean of a sample of many tracks is meant. Usually this is the case in plots, where the dependence of dE/dx on some variables is shown. If a clear separation between single track dE/dx and the mean $\langle dE/dx \rangle$ of a track sample is needed for clarification, the angle brackets are used.

An important distinction has been kept between the ionisation rate dE/dx and the signal height s. Whereas dE/dx always stands for the ionisation per path-length, the signal height is used for the pulse height at the wire. Both are related by the track topology (projection of the particle's path onto the wire) and correction factors (related to track topology or other parameters).

A compilation of frequently used variables can be found in App. A.

Chapter 4

Corrections of dE/dx for the ZEUS CTD

In this chapter twelve corrections of the dE/dx measurement will be introduced and the method of their optimisation will be presented.

In order to tune the dE/dx measurement on a track, one needs to prepare track data samples with a known expected ionisation. As the ionisation itself depends on $\beta\gamma = p/m$, in a tuning sample the mass of the particles causing the tracks has to be known.

There are several independent mechanisms affecting the measurement of dE/dx. They all have in common, that there are track-specific variables, which separate the strength of the systematic influence on the dE/dx-measurement of these effects (for example, the bias on the measured dE/dx due to a threshold-effect for sure depends on the height of the signal). The comparison between the measured dE/dx_{meas} and a prediction dE/dx_{exp} in bins of these variables offers a handle to measure the size of the effect and to calculate a corresponding correction factor.

The algorithm for the optimisation of the dE/dx corrections is based on the tuning samples (with known particle species) as well as on a prediction of the Bethe-Bloch curve dE/dx_{exp}. The output of this algorithm is a set of parameters to be used for the dE/dx-correction.

The Bethe-Bloch prediction dE/dx_{exp} is the result of a fit of Eqn. 3.3 to dE/dx-data and can only be determined with already corrected dE/dx data.

Thus, there are two independent calculations, each of them requiring the result of the other one. In order to solve this circular dependence one benefits from the fact, that the method to find proper dE/dx corrections is robust against a slightly wrong Bethe-Bloch prediction. Therefore in the beginning any rather well measured Bethe-Bloch curve can be used to optimise the dE/dx corrections. The corrections try to reproduce the Bethe-Bloch curve with the corrected dE/dx measurements; in case of a slightly wrong Bethe-Bloch prediction the distribution of corrected dE/dx versus $\beta\gamma$ is shifted from the applied (wrong) Bethe-Bloch curve towards the correct one. Consequently one extracts a 'better' Bethe-Bloch prediction from these data. The loop is closed by optimising again the dE/dx corrections, this time using this 'better' Bethe-Bloch curve. This procedure converges quite fast. After a few iterations the Bethe-Bloch prediction as well as the dE/dx corrections do not change anymore. At this point both represent the final result. The general flow of the described procedure is illustrated in Fig. 4.1.

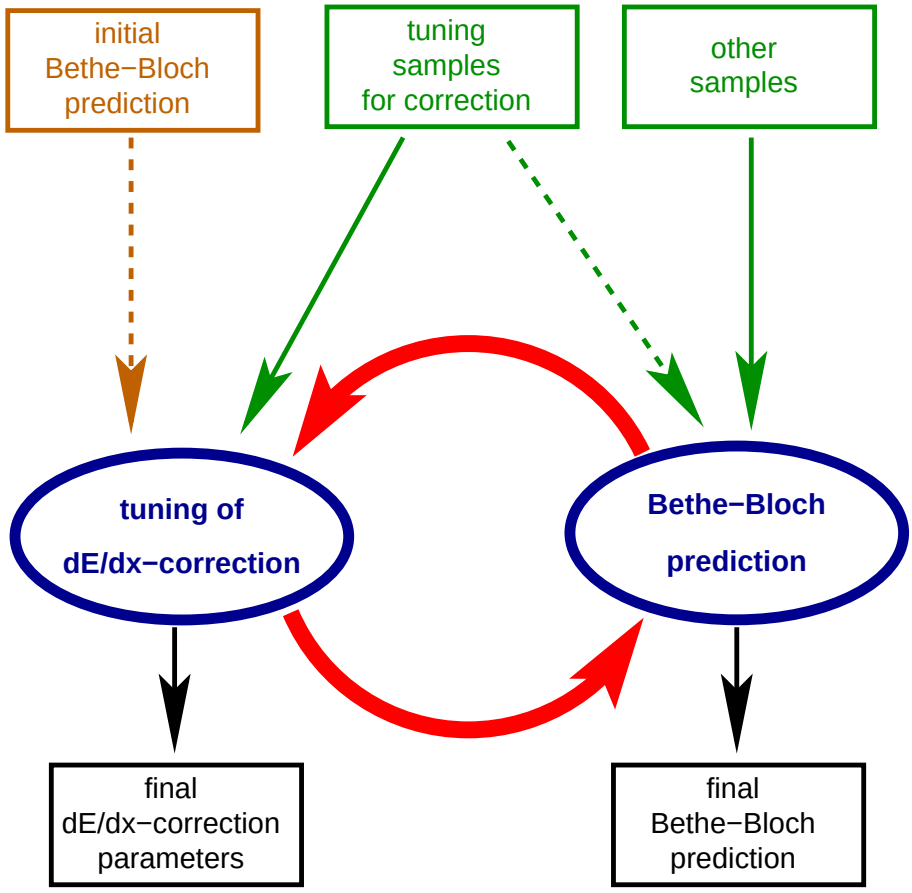

Figure 4.1: Sequence of operations for tuning the dE/dx corrections as well as the predicted BETHE-BLOCH curve dE/dx_{exp}.

The data samples, which will be introduced in Sect. 4.1, are separated into two groups: corrections-tuning samples and other samples. Within the optimisation algorithm only the corrections-tuning samples are used. For these dE/dx corrections the other samples are utilised for test purposes only. In order to minimise the impact of systematic shifts in the dE/dx corrections on the BETHE-BLOCH prediction, this prediction is dominated by the other data samples. Details will be given in Sect. 4.4. The meaning of the two sample groups is summarised in Tab. 4.1.

	corrections-tuning samples	other data samples
dE/dx corrections tuning	used for tuning	for test purposes only
BETHE-BLOCH fit	partially used	main contribution

Table 4.1: Splitting of data samples into groups and their meaning for the corrections and the BETHE-BLOCH prediction.

In Sect. 4.2 the identified effects influencing the dE/dx measurements will be introduced. The method of correcting for them will be the heart of this chapter and is presented in Sect. 4.3. In Sect. 4.4 one finds the result of the BETHE-BLOCH fit from the previously mentioned iterative procedure.

4.1 Track data samples

In order to tune the dE/dx measurement on a track, one needs to prepare track data samples with a known expected ionisation. As the ionisation itself depends on $\beta\gamma = p/m$, in a tuning sample the mass of the particles causing the tracks has to be known. Particles which produce tuning tracks therefore need to be identified without using their dE/dx.

It is possible to obtain such samples by exploiting well known and understood decay channels or production processes. For tuning the dE/dx measurements a maximised sample purity is at premium, the sample selection focuses on this demand. In contrast to other analyses, there is no need to know or understand the selection efficiency.

In order to properly investigate the behaviour of the CTD, huge tuning samples must be available; even in less populated kinematic ranges or geometrical regions statistics of the tuning samples have to be large enough to show systematic effects. This may be the reason behind the fact, that such an approach for CTD dE/dx calibration is tried only now.

The first two sections 4.1.1 and 4.1.2 will describe the samples for corrections tuning and the other samples. Details about their selection are given in App. B. Section 4.1.3 gives a short overview on purity and size of the samples. The next two sections 4.1.4 and 4.1.5 will introduce and motivate general track quality cuts and a cut against saturation effects. The separation of the data into different data taking periods will be described in the last section 4.1.6.

4.1.1 Corrections-tuning samples

If the samples used for tuning the dE/dx measurement depend on the Bethe-Bloch curve, it is very difficult or even impossible to decide, if deviations between the measurement and the prediction lead to an effect on the measurement to be corrected for or to a wrong prediction dE/dx_{exp}. Therefore, for tuning the dE/dx measurement it is important

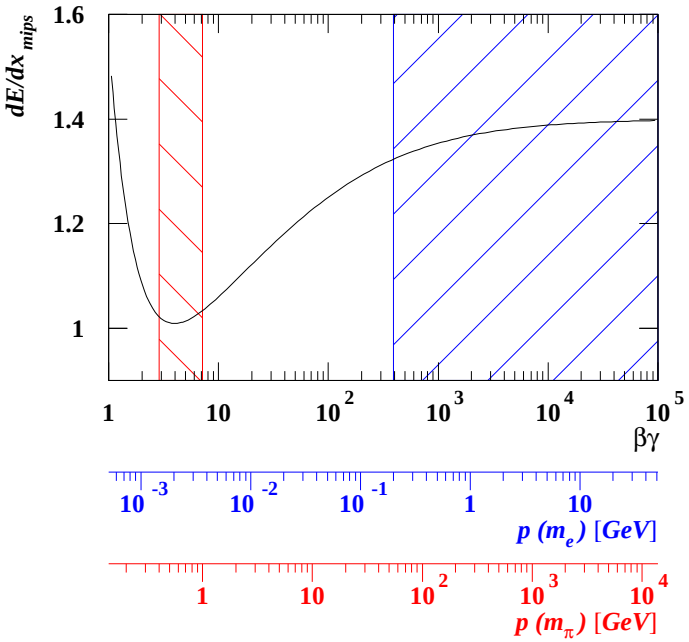

Figure 4.2: Ranges in $\beta\gamma$ versus dE/dx_{mips}, covered by the tuning samples used. The two sample ranges are indicated by the hashed areas. The electron tuning sample covers the plateau of the Bethe-Bloch curve; the range of the pion tuning sample matches with the minimum of the dE/dx prediction.

to use samples, which have only a minor dependence on the BETHE-BLOCH curve. This reduces the impact of a systematically wrong description of this theoretical prediction. It was already mentioned, that electrons fulfil this criterion as they are found at very high $\beta\gamma$ values, where the BETHE-BLOCH curve forms a plateau as shown in Fig. 4.2. Therefore all measured electrons have roughly the same expected mean ionisation. For simplicity, the combination of all 3 used samples for electrons will be called 'the electron tuning sample'.

Another useful region of the BETHE-BLOCH curve is that around its minimum (Fig. 4.2). Within a fairly wide range in $\beta\gamma$ about the minimum the variation of the expected dE/dx is very small. It makes sense to use a pion sample for tuning issues in this range. As most of the tracks are pions anyway, most of the background tracks in such samples are pions, too. This helps a lot to fulfil the criterion of high purity in terms of the particle type in the tuning samples. In this analysis a $K^0 \to \pi^+\pi^-$ sample with pion track momenta in the range $400\,\text{MeV} < p < 1000\,\text{MeV}$ is used as a second tuning sample, which in the following will be called 'the pion tuning sample'.

4.1.1.1 Electron samples

Observable electrons can be obtained from different sources. The electron tuning sample is composed from 3 different sources:

1. **Photon conversion electrons**,
   available with high statistics in the low momentum regime.

   Photons which are passing through matter may convert into an electron-positron pair. As photons are massless, the opening angle between these two tracks at their point of origin vanishes. This, together with the fact that appreciable amounts of matter are situated far away from the nominal interaction point, causes a clear signature for photon conversions. There exists already a well-tested software package, named CONVERT2 [50], to identify conversion pairs (see App. C.3). This software package was tuned for HERA I data. Investigations have been done to check the purity of the photon conversion sample for HERA II data to ensure, that the used tuning sample is clean enough for this purpose. Nevertheless it should be kept in mind, that a future re-tuning of CONVERT2 for new data may also have an influence on this correction package.

   The point of closest approach between the two helices indicates the position, where the photon conversion occurred. This information can be used for various cleaning cuts. As photon conversions can only happen within matter this point has to be in an area of high matter density. Even more so, by using the momenta of both tracks at this point, it is possible to calculate the momentum vector of the parent photon. Most of the photons are produced in decays of π^0's, which are emerging from the primary interaction point. Therefore the distance of closest approach between the reconstructed photon direction and the primary vertex has to be small.

   Fig. 4.3 shows the origin of photon conversions in the xy-plane for HERA I data. This plot looks like a 'dead material map'. It clearly shows the two rings of the beampipe and the CTD inner wall. Inside the CTD the wires of the first superlayer are visible. In the gap between CTD and beampipe some cables, which connect FTD

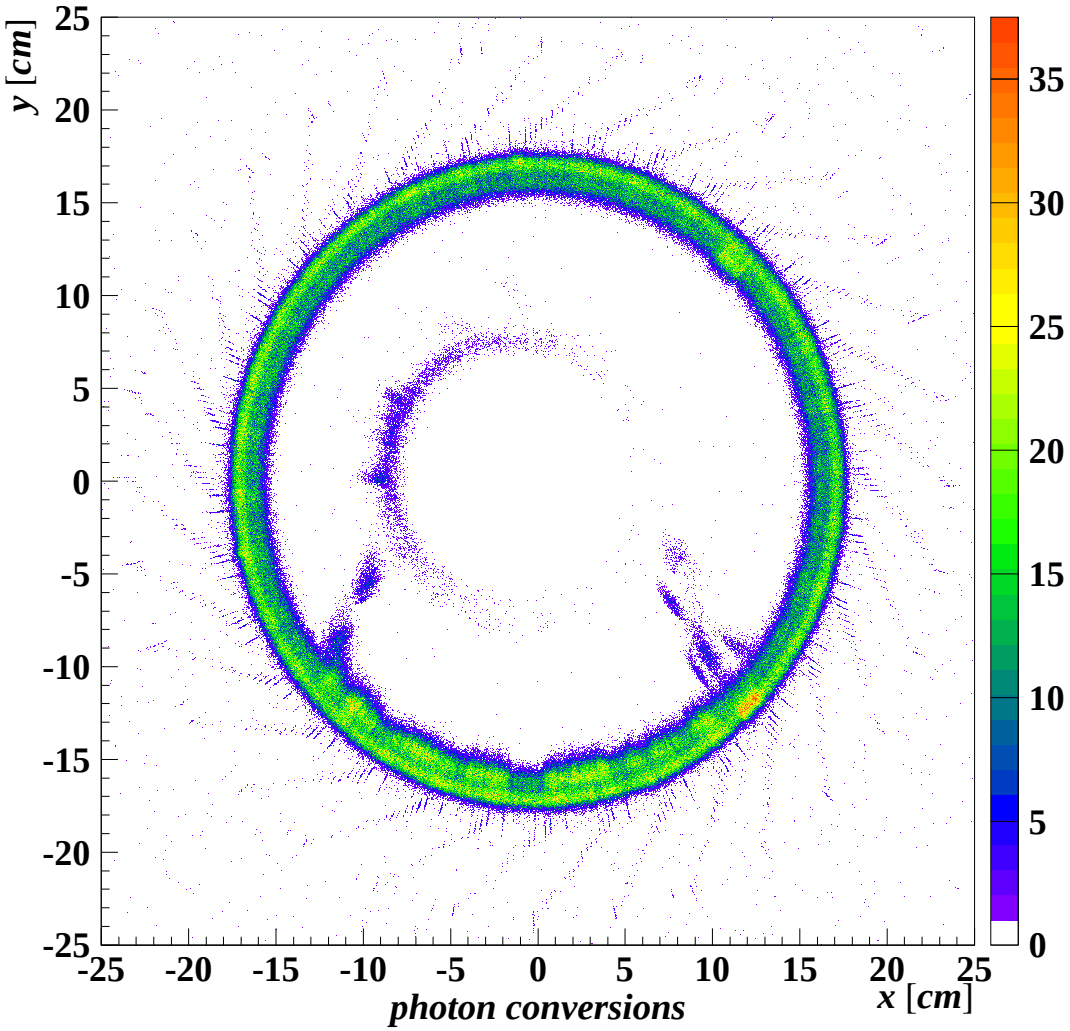

Figure 4.3: Sources of photon conversions in the xy-plane using the HERA I data sample, without a cut on the xy-position of the conversion.

and RTD, protrude. In the centre, a circle of 5 cm radius shows no candidates. This is an artefact of CONVERT2 which searches only for conversions outside this circle.

The photon conversion sample is the biggest and most important electron sample for this analysis.

2. $J/\Psi \to e^+e^-$ **decays**,
   available with low statistics (in case of a selection with high purity), covering higher momenta than photon conversions. Even with strong selection cuts, the purity of this sample is significantly lower than for the other electron samples. This is in particular true for HERA II data (no dedicated J/ψ trigger).

3. **DIS electrons**,
   covering the momentum regime beyond 5.5 GeV but strictly limited in their coverage of the polar angle (backward tracks) and available only with one charge sign within each data taking period.

4.1.1.2 $K^0 \to \pi^+\pi^-$ sample

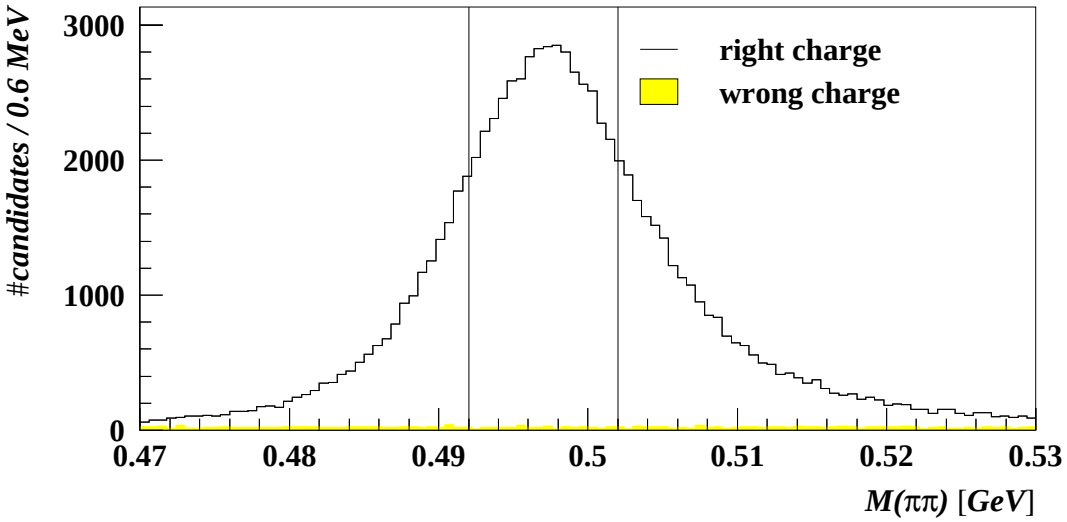

Figure 4.4: Invariant mass of K^0 candidates. The wrong-charge combinations give an estimate for the amount of combinatorial background in the sample. The vertical lines indicate the mass range used for the tuning sample.

As mentioned above, the second important source for tuning samples are the pions. They cover a big part of the BETHE-BLOCH curve and they are available with high statistics. The $K^0 \to \pi^+\pi^-$ sample is used for dE/dx tuning, as it has the highest statistics achievable with high purity and the best geometrical coverage of all pion samples. As shown in Fig. 4.4, the sample has a very high purity of about 99%. For tuning only pions in the momentum range $400\,\text{MeV} < p < 1000\,\text{MeV}$ are used.

4.1.2 Other samples

Several other samples were generated for testing the behaviour of the dE/dx tuning as well as for extracting the correct BETHE-BLOCH curve. They are not used for the calibration itself, so they are a tool for an independent test. They cover $\beta\gamma$ ranges different from the tuning samples, like the proton and the muon sample, and they have different event topologies. Therefore they can be used for powerful stability tests for any corrections. Available samples are:

- **$K^0 \to \pi^+\pi^-$ decays**

  Pions in the $K^0 \to \pi^+\pi^-$ sample, which are not used for tuning, are available in the test sample. This are pions with $p < 400\,\text{MeV}$ or $p > 1000\,\text{MeV}$.

- **$\rho^0 \to \pi^+\pi^-$ decays**

  Like the $K^0 \to \pi^+\pi^-$ sample, the exclusive $\rho^0 \to \pi^+\pi^-$ sample is of high statistics as well. But in contrast to the K^0, the ρ^0 resonance is very wide and therefore the purity of this sample is not as high as for the K^0 decay and it is difficult to quantise the purity properly. For this reason the ρ^0 sample is only used for test purposes.

As it is an exclusive sample with high statistics, it can be used to test the dE/dx corrections for events with low track multiplicity.

- $\Phi \to K^+K^-$ **decays**

  This is the main source for kaons. Especially at low momenta the background pollution by pions is high.

- $\Lambda \to p\pi$ **decays**

  The chain $\Lambda \to p\pi$ is another source of pions and the only source of protons.

- $D^* \to K\pi\pi_s$ **decays**

  The D^*-decays are yet another source of kaons and pions. In order to achieve the needed purity in the sample, rather strong cuts have to be applied. As a side effect of these cuts, in comparison to the others, the statistics of this sample is quite small. Anyway, it is not possible to reach a purity of the same level as for the other samples peresented. Therefore it is not used for tuning.

- **Cosmic muons**

  This is quite an interesting test sample. As cosmics are not related to the bunch crossings, they have a different timing than collision events. Furthermore, they are not related to the interaction region of the ZEUS detector. As long as they pass the trigger (which of course gives an indirect but not too strong relation to the bunch crossing time and the centre of the detector) they can be found everywhere in the CTD. So they are a source for topologically problematic tracks. Testing the corrections with this sample offers the possibility of testing their stability under extreme conditions.

4.1.3 Purity and size of data samples

Special attention has been paid to generate data samples with high purity. Details about the measurement of the purity can be found in App. B; in this section only the results will be summarised in Tab. 4.2.

The samples are used as clean samples for particle types; their source (decay chain) is meaningless. Consequently, not the purity of the sample selection is the relevant quantity, but the purity of the particle type. This makes an important difference for the pion samples: as about 80% of all particles are pions, only 1/5 of the background candidates from the selection are background in these samples in terms of the particle type. In case of the pion samples Tab. 4.2 distinguishes between the sample selection contamination and the particle type contamination. For the other samples this difference is small and therefore neglected, which renders the estimate of the sample-contamination even more conservative.

The number of tracks selected in each sample are also shown in Tab. 4.2. The size of the samples varies within 3 orders of magnitude.

sample	sample contamination		particle type contamination		number of candidates	
	HERA I	HERA II	HERA I	HERA II	HERA I	HERA II
corrections tuning samples						
e from photon conv.	0.4%	0.4%	0.4%	0.4%	1,767,490	531,661
e from J/ψ-decay	1.7%	6.5%	1.7%	6.5%	24,968	565
e from DIS	$< 0.1\%$	$< 0.1\%$	$< 0.1\%$	$< 0.1\%$	35,146	58,209
π from K^0-decay	1.3%	2.1%	0.3%	0.4%	3,072,338	3,446,934
other samples						
π from K^0-decay	1.7%	2.5%	0.3%	0.5%	2,876,015	3,402,227
π from ρ-decay	9.2%	9.3%	1.8%	1.8%	529,736	79,946
π from Λ-decay	4.2%	10.3%	0.8%	2.1%	653,141	562,037
π from D^*-decay	4.9%	5.9%	1.0%	1.2%	10,749	4,068
K from Φ-decay	12.8%	14.3%	12.8%	14.3%	37,826	6,254
K from D^*-decay	4.9%	5.9%	4.9%	5.9%	5,258	1,999
p from Λ-decay	4.2%	10.3%	4.2%	10.3%	433,320	375,381
cosmic μ	$< 0.1\%$	$< 0.1\%$	$< 0.1\%$	$< 0.1\%$	133,393	381,687

Table 4.2: Estimated background contaminations in the data samples and their count. The contaminations are conservatively calculated upper limits.

4.1.4 General track quality cuts and weighting

For tuning the dE/dx measurement with data, it is mandatory to use only well reconstructed tracks. This demands track quality cuts, which are applied to every track in all samples.

A way to reject obviously wrongly reconstructed tracks is to look at the χ^2/NDF of the track reconstruction. The applied cut is $\chi^2/NDF < 10$.

If the transverse momentum p_t becomes small, its resolution is very bad. Consequently the resolution of the momentum measurement is also bad for such tracks. Tracks with $p_t < 120\,\text{MeV}$ are rejected in this analysis. Furthermore, most of the investigated channels require a stronger cut on p_t. For the purpose of generating the tuning samples stronger requirements on the track quality have to be applied. For them, the p_t-limit is set to 160 MeV for electrons. The pion tuning sample has an intrinsic p_t cut due to the requirement $400\,\text{MeV} < p < 1000\,\text{MeV}$.

This analysis focuses on the measurement of dE/dx of tracks, which is given as the mean value of the dE/dx measurements of contributing hits. The resolution of the track dE/dx measurement is therefore expected to depend on the number of used hits, $\#hits$[1]: $\sigma \approx \frac{1}{\sqrt{\#hits}}$. To take this into account all tracks are weighted proportional to $\#hits$. In addition to a proper weighting one wants to keep track on the total statistics in the investigated plots. This can be fulfilled by normalising the weights to 31, the mean number

[1]In this thesis, 'number of used hits' stands for the number of hits, which are used for the calculation of the track's dE/dx. This is in contrast to the nomenclature in the ZEUS Phase I reconstruction code and the ADAMO table, where used hits stands for the number of hits after truncation but before rejection of saturated hits. The term 'used hits' in this thesis corresponds to the variable `trk_dedxctdnh(trk_ntracks)` in the ZEUS analysis software package ORANGE. (see also Sect. 2.5)

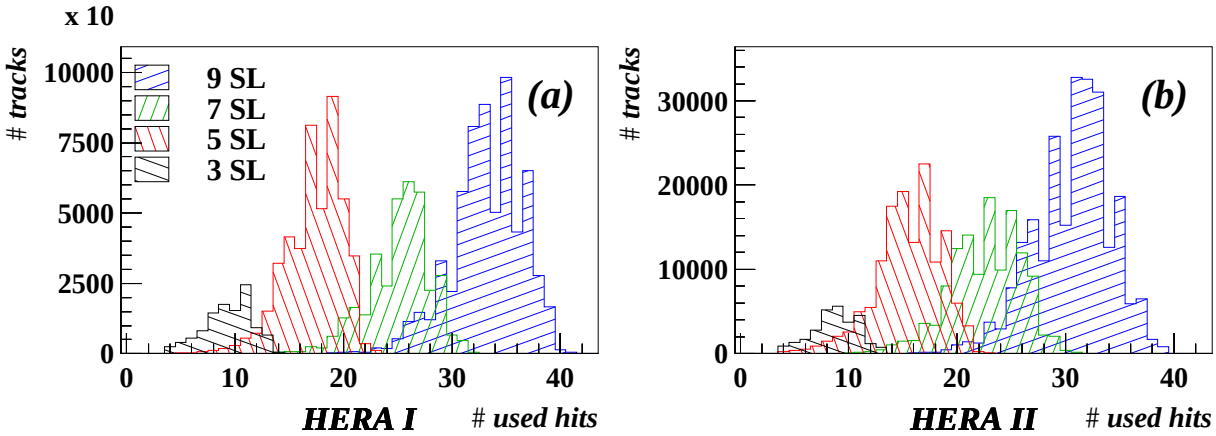

Figure 4.5: Abundance of tracks versus number of used hits for dE/dx calculation, separated by the outermost reached superlayer. The shown samples are photon conversion electrons from (a) HERA I (b) HERA II

of used hits for single tracks, so that the mean weight for one track is approximately = 1. Finally the used weight factor is

$$weight_{track} = \frac{\#hits}{31} \quad . \tag{4.1}$$

If $\#hits$ for one track is very small, the probability for a track being badly reconstructed increases. It is likely, that such wrongly reconstructed tracks will bias the corrections. Therefore a cut on $\#hits$ has to be applied.

Such a cut on $\#hits$ implies further cuts. Fig. 4.5 shows the distribution of $\#hits$ separated for different outermost superlayers. It shows, that for almost any cut on $\#hits$ the majority of the 3-superlayer tracks fall below such a cut limit. As $\#hits$ is correlated with the number of saturated hits, the remaining high end of the distribution is biassed by tracks with a small number of saturated hits and therefore tracks with a small dE/dx. As such a bias will also affect corrections, which are extracted from the remaining sample, it is necessary to cut on the number of superlayers, too. For tuning, tracks are only accepted, if their outermost superlayer is at least the 5^{th}.

The comparison of HERA I and HERA II data in Fig. 4.5 and Fig. 4.6 furthermore shows, that the single hit efficiency has changed between the two periods. The average $\#hits$ became reduced by about 3 hits for 9-superlayer tracks down to 1 hit for tracks ending in the 3^{rd} superlayer.

The cut on $\#hits$ has to be a compromise between high reconstruction quality (high cut level) and small bias on the sample (low cut level). The cut position has been chosen in such a way, that not more than 5% of the 5-superlayer tracks are lost (Fig. 4.6). For HERA II data this leads to a cut at 10 used hits. Using the same limit for HERA I data will remove a much smaller fraction of the 5-superlayer tracks. This could cause a different behaviour of the two periods in the tuning algorithm. In order to render the two samples beforehand as compatible as possible, for HERA I data a higher limit of 13 used hits was chosen. With this limit the fractions of removed tracks are almost the same for both data taking periods.

Only the electrons from photon conversions are used to estimate these cut limits. As

electrons have a higher dE/dx than pions in the tuning samples, they suffer more from saturation. Therefore the electron sample tends to have less hits available for the dE/dx measurement than the pion sample. Consequently, the fraction of rejected pions is smaller than 5%.

To give a better overview, the cuts introduced in this section are listed below:

- $\chi^2_{trackfit}/NDF < 10$;
- $p_t > 120\,\text{MeV}$, for tuning samples $p_t > 160\,\text{MeV}$;
- outermost superlayer ≥ 5;
- number of used hits for dE/dx calculation ≥ 13 for HERA I and ≥ 10 for HERA II.

4.1.5 Cuts to reduce the influence of saturated hits

As will be mentioned in more detail in Chapter 4.2.1.4, tracks with more than 30% saturated hits (saturated tracks) require special handling. A correction function, which transforms their truncated mean into a value, which is comparable to that of other tracks, has been given by Wouter Verkerke [51, 34]. This correction reduces the effect of saturation in the dE/dx measurement from up to 60% to a level of up to 10% as Section 4.3.1.4 will show. Even though this is a big improvement, deviations of up to 10% are much larger than the level of accuracy of the other dE/dx corrections shown in this thesis. To make the tuning of the other corrections independent of this influence, the tuning samples have to be selected in a way, that the influence of saturated tracks is minimised. It is not appropriate to simply restrict the samples to tracks which are not saturated, because this will systematically bias the tuning samples: given a sample of tracks with a certain probability to saturate, its saturated subset will tend to be at the high end of its dE/dx distribution. If these tracks are removed from the sample, the remaining sample will be biased towards smaller values of dE/dx. Using this sample as an input for tuning has the effect that the corrections will try to compensate for this bias and therefore will end up at too high dE/dx values.

The probability to find saturated hits for a given track has to be related to the mean signal expected on each wire. This scales with dE/dx itself as well as with $1/\sin\theta$ which reflects the projection of the track onto the signal wire. Thus a cut on θ appears to be a good choice, especially as tracks with small angles between the wires and the track anyway offer

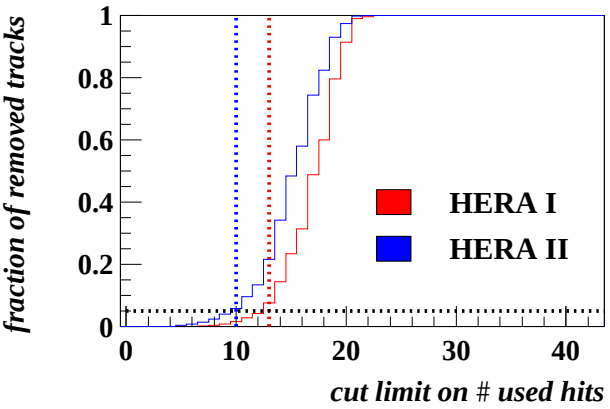

Figure 4.6: Ratio of removed 5-superlayer tracks as a function of the cut limit on $\#hits$, shown for photon conversion electrons. The applied cut limits are indicated.

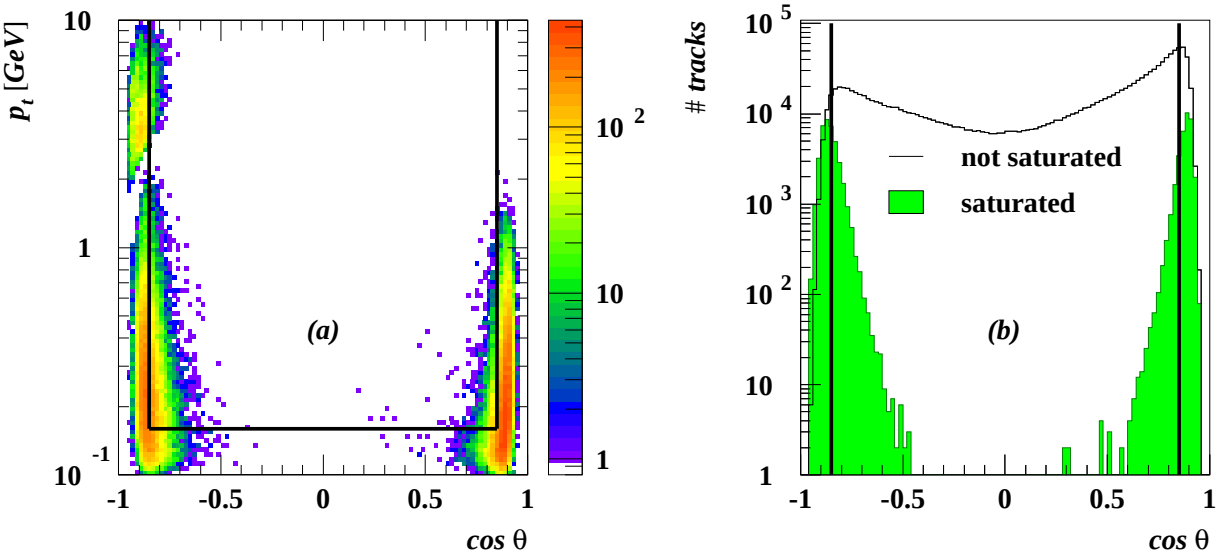

Figure 4.7: (a) Abundance distribution of saturated electron tracks in the (p_t , $\cos\theta$)-plane. (b) Abundance distribution of saturated and not-saturated tracks as a function of $\cos\theta$. The lines indicate cuts for the tuning samples. In both plots only tracks from electrons are shown.

only a small total number of hits and therefore have limited accuracy. Furthermore, low momentum (and therefore also low transverse momentum) tracks can have a very high dE/dx, thus their probability to saturate increases. The dependence of the occurrence of saturated tracks on $\cos\theta$ and p_t is shown in Fig. 4.7. As the pion tuning sample is limited to the minimum of the Bethe-Bloch curve and therefore not very sensitive to saturation, the electron tuning sample was used for these plots. For tuning only tracks with $|\cos\theta| < 0.85$ and $p_t > 160\,\text{MeV}$ were used. In terms of saturated tracks the sample is almost clean after this cut. The fraction of saturated tracks is less than 1% for almost all θ angles. Only in the very backward region this fraction rises up to 5%. This is a compromise between cleaning up the sample and keeping the accessible topological area as big as possible.

4.1.6 Data taking periods

The running conditions for the CTD have varied with time. Therefore it is necessary to split up the data into several time periods.

Except for aging effects, from 1996 until 06/06/2000 the running conditions were stable. As mentioned in Chapter 2.2.1, on 06/06/2000 water was added to the CTD gas mixture to reduce the Malter effect. The resulting reduction of the gain factor was compensated by a change of the high voltage from 06/19/2000 on. The change of drift velocity and Lorentz angle was partially cancelled by using a slightly different gas mixture[2] from 07/17/2000 onwards. As all these changes may have an influence on the dE/dx measurement, therefore the 2000 data are split up into 4 periods.

[2]The ethane content of the mixture was increased by 2% with a corresponding drop in CO_2 whilst keeping the argon concentration constant.

date	run range	Luminosity	name
HERA I			
07/07/1996 - 10/13/1997	20718 - 27889	$38.6\,\mathrm{pb}^{-1}$	1996/1997 e^+-data
09/02/1998 - 04/26/1999	30758 - 32906	$16.7\,\mathrm{pb}^{-1}$	1998/1999 e^--data
07/19/1999 - 12/13/1999	33125 - 34486	$19.7\,\mathrm{pb}^{-1}$	1999 e^+-data
01/22/2000 - 06/06/2000	35031 - 36560	$28.6\,\mathrm{pb}^{-1}$	2000 e^+-data without water
2000 with water			
06/06/2000 - 06/19/2000	36561 - 36720	$2.2\,\mathrm{pb}^{-1}$	2000 e^+-data with water, old HV
06/19/2000 - 07/17/2000	36721 - 37200	$7.8\,\mathrm{pb}^{-1}$	2000 e^+-data with water, new HV
07/17/2000 - 08/23/2000	37201 - 37715	$7.9\,\mathrm{pb}^{-1}$	2000 e^+-data water, new HV, gas
HERA II			
10/30/2003 - 08/12/2004	45783 - 51245	$40.8\,\mathrm{pb}^{-1}$	2003/2004 e^+-data
02/03/2005 - 05/17/2005	53093 - 54700	$47.4\,\mathrm{pb}^{-1}$	2004/2005 e^--data part 1
05/26/2005 - 10/23/2005	54758 - 56831	$62.0\,\mathrm{pb}^{-1}$	2004/2005 e^--data part 2

Table 4.3: Run periods for dE/dx corrections. For each of them a separate set of correction parameters has been generated.

The rest of the data taking is split up into longer periods. This allows the corrections to react on long term aging effects of the CTD. Separate tuning sets are generated for the data-taking periods shown in Tab. 4.3.

The e^--data-taking period 2004/2005 had very high statistics, so it was possible to split it into two parts without loosing accuracy due to limited statistics.

A slightly different treatment has been used for the wire gain corrections. The correction method itself needs more statistics than offered in the short periods with water in 2000. As in addition it is expected that the change of wire gains is a pure ageing effect and as these three periods are all very short, they are combined into one 2000 water period.

The following conventions will be used in this thesis:

- **HERA I data**: all HERA I data between 1996 and 2000 without water in the CTD,
- **HERA II data**: all HERA II data between 2003 and 2005.

4.2 The effects corrected for

In this chapter several effects which have a detrimental impact on the measurement of dE/dx will be introduced. Several of these effects were already partially corrected for in the past, during track reconstruction or within analysis code. With the availability of huge tuning samples, the understanding of such influences can be enhanced tremandously. This also allows for improvement of correction procedures. Other effects not investigated in the past appear as 'new effects'.

This chapter will highlight and explain these effects, giving control plots which prove their existence. The corresponding corrections are the topic of Section 4.3.

4.2.1 Corrections applied formerly

During the first decade of ZEUS data taking several corrections of the dE/dx measurement were introduced and established. This chapter describes how the measurement was corrected and used in analyses until the year 2000.

4.2.1.1 Phase I corrections

Most effects are related to single CTD-wire signals. As this information is not saved in processed data, their corrections are done when processing the events. These corrections are part of the Phase I reconstruction code [32]. The result after applying these corrections can be found in the ADAMO table VCTRHL.

These corrections are based on:

- the trajectory's polar angle θ;
- the relative gain of used sense wires compared to their mean gain;
- each hit's z-position;
- the drift distance of the ionisation electrons within the CTD cell;
- the angle ψ' between the trajectory's azimuthal angle ϕ and the radial direction in the CTD;
- the local Lorentz angle α_l.

4.2.1.2 Run-by-run corrections

There are many different causes for a bias in the dE/dx measurement. Some of these influences may change slowly with time (slowly means, they cause systematic changes between different runs). Very familiar is the influence of the air pressure on the measurement. The CTD is an 'open system', i.e. the gas flow out of the CTD depends on the pressure difference between the air outside and the gas within the CTD. The gas flow into the CTD is constant with time. This means, the gas pressure in the CTD follows with some delay the air pressure outside. As the pressure has an impact on the measured dE/dx, we observe different measured mean dE/dx values for different runs. This is reflected by

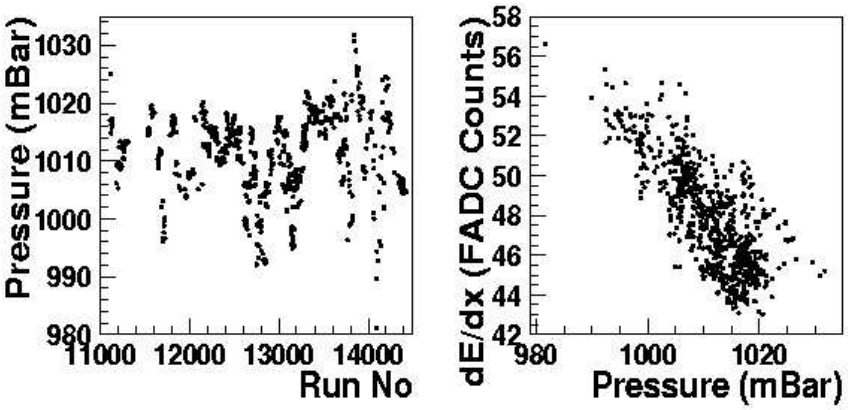

Figure 4.8: Dependence of the dE/dx measurement on the air pressure. These plots are generated from 1995 data. [25, 5]

Fig. 4.8, which shows how the mean air pressure differs between runs (left) and how the air pressure and the mean measured dE/dx are correlated (right).

This is just one example of slowly changing parameters; there may be many more. Even without knowing about their existence and appearance, it is possible to apply a 'run correction' against them. For each run a global correction factor for dE/dx is calculated separately. This is done by using all tracks with momenta between 300 MeV and 400 MeV (pion dominated sample, close to minimum ionisation) and fitting a Gaussian to the dE/dx_{FADC}-distribution. This Gaussian will roughly describe the dE/dx distribution of pions with minimum ionisation. The measured dE/dx_{FADC} values then become normalised by the mean f_r of the Gaussian fit. The resulting dE/dx_{mips} therefore are to first order independent of the particular CTD conditions during the run and minimum ionising particles get a value around 1 (hence the suffix *mips*).

4.2.1.3 'Old' space-charge effect correction

The space-charge effect (see Sect. 4.2.2.7) was already found in the 90's [5] as a dependence of the measured dE/dx on the polar angle θ of the track. This was quantised in bins of θ, using a sample of electron tracks. The correction was done by normalising dE/dx bin-wise in θ using the distribution from the electron sample. This implies, that the space-charge effect is multiplicative in dE/dx and independent of the particle type. A more sophisticated, un-binned correction method has been developed now. Details about this method will be found in Sect. 4.3.1.9.

4.2.1.4 Compensation for many saturated hits

If a hit is in saturation, it is not possible to measure its dE/dx. The only information available is, that this hit lies above the saturation limit. This means, that such hits cannot be used for the calculation of the mean dE/dx of a track. As long as less than 30% of all hits of a track are saturated, this causes no problem, since the truncated mean calculation anyway neglects the highest 30% of all hits. If more hits are saturated and have to be

neglected in this calculation, the window for the truncated mean becomes narrower. This affects only the upper limit of the truncation-window, which becomes the lower the more saturated hits there are. Consequently, this causes a systematic shift for the measured $dE/dx_{FADC} = \langle dE/dx_{hit} \rangle$ to too low values. In the end, the user wants to compare dE/dx measurements that are independent of such effects. A way to compensate for this shift was given by Wouter Verkerke [51, 34].

4.2.2 Corrections newly developed

After many years of data taking a completely new approach to understand the measurement of dE/dx with the ZEUS CTD can be conducted by using tuning samples, in which even without using ionisation measurements, the kind of particle, forming the track, is already known. In the early 90's the tuning was done with *all* tracks in the momentum range $300\,\text{MeV} < p < 400\,\text{MeV}$, which corresponds to a pion-enriched sample close to minimum ionisation. Now looking at tracks of particles far away from minimum ionisation opens a totally new test field. This section shows the effects which were discovered and quantified by this approach.

4.2.2.1 Wire-by-wire corrections

The wire gains of the CTD have never been calibrated since 1996. Ageing effects and replacements of broken hardware can have an influence on the calibration. A way to detect such effects is to look at dE/dx in bins of ϕ_{track}. We expect to see no dependence at all. Figure 4.9 shows, that before corrections this is not fulfilled. The figure also demonstrates, that shortly after the calibration in 1996 the ϕ_{track}-dependence was quite small, but then increased over the years. To compensate for this effect, correction factors for each signal wire must be applied. It is obvious, that without using raw data it is not possible to resolve the gain corrections at wire level, but even corrections at supercell level yield a big progress. A sophisticated method for a correction at supercell level without direct access to supercell information in processed data will be introduced in Sect. 4.3.1.1.

4.2.2.2 Truncation-window and mean calculation effect

A truncated mean method is used for dE/dx measurement. After ordering the hits of a track by their signal height, the lowest 10% and the highest 30% of all hits are discarded. The total number as well as the truncated number are both integers, thus the truncation does not happen exactly at 10% and 30% but somewhere close to these fractions. The really used fractions depend on the total number of hits. Therefore, the really applied truncation-window, and consequently the expected truncated mean, depends on the number of hits, as shown in Fig. 4.10.

The hit-number dependent range of the truncation is not the only effect in the truncated mean method, which has an influence on the calculated value. The probability density for single hits is strongly asymmetric (Landau shape). The mean value $\langle x_i \rangle$ of a finite number of values x_i, which are generated with an assymetric probability density, depends on the number N of values taken into account. Figure 4.11 illustrates this effect. The left plot shows the standard Landau function according to Eqn. 3.4, which is used as the density probability for randomised numbers; the right plot shows the mean $\langle x_i \rangle$ of such

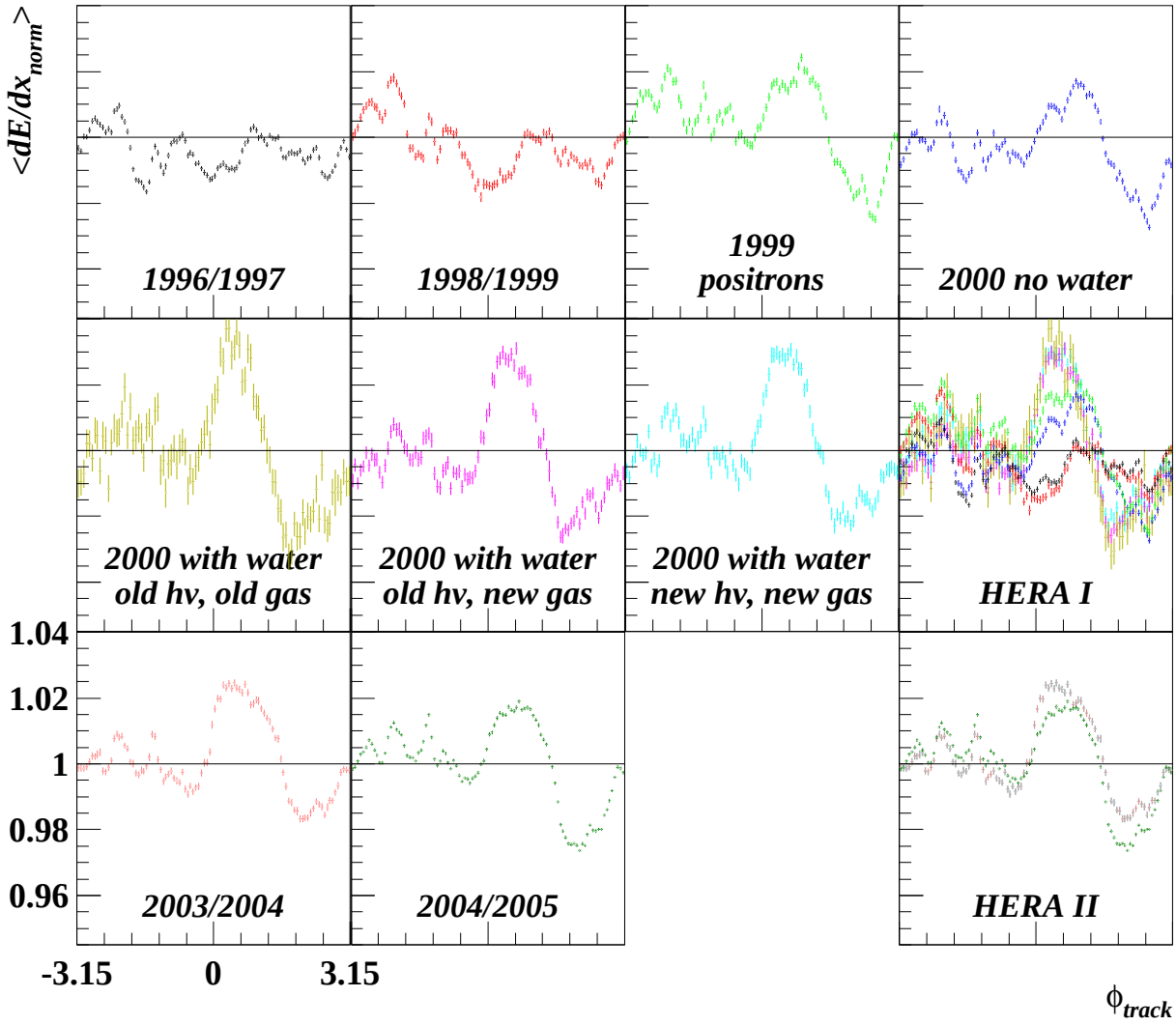

Figure 4.9: ϕ_{track}-dependence of $\langle dE/dx_{norm} \rangle$, using the K^0 sample and its evolution with time.

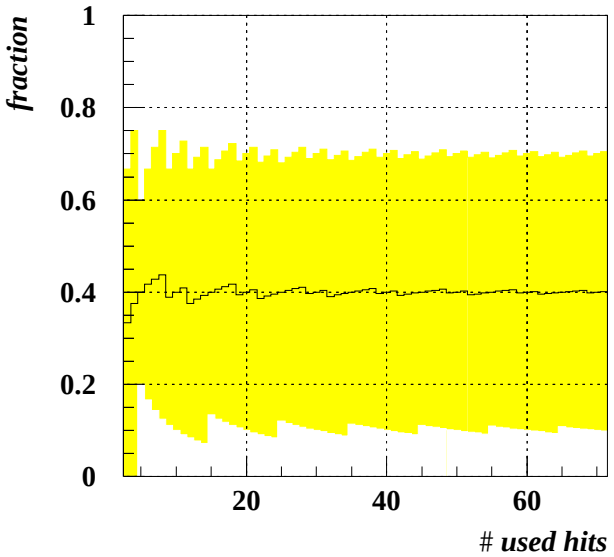

Figure 4.10: Truncated-mean window in bins of the number of used hits. The coloured band indicates the truncation range, the line its mean value.

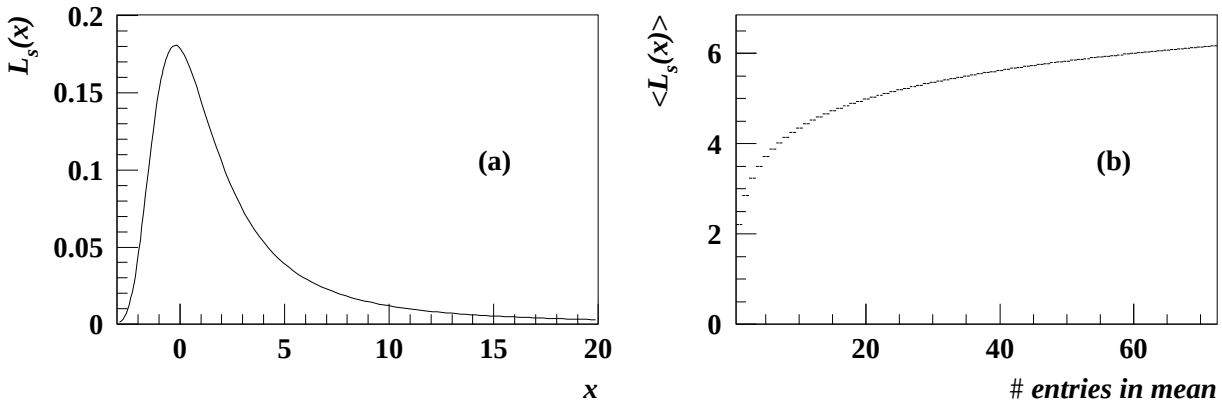

Figure 4.11: (a) The shape of the standard LANDAU distribution. (b) Mean values of randomised values with a LANDAU-shaped probability density and their dependence on the number of values in the mean calculation.

random values, depending on the number N of values used for the mean calculation. The mean value obviously grows with increasing number of entries in the mean calculation.

4.2.2.3 Threshold effect

To reduce noise, a threshold is applied in the electronic readout of the signal wires. If the signals are very low, they may fall below this threshold. As such a signal is lost for

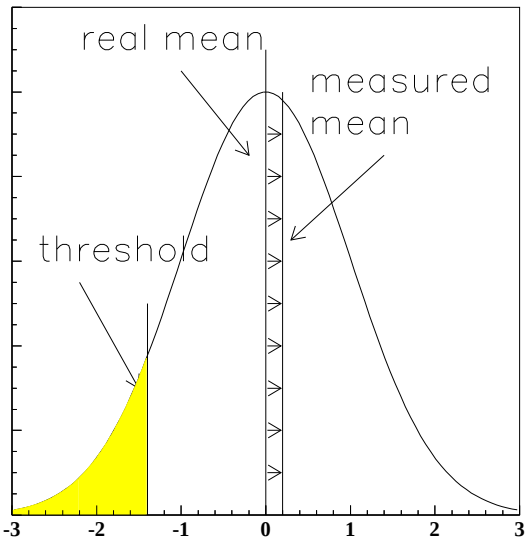

Figure 4.12: Schematic depiction of the threshold effect. Cancelling the lower tail of a distribution forces the mean value of its remaining part to move up.

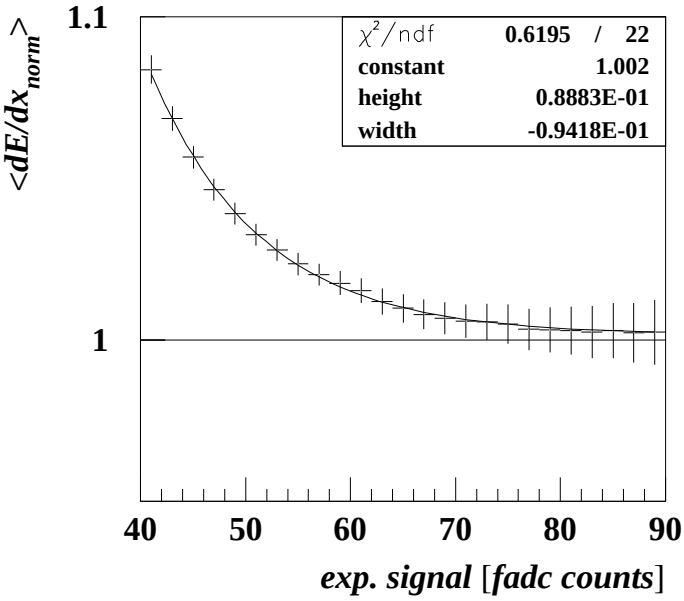

Figure 4.13: Dependence of the normalised mean $\langle dE/dx_{norm} \rangle$ on the expected signal. Pion sample, HERA II data. The fit function is given in Eqn. 4.8.

calculating the mean signal of all hits corresponding to a track, the consequence will be a systematic shift to higher mean values (Fig. 4.12). The probability for this effect to occur depends on the signal height itself. The lower the signal, the higher the probability to loose hits due to the threshold. Loosing hits means, that the measured signal increases.

In order to prove the existence of this effect with measured data, first of all it is mandatory to define what 'signal' means. The measured signal is defined here to be the measured dE/dx value in FADC counts, divided by the correction factors on $\overline{\psi'}$ and $\bar{z}$ corresponding to the corrections applied in the Phase I reconstruction, and divided by $\sin\theta$. For measured signals this is the best approximation of the signal height seen by the front-end electronics at the wire. To keep maximum compatibility between measured and expected values, the expected signal is calculated in the same way, by replacing the measured dE/dx_{FADC} by the expected dE/dx_{exp} using the BETHE-BLOCH curve divided by the run-by-run correction factor for the corresponding track.

Figure 4.13 shows that for high expected signals the measured signal $\langle dE/dx_{meas}\rangle$ is equal to dE/dx_{exp}. Without threshold effect this should be true for any signal. For lower expected signals, the measurement overshoots the expectation. This is evidence for the presence of the threshold effect in the data.

4.2.2.4 Neighbourhood effect

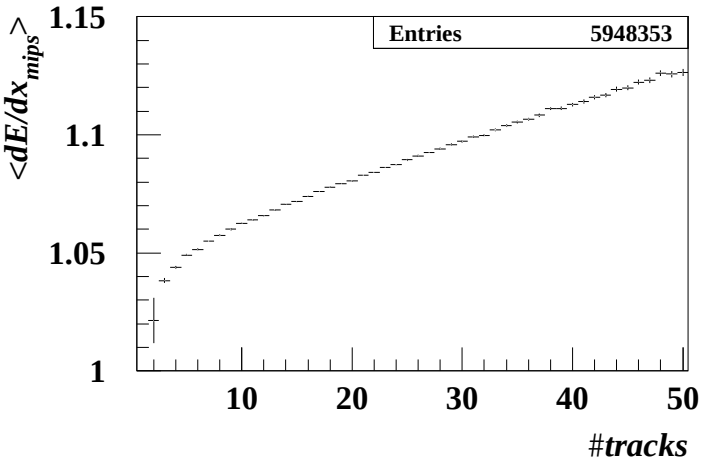

Figure 4.14: $\langle dE/dx_{mips}\rangle$ after run-by-run corrections vs number of tracks. K^0 sample, HERA I data.

The pulse at a signal wire, caused by a track, vanishes within a time window of roughly 50 ns [25]. If there is a second hit present within this time-slot, it is problematic to do a proper measurement of such a second signal. The pulse of the second hit will add up on top of the tail of the previous pulse. As the maximum height of the pulse is used to give the measured dE/dx_{FADC}, this will corrupt the dE/dx measurement. It has turned out, that the measurement accuracy and efficiency of the second hit is not very good [19]. To be safe against such pile-up, a veto of 100 ns after a hit is used in the tracking. But it still can happen, that two pulses are too close together to be separated. In this case, the signals of the two hits will sum up to one high pulse. Such pile-up pulses increase the mean pulse height of the involved tracks.

The simplest way to prove the existence of this effect is to check the dependence of signal heights on the track multiplicity of the event. The probability to get pile-up increases with increasing track multiplicity. Figure 4.14 clearly shows this dependence.

4.2.2.5 End-plate effect

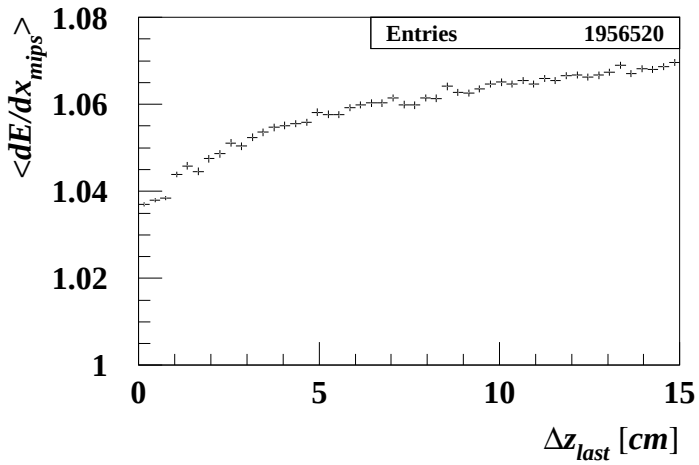

Figure 4.15: $\langle dE/dx_{mips} \rangle$ after run-by-run corrections vs Δz_{last}. K^0 sample, HERA I data with $400\,\text{MeV} < p < 1000\,\text{MeV}$.

In the central area of the CTD the shape of the electric field is given only by the field forming wires. This is not true close to the end-plates. Of course these electric conductors affect the electric field close to them.

Also, the magnetic field of the solenoid varies depending on the geometrical position in the CTD. In the central part of the CTD it is almost homogeneous and oriented in z-direction, but close to the end-plates it picks up a component in radial direction.

A different field topology reflects in different drift paths and velocities for the ionisation electrons. Also the gradient of the electromagnetic field close to the signal wires can be different, which causes gain changes. All this can modify the measured signal for hits close to the CTD end-plates.

A way to visualise the existence of such effects is to plot the dE/dx distribution in bins of the distance Δz_{last} of the outermost hit to the end plate as shown in Fig. 4.15. This Figure shows, that indeed the mean measured dE/dx decreases for tracks with hits close to the end-plate.

4.2.2.6 Dispersion along the signal wire

A signal changes its shape, while propagating along the signal wire. Due to dispersion it becomes widened and less high. As the ZEUS CTD has its readout only at the rear end, the measured signal depends monotoneously on the propagation length. To compensate for this, a z-dependent correction is applied in the Phase I reconstruction. But this effect depends on more than just the z-coordinate. If a signal is already produced as a wide low signal, there will be almost no visible effect, whereas a very short high signal will suffer much more from the dispersion. It has to be expected, that the Phase I correction only partially compensates (or over-compensates) for this effect. This leads to systematic errors depending on dE/dx itself, as shown in Fig. 4.16. The plots show the dependence of the measured dE/dx after Phase I corrections on the mean $\bar{z}$ of all possible hit z-coordinates of the track. First of all one observes a deep dip in the electron sample for $\bar{z} \approx 0\,\text{cm}$, which is caused by the space-charge effect (Sect. 4.2.2.7). Furthermore, we see for both samples, that for large $|\bar{z}|$ the measured dE/x_{mips} becomes smaller. This can be related to the end-plate effect (Sect. 4.2.2.5). At this point we should ignore this and focus on something else: The electron sample looks rather symmetric in this plot, whereas pions in forward

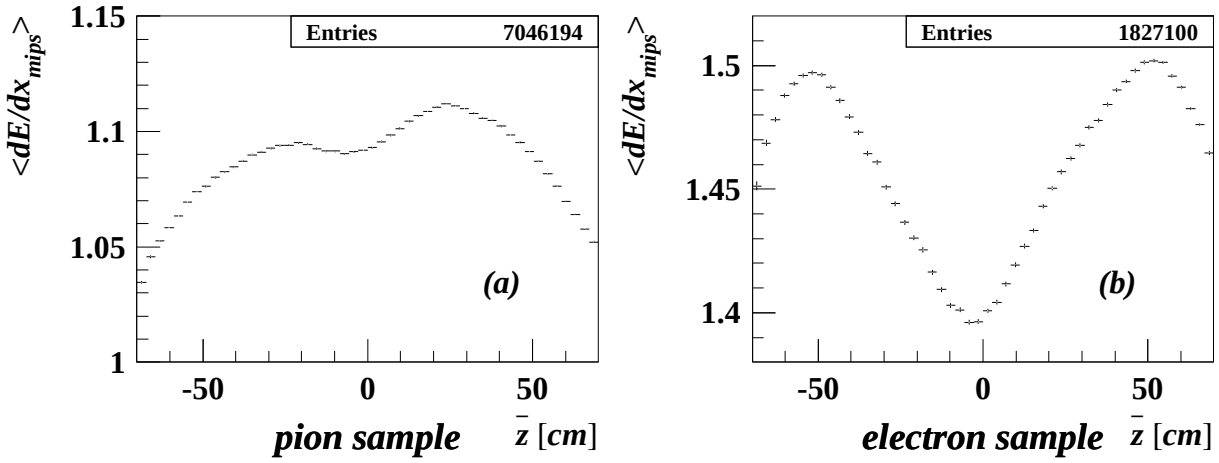

Figure 4.16: $\langle dE/dx_{mips}\rangle$ after run-by-run corrections vs $\bar{z}$, HERA I data.

direction have a higher dE/dx than those going backwards. The pion sample is selected to represent the minimum possible dE/dx, i.e. their signals are not very high. Therefore the signal height is changing only little during propagation. For a long propagation distance (positive $\bar{z}$) the Phase I correction overestimates the change in signal-height and therefore corrects the signal too much.

4.2.2.7 Space-charge effect

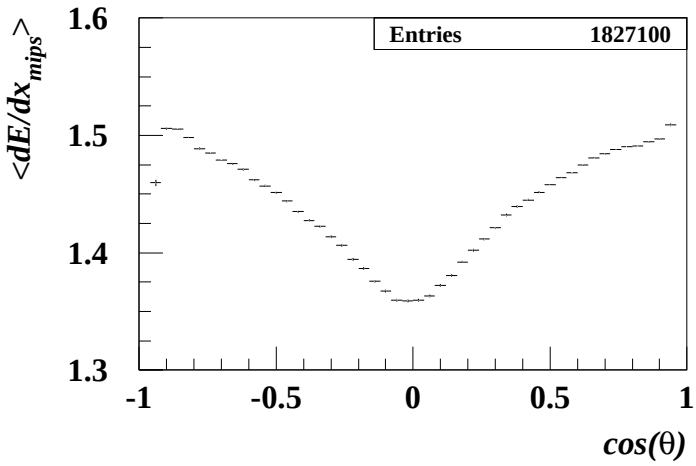

Figure 4.17: $\langle dE/dx_{mips}\rangle$ after run-by-run corrections vs $\cos\theta$. Photon conversion sample, HERA I data.

The space-charge effect[3] was already observed in 1994. It was found in an electron sample as a non-uniformity in the $\langle dE/dx\rangle$ distribution as a function of the polar angle θ. Close to the sense wire the avalanche occurs, the released electrons are collected at the anode and a cloud of positively charged ions is left. As the ions are much heavier than the electrons, this ion cloud moves only slowly away from the anode. If more electrons coming from primary ionisations move into this cloud, there is a probability for them to be caught by an ion and therefore not to contribute to the measured signal. Finally, the measured signal comes out too low.

[3]In some literature this effect is named saturation effect.

The probability for primary ionisation electrons to end up in such an ion cloud depends on their distance to each other, when they reach the area close to the anode wire. This distance shrinks with decreasing $|\cos\theta|$ (polar angle close to 90 °). Figure 4.17 illustrates this effect.

4.2.2.8 Drift-time effect

For a single primary ionisation in the CTD gas, the corresponding pulse shape at a signal wire is always the same. But a traversing particle causes several primary ionisations. Therefore the measured pulse is an overlay of several 'single electron pulses'. The time between a primary ionisation in the sensitive gas volume and the corresponding signal at the wire depends on the position of the primary ionisation. This so called drift-time is not the same for different primary ionisations coming from the same track. The measured signal shape is the sum of single ionisation shapes, taking these drift-times into account. This means, the measured signal does not only depend on the dE/dx of the ionising particle, but also on its direction of motion within the sensitive area of the signal wire.

A proper observable to investigate this dependence is the angle ψ', defined in the xy-plane as the angle between a tangent to the track and the radial axis in xy (Fig. 4.18). The geometry of the ZEUS CTD is such, that for all sense wires only two parameters, the angle ψ' and the distance of closest approach of the track to the sense wire, are sufficient to describe the direction of motion of the particle. Figure 4.19 even shows, that, neglecting the area very close to the sense wire, the drift paths and isochrones are independent of the distance of closest approach. Therefore it is sufficient to restrict to the ψ' dependence of the measured dE/dx to investigate the drift-time effect. Figure 4.19 furthermore shows an asymmetry in the shape of the isochrones. This is caused by the combination of the electric and the magnetic fields in the CTD. As the drift paths 'curl in' to the sense wire, the isochrones do not have a circular but an approximately elliptic shape.

The distribution of times, when the primary electrons arrive at the sense wire, and therefore the shape of the signal, is given by the distribution of the isochrones, which are traversed by the track at the moments of the primary ionisations. The velocity of the ionising particle is much higher than the drift velocity of the electrons in the CTD gas. Therefore it is a good approximation to say, that all primary ionisations happen at the same time. The primary ionisations happen statistically distributed along the trajectory

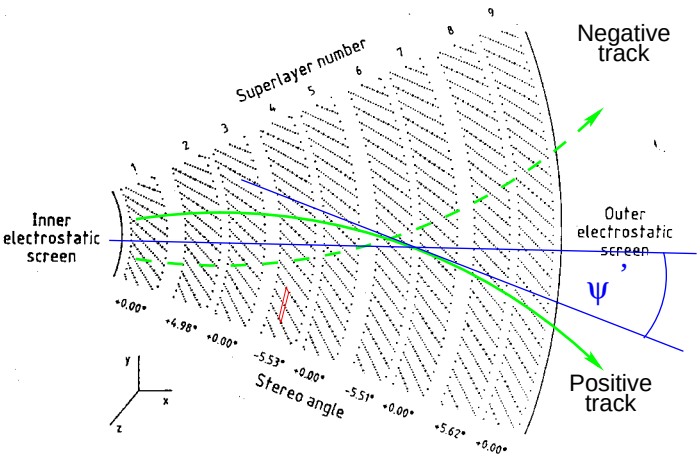

Figure 4.18: xy-view of one octant of the CTD indicating particle tracks and the angle ψ'. The red box indicates the sensitive area of one signal wire, shown in Fig. 4.19.

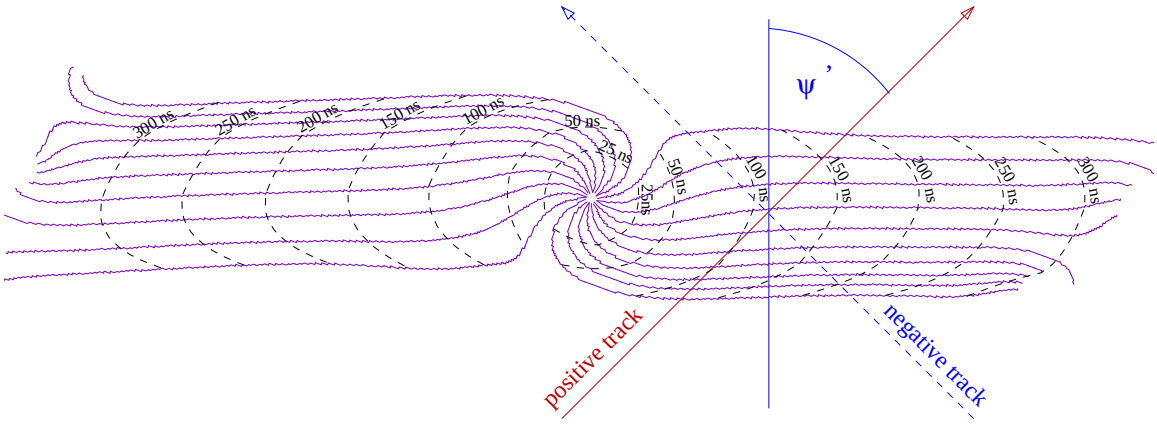

Figure 4.19: xy-view of the sensitive area of a signal wire. Shown are the drift paths and the isochrones. (based on a plot in [19])

of the particle. For simplicity, let's think about an equidistant distribution of primary ionisations. The arrival time difference on the wire between two consecutive ionisations scales with the opening angle between the particle's trajectory and the isochrones. If this angle is big, the time difference is also big. As the pulse of a single primary ionisation at the signal wire fades away rather quickly, the pulse of the second primary ionisation will show up at the steeply falling tail of the first pulse. The total height of this signal will not be much higher than the height of a single primary ionisation pulse.

This situation is different, if the previously mentioned opening angle is small. In this case, even a long spatial distance of the primary ionisations will end up in a very small time difference of their pulses and the combined pulse will be much higher than a single ionisation pulse. This means, the maximum height of the total pulse, given by the combination of all primary ionisations of the same track within the sensitive area of a sense wire, is given by the ionisations which occur on that part of the track, that it is almost

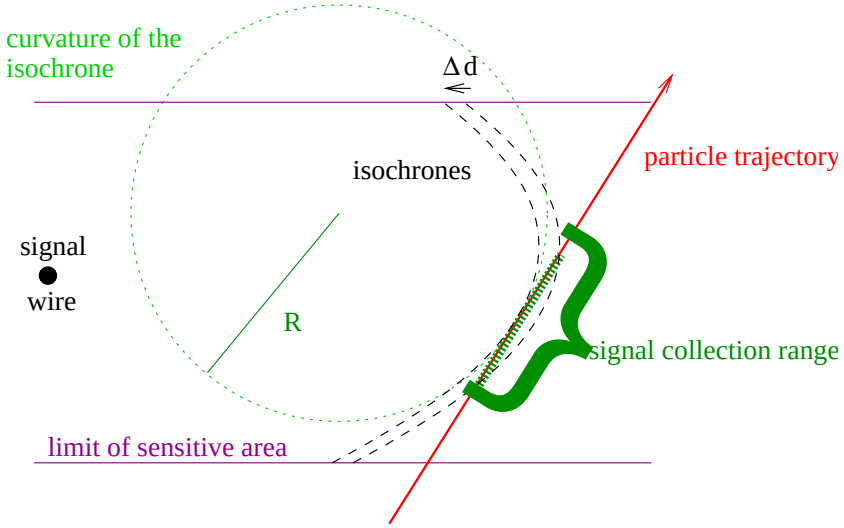

Figure 4.20: Schematic view of how to find the relevant piece of the track for the signal height calculation.

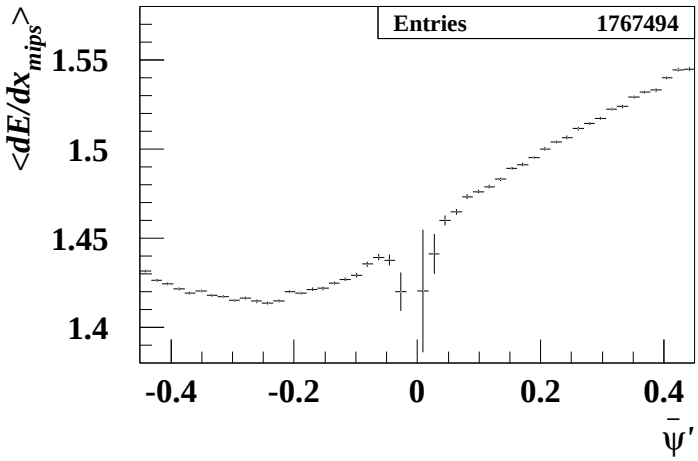

Figure 4.21: $\langle dE/dx_{mips} \rangle$ after run-by-run corrections vs $\overline{\psi'}$. Photon conversion sample, HERA I data.

parallel to the isochrones. It is a fair assumption to expect, that only the electrons within a narrow fixed time window at the beginning of the pulse are relevant for the height of the signal and therefore for the dE/dx measurement. Such a time window is given by the rise time of a signal which is of the order of 18 ns [13]. Using the typical drift velocity $v_d = 47\,\mu\text{m/ ns}$, this time corresponds to a drift distance $\Delta d \approx 1\,\text{mm}$. Thus the measured signal is the product of the ionisation dE/dx and the piece of the track, which corresponds to this time window. Figure 4.20 illustrates how to find this track length. The first electrons arriving at the sense wire are coming from the position, where the track trajectory touches an isochrone tangentially. All electrons, which are released in the area between this isochrone and the one shifted by Δd, will contribute to the measured signal. This length is given by the distance between the two crossing points of the track trajectory with the shifted isochrone. In a very good approximation this length depends linearly on the radius R of curvature of the touched isochrone in its touching point with the track trajectory.

To conclude from this information, the measured signal is proportional to the product of the track's dE/dx and the curvature of the touched isochrone in the touching point. Figure 4.19 teaches, that for positive ψ' (positively charged tracks) this radius is larger than for negative ψ'. This means, positively charged tracks always produce higher signals than negatively charged ones. In particular, the signal height is a function of ψ'.

In the Phase I reconstruction a ψ'-dependent correction factor is applied. This correction factor was tuned with a pion enriched sample in the minimum ionisation range. It turns out, that for higher dE/dx this correction is underestimated. Figure 4.21 shows $\langle dE/dx \rangle$ versus $\overline{\psi'}$, the mean ψ' of the whole track, using an electron sample. As single hit information is not available in processed data, $\overline{\psi'}$ is the best available observable which is highly correlated to the ψ'-value of the single hit. It is clearly visible, that at dE/dx values far away from the minimum ionisation the drift-time effect is not fully compensated for by the Phase I correction.

4.2.2.9 Superlayer factors

After applying corrections to all effects mentioned above still a clearly visible dependence on the range of superlayers, covered by the track, is left. The origin for this dependence is not found yet, but there are various possibilities.

The single wire gains have been calibrated using the dE/dx_{hit} measurements after Phase I

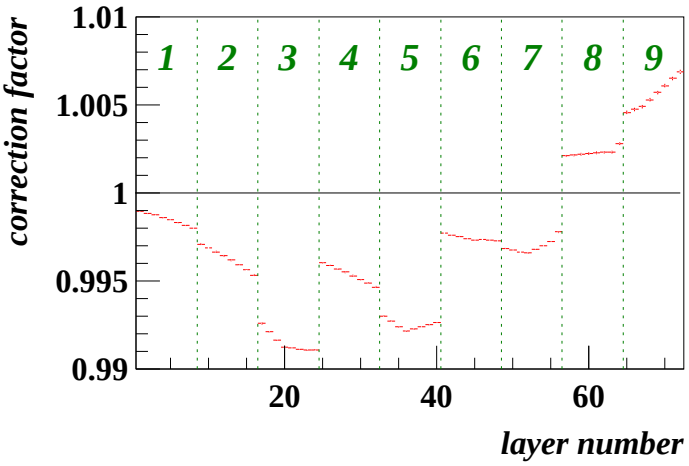

Figure 4.22: Monte Carlo simulation for the effect of the Lorentz angle correction on the wire gains, using a θ-distribution of the tracks as in real data. The mean factor caused by the Lorentz angle correction is shown versus the outermost layer of the tracks. The numbers in the plot indicate the superlayer number.

corrections. Therefore the (wrong) Lorentz angle correction (Sect. 4.2.3) has already been applied to the data. As this correction has its biggest effect for hits close to the end-plates it can also be visible in layer-dependent distributions: the smaller the number of traversed layers, the larger the fraction of hits close to the end-plate. Using a Monte-Carlo simulation (Fig. 4.22) one can derive the size of this influence on the calibration constants. The simulation comprises the radial geometry of the signal wires and basic rules of the ZEUS CTD tracking: if the track ends in the 4^{th}, 6^{th} or 8^{th} stereo superlayer its hits in the outermost superlayer are not taken into account. This treatment of the geometry causes the jumps between superlayers. It can explain an influence on the dE/dx calibration in the order of 1%.

There might be other sources for superlayer-dependent shifts in the measured dE/dx, like for example the neighbourhood effect (which is not compensated for in Phase I). Even if the sources are not completely understood, the remaining dependence on the outermost superlayer can be removed.

4.2.3 Removed Phase I Lorentz angle correction

As shown in Section 4.2.2 several corrections, which are done in the Phase I reconstruction, are replaced or supplemented by more sophisticated ones. But there is one correction in Phase I, the Lorentz angle correction, which is completely removed. For each hit, a correction factor

$$f_l = \frac{\cos 45\,^\circ}{\cos \alpha_l} \tag{4.2}$$

depending on the local Lorentz angle α_l is applied in Phase I. This can be understood as a geometrical correction under the assumption, that all primary ionisations happening within the sensitive range of a signal wire take part in the measured signal.

Figure 4.23 illustrates the relevant variables. Depending on the Lorentz angle α_l the length of the track section w', where all primary ionisations will be collected from by one signal wire, differs. The enlarged triangle in the right illustration gives for $\alpha_l \approx 45\,^\circ$:

$$\begin{aligned} \beta &= \alpha_l + 45\,^\circ \\ \sin\beta &\approx \sin 90\,^\circ = 1 \\ d &\approx \frac{d}{\sin\beta} = \frac{w'}{\sin(90\,^\circ - \alpha_l)} = \frac{w'}{\cos\alpha_l} \quad . \end{aligned}$$

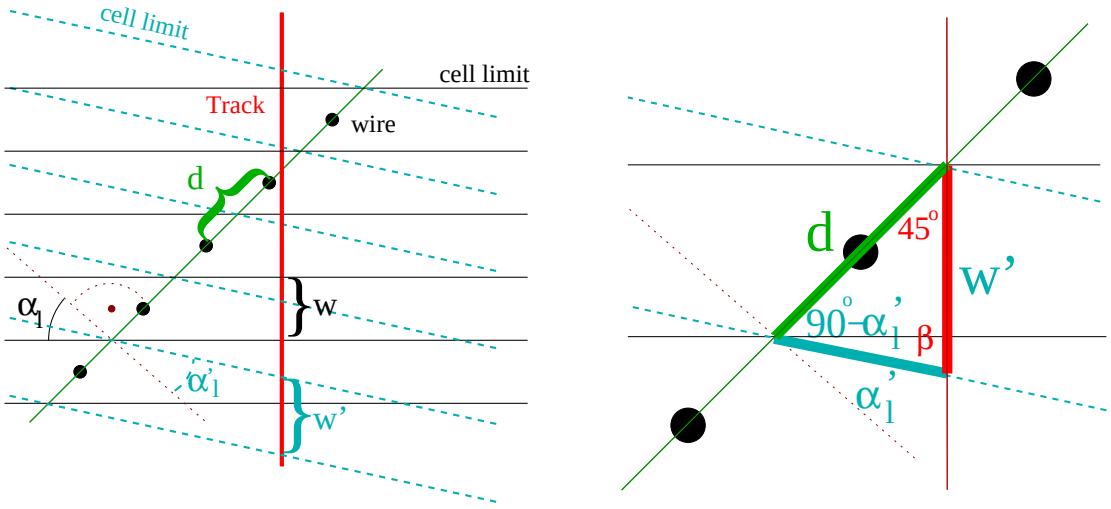

Figure 4.23: Schematic view of the geometrical situation for local Lorentz angle correction. The design cell limits are shown in black (Lorentz angle 45 °); the corresponding limits for another Lorentz angle are blue. In red a track with high momentum ($\psi' = 0$) is shown. The right picture shows an enlargement of one cell.

Using the design Lorentz angle of 45 ° as a normalisation, this leads to the correction factor in Eqn. 4.2:

$$f_l = \frac{w}{w'} \approx \frac{d \cdot \cos 45\,^\circ}{d \cdot \cos \alpha_l} \quad .$$

Unfortunately, the details of Section 4.2.2.8 show, that the presumed conditions for this approach are not fulfilled. Comparing the typical signal collection-time up to the signal maximum of around 18 ns with the range of isochrones, which are passed by a track within one cell (Fig. 4.19), obviously only a small part of the track within the sensitive range participates in the measured signal. The rest of the primary ionisations build up the tail of the signal. This means, if the Lorentz angle is changed due to a (locally) changed magnetic field or a changed drift velocity of the electrons in the gas, in first order the drift path and isochrones pattern in Fig. 4.19 will be rotated around the wire. Consequently only the position where the 'closest isochrone' will be touched, is slightly changed. This causes a negligible second order effect on the measured signal height, because at this different position the curvature of the isochrone might be slightly different. Furthermore the degree of spiraling in on the wire changes with a changing magnetic field. This also affects the curvature of the isochrones.

Anyway, for the dE/dx measurement there is no first order effect due to the Lorentz angle. The remaining second order effects are small and difficult to handle. Thus it makes sense to ignore them. Consequently, the Phase I Lorentz angle correction is removed.

4.3 Correction methods

The final outcome from this work should be a software package for corrections on dE/dx measured by the ZEUS CTD for HERA I and HERA II data. As a reprocessing of HERA I data is not forseen, the corrections will have to act on already processed data. This has to be taken into account when selecting observables to be used for the corrections. For example most of the described effects occur at wire level. The natural consequence would be to use single hit data and do corrections on them. However, in processed data only observables at track level are available, the information on single wires has been abolished to save disk space. Therefore the most natural and direct access for doing corrections is prohibited. This fact has to be kept in mind for almost all means and methods that will be described in this chapter.

4.3.1 Corrections for the effects in separation

In this section the correction methods against the effects introduced in Sect. 4.2 will be described one by one. To point out the signatures of each effect in the shown histograms, partially corrected dE/dx values were used. If not explicitly written otherwise in the figure-caption, dE/dx_{meas} values are **corrected against all other effects except for the one shown in the histogram or described in the corresponding section**.

At this point each effect including its correction is treated as being independent of the other effects. This is done to facilitate the understanding of the corrections. The treatment of the correlation between the partial corrections will be covered in Section 4.3.2.

Another standard method used in this chapter is the normalisation of the corrected dE/dx values to a Bethe-Bloch curve. The determination of this curve will be displayed in Sect. 4.4. Using an expectation function is, of course, a source for systematic errors, if this function is not correct. Therefore, the used test samples are restricted to ranges, where the Bethe-Bloch curve is almost flat and its expectation value quite trustworthy. Anyway, it is necessary to apply such a kind of normalisation to reduce the intrinsic momentum dependence within the samples. The global scale of dE/dx is of minor relevance for most applications. Therefore the shape of the theoretical Bethe-Bloch curve is much more relevant than its scale. As within the used $\beta\gamma$ regions this shape is very insensitive to variations of the parameterisation of this curve it is appropriate to use this kind of normalisation dE/dx_{norm}:

$$dE/dx_{norm} := \frac{dE/dx_{meas}}{dE/dx\ _{exp}} \quad . \tag{4.3}$$

4.3.1.1 Wire-gain correction

It is a bit complicated to comprehend the wire-gain correction introduced in this section in all its details. Therefore this section starts to describe the basic idea of the correction. The second half of this section explains the details which are left out in the first half and modifications of the algorithm to improve its efficiency are shown.

The main challenge for this correction is the extraction of information on single wires from data, which is available only for whole tracks. The solution to this problem is to reconstruct the trajectory of the track using its helix parameters. One geometrically reconstructs,

which wires were passed by the particle, i.e. which wires the particle had a chance to leave a signal at. Histograms for wires are then filled by booking entries for each track passing that wire. Figure 4.24 shows such a histogram.

If for example a wire has too low a gain, all tracks passing this particular wire will be affected and their measured dE/dx will be too low. Therefore all bins in Fig. 4.24, which are touched by these tracks, will show values below 1. Nevertheless, only in the bin corresponding to the wrongly calibrated wire *all* tracks will be affected. So this bin will show a *strong* deviation from 1. In the other affected bins, only a fraction of the entries will be affected, whereas the other entries will be coming from tracks, which pass the CTD in another way without hitting the problematic cell. So these other entries will spread around 1 and the mean value of all entries will be shifted only a little bit (corresponding to the fraction of entries, coming from tracks, which hit the wrongly calibrated cell). This histogram allows to trace back, which wires were causing problems, by searching for the cells with the largest deviations from 1.

Figure 4.24 shows, that there are different signatures of wrong calibrations. First of all there are some positions where single wires are badly calibrated. This becomes visible by

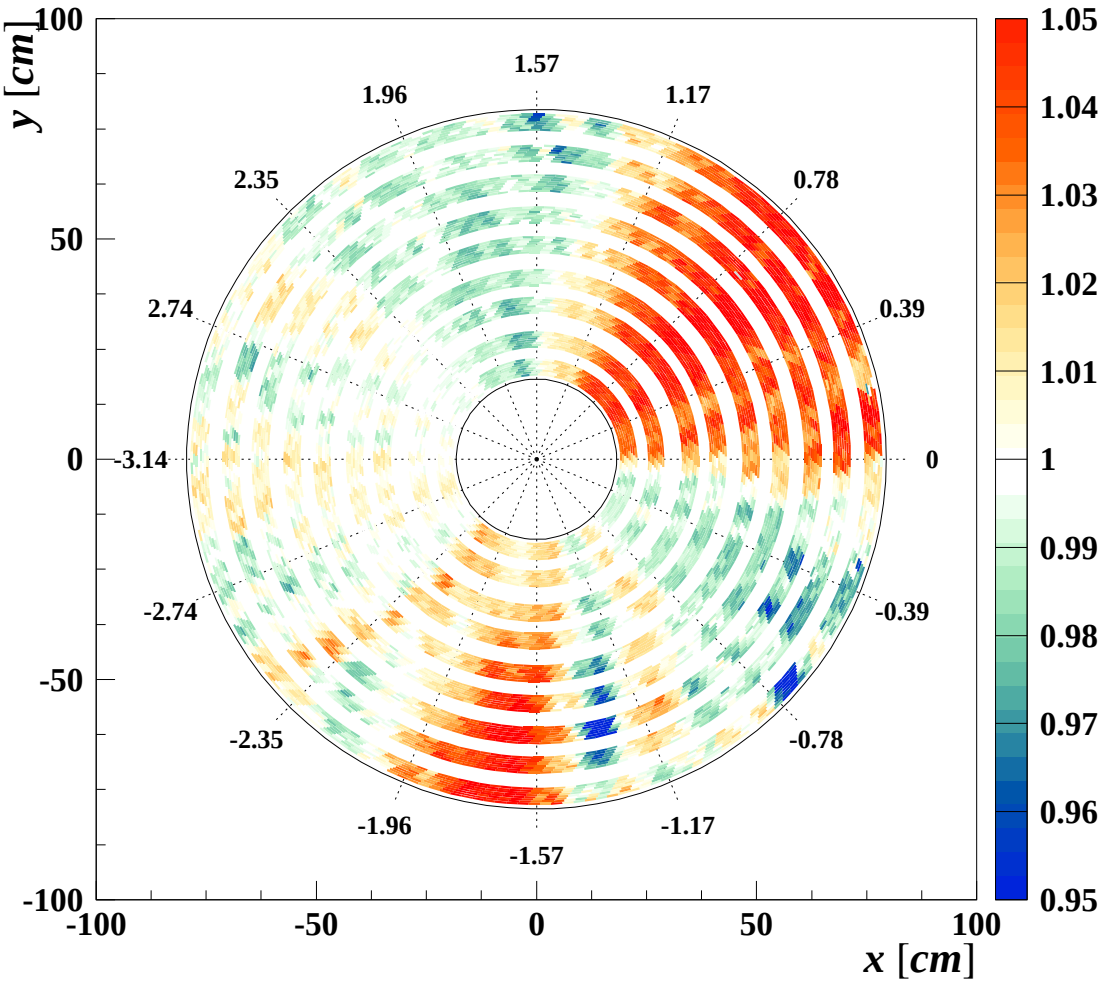

Figure 4.24: $\langle dE/dx_{norm} \rangle$ of the pion tuning sample for all sense wires. The numbers in the plot denote the angle ϕ. 2000 data with water, new high volatage and new gas mixture.

a large deviation from 1 in small ranges in layer number and ϕ. In other cases, not only single wires are affected, but a whole supercell seems to be wrongly calibrated, e.g. the 7^{th} superlayer at $\phi \approx -1.3$. In some cases this may be fake, as the resolution of this approach is much worse in radial direction than in ϕ. But especially the two deepest dips are too far away from 1 to be explained by only one wire. To cause a dip of this depth, a single wire must have a negative signal, which is impossible. Thus these dips must result, from a whole set of signal wires being wrongly calibrated. This is also likely to happen due to the design of the CTD, as all signal wires of the same supercell are lumped together in the same frontend electronics. If such an electronics card is wrongly calibrated, the whole bunch of signal wires will be affected.

Finally, for $0 < \phi < 1$ all channels are too high. Such an effect can be caused for example by a wrongly calibrated power supply for the CTD high voltage, which serves one complete octant of the CTD.

Now in possession of a proper tool to identify badly calibrated channels, a correction method has to be applied. As there are many correlations and fake information in Fig. 4.24, it is impossible to extract correction factors for all wires directly from that histogram. Instead, it is only used to localise the problems and an iterative procedure is applied to find proper corrections. This procedure works as follows:

As already stated, the worst offenders cause the largest deviations from 1 in Fig. 4.24, whereas smaller deviations in their neighbourhood may be fake. To take this into account, the wire position for the largest deviation is extracted from Fig. 4.24. Next, a correction factor for this wire is calculated. This factor takes into account, how far the bin content is away from 1. To reduce the probability of over-corrections, the allowed range for correction factors is limited between 0.2 and 5. It is not necessary to find the right correction factor for this channel in this step as in later iterations the same channel might become corrected again. As long as by changing the correction factor the result becomes better, i.e. if the result improves with each iteration, everything is fine.

As a next step, the graph in Fig. 4.24 is redone. This time a modified dE/dx_{norm} value is used for each track. Again all passed wires are identified using the track's helix parameters. Then the mean value of all wire correction factors for these wires is calculated. In contrast to the 0^{th} iteration, this time the dE/dx_{norm} value of the track becomes corrected using this mean correction factor. This approach ignores the fact, that only a fraction of all passed wires are used for the dE/dx measurement (truncated mean, inefficiencies of single wires, dead wires), but as no information is available at processed data level, which wires were used for the calculation, this is the best approximation possible.

After filling Fig. 4.24 in this way, the next iteration starts. Again, the worst offenders are found, correction factors for them are calculated; if some of these offenders were already corrected in an earlier step, new factors are calculated for them in a proper way, and the next iteration can start. The only part yet missing is an objective criterion when to stop the iterations.

In principle, this is already the complete mechanism to find wire corrections. However this method converges extremely slowly. There are more than 4000 signal wires in the CTD and in each iteration only one of them is corrected. And for each iteration the program needs to run over the whole data sample, which takes a lot of time. To reduce the calculation time, the following modifications of this algorithm have been developed:

- For better efficiency, not only one worst offender, but the 20 highest and 20 lowest bins are corrected in each iteration. This increases the risk of over-corrections, if neighbouring channels, which are affected by correlations, are touched at the same time. The limit of 20 channels at 'each end' of the list turned out to be safe.

- The goal of the mentioned iterative procedure is to unfold the calibration for signal wires from the pattern shown in Fig. 4.24. The unfolding is sensitive to the shape of the tracks in the xy-plane, which are used to fill Fig. 4.24. The number of tracks entering in Fig. 4.24 is quite high. Therefore, a high computing time is needed to loop over all these tracks in order to process one iteration. The computing time is strongly reduced by replacing the really measured tracks with simulated tracks, which are fastly generated.

  The unfolding depends on two track parameters: the azimuthal angle ϕ and the curvature of the tracks in the xy-plane, which is a function of p_t. The ϕ-distribution of the tracks is flat[4]. For a proper simulation, the p_t distribution of all tracks taken is measured beforehand. A sample of tracks respecting this p_t distribution and uniform in ϕ is generated and used instead of the real tracks. Compared to the usage of really reconstructed tracks, the unfolding using these simulated tracks is faster by roughly an order of magnitude.

  One has to find a good balance between efficiency (simulated tracks) and reality (real data). A good compromise turned out to do the iterations in lumps of 5, with 4 of them by the MC approach and every 5^{th} (so called grand iteration) with real data.

With these modifications the calculation of correction factors can be carried out in an acceptable time. There is, however, still room for improvements. For example, tracks that reach only the 5^{th} superlayer cannot be affected by problems in the 6^{th} to 9^{th} superlayer. Therefore they are more sensitive to problems in the first 5 superlayers than 'longer' tracks. To take advantage of this, the tracks are split up into three disjunct classes, tracks that reach the 5^{th}, the 7^{th} and the 9^{th} superlayer. For each of these classes the algorithm shown before is used separately. Only after each grand iteration the results of the three classes are combined to find correction factors for all wires together.

Furthermore, a wrong expectation function for the Bethe-Bloch curve could cause a problem. Remember that all entries in Fig. 4.24 are dE/dx values normalised to dE/dx_{exp}. For example, if this expectation is too high, naturally all entries in the histogram tend to have values below 1. To become less dependent on this, 'deviation from 1' has to be replaced by 'deviation from the mean value of all bins in the histogram' in the description above.

Control plots for the partially corrected data after each grand iteration are displayed in Fig. 4.25. These plots contain the same information as Fig. 4.24; the coordinates of the wires are transformed from cartesian coordinates to polar coordinates. The angle ϕ is transformed into $\phi\prime$, taking into account the tilt by 45 ° in ϕ of the supercells: all wires of the same supercell are located at the same $\phi\prime$. The radial coordinate is shown in layer numbers; the separation of superlayers is illustrated by black lines. The control plots in

[4]For HERA II data, the ϕ-distribution of all tracks is not totally flat. The asymmetry of the MVD in ϕ leads to a non-uniform tracking efficiency in ϕ. Nevertheless, for the application shown here, this non-uniformity has a negligible impact on the result of the method.

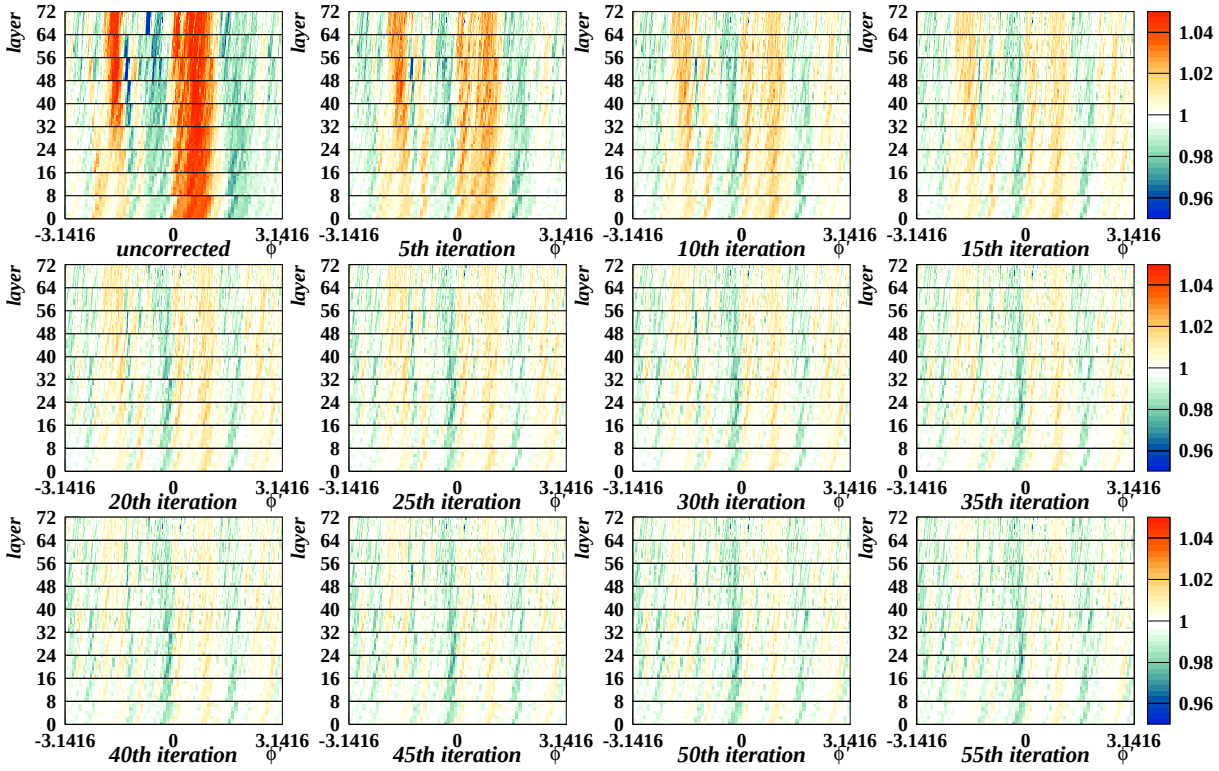

Figure 4.25: $\langle dE/dx_{norm} \rangle$ of the pion tuning sample as a function of layer number and $\phi\prime$. Result after each grand iteration. 2000 data with water, new high volatage and new gas mixture.

Fig. 4.25 prove, that this algorithm really works. The same distribution as in Fig. 4.24 is shown after each grand iteration. Obviously the distribution levels out very fast.

At this point it is still open when to terminate the iterations. Therefore the resolution of the dE/dx measurement (the RMS of dE/dx_{norm}) was checked. As long as the next iteration leads to some improvement, the resolution of the measurement should become

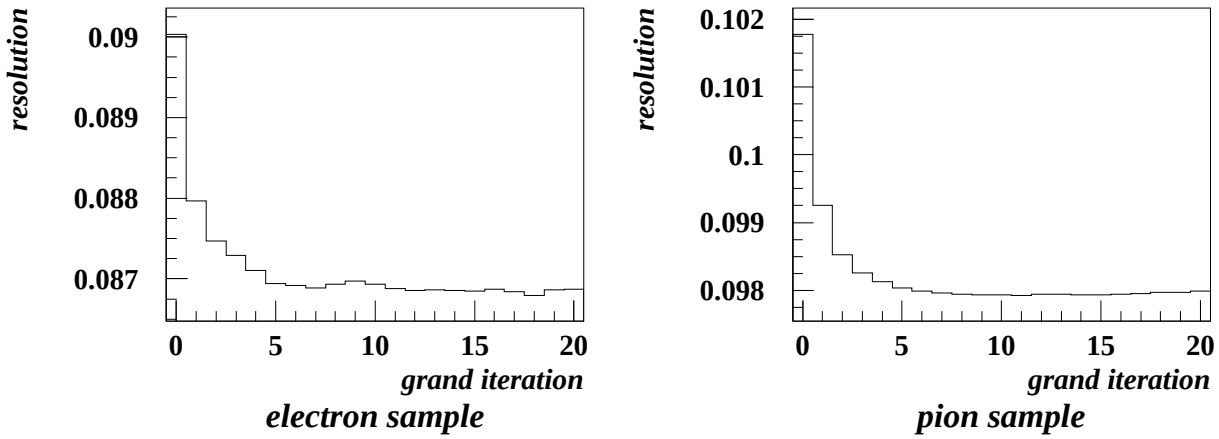

Figure 4.26: RMS of dE/dx_{norm} measurement as a function of the number of grand iterations. 2000 data with water, new high volatage and new gas mixture.

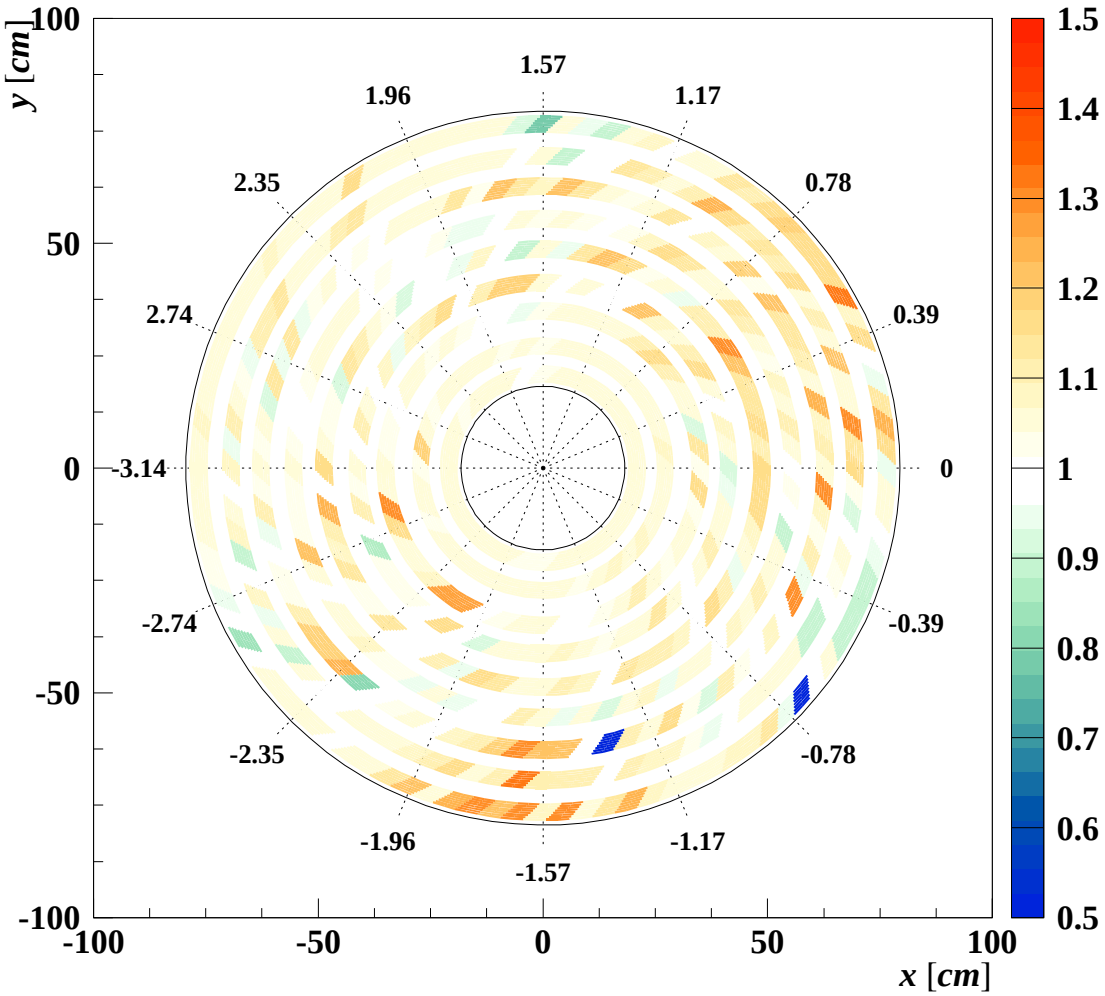

Figure 4.27: Deviations of supercells from their expected gain. The reciprocal values are the correction factors applied to hits reconstructed in these cells. 2000 data with water, new high volatage and new gas mixture.

better. If the resolution does not improve anymore, it does not make sense to continue changing the correction parameters. Figure 4.26 shows, that this is the case after about 6 grand iterations. The same behaviour was found for all investigated data taking periods.

It was already mentioned, that the method introduced is more sensitive in $\phi\prime$ than in layer numbers. This prompts the question, whether extracting correction factors for each sense wire is already overstraining the method. As Fig. 4.24 also shows, the sensitivity for the separation between different superlayers is fine, a good alternative will be to calculate correction factors for whole supercells, which are calculated as the mean correction factor of all 8 involved wires. It turned out, that the resolution of the corrected dE/dx does not change when replacing the single-wire correction by a supercell correction. This indicates, that indeed calculating corrections for each wire is more than the algorithm can accomplish. The finally used correction is therefore a supercell correction.

In Fig. 4.27 the deviations of supercells from 1 are shown. The correction factors are given by the reciprocal values. It is remarkable that many cell gains are off by 30% or more.

4.3.1.2 Truncation-window correction

For a given number of hits it is possible to calculate, how many of them are rejected due to the upper and lower truncation limits (remember that due to integer effects this is not exactly 10% and 30% of all hits). Dividing these numbers by the total number of hits gives the rejected range fraction, as was shown in Fig. 4.10. The question under investigation in this section is, how these jumps in range influence the dE/dx measurement.

The probability density of signal heights for single hits in the CTD can be described by a LANDAU distribution. This function (in the following named 'reference LANDAU distribution' L_h) is given by a 'standard LANDAU distribution' L_s with a linearly transformed argument. The two parameters of this linear transformation will be fixed later in this chapter. First of all, we investigate the influence of the above mentioned integer effects on a standard LANDAU distribution.

For each number of hits n, the mean value $\langle L_s(n) \rangle$ after truncation can be calculated by integration (Fig. 4.28). Unfortunately, the total number of hits is not available in processed data, only n_h, the number after truncation, can be extracted. Therefore, the results shown in Fig. 4.28 have to be transformed into a distribution depending on the truncated number of hits, shown in Fig. 4.29. If more than one bin before truncation ends up in one bin after truncation, their mean value is used at this point.

There is still one step missing on the way to a correction factor: the transformation from L_s to L_h has to be done. Figure 4.29 with $\langle L_h \rangle$ instead of $\langle L_s \rangle$ on the ordinate will then give the deviations dependent on the hit number. Normalised to $\langle L_h \rangle$ for an ideal truncation-window of 10-70%, this plot will give the reciprocal correction factor.

The linear transformation $L_s \rightarrow L_h$ is fixed by two parameters, slope and offset. The used reference should represent the distribution of single hit measurements around their truncated mean. In other words, the truncated mean of the reference LANDAU should be at 1. This fixes the offset as a function of the width, so we are left with one free

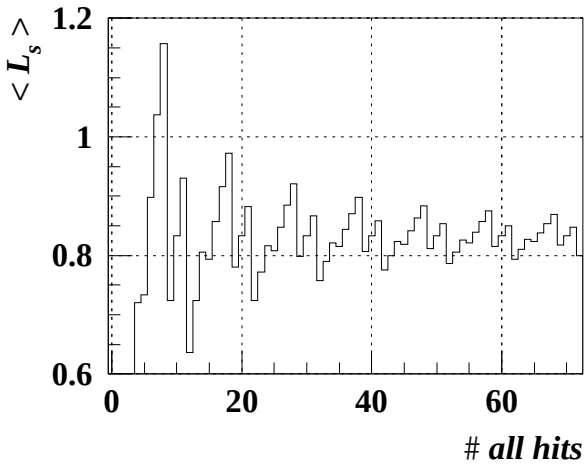

Figure 4.28: Effect of the truncation-window in bins of the total number of hits on a standard LANDAU distribution L_s.

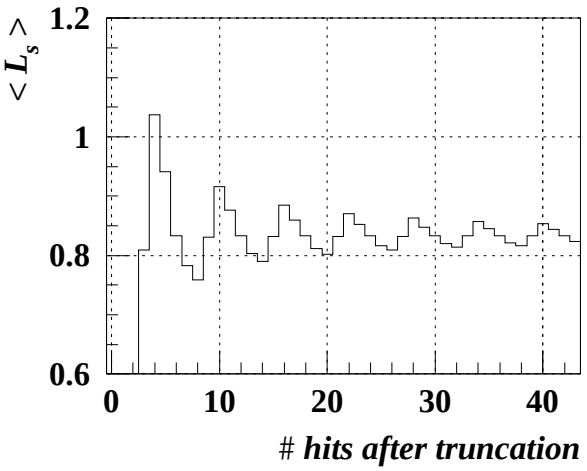

Figure 4.29: Effect of the truncation-window in bins of the number of hits after truncation, using the standard LANDAU distribution L_s.

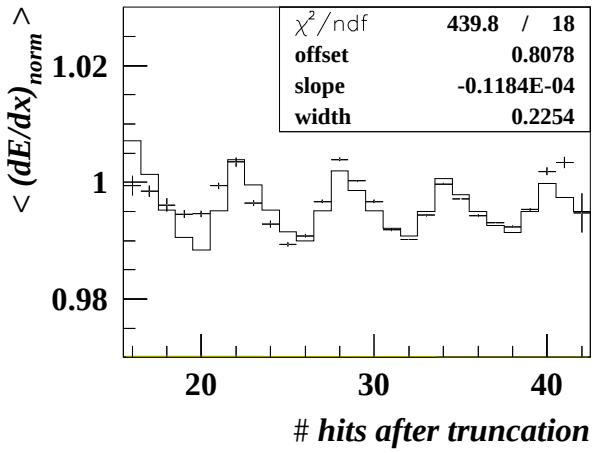

Figure 4.30: Fit to fix the width of the reference LANDAU distribution. The shown data points are the HERA I data pion sample with $p > 400\,\text{MeV}$, the fit function is the sum of a linear function and the distribution of Fig. 4.29, using a standard LANDAU distribution.

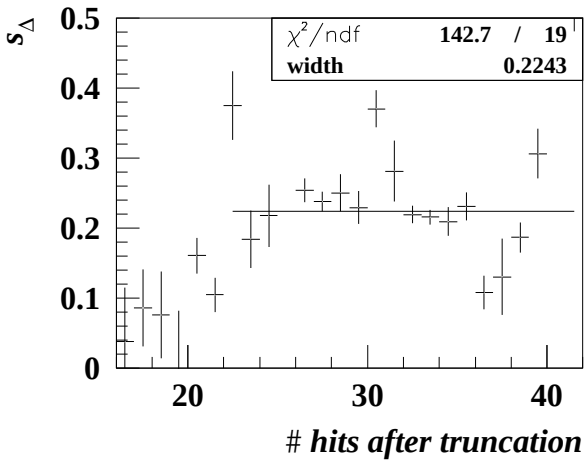

Figure 4.31: Differential view of Fig. 4.30. Dependence of s_Δ on the number of hits after truncation. The definition of s_Δ is given in Eqn. 4.4.

parameter. This parameter can be extracted from data by comparing Fig. 4.29 with the corresponding distribution for real data (remember, up to this point only integrations of LANDAU distributions are done). The ordinate of Fig. 4.29 scales with the searched slope for the linear transformation. Fitting the distribution of Fig. 4.29 plus a free offset to the corresponding data distribution will provide the searched slope w (= scale factor for the reference LANDAU distribution).

At this point it is necessary to drop a few words about the data sample used for this business. As Fig. 4.30 shows, the variation of the normalised dE/dx in bins of the number of hits is only of the order of $1-2\,\%$. The fit, which will be applied to the data, has to quantise these variations. The other applied corrections to the dE/dx measurement are only known up to a level of $1-2\,\%$, not to forget other effects, which are not investigated at all. As long as these effects are not correlated to the number of hits of a track, this does not cause any problems, as they will equally shift all bins of the distribution under investigation. However, as soon as they affect different bins in Fig. 4.30 differently, they can have a big impact on the searched fit parameter. Unfortunately this is the case, as the number of used hits is correlated with the track kinematics. Small numbers of hits in most cases correspond to small polar angles. This has to be taken care of. To minimise the impact from effects other than the truncation-window, it is necessary to use an even cleaner data sample for this fit than used for any other tuning shown in this section. First of all it has to be taken into account, that the measured dE/dx of tracks with many saturated hits (Section 4.3.1.4) strongly depends on the single hit signal distribution, i.e. the searched parameter. To avoid any bias, only tracks without saturated hits below the upper truncation limit are used here. Furthermore, the influence of a badly described dE/dx expectation has to be minimised. This is sufficiently fulfilled by the restriction of the pion sample to momenta above 400 MeV. Actually there are pion and electron tuning samples available, but there are two reasons not to use the electron sample for

this fit: One reason is, that due to the higher $\langle dE/dx \rangle$, the probability for saturation is higher than in the pion sample. Of course, neglecting all tracks with critically high saturation to first order solves this problem, but as already mentioned before, this kind of selection causes a bias in dE/dx of the data sample. As this bias is not identical for all bins (saturation becomes enriched for small polar track angles), it is safer to restrict to the less biased sample beforehand. The second argument against the electron sample is its smaller statistics compared to the pion sample.

Even with this particulary cleaned data sample, a special handling is necessary for the needed level of accuracy. This becomes possible due to a simple fact: The effect of the used truncation window happens in small ranges of the abscissa (already clearly visible in neighbouring bins), whereas other effects only affect these distributions in wide ranges of the abscissa. This renders the fit less sensitive to wide ranges of the abscissa. A way to achieve this is to replace the fitted offset by a linear function. The slope of such a function in first order compensates long range dependencies. Furthermore, Fig. 4.30 shows, that there is a deviation in the lowest bins. Small numbers of used hits correspond to small p_t which is correlated to small p of the tracks. In the final results shown in Chapter 5 it is still visible, that for low $\beta\gamma$ the corrected data deviates from the expectation (keep in mind that at this point we are speaking about sub-percent accuracy). This $\beta\gamma$ range corresponds to the low momentum tracks in the pion sample and therefore this causes an unexpected slope in the first bins of Fig. 4.30 and renders them useless for the fit. Finally, the fit is done starting at 22 hits. The result of this fit is also shown in Fig. 4.30. As a cross check, the same was also done using the electron sample. In this sample, the lowest bins are mainly filled with DIS electrons, having a $\beta\gamma$ without such problems, and indeed, the data distribution looks fine down to the lowest bins.

A risk of this approach is, that there may be a correlation between the slope of the linear 'long range dependence' and the scale of the fitted histogram, leading to a wrong extracted width parameter. An alternative for finding the searched scale is to look differentially at the distribution. A new histogram (Fig. 4.31) is filled with the differences of neighbouring bins, normalised to the corresponding difference calculated with the standard Landau distributions:

$$s_\Delta(n) = \frac{\langle dE/dx_{norm} \rangle (n) - \langle dE/dx_{norm} \rangle (n+1)}{L_s(n) - L_s(n+1)} \quad . \tag{4.4}$$

The mean value of this distribution gives the searched scale. The benefit of this approach can be appreciated by comparing the data points and the fit function in Fig. 4.30. It looks like there are offsets for whole ranges in the abscissa between these two distributions. They can be caused by the jumpy relation between the number of hits and the polar angle. Depending on the number of passed superlayers, tracks are lumped in different ranges of number of hits. For example, tracks with 5 superlayers usually do not have more than 22 used hits. As the tracks which reach the 6^{th} superlayer are only reconstructed up to the 5^{th} one, the whole θ range corresponding to these two superlayers is covered in the bins up to 22 hits. The next bins are dominated by the θ range of the 7^{th} and 8^{th} superlayer. The transition between these two ranges is not very smooth in the number of used hits, so θ-dependent deviations can cause such jumps in the shown distribution. Fitting Fig. 4.30 directly means, that whole groups of bins will be off and will pull the fit, whereas in the differential approach, only one bin is affected by these jumps. This makes the differential fit less sensitive to them. The finally used value for the slope is the fit result in Fig. 4.31:

$$w = 0.2243 \pm 0.0045 \quad . \tag{4.5}$$

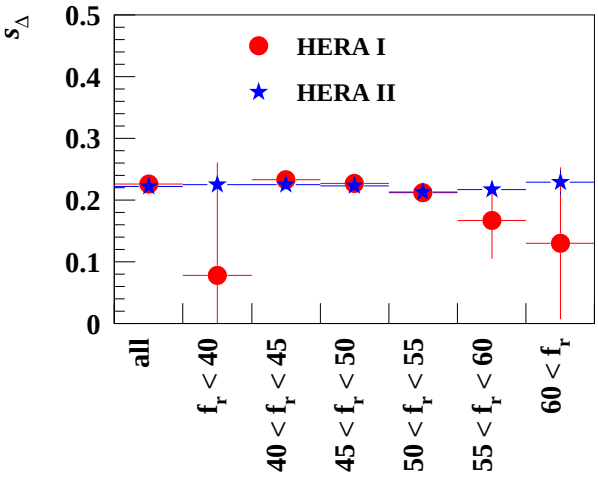

Figure 4.32: s_Δ (see Eqn. 4.4) as a function of the CTD working point, represented by the run-by-run correction factor f_r The definition of f_r can be found in Sect. 4.2.1.2.

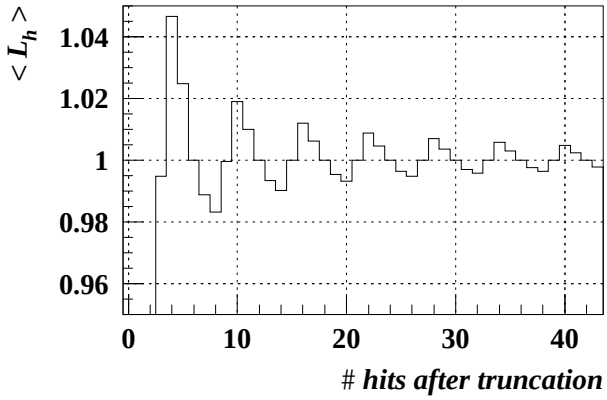

Figure 4.33: Effect of the truncation-window in bins of the number of hits after truncation, using the reference LANDAU distribution L_h (similar to Fig. 4.29), normalised to the expected mean for a standard 10-70% truncation window.

A comparison of the two fit results shows, that they are anyway very close together. Various checks were done to investigate the stability of these two methods. To check whether the relative width of the reference LANDAU distribution depends on the working point of the CTD, the data samples were split in bins of the 'run-by-run correction factor'. Figure 4.32 shows, that no such dependence was found. Even the comparison with HERA II data does not reveal a significant change. Therefore a universal width can be used for the whole data set.

For completeness, Fig. 4.33 shows the same as Fig. 4.29 using the reference LANDAU distribution, normalised to a reference truncation-window of 10-70%. The bin content in this plot directly gives the reciprocal correction factor.

The determination of the truncation-window correction is summarized as follows:

- The probability density distribution of the signal height for single hits is expressed by the reference LANDAU distribution L_h. This function is related to the standard LANDAU distribution L_s by a linear transformation.

- If one knows L_h the calculation of the truncation-window effect and its correction is straight-forward. Thus, the task is to measure the two parameters of the linear transformation $L_s \rightarrow L_h$.

- The number of rejected hits due to truncation is integer. Thus, the fraction of rejected hits varies depending on the total number of available hits. The exact fractions for the lower and upper truncation have been calculated as a function of the total number of hits.

- The mean value of the truncated standard LANDAU distribution has been calculated as a function of the number of hits (Fig. 4.28).

- This function has been transformed into a function of the number of hits after truncation, n_h (Fig. 4.29).
- If one does the previous steps with the (unknown) function L_h instead of L_s, the shape of the resulting function $L_h(n_h)$ will be the same as for $L_s(n_h)$; the scale between these two functions is the same as the slope of the linear transformation $L_s \rightarrow L_h$.
- $L_h(n_h)$ describes the n_h-dependent fluctuations of the truncated mean, i.e. the distribution $\langle dE/dx_{norm} \rangle (n_h)$ fits with $L_h(n_h)$.
- $\langle dE/dx_{norm} \rangle$ integrated over all n_h is equal to 1. This constraint fixes the offset of L_h and hence the offset of the linear transformation $L_s \rightarrow L_h$.
- The remaining parameter (the slope of the transformation) has been found by a fit of $L_s(n_h)$ plus a linear function to $\langle dE/dx_{norm} \rangle (n_h)$. The scale of this fit is the searched parameter w (Fig. 4.30). One could close this section at this point.
- The method described is sensitive to incompletely corrected other effects on the dE/dx measurement. These other influences affect $\langle dE/dx_{norm} \rangle$ on a long scale in n_h whereas the truncation-window effect is reflected in the differences of $\langle dE/dx_{norm} \rangle$ in neighbouring bins ($\Delta n_h = 1$). This feature has been exploited by using the distribution of s_Δ to extract w (Fig. 4.31).

Figure 4.33 illustrates that for trustful tracks (more than 16 hits) the effect under investigation is quite small ($\approx 1\%$). Anyway, as this effect is not caused by chamber physics, but by pure arithmetics, it is simple to correct it without any risk of misinterpretation of the tuning samples. Moreover, this approach gives a good measurement of the width of the reference LANDAU distribution, which is also needed for the saturation correction as described in Sect. 4.3.1.4. As that correction shows a very strong dependence on this width, its accurate measurement is important.

4.3.1.3 Correction for truncated mean with limited number of hits

As shown in Sect. 4.2.2.2 the number of values taken into account for a mean calculation has an influence on the result, if the probability density distribution for the single values is asymmetric. This is true for the LANDAU shaped probability distribution for the dE/dx of single hits. In the end one is interested in a corrected dE/dx measurement which does not depend on the number of used hits, thus it is needed to apply a proper correction for this effect.

In Section 4.3.1.2 the reference LANDAU distribution L_h for the single hit dE/dx distribution was determined. One can use this distribution in a Monte Carlo simulation to calculate the truncated mean of randomised 'standard hits' and compare the result with the expected mean value calculated by truncated integration of L_h. This integral represents the expected mean value for an infinite number of hits. Figure 4.34 shows the result of this comparison. The mean value increases with decreasing number of hits. Some small fluctuations can be seen in each sixth bin. This is an artefact of the truncation method: some bins in n_h correspond to one, others to two bins in the number of hits before truncation. As the shown effect does not only depend on the asymmetry in the

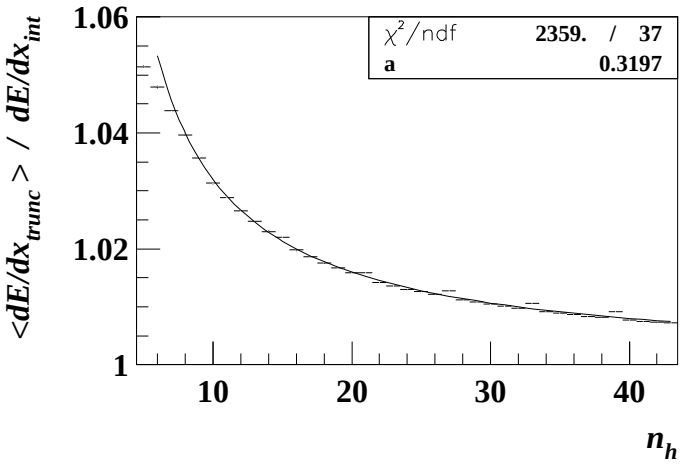

Figure 4.34: Dependence of the truncated mean on the number of used hits. Monte Carlo simulation with a LANDAU shaped probability density for single hits. The width of the LANDAU function is extracted from data.

LANDAU distribution, but also on the truncation-window, this kind of integer effects is visible in the shown distribution. One can also see, that this dependence can be described by a function of the form

$$f_m = 1 + \frac{a}{n_h} \quad . \tag{4.6}$$

Only in the first bins the fit overshoots the Monte Carlo results. This can be ignored, as tracks with less than 10 hits used for the dE/dx calculation anyway are by far not well enough measured to be used.

As the Monte Carlo is generated with the proper parametrisation for L_h the found parameter a is also valid for real data; thus $1/f_m(n_h)$ is used as a correction factor.

4.3.1.4 Correction for tracks with many saturated hits

As already mentioned in Sect. 4.2.1.4, tracks which have more than 70% of their hits below the saturation limit, are all treated equally in their dE/dx calculation, whereas all other tracks (saturated tracks) need a special treatment. This additional correction can become very large (of the order of a factor 2). If it is not perfect, it can cause a big bias on the measured dE/dx. In order to tune correction for other effects than this one, such a big bias may become critical. It is therefore mandatory to clean up the tuning samples from saturated tracks as much as possible, as shown in Sect. 4.1.5.

Nevertheless, the user, who wants to apply the dE/dx corrections, would like to apply them also for less ideal tracks. So even if saturated tracks are insignificant for the correction tuning, in the end they should be available for the user. In contrast to most of the other effects described in this thesis, the correction for saturated tracks has nothing to do with the CTD itself, but is a pure algebraic effect; it only depends on integrals of LANDAU distributions. Thus, the best way to deal with it is to build a toy model, which covers the relevant algebra, and to extract the correction function from this model. The used model works as follows:

- For each single hit on a wire, the signal is calculated using the expected signal multiplied by a random number. The probability density for these random numbers is given by a reference LANDAU distribution as described in Section 4.3.1.2.
- The lower threshold for single wires was set to 0.2 mips in the model. It turned out, that the influence of this threshold on the output of the model is negligibly small.

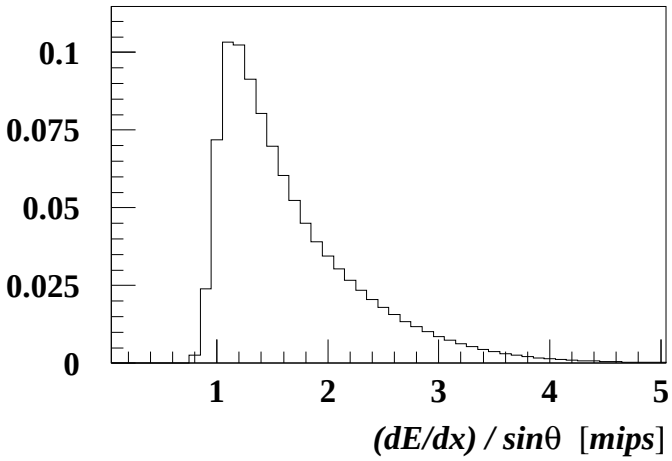

Figure 4.35: Probability distribution for $(dE/dx)/\sin\theta$ for a real data sample. In this plot, the run-by-run corrected dE/dx was used.

- The wire efficiency was set to 90%. This represents inefficiencies due to dead channels and the rejection of hits within 100 ns after the previous one.
- The global scale for the transformation between mips and FADC-counts was taken to be the mean scale factor of HERA I data.
- For control plots the θ-distribution of the tracks is selected. This is not needed for the correction algorithm itself. Therefore, missing knowledge about this distribution cannot affect the correction. For best coverage of the upcoming plots in this section, a flat distribution was chosen.
- All tracks are calculated to have their origin at the nominal vertex and to be straight lines in the Rz-plane. Using the known topology of the CTD, this allows to calculate the outermost wire reachable for each track.

For each track represented by its real dE/dx and its θ it is possible, to calculate its 'real signal' given by $(dE/dx)/\sin\theta$. Figure 4.35 gives a rough estimate which signals are expected from real data. This is only needed to have an idea about the range of 'real signal' it is important to deal with. By using θ of the track, it is also possible to calculate the possible number of hits, and for each of them, a dE/dx value can be randomised. As a next step, the model parameters define, which hits have to be neglected due to chamber inefficiencies, as well as the lower threshold and truncation limits, and the number of used and saturated hits can be counted.

The ratio (#saturated hits)/(#used hits) represents the area fraction below the already mentioned Landau distribution above the saturation limit (after cutting away the part below the lower threshold). This area can be used to calculate the position where saturation cuts into this Landau distribution. The last but one step is to calculate the mean of this function in the range between the lower truncation limit and the saturation limit and the higher truncation limit, respectively. Finally, the ratio of these two mean values gives the correction factor.

The benefit of this approach is, that it can also be used for real data, for which the true dE/dx is not known. The only step, where the true dE/dx value enters the calculation, is for estimating the area below the Landau, which is cut away by the lower threshold. This area is anyway very small and does not vary much with changing dE/dx. So it is appropriate for this business to estimate the true dE/dx very roughly by using the area

fraction of the saturated hits. The error caused by this approximation is far below a tenth of a percent.

The toy model can also be used to test the accuracy of the corrections. As the 'real signal' is known in the model, corrected values can be compared with it. This is done in Figures 4.36, 4.37, 4.38 and 4.40. Separate plots are shown for different 'real signals'. Each plot is binned in numbers of saturated and all hits. The colour represents the relative deviation of the corrected dE/dx from the value expected if there was no saturation problem. Without correction (Fig. 4.36), the measured dE/dx is always too low. The deviation rises with increasing number of saturated hits. This is expected, as the high end of the LANDAU distribution is cut by taking saturated hits into account. WOUTER VERKERKE's correction function takes out most of the dependence on the number of saturated hits (Fig. 4.37). For low real signals it tends to slightly too low values; if the number of saturated hits is very high, also the corrected dE/dx ends up too high. In all shown distributions some vertical structures can be seen. They are caused by integer effects, as, depending on the total number of hits, the truncation does not cut away exactly the lowest 10% and the highest 30% of the signals (Sect. 4.3.1.2). This causes visible fluctuations in the expected truncated mean.

The correction described above does not show these fluctuations, as the correct truncation-

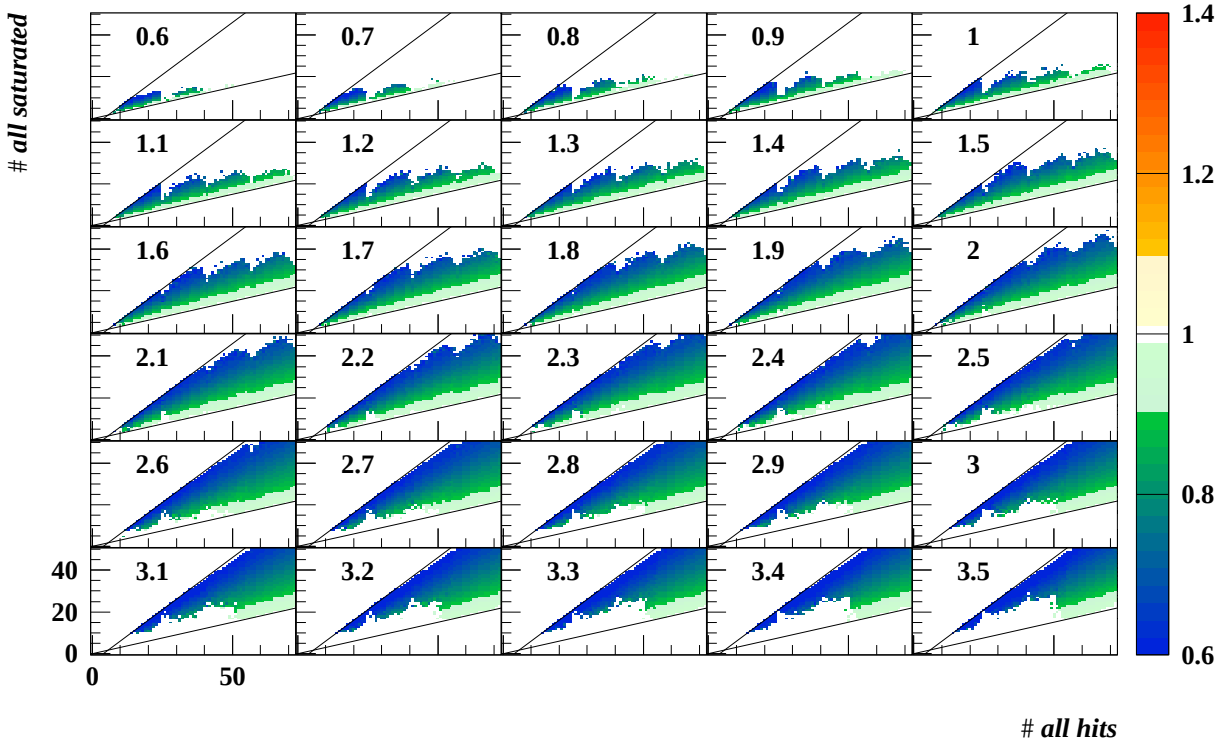

Figure 4.36: Without any saturation correction: (10%-70%) truncated mean after saturation divided by truncated mean without saturation in bins of the total number of saturated hits vs the total number of hits. The different plots show different signal bins (real $(dE/dx)/\sin\theta$), given by the numbers in the plots. The lower line indicates the 70% truncation limit, the upper one is the limit (#used - #saturated)=4, which is the minimal constraint for dE/dx calculation within the ZEUS Phase I reconstruction code.

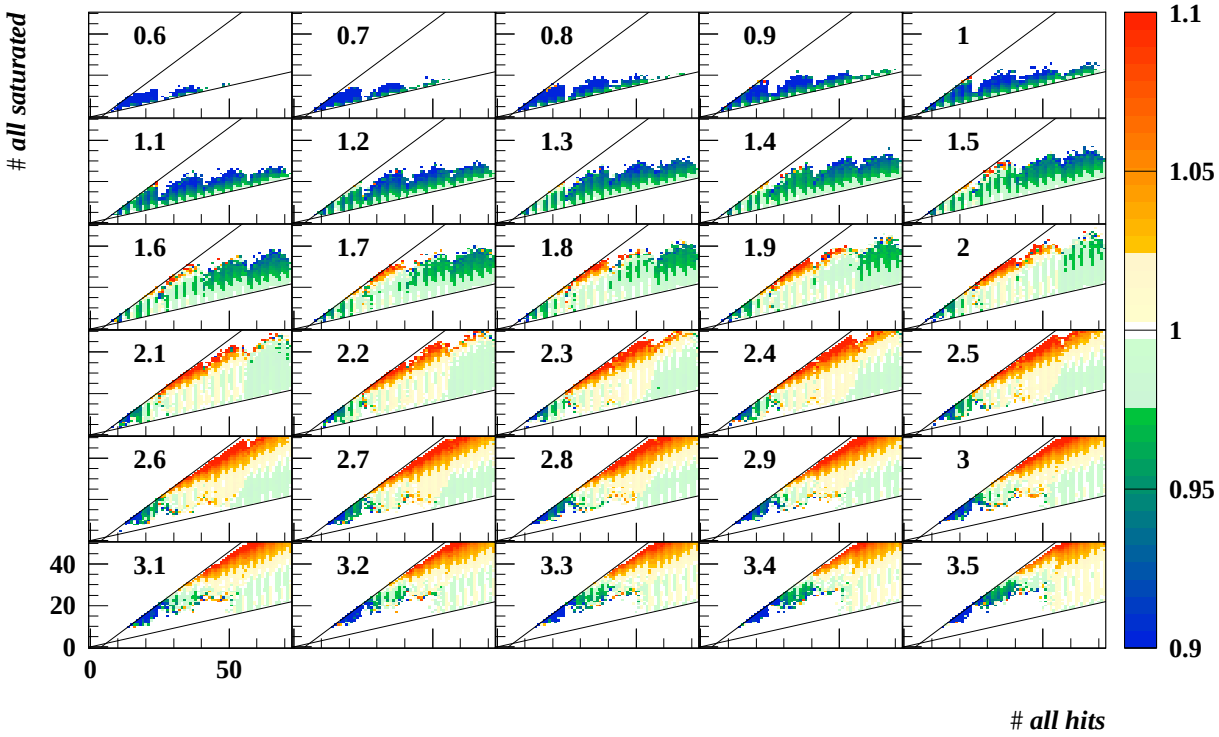

Figure 4.37: After correction by Wouter Verkerke: same plots as in Fig. 4.36 with modified scale in the colour code.

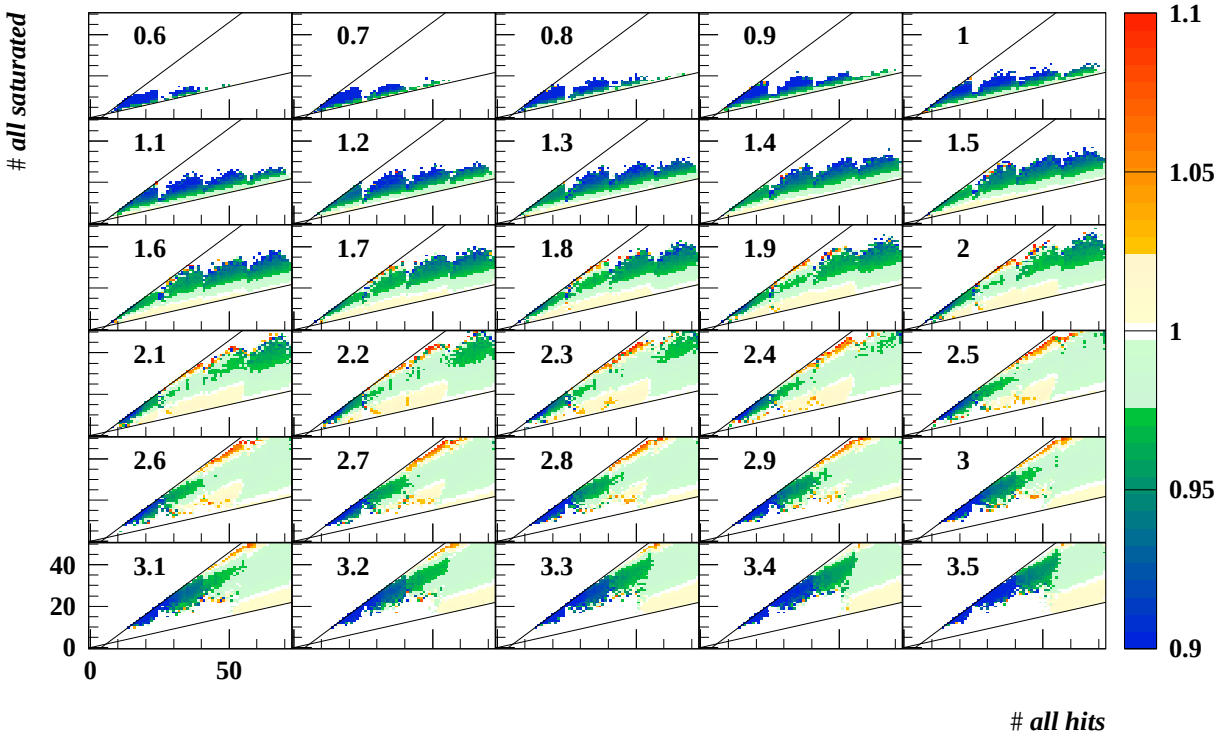

Figure 4.38: After toy model correction. Same plots as in Fig. 4.36 with modified scale in the colour code.

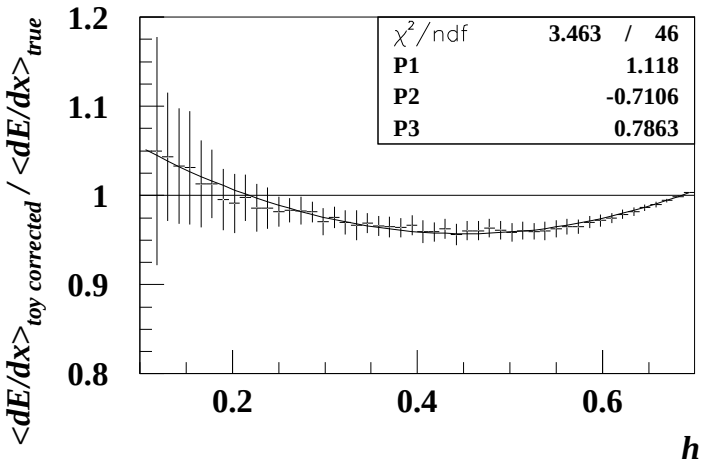

Figure 4.39: Dependence of the distribution shown in Fig. 4.38 on the parameter h. The shown fit is a polynomial of second order of h.

window is taken into account. This makes sense, as the shifts due to variations in the truncation-window are compensated elsewhere. For most cases, the corrected values are within ±2% about the expectation (Fig. 4.38). Anyway, the result is still not optimal. At the limits of the accessible (#all hits, #all saturated)-plane the result tends to be slightly too high, whereas in the central area it tends to lower values. This is the same kind of dependence, Wouter Verkerke corrects on. In addition to the mentioned correction using integrals of the Landau distribution, a phenomenological fit is used to compensate for this remaining dependence. The deviation from the expectation, as seen in Fig. 4.38 is plotted against the same parameter as used in the approach of Wouter Verkerke:

$$h = \frac{\#\text{all hits} - \#\text{all saturated}}{\#\text{all hits}} \quad . \tag{4.7}$$

Figure 4.39 clearly shows the mentioned dependence and can be fitted[5], using a polynomial of second order in h. As most of the needed correction is already done by the first step, the deviations from 1 are not very large (within ±5%), so this is really only some kind of 'fine tuning' of the correction mentioned above. Dividing the toy-model-corrected dE/dx by this function gives the final result of this correction (Fig. 4.40).

This general concept is important enough to be summarised at this point: The main part of the correction for saturated tracks is done using an approach, which is based on the traceable algebra of the varying upper truncation limit. The phenomenological part of the corrections is only a small adjustment on top of this.

At first glance, this result may be worse than before the last step, but the probability, where to find tracks in these distributions, also has to be considered. In Fig. 4.41 the real data abundance is shown. The areas with highest abundance are the ones, where in Fig. 4.40 the correction has to be best. The most important areas can be found for 'real signals' between 1.0 and 1.5, for small numbers of used and saturated hits. It turns out, that using the last step of corrections, the results have improved a lot. The worst areas after correction are high real signals with very high numbers of saturated hits. In these cases, the resolution of the dE/dx measurement becomes very bad anyway, as there is only a very small number of unsaturated hits left for the measurement. Furthermore, very

[5]This graph is generated based on the binned contents of Fig. 4.38. The error bars represent not only the variance between single track entries, but also differences in the bin-mean-values in Fig. 4.38. Consequently, the errors are overestimated, leading to an incorrectly small χ^2 of the fit. This does not cause a problem, as the shape of the fit is not influenced by systematically scaled error bars.

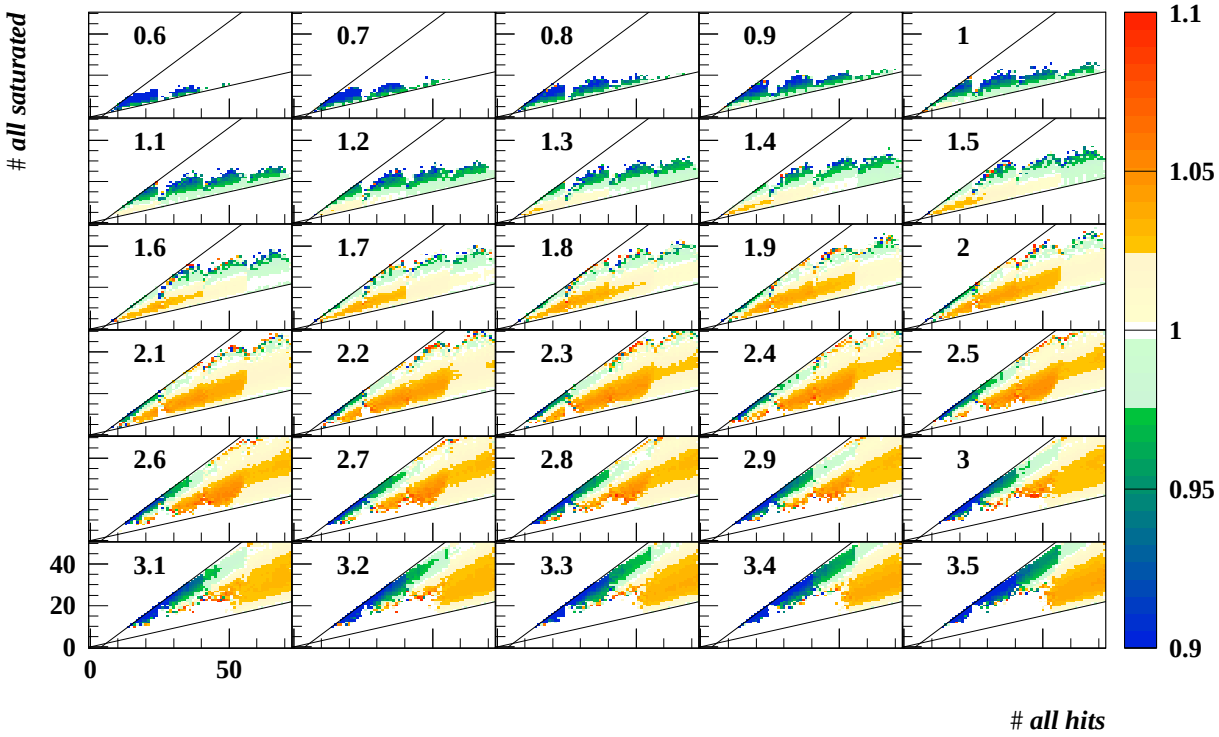

Figure 4.40: After toy model correction including correction on h. For details see text. Same plots as in Fig. 4.36 with modified scale in the colour code.

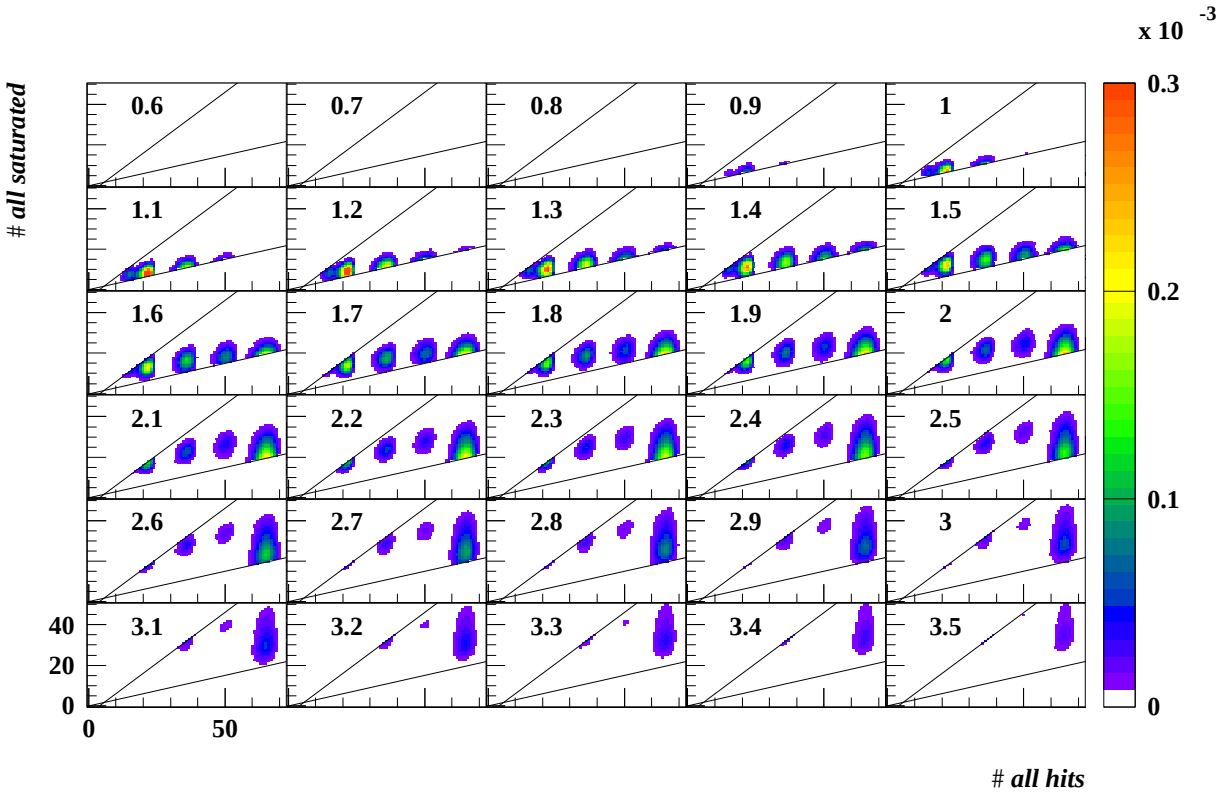

Figure 4.41: Abundance density distribution. The $(dE/dx)/\sin\theta$-bins are weighted, using Fig. 4.35.

high signals correspond to high dE/dx. In the high dE/dx range, different particle types are clearly separated. As, in the end, the dE/dx measurement is only used for particle identification, for such tracks it does not matter, if the measurement is systematically wrong by 10%, as the separation is good enough anyway.

4.3.1.5 Threshold-effect correction

The expected signal shown in Fig. 4.13 already seems to be a good observable to extract the threshold effect. Unfortunately it contains the problem, that for the normalisation to dE/dx_{exp} it is necessary to know the species of the particle. This is available for tuning samples, but in application on data, it must be possible to use the correction method for any track without possessing this knowledge. One way to get rid of this problem would be to replace the expected signal at the abscissa by the measured signal, but this causes a new problem: The measurements are distributed around the expectation. If a measurement is high compared to the expectation, the normalised measurement will also be high. Therefore, abscissa and ordinate of the histogram are related to each other. The shape of the resulting profile is a complicated folding of this correlation, the frequency distribution of track candidates in the expected signal and the threshold effect itself. Fig 4.42 shows the resulting distribution. It is not usable to extract a correction function for the threshold effect.

The method developed here is a bit tricky. It is based on the following idea: Taking a set of tracks with the same expected signal their measured signals should be distributed around this expectation value and its mean should be equal to the expectation value. Therefore, restricting to these mean values, no difference exists between looking at $signal_{exp}$ or $signal_{meas}$ on the abscissa of Fig. 4.42. For these mean values a correction function extracted from Fig. 4.13 should be perfect. The trick is now, to extract a correction function depending on $signal_{exp}$ from Fig. 4.13 and to apply this correction on $signal_{meas}$ for each single track. If the signal of the track is far off its expectation, this correction will of course be wrong, but as long as it is close to the expectation, it is fine.

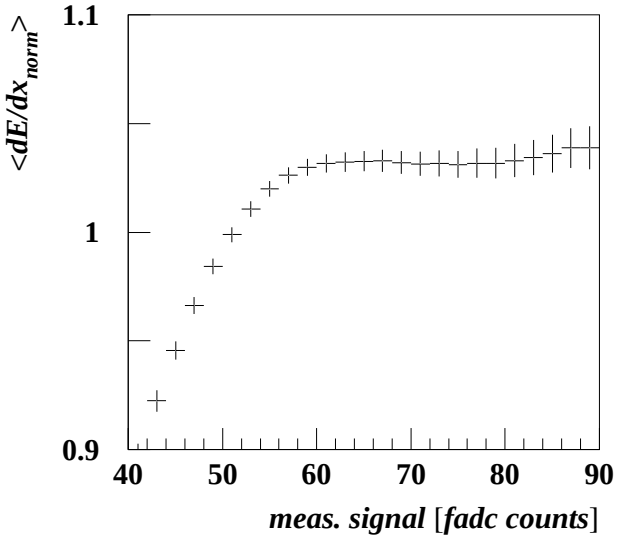

Figure 4.42: Profile of $\langle dE/dx_{norm} \rangle$ vs measured signal. Pion tuning sample, HERA I data.

Another way to look at this approach is to envisage the distribution in Fig. 4.13 folded with the single-track dE/dx resolution. The effect of this folding will be, that the distribution will retain its shape but will become flatter. The deviation between the folded and the unfolded distributions will depend on the slope of the curve in Fig. 4.13. It will be biggest for the smallest signals. This implies, that for a correction function, extracted from the unfolded distribution, the biggest error appears for the smallest signals. To avoid an overcorrection a special handling is needed in this low signal regime. The most simple way out is a cutoff for the correction factor. The correction is limited to a maximum of 20%. This is a limit, which has turned out to be safe and stable.

This correction method can be applied to any kind of data sample. As the threshold effect occurs at very low signals, it makes sense to use a sample with high statistics in the low signal regime, namely the pion tuning sample. In addition, there are correlations in the corrections of the threshold effect and the space-charge effect. As the electron sample is

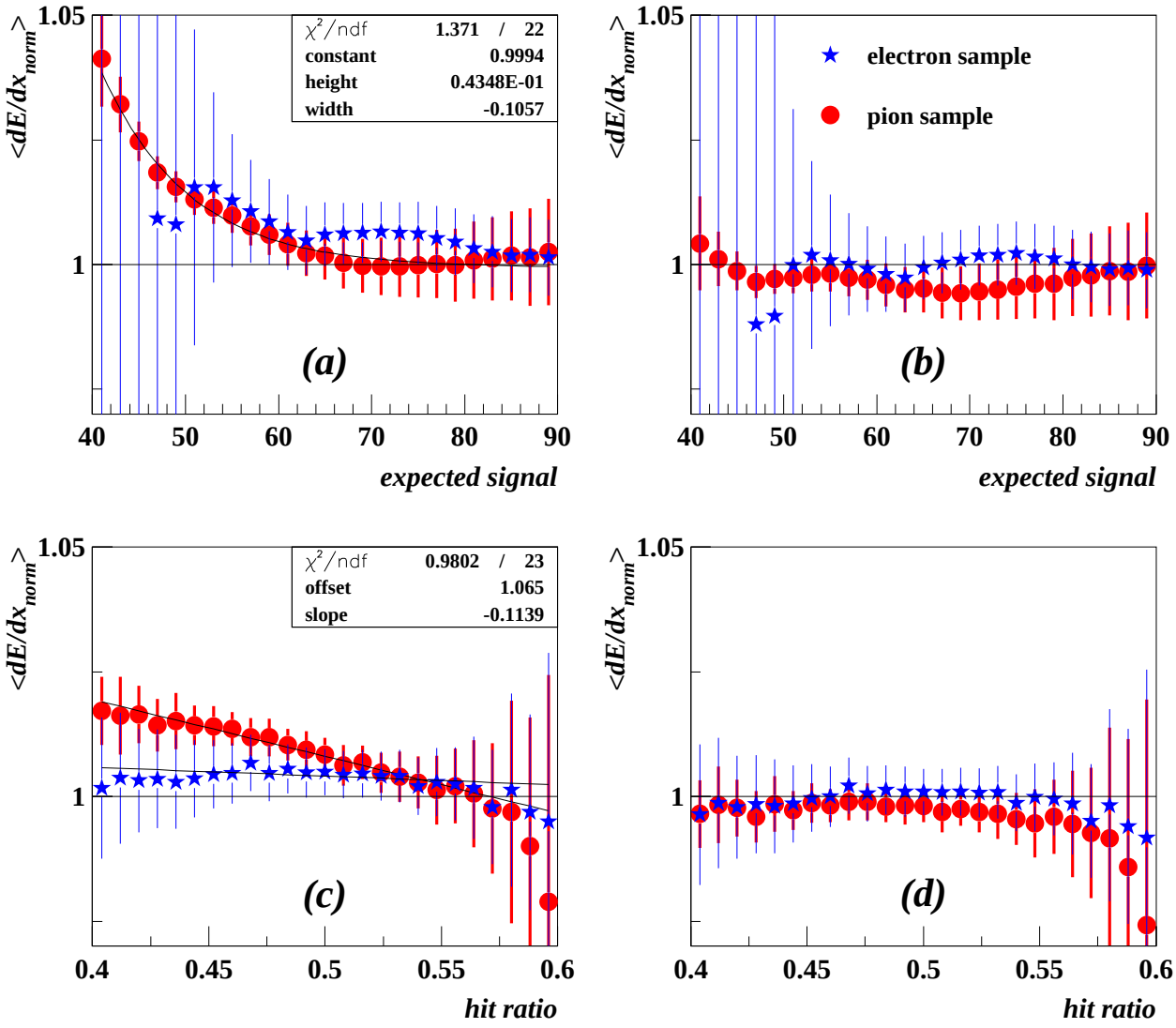

Figure 4.43: Control plots for the correction against the threshold effect. The left column shows profiles without threshold correction, the right column after threshold correction. Normalised dE/dx vs expected signal (a, b) and vs hit ratio (c, d).

more affected by the space-charge effect than the pion tuning sample, it makes sense to discard the electron sample for tuning the threshold effect correction.

Following the calculations in Appendix D, the used fit function is given by

$$f_{threshold} = constant + height \cdot \exp\left(\frac{width}{signal}\right) \quad . \tag{4.8}$$

Compared to the result in Eqn. D.9 the constant 1, which represents the correction factor in case of no threshold effect, is replaced by a free constant. This is done, because the global normalisation in the sample may be off. The further treatment of this parameter will be explained in Sect. 4.3.2.

As $f_{threshold}$ describes the threshold effect itself, the corresponding correction factor has to be

$$c_{threshold} = \frac{1}{f_{threshold}} \quad . \tag{4.9}$$

It is not ensured by default, that the replacement of $signal_{meas}$ by $signal_{exp}$ is safe or that the correction might run out of control by this. Therefore it is highly recommended to check the outcome of this correction method. Figure 4.43 shows the normalised dE/dx vs. the expected signal before (a) and after (b) threshold effect correction. After correction the distribution is significantly flatter than before. As most of the tracks in the electron sample are in the high signal regime, the biggest deviations from 1 in this distribution affect only a very small fraction of tracks in the electron sample. The comparison between Fig. 4.43 (a) and (b) clearly shows that the correction works well.

Another test can be made using the hit ratio. If a hit is below the threshold it is not used for the track reconstruction. Therefore tracks, which are affected by the threshold effect, will be reconstructed with a smaller number of hits than unaffected tracks. To be independent on the track topology, the hit ratio, given as the number of used hits for dE/dx reconstruction divided by the number of passed wires, is used. The truncated mean method gives an upper limit of 0.6 for this hit ratio. Smaller values are caused by the threshold effect and other reasons (dead wires, quality cuts in the Phase 1 reconstruction). Figure 4.43 (c) shows a strong dependence on the hit ratio for the pion sample and a slight one for the electron sample. This matches with the expectation as electrons are almost unaffected by the threshold effect. After correction (Fig. 4.43 (d)), both distributions are flat with a mean value at 1, as they should be. The hit ratio does not depend on the expected signal. Thus, Fig. 4.43 (c, d) is a test for the correction, which is not biased by the correction method itself. Its result is a very powerful proof, that the used correction method is efficient.

4.3.1.6 Neighbourhood-effect correction

As usual, the definition of a correction function is split into two steps. First of all, a proper parameter (or maybe several parameters), which the effect under investigation depends on, has to be found. The parameter(s) should be as close as possible to the origin of the corrected effect. Only if this criterion is fulfilled, it is possible to correct the effect with high efficiency. As a second step, a correction function depending on the parameter(s) has to be derived.

First of all, the focus is on the extraction of a parameter, which the neighbourhood effect depends on. To properly correct against pile-up coming from close neighbours, it

is necessary to trace back the trajectory of all tracks within one event, using the known track helices. This opens the possibility to count, how often two tracks share the same signal wire. Furthermore, it is possible to reconstruct the distance D_i^w between a track i and the signal wire w. A pile-up will occur, if two (or more) signals are left on the same wire at almost the same time. Therefore we are interested in the difference of the drift-times of two signals measured at the same wire. The drift velocity of free electrons within the CTD is almost constant. It changes only very close to the signal wire where the electric field gradient changes rapidly. As we are only interested in drift-time differences, we don't need to care about this region close to the wire (all electrons will take the same time to pass through this region, so the difference of their drift-times through this region is always zero). Thus the drift-time difference Δt_{ij}^a between two signals of tracks i and j at wire a is proportional to the distance difference $\Delta D_{ij}^a = ||D_i^a| - |D_j^a||$.

At this level it is still not known, how the neighbourhood effect at a single wire depends on ΔD_{ij}^a. This dependence has to be given in a weight function $W(\Delta D_{ij}^a)$. In the next step it is necessary to transform the single wire information into a track information. To reflect the method of calculating dE/dx of the track, the best possible way is to introduce a neighbourhood parameter n_w by calculating the mean weight of all possible hits of the track

$$n_w(i) = \frac{\sum\limits_{passed\ wires\ a} \sum\limits_{j \neq i} W(\Delta D_{ij}^a)}{\sharp passed\ wires} \quad . \tag{4.10}$$

At this point, the last open question for fixing the parameter n_w is to find a proper weight function $W(\Delta D_{ij}^a)$. It is obvious, that the pile-up cannot increase with increasing ΔD_{ij}^a. It is also clear, that neighbourhoods beyond some threshold value ΔD_{max} will not contribute to pile-up. This splits the formation of the weight function into two steps. First of all, the limit ΔD_{max} will be found, then the shape of $W(x),\ x < \Delta D_{max}$ can be specified.

By definition, a track without any neighbours within a distance ΔD_{max} should not be affected by the neighbourhood effect whereas tracks with at least one hit below this threshold should end up with a too high dE/dx_{meas}. Even more, tracks that pass only cells, which are not touched by any other track (lone tracks), are a good reference for tracks without a neighbourhood effect.

A side remark is needed at this point: The suggestion may arise, that there may be a pile-up between two signals coming from different bunch crossings. From an academical point of view this should be possible, as in the time between two bunch crossings electrons in the CTD gas drift only about 4.5 mm whereas the drift distance between primary ionisation and the sense wire is up to 25 mm. Therefore electrons from up to 5 bunch crossings can be found in the CTD at the same time. Anyway, the rate of collision events per bunch crossing in the ZEUS detector is extremely small. The probability to hit the same cell in the CTD twice within 5 bunch crossings is negligibly small. We can return to the argumentation above without any raise of fears.

An efficient method to find the threshold distance ΔD_{max} is given by looking at mean dE/dx values for all tracks without neighbours below a distance limit ΔD_{limit} minus the mean dE/dx of lone tracks. As neighbours beyond the limit ΔD_{max} do not contribute to pile-up, tracks without any neighbours within this limit should behave like tracks without any neighbours at all (lone tracks). Thus the mentioned difference should be zero for all $\Delta D_{limit} > \Delta D_{max}$. For smaller ΔD_{limit}, some of the hits will be affected by pile-up, so $\Delta(dE/dx)$ should be positive. The smaller ΔD_{limit}, the more pile-up will contribute and

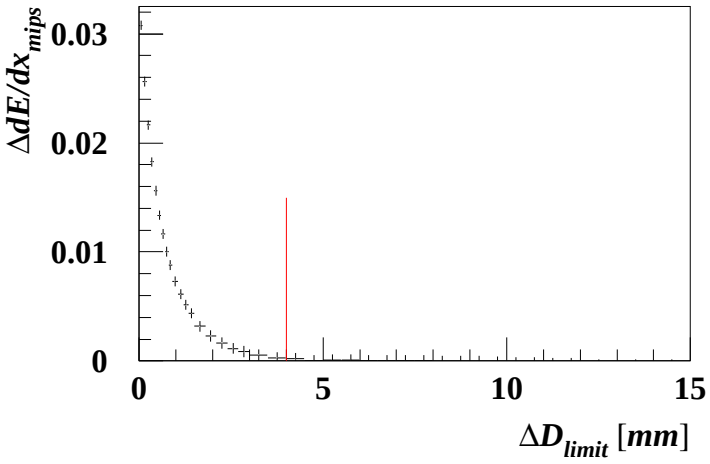

Figure 4.44: Search for the maximal distance ΔD_{max} for the neighbourhood effect, using the pion tuning sample. Each bin contains the mean dE/dx - $dE/dx_{lone\ tracks}$ for all tracks without any neighbours in a range up to ΔD_{limit}. Note that the bins are correlated! The finally used limit is indicated by the red line.

the larger $\Delta(dE/dx)$. This is shown in Fig. 4.44. The point of ΔD_{limit} where this curve becomes flat is the ΔD_{max} searched for. As Fig. 4.44 shows, a limit of

$$\Delta D_{max} = 4\,\text{mm} \tag{4.11}$$

is a safe choice.

The next step is to find a proper weight function $W(\Delta D)$ for $0 < \Delta D < \Delta D_{max}$. As already mentioned, this function should be falling, as the pile-up should be the larger the closer the neighbour is. But another aspect has to be taken into account as well: The reconstruction of distances between a track and the signal wires using the track helix has its limitations. The helix is calculated in such a way, that it is correct at the point of origin of the track. On its way through the detector the particle loses energy due to ionisation, in some cases it can do hard scattering with matter of the detector itself or the trajectory can differ from a perfect helix due to an imperfect homogeneous magnetic field. All of these are reasons, why the track helix only approximately describes the trajectory of the particle. Thus the calculated distances D_i^w and consequently ΔD_{ij}^a are only approximately correct. Even more, the spatial distance D_i^w is used to represent the drift time. But the drift velocity, which associates these two variables, is only a mean velocity. There is some divergence in each 'cloud' of primary electrons. The searched weight function therefore is a convolution of the 'real' ΔD-dependence of the pile-up and the resolution function for the reconstruction of ΔD. The misreconstruction of D_i^w can be estimated by inspecting at low p_t tracks which are looping back to the beampipe within the CTD. The difference ΔD_h in their distance of closest approach to (0,0) in the xy-plane before and after one loop is twice the error of their reconstructed position in xy at their end point (the point of maximum distance to the nominal interaction point). Figure 4.45 shows, that the median of such a distribution is at $\approx 5\,\text{mm}$. This kind of estimation reflects, that the miscalculation of D_i^w is of the same order of magnitude as ΔD_{max}. Therefore the weight function $W(\Delta D)$ is dominated by the resolution of the trajectory reconstruction and not by the distance dependence of the neighbourhood effect.

Figure 4.46 shows various weight functions which were tested. It has turned out that the difference in the effect of using any of them is marginally small. Therefore it does not matter which of the tested parameterisations is used for the weight function. Thus, it makes sense to choose the most simple one, which is the step function

$$W(\Delta D) = \begin{cases} 1 & : \quad \Delta D \leq 4\,\text{mm} \\ 0 & : \quad \Delta D > 4\,\text{mm} \end{cases} . \tag{4.12}$$

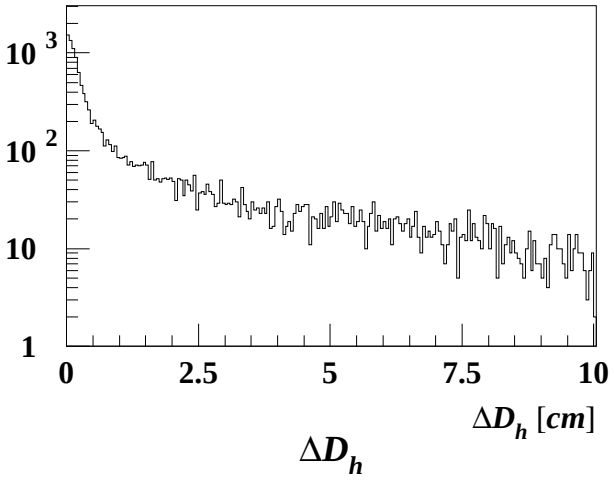

Figure 4.45: Difference in the track parameter D_h for the two parts of tracks, which turn back within the CTD.

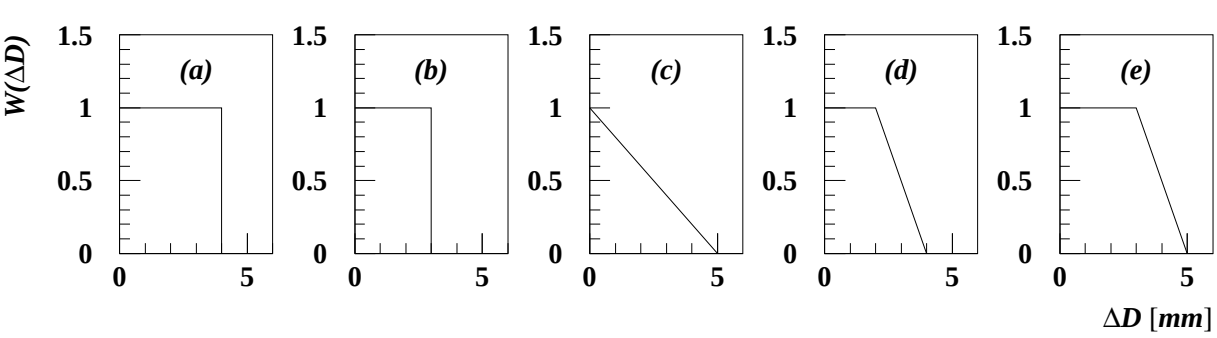

Figure 4.46: Different tested weight functions $W(\Delta D)$. Function (a) was chosen.

Using this weight function, Eqn. 4.10 simplifies to

$$n_w(i) = \frac{\sum_{passed\ wires\ a} \sharp(\Delta D^a_{ij} < 4\,\mathrm{mm})}{\sharp passed\ wires} \quad . \tag{4.13}$$

The calculation of n_w for each track is finished now. The next step on the way is to find a correction function depending on n_w. First of all a decision on the type of correction has to be made. Most other effects are corrected by applying correction factors because these effects are scaling the measured dE/dx. For the neighbourhood effect the situation is different: Piling up a signal means that something is added on top of the signal. To take this into account, the correction against the neighbourhood effect must be additive (and not multiplicative).

Figure 4.47 shows the difference $\Delta dE/dx = \langle dE/dx\rangle - \langle dE/dx\rangle_{lone\ tracks}$ in bins of n_w for the photon-conversion and the pion tuning sample[6]. A linear increase was found; the slope for both distributions is identical, but they have different offsets. This is due to a simple technical reason. In the pion sample lone tracks are defined as tracks, for which in every CTD cell passed by this track no other track is found within the sensitive region. Even with the already mentioned limitations on the reconstruction of the track path, this should be a very clean sample of lone tracks. This fact is also reflected in the almost zero offset of the linear fit. In case of the electrons from photon conversions another definition

[6]Electrons from J/ψ decays and DIS electrons are not used for these plots, as they are mostly lone tracks, thus sample-dependent deviations will affect only the first bin of this plot.

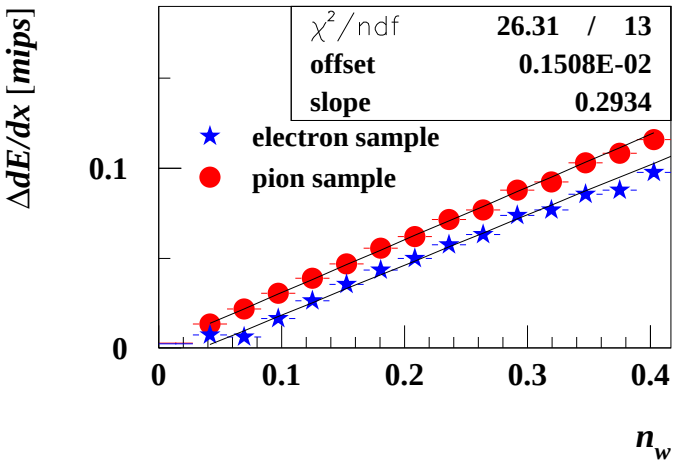

Figure 4.47: Correction function for neighbourhood effect, using the full HERA I data set. The shown fit parameters correspond to the pion sample.

had to be chosen. Almost all of the photon conversions happen within the CTD inner wall. The pair-produced electrons and positrons start to travel on identical paths. Due to the magnetic field they become separated in the xy-plane. Therefore in almost all cases, both tracks pass the same cell in the innermost CTD layer. It is not possible to use the same definition for lone tracks as in the pion sample for these electrons, because it will yield extremely low statistics. For normalising the $\langle dE/dx \rangle$ distribution it is necessary to have sufficiently high statistics; otherwise the resulting distribution will be dominated by the statistical fluctuations of the $\langle dE/dx \rangle_{lone\ tracks}$ sample. To get rid of this problem, in case of the electrons a limitation to $D^a_{ij} > 16\,\text{mm}$ was used for the $\langle dE/dx \rangle_{lone\ tracks}$ sample. This sample is already partially contaminated by pile-up. Therefore the normalisation is higher than in the pion case, and the difference $\langle dE/dx \rangle - \langle dE/dx \rangle_{lone\ tracks}$ becomes lower.

As the normalisation in the pion sample is much easier than in the electron sample only the pion sample was used to extract the correction parameter. The only parameter needed is the slope of the fit. Additional arguments for using the pion sample are its larger statistics and the fact, that the topology of photon conversions has many more constraints than that of tracks coming from K^0 decays. Therefore the risk to see a reflection of the special event topology in the investigated distributions is much greater for the electron sample than for the pion sample. Finally, the electron sample is only used as a cross check for the neighbourhood effect correction.

Some control plots can be seen in Fig. 4.48. As mentioned in Sect. 4.2.2.4, without any correction the mean measured dE/dx is related to the track multiplicity of the events. After applying the neighbourhood correction, this dependence has almost disappeared.

The plots also show some other characteristics of the used data set. They are generated with all available test data sets together. As the different samples are not equally distributed in the shown kinematic range, differences between the samples can cause 'strange' distributions in this plot. For example, in the electron set the data points for the lowest track multiplicity are far below any expectation for track momenta above $\approx 1\,\text{GeV}$. This is caused by the electrons from the J/ψ-sample. As J/ψ-candidates are selected in exclusive production, they can only show up in the lowest track multiplicity bin. The lower cut on the momentum of tracks for J/ψ-candidates ($p > 900\,\text{MeV}$) enriches the lowest bins, with tracks at $\theta \approx 90\,°$. These are the tracks, which are most affected by the space-charge effect, i.e. the aberration of the data points from the expectation has nothing to do with the neighbourhood effect.

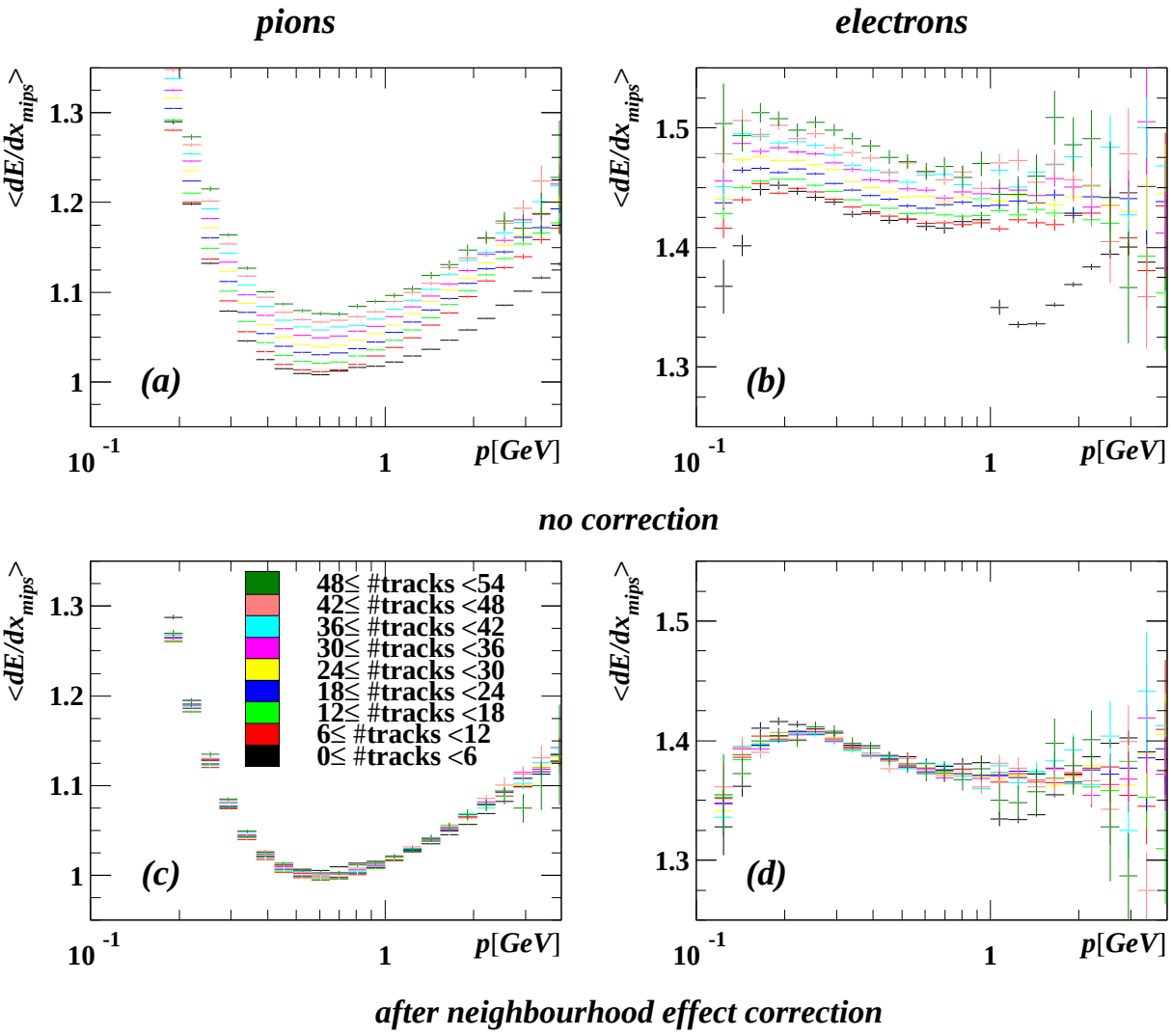

Figure 4.48: $\langle dE/dx_{mips} \rangle$ vs momentum p for pion and electron samples before and after the neighbourhood correction. The data is split up in bins of track multiplicity.

Another feature can be found in the pion sample for $\#tracks < 6$. Without correction their $\langle dE/dx \rangle$ is very low for momenta above 1 GeV. This is the range, where the ρ-sample becomes important. In exclusive production, these candidates always have track multiplicity of 2 (or 3), which is below the mean value of the lowest track multiplicity bin. Therefore, the centre of gravity of the lowest track-multiplicity bin varies depending on the momentum which results in very low $\langle dE/dx \rangle$-values for high momenta.

4.3.1.7 End-plate-effect correction

The correct chamber physics happening close to the end-plates is too complicated to describe properly in a correction algorithm. Anyway, a phenomenological correction is possible. The idea of such a correction is to find correction factors for the measured dE/dx of single hits depending on their distance to the end-plate. It is expected that beyond a certain value of that distance no such correction is needed. Thus the first step to find a proper correction is to find this distance limit Δz_{lim}.

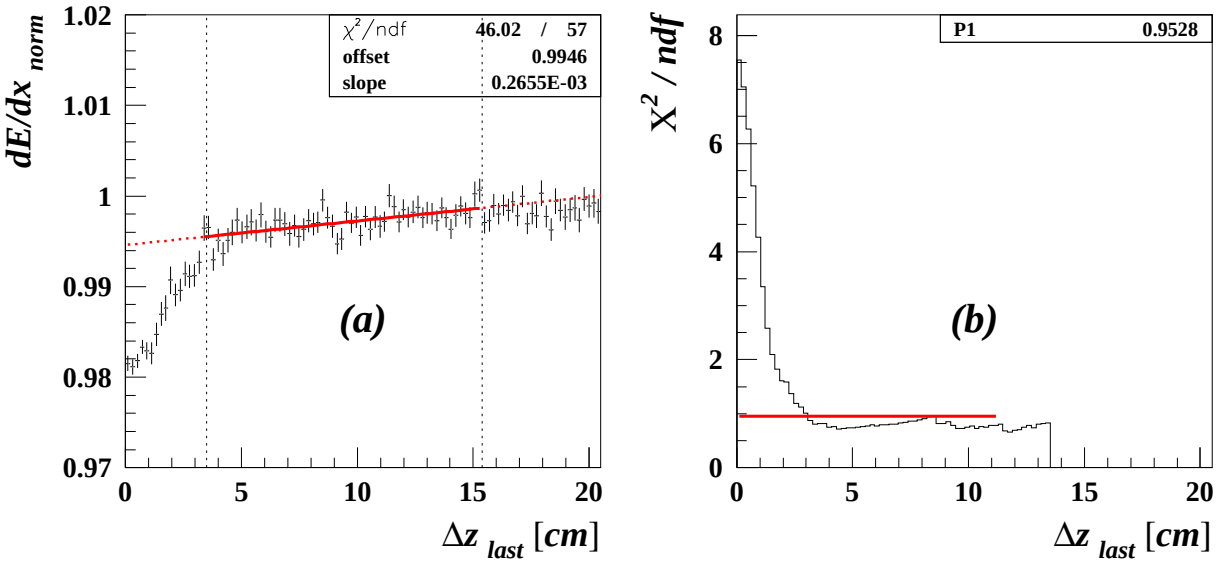

Figure 4.49: (a) dE/dx_{norm} vs Δz_{last}. The vertical lines indicate the fit range. The linear fit is extrapolated over the whole histogram range. (b) χ^2/ndf in bins of the fit range.

Some complications arise in the search for this limit. One of them is the dependence of the measured signal on the propagation distance along the signal wire. Any dependence on the distance between a hit and an end-plate is also related to this different effect. Another correlation can be found in the track kinematics. For example a vertex track with $\theta \approx 90\,^\circ$ will have no hits close to the end-plate, whereas a track with a small θ (or $\pi - \theta$) which leaves the CTD within the 3$^{\text{rd}}$ superlayer has most (or all) its hits close to the end-plate. If the dE/dx measurement depends on θ, this dependence will also be visible in a z-dependent distribution. Thus the task for the moment is to separate the end-plate effect in the investigated distributions from other effects which should be corrected elsewhere.

Figure 4.49 (a) shows the dependence of the normalised dE/dx on the distance of the outermost hit to the end-plate, Δz_{last}. This is a useful variable to search for the parameter Δz_{lim}: tracks with $\Delta z_{last} > \Delta z_{lim}$ should not be affected by the end-plate effect whereas the others are. Thus Δz_{lim} is the limit at which the data points shown in Fig. 4.49 (a) start to differ from their 'normal shape', which is caused by other effects. The big benefit of this distribution is the way, how it depends on other kinematic variables than the z position of the hits. As an example, the θ-dependence will be shown here. Figure 4.50 shows the relation between Δz_{last} and θ for ideal tracks (starting at the nominal vertex; infinite momentum limit). One can see, that due to the superlayer structure of the CTD several bands of θ take part in the same band of Δz_{last}. Looking at any measurement in one bin of Δz_{last} means to pick up data in several bins of θ together. If the measurement depends on θ, only the mean of these θ bins will be visible. If the same measurement will be done in another bin of Δz_{last}, it will correspond to another set of θ bins. But according to Fig. 4.50 this set will be very close to the previous one and the mean effect on all bins should be almost the same. In other words, if dE/dx_{norm} depends on θ, this dependence should show up almost identically in all bins of Fig. 4.49 (a). This is true up to $\Delta z_{max} \approx 15\,\text{cm}$. For larger distances tracks which pass the end-plate in the 9$^{\text{th}}$ superlayer

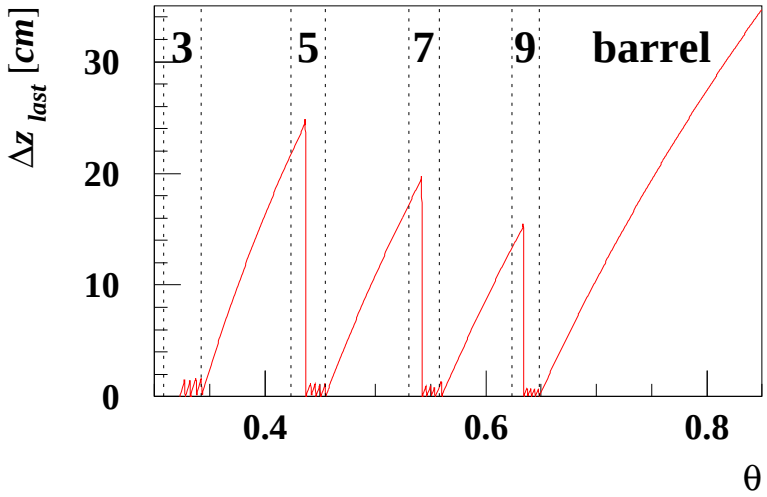

Figure 4.50: Relation between Δz_{last} and θ for tracks from the nominal vertex and infinite momentum (straight lines in the Rz-plane). The CTD geometry (wire positions) and track algorithm rules (outermost hit in axial layer, at least 3 hits in the outermost used superlayer) are taken into account.

do not contribute and therefore the θ distribution of the sample changes significantly.

So far it is shown, that for small Δz_{last} Fig. 4.49 (a) should be almost independent on most effects which can bias the dE/dx measurement. Deviations from a flat distribution have to be dominantly caused by the z positions of the hits. Global dependencies like the already mentioned effect of the one-sided CTD readout should change slowly and smoothly within small Δz_{last} variations. Within the small range of 15 cm they should be described quite well by a linear function. End-plate related effects should show up in this histogram as a deviation from a linear slope. The value for which the shown distribution starts to be non-linear is the searched value Δz_{lim}.

This limit is found using the following method: for each Δz_{last} a linear fit, limited to the interval $[\Delta z_{last}, \Delta z_{max}]$ is done. A new histogram is filled with the χ^2/ndf for each of these fits (Fig. 4.49 (b)). If the data in the fit range has a linear slope, one expects that χ^2/ndf is approximately 1; if the fit range contains also non-linear parts of the distribution, the χ^2 should rise. This is exactly what Fig. 4.49 (b) shows: for high values of Δz_{last} the distribution of χ^2/ndf is flat and close to 1 whereas for small Δz_{last} the χ^2/ndf becomes larger. The searched Δz_{lim} is now defined to be the Δz of the first bin with a χ^2/ndf smaller than the mean value of all χ^2/ndf with $\Delta z_{last} < 11$ cm. The upper limit for this mean is chosen to be small enough to render the method not too sensitive to statistical fluctuations and high enough to cover a big part of the flat distribution in Fig. 4.49 (b). Small variations of this limit have almost no influence on the result, thus it is not needed to find a more sophisticated method to locate this limit.

The second step to find a proper correction of the end-plate effect for single hits is to estimate the size of such an effect, depending on the distance to the end-plate, Δz. It is expected, that such an effect becomes larger, as closer to the end-plate the hit happens.

Before contemplating about the shape of such a function $f(\Delta z)$, it is useful to have a look on the resolution of the measurement of Δz. The position of the end-plates is very well known, thus the error on Δz is given by the error of the z-component of the helix fit at

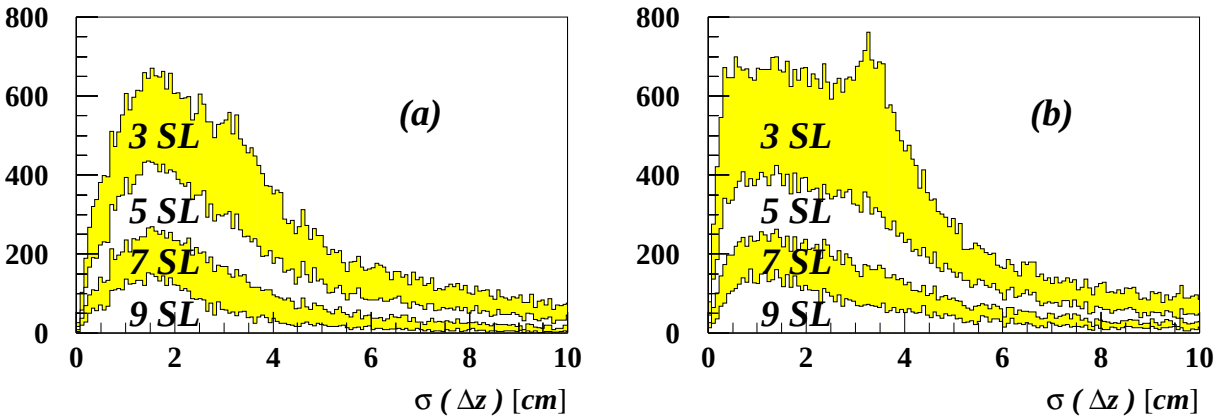

Figure 4.51: Resolution of $\Delta z_{end-plate}$, calculated with the covariance matrix of the helix fit. Small subsamples of (a) HERA I, (b) HERA II data. The tracks are classified according to their outermost superlayer.

the position of the end-plate. This error can be calculated by error propagation, using the helix parameters and their covariance matrix (Fig. 4.51). The typical resolution is between 0.5 cm and 4 cm, which is roughly the same as the already found Δz_{lim}. Therefore any kind of end-plate correction will be limited by the measurement of Δz and it does not make sense to search for a complicated correction function which 'knows' about details close to the end-plate.

It is mandatory to issue a critical remark for this resolution test. The error calculation for the track helix is a very sophisticated approach optimised for best possible track reconstruction, thus these errors are not gaussian errors in the strict sense. It is known, that the helix error matrix does not perfectly describe the error of the track [33]. But anyway it gives an estimate about the size of the error. One can also give a similar estimate based on Fig. 4.45, which shows, that for $\approx 40\%$ of very low-p_t tracks the parameter ΔD_h is larger than 1 cm. This means, their helix parametrisation describes their coordinate at the outermost point in the CTD wrongly by more than 5 mm. This is roughly the radial distance between the CTD layers, so for 40% of all low-p_t tracks the outermost layer is reconstructed wrongly, if one uses the track helix for this reconstruction. A shift of one wire corresponds for end-plate tracks to a jump in Δz_{last} of roughly 1 cm, which is in the same order as the resolution mentioned above.

As there is no effect for $\Delta z > \Delta z_{lim}$ obviously $f(\Delta z) = 1$ for this range. The most simple function, which is continuous for all Δz will be linear for $\Delta z < \Delta z_{lim}$ with $f(\Delta z_{lim}) = 1$. But it turned out, that such a function will overestimate the investigated effect for very small Δz. This can be explained with the bad Δz resolution: If $f(\Delta z)$ represents a very big effect for hits very close to the end-plate, tracks with their outermost hit at $\Delta z \approx 2$ cm can be treated as strongly influenced just because the measurement gives $\Delta z \approx 0$ cm. A safer way to describe the end-plate effect on the level of measured Δz is to use a constant function $f(\Delta z)$ for small values of Δz. Finally, this function is chosen to be constant for $\Delta z < \Delta z_{lim}/2$. The benefit of this choice is that f can be fully described with one free parameter (in addition to Δz_{lim}). The following calculations will show, why the region A as shown in Fig. 4.52 is a good choice for this parameter.

To understand the choice of the parameter A it is needed to think once more about the

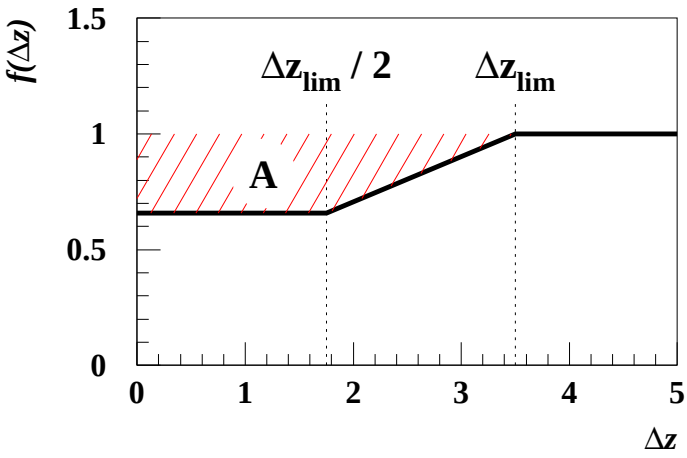

Figure 4.52: Schematic view of the Δz dependence of the signal. The two parameters to describe this function are Δz_{lim} and A.

available data for this measurement. Up to now, all arguments were related to single hits. But only mean values of whole tracks are available. So what does the end-plate effect look like for the mean dE/dx of a whole track?

To simplify the following calculations, for the moment let us replace the function f by a non-continuous but very simple step function:

$$f(\Delta z) = \begin{cases} 1 & : \quad \Delta z \geq \Delta z_{lim} \\ 1-c & : \quad \Delta z < \Delta z_{lim} \end{cases} \tag{4.14}$$

which implies

$$A = \Delta z_{lim} \cdot c \quad . \tag{4.15}$$

It is straight-forward to extend the shown calculations to the real shape of f (Appendix G).

Most of the hits will be far away from the end-plate and will not suffer at all. Only the last few hits on the track can be affected. The measured dE/dx of the track can be calculated as

$$\frac{dE}{dx}_{meas} = \left\langle \frac{dE}{dx}_{i\ meas} \right\rangle = \frac{1}{\#\text{hits}} \sum_{i=1}^{\#\text{hits}} f(\Delta z_i) \cdot \frac{dE}{dx}_{i\ \text{unaffected}} = f \cdot \frac{dE}{dx}_{\text{unaffected}} \tag{4.16}$$

with

$$\begin{aligned} f \ &:= \ \frac{\#\text{unaffected} \ + \ (1-c)\#\text{affected}}{\#\text{hits}} = 1 \ - \ c\frac{\#\text{affected}}{\#\text{hits}} \\ &= \ 1 \ - \ \frac{A}{\Delta z_{lim}} \cdot \frac{\#\text{affected}}{\#\text{hits}} \quad . \end{aligned} \tag{4.17}$$

As long as the hits are distributed equidistantly in z, #affected and Δz_{lim} scale in the same way. The scale cancels in Eqn. 4.17 and therefore the parameter A is independent of Δz_{lim}. In other words, for a track with equidistant hits in z a change of Δz_{lim} alone does not change f. The size of the end-plate effect is reflected by A alone. A descriptive way to understand the meaning of the size A within the calculation of the mean dE/dx for a track is to understand the size A as the total number of hits, which contribute to the mean with a value of 0 FADC counts.

This provokes the question, why do we need Δz_{lim} as a parameter, if A already describes the end-plate effect? The answer can be found in the condition of equidistant hits. As long

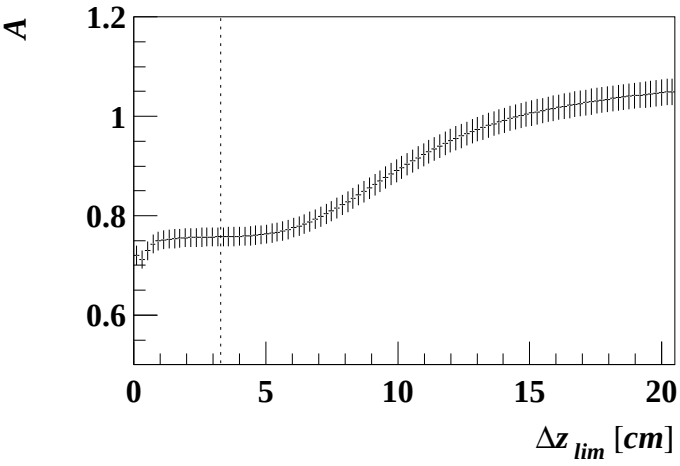

Figure 4.53: A as a function of Δz_{lim}. The used value of Δz_{lim} is indicated as a vertical line.

as this condition is fulfilled, indeed one can set Δz_{lim} to any value and one will always get the same results (except of integer effects: don't forget that the number of affected hits is an integer). But the real conditions are different. The sense wires are placed in lumps (superlayers) and we ignore outermost hits if they take place in stereo layers. Thus it can happen, that even if a track passes through the end-plate, the measured dE/dx is not at all affected by the end-plate effect: it can happen that no hit within the critical distance to the end-plate is used for the dE/dx measurement. The proper setting of Δz_{lim} allows to take this inhomogeneous hit distribution into account.

Let us summarise what we have achieved up to now. Knowing the helix parameters of a track and the geometry of the CTD, one can calculate the z position of each possible hit z_i. The critical distance Δz_{lim} is extracted from data. Using this and the previously calculated z_i, the number of all possible hits and the number of affected hits can be counted. If one also knows A, one can calculate f using Eqn. 4.17 and the searched correction factor will be $1/f$ due to Eqn. 4.16. Thus the last missing piece in this puzzle is the measurement of A.

The intention of the end-plate-effect correction is to make the graph in Fig. 4.49 (a) linear down to $\Delta z_{last} = 0\,\text{cm}$. That can be achieved by using the shown linear fit $g(\Delta z_{last})$ as a reference:

$$\frac{dE}{dx}_{ref} := \frac{\frac{dE}{dx}_{norm}}{g(\Delta z_{last}) \cdot f(A)} \quad . \tag{4.18}$$

The searched A fulfils the condition

$$\left\langle \frac{dE}{dx}_{ref} \right\rangle = 1 \quad . \tag{4.19}$$

Combining Eqn. 4.17, 4.18 and 4.19 leads to a linear function to calculate A:

$$\begin{aligned} 1 &= \left\langle \frac{1}{\frac{dE}{dx}_{ref}} \right\rangle = \left\langle \frac{f(A)}{\frac{dE}{dx}_{norm}/g(\Delta z_{last})} \right\rangle = \left\langle \frac{1 - \frac{A}{\Delta z_{lim}} \cdot \frac{\#\text{affected}}{\#\text{hits}}}{\frac{dE}{dx}_{norm}/g(\Delta z_{last})} \right\rangle \\ &= \left\langle \frac{1}{\frac{dE}{dx}_{norm}/g(\Delta z_{last})} \right\rangle + \left\langle \frac{-\frac{1}{\Delta z_{lim}} \cdot \frac{\#\text{affected}}{\#\text{hits}}}{\frac{dE}{dx}_{norm}/g(\Delta z_{last})} \right\rangle \cdot A \quad . \end{aligned} \tag{4.20}$$

The mean values in Eqn. 4.20 can be measured and thus a way to measure A is found.

It is obvious, that for the measurement of A an end-plate problem enriched sample should be used. This is done by selecting only tracks which pass through the end-plate in the outer half of one of the axial super layers. For high statistics the pion tuning sample is used. In Fig. 4.53 one can see A as a function of Δz_{lim}. For very small values of Δz_{lim} integer effects can corrupt the shown distribution; even if a track suffers from an end-plate effect, its outermost hit can be outside the critical Δz range, if this range is chosen so small. According to the geometry of the CTD this can happen for Δz_{lim} below $\approx$ 1 cm. It was mentioned before, that for equidistant hits A should be independent of Δz_{lim}. This is approved by Fig. 4.53 up to $\Delta z_{lim} \approx 5$ cm. For larger distances it can happen for the used sample, that the corresponding parts of the track helices lie within the gap between the superlayers. Then A becomes larger. Anyway, the measured and used Δz_{lim} matches perfectly with the constant part of $A(\Delta z_{lim})$, which means, that A is measured well.

4.3.1.8 Dispersion correction

The change of the signal height due to the dispersion of the signal during its propagation along the wire depends on two parameters. The obvious one is the distance of propagation. Without single hit information only the mean propagation distance of all hits according to one track can be calculated. It is given by the distance between the readout (rear end-plate) and the mean z, $\bar{z}$, of the track.

The second relevant dependence of the dispersion is the shape of the signal itself. A short and high pulse will change much more during propagation than a long and low one. The ratio of pulse height over pulse length will be a proper parameter for this dependence. It was already shown [19], that the height of the signal scales with the collected charge (the area below the signal) which leads to the conclusion, that all signals have the same pulse length. Thus the signal height itself is a good variable to parametrise the signal shape. To cover a big range in this variable it makes sense to use the full tuning samples, pion and electron sample, together.

As already shown for the threshold correction, it is inappropriate to look at dE/dx in bins of the measured signal height, because these two variables are correlated. To get an unbiased distribution for fitting, the measured signal has to be replaced by the expected signal s_e, which is available for the tuning samples, as their particle types are known.

The use of s_e for this correction leads to a problem, because the drift-time-effect correction (Section 4.3.1.10) uses the same parameter, too. One has to take care, that these two corrections are kept disentangled, otherwise the algorithm to combine the partial corrections (Section 4.3.2) will become numerically instable. To be more explicit, such a problem will occur as soon as both corrections will handle a dependence on the signal height alone. If this happens, none of them can 'know', what the other will do with this dependence. An efficient solution for this is to allow only one of the two corrections to handle the one-dimensional dependence on s_e. In this case, the drift time effect correction should do that job.

Now one has to distinguish two different steps: one is to fit a proper function to a measured distribution in order to extract the fit parameters, the other is to apply the inverted fit function as a correction function. For the fit one cannot expect, that the data is free of any one-dimensional dependence on s_e. Even if this correction should not compensate such a dependence, the fit function has to cope with it. For the application of the fit function as a

correction, this one-dimensional s_e dependence should be ignored.The most simple setup for a correction function which satisfies this functionality is to use a factorised function

$$f(s_e, \bar{z}) = f_1(s_e) \cdot f_2(s_e, \bar{z}) \tag{4.21}$$

where f_1 contains the one-dimensional dependence on the signal and f_2 the remaining two-dimensional part. In this case, the correction function will be simply f_2^{-1}.

The pure s_e dependence is described with a linear function of $\log_{10}(s_e)$. This shape is completely covered in the drift-time-effect correction, which ensures that the corresponding correction will be done there.

For the remaining part of the fit function certain boundary conditions can be taken into account. If there is no signal at all ($s_e = 0$) the height of this 'signal' cannot change during its propagation. This means, in the limit $s_e \to 0$ the fit function should be 1: $f_2(s_e \to 0, \bar{z}) = 1$. The same is true, if the propagation distance is 0. If the signal does not propagate, it cannot change its height: $f_2(s_e, \bar{z} = z_{readout}) = 1$.

The most simple non-trivial function which fulfils these conditions is a polynomial of 2$^{\text{nd}}$ order. If one writes the dependence on the two parameters as $g_1(s_e)$ and $g_2(\bar{z})$ such that $g_1(0) = 0$ and $g_2(z_{readout}) = 0$, most of the components of such a polynomial disappear due to the boundary conditions and we end up with

$$f_2(s_e, \bar{z}) = 1 + a \cdot g_1(s_e) \cdot g_2(\bar{z}) \tag{4.22}$$

where a is the only free parameter.

One can expect, that the height of the signal varies exponentially with respect to the propagation distance. Together with the boundary condition this leads to

$$g_2(\bar{z}) = 1 - e^{(z_{readout} - \bar{z})/a_z} \tag{4.23}$$

where a_z is the scale for z.

The signal-height dependent part of the fit function is more phenomenological:

$$g_1(s_e) = 1 - e^{-s_d/a_s} \tag{4.24}$$

which fulfils the boundary condition $g_1(0) = 0$, is monotonically rising (larger signal causes larger effect) and has an upper limit (the effect cannot be larger than total annihilation of the signal).

In Phase I the z-correction does a first order correction of the dispersion effect. For a correction as described in this section it is needed to first remove this Phase I correction. This is done in Fig. 4.54 (a, b). Furthermore, one has to handle two different philosophies for the currently introduced correction and the Phase I correction. In this section the used fix-point is the case, that the signal does not have to propagate at all. Therefore the dispersion can only reduce the signal height; unchanged signals should be found for hits at $z = z_{rear\ end-plate}$. The reference for the Phase I z-correction is the centre of the ZEUS detector, i.e. hits with positive (negative) z are corrected up (down). The transformation between these two references is given by the scale factor 1.15, which is the Phase I z scale at the position of the rear end-plate. Such a scale has no influence on the final result of the corrections as it is compensated by the drift-time-effect correction (Sect. 4.3.1.10). The plots in Fig. 4.54 (a, b) are scaled up by this factor. As the drift-time-effect correction is

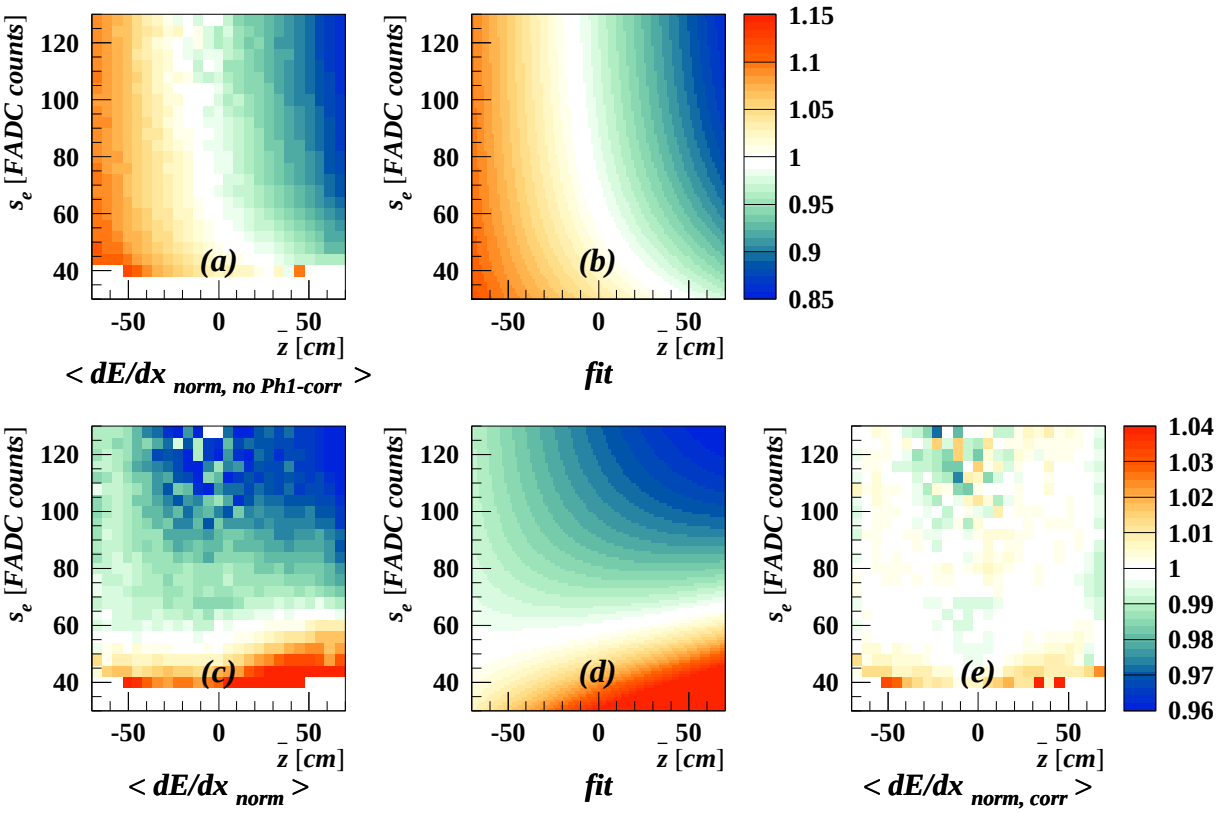

Figure 4.54: Expected signal s_e versus $\bar{z}$, the normalised $\langle dE/dx_{norm} \rangle$ is indicated in colour. In the first row (a, b) the z-correction from Phase I is removed. The second row (c, d, e) shows the same plots after Phase I z-correction (different colour scales!). $\langle dE/dx_{norm} \rangle$ without dispersion correction (a, c), the corresponding fit function (b, d) and the result of the correction applied (e). The plots contain pion and electron tuning samples of HERA I. Bins with less than 40 entries are shown white in order to remove the worst statistical fluctuations.

calculated using the dispersion-corrected data, this scaling allows to interpret the colours quantitatively as the dispersion effect. This is a benefit in Fig. 4.54 (a) but can cause confusion in the fit function Fig. 4.54 (b). The dispersion itself can only reduce the signal height (values below 1) but due to the scaling, this limit is shifted to 1.15. Both plots show, that the signal height mainly depends on $\bar{z}$ but is not totally independent of s_e.

To be more sensitive to details it is helpful to look at similar plots after applying the Phase I corrections. Such plots show the deviation of the data from the Phase I-corrected results. This is done in Fig. 4.54 (c, d, e), using a proper colour scale. Figure 4.54 (c) shows the normalised dE/dx before applying a dispersion correction. In Fig. 4.54 (d) one finds the corresponding fit function, which is the product of Eqn. 4.21 and the Phase I z-correction function. Finally, Fig. 4.54 (e) shows the data distribution after applying the dispersion correction. The remaining systematic deviations from expectation are less than 1% for the whole range covered in $(s_e, \bar{z})$.

A way to check the effect of the dispersion correction is to look at the profile of Fig. 4.54 (e). As a reference the same profile without any dispersion correction has to be used. It is not enough to look at the profile of Fig. 4.54 (c), because other corrections, especially the

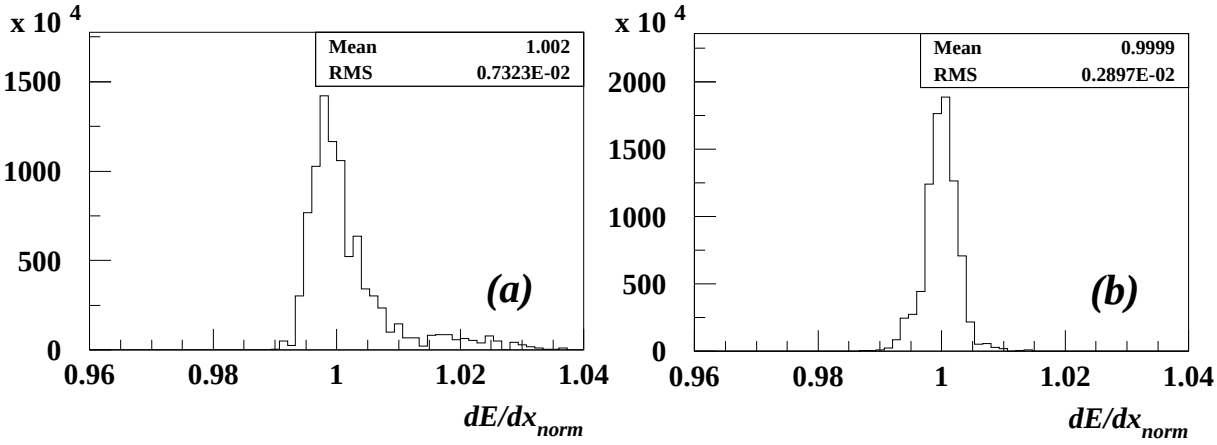

Figure 4.55: Profile of Fig. 4.54 (e) without (a) and with (b) dispersion effect correction. The entries are weighted according to the statistics in the bins of Fig. 4.54 (e).

drift-time-effect correction, react on the dispersion effect, too. Furthermore, it is needed to generate the whole set of fit parameters without any dispersion correction. Such a comparison yields direct information about the improvements by applying this correction. One observes in Fig. 4.55 the RMS of the profile improves from 7.2% to 3.1%. Furthermore, before correction this distribution has a long tail to high values whereas after correction it is symmetric about 1.

4.3.1.9 Space-charge-effect correction

The first step in finding a correction mechanism is, once more, to find out, on which parameters the effect depends. Within the phenomenological view of the space-charge effect it is obvious, that such a parameter is the mean distance between the primary electrons, when they reach the signal wire. This distance can be extracted using several inputs. First of all, the mean distance of primary electrons along the trajectory is reciprocally proportional to the ionisation rate of the particle which causes the track:

$$\langle distance \rangle \approx \frac{1}{dE/dx_{true}} \quad . \tag{4.25}$$

Be aware, dE/dx_{true} is NOT a unique value, which is always the same for the same kinematics and particle type. This is not the searched dE/dx after applying all corrections, but the ionisation rate, which still depends on parameters like the gas mixture, the air pressure, etc.

But this is not all we need. The primary electrons drift to the sense wire. Only very close to the sense wire the avalanche and therefore the space-charge effect occurs. Thus, the trajectory has to be projected on the sense wire to get the topology of the ion clouds caused by the avalanche. In addition it is necessary to model (very roughly) the shape of the ion clouds. Simulations of the evolution of ionisation clouds have been done elsewhere [52, 53]. For the current purpose, it is only important to keep in mind, that the shape of the cloud is not symmetric about the drift path of the electron. In the Rz-plane, the electric field lines (and the drift paths) are orthogonal to the wire which gives a field of

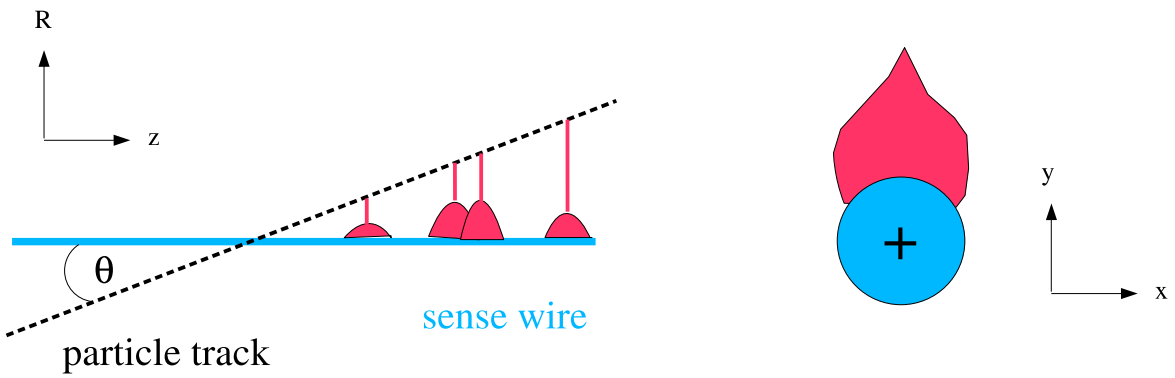

Figure 4.56: Schematic view of the formation of ionisation clouds on a sense wire. Taken from [54].

parallel drift paths. In the xy-plane the drift paths all join at the same point (at the wire); they are concentric. For the ion cloud this means, that it will be larger in z than in $R\phi$. At this point it is also important to remember, that the electrons which are responsible for the measured signal appear almost at the same time at the signal wire. Therefore the time evolution of the ion cloud is almost negligible. The relevant shape of the cloud is still like drafted in Fig. 4.56.

In the Rz-plane the size of the cloud can be described by its size in z. In xy the picture is a bit more complicated. We are interested in the width of the cloud in $R\phi$. Taking a fixed R (the mean radius of the ion cloud, roughly twice the radius of the wire), this width can be parametrised linearly using an angular width ϕ.

We want to find a variable which represents the probability for primary electrons to end up in the avalanche cloud of another primary electron coming from the same track. To get this, one has to compare the mean distance of one of the primary electrons close to the signal wire with the size of the ion cloud, caused by the other one. As the cloud shape differs between the Rz- and the xy-view, it makes sense to keep this separation for the following calculations. To find the mean distance of the primary electrons at the wire, the trajectory has to be projected on the two planes mentioned.

In the Rz-plane, the projection of the trajectory gives an additional factor $|\cos(\theta)|$ (Fig 4.56 left). In xy one has to obey further restrictions. First of all we can assume, that most of the trajectories pass through the sensitive region of a signal wire in a certain distance to the wire itself. Figure 4.19 shows, that in this usual case the trajectories for the primary electrons are almost parallel and that the distance between the drift paths is proportional to their opening angle ϕ at the wire. This linear dependence implies, that the previously mentioned angular width ϕ of an ion cloud corresponds to a spatial distance d between drift paths. To parameterise the xy-component of the searched variable, one has to project the particle trajectory on the direction of this distance, which gives a factor $\sin(\theta) \cdot \cos(\psi\prime)$. Now we have separate parameterisations of a distance in Rz and xy which have to be combined. As the exact influence of the different topology in these two projections on the cloud shape is not calculated, the 'mixing' of these two dimensions is kept as a free parameter a. Combining all pieces of the puzzle with Eqn. 4.25 gives the

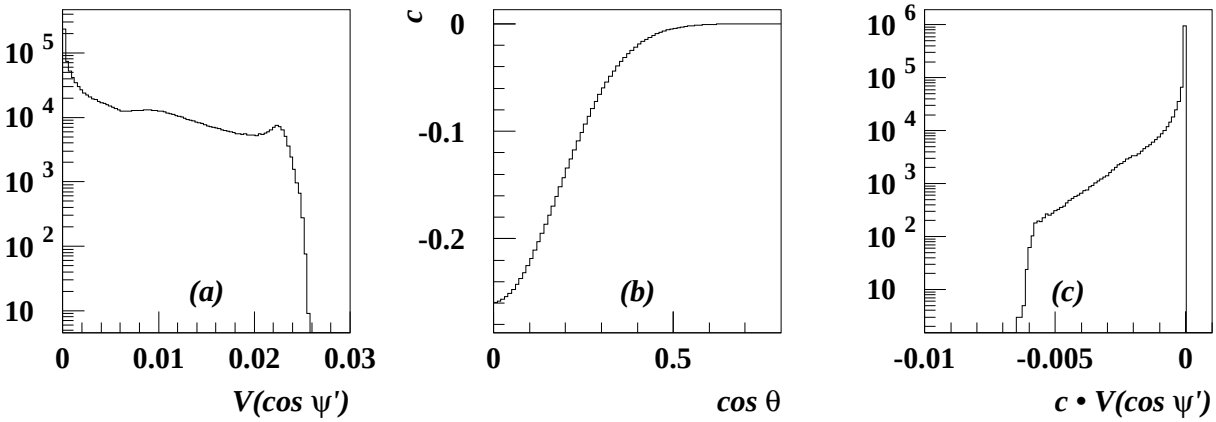

Figure 4.57: Remainder term approximation for $\cos\overline{\psi'}$ in the space-charge-effect correction, using the electron sample. (a) Variance of $\cos\psi'$, (b) quadratic term of the $\cos\psi'$-dependence in the correction function, (c) relative effect on the result.

final parameter x_t for the correction function:

$$\langle distance\rangle \sim \frac{|\cos\theta| \oplus a\cdot\sin\theta\cdot\cos\psi\prime}{dE/dx_{true}} =: x_t \quad .^{7} \tag{4.26}$$

Up to now this model is dealing with a single wire. But, as already mentioned, in processed data only track variables are accessible. One needs to use something like the mean x_t of all hits corresponding to one track. Investigating the input variables of x_t it is obvious, that $\psi\prime$ is the only critical one. dE/dx_{true} is a track variable anyway, and under the assumption of a perfectly collinear magnetic field within the CTD, θ is constant for the whole track. Therefore, the replacement of $\psi\prime$ by $\overline{\psi'}$ in Eqn. 4.26 is the only modification needed.

This replacement of $\psi\prime$ by $\overline{\psi'}$ needs further investigation. Appendix E shows how to calculate the remainder term, and therefore the error of this replacement. In this case, the variable ξ_i, which is changing between the different hits, is $\cos(\psi'_i)$. Its variance V can be extracted directly from data and is shown in Fig. 4.57 (a). The dependence of the correction factor on $\cos(\psi'_i)$ cannot be extracted directly from the correction function. To get an idea of its size, the correction function $f(x_t)$ is calculated in bins of $\cos\theta$, using the (later found) fit parameters for the 1996-2000 no water data taking period. The resulting distribution as a function of $\cos\psi'$ is then fitted by a polynomial of 2$^{\text{nd}}$ order to obtain the searched parameter c as a function of $\cos\psi'$ (Fig. 4.57 (b)). As expected, the biggest factor is found for small $\cos\theta$, because in this case the numerator in Eqn. 4.26 is dominated by the $\cos\theta$ term. Finally in Fig. 4.57 (c) the histogram of $V(\cos\psi')\cdot c$ is shown. This is the relative error caused by the replacement of ψ' as a function of $\cos\theta$. The effect is below 1% for all tracks and for most of them even below 1‰. As the single track resolution is of the order of 1%, this effect can be neglected.

Now we have a parameter x_t, calculable for each track:

$$x_t = \frac{|\cos\theta| \oplus a\cdot\sin\theta\cdot\cos\overline{\psi'}}{dE/dx_{true}} \quad . \tag{4.27}$$

[7] The symbol $\oplus$ denotes the sum in quadrature.

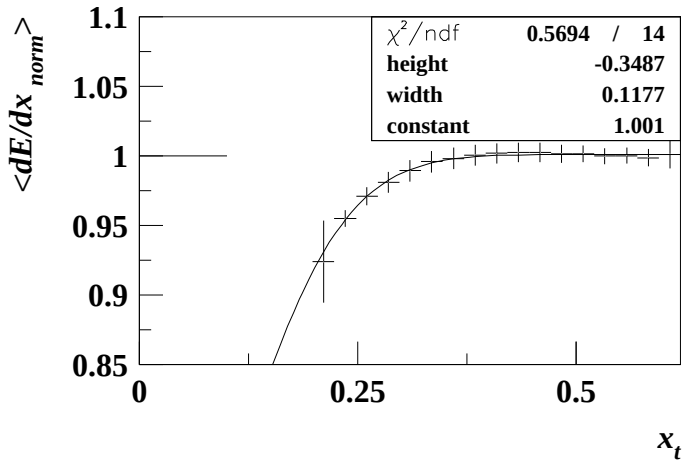

Figure 4.58: $\langle dE/dx_{norm} \rangle$ vs x_t.

Whereas the numerator of x_t is given by track geometry, the denominator is influenced by the particle type, or more precisely, by the BETHE-BLOCH curve. The smaller x_t, the larger the space-charge effect should be. To find a good parameterisation of this effect, one needs high statistics at small x_t. Consequently, the tuning sample should not be the pion sample, which covers the minimum of the BETHE-BLOCH curve. The tuning of the space-charge-effect correction is done using only the electron tuning sample. Therefore all plots with tuning-sample data in this section show the electron sample only.

The dependence of the normalised measured dE/dx on x_t is shown in Fig. 4.58. The function $f(x_t)$ represents the factor on dE/dx_{norm}, given by the space-charge effect. For big x_t it is 1 (no effect) whereas for smaller x_t it becomes smaller than one (the space-charge effect 'steals' some fraction of the signal). At very small x_t the sample dies out.

The fit function, shown in Fig. 4.58, is a constant minus a Gaussian with its maximum at zero. The constant describes the factor in the range of big x_t, where no space-charge effect should happen and thus is expected to be close to 1.

Figure 4.58 is very instructive to understand this correction function, but it cannot be used to extract the fit parameters. The mixing parameter a is part of the calculation of x_t, so a has to be known already before filling the profile in Fig. 4.58. To keep a as a free fit parameter, the fit has to be done in a two dimensional profile with $|\cos\theta|/(dE/dx_{true})$ and $\cos\overline{\psi'}/(dE/dx_{true})$ at the two axes. This becomes obvious, if x_t is rewritten as

$$x_t = \frac{|\cos\theta|}{dE/dx_{true}} \quad \oplus \quad a \cdot \frac{\sin\theta \cdot \cos\overline{\psi'}}{dE/dx_{true}} \quad . \tag{4.28}$$

At this point, an expression to calculate dE/dx_{true} is needed. This is given approximately by the product of the expected dE/dx and the run-by-run factor. Figure 4.59 shows this plane. To simplify the interpretation, the axes are normalised to the mean value $\langle dE/dx_{true} \rangle$. As usual the variation of $\langle dE/dx_{true} \rangle$ is not very large, they can be approximately read as shown in the labels, as $|\cos\theta|$ and $\cos\overline{\psi'}$. The colour indicates the mean dE/dx_{norm}. As expected, there is a strong dependence on $|\cos\theta|$. The signals become smallest for $|\cos\theta|$ close to zero. For small $|\cos\theta|$ a much weaker, but still visible dependence is given in $\cos\overline{\psi'}$. For large $|\cos\theta|$ the primary electrons are separated enough in z direction to avoid any space-charge effect. Therefore $\langle dE/dx_{norm} \rangle$ is around 1 and also in $\cos\overline{\psi'}$-direction there cannot be any dependence.

To fit such a distribution it is helpful to see not only the mean values of the bins but also their errors. This is done in Fig. 4.60, where the two-dimensional histogram is shown

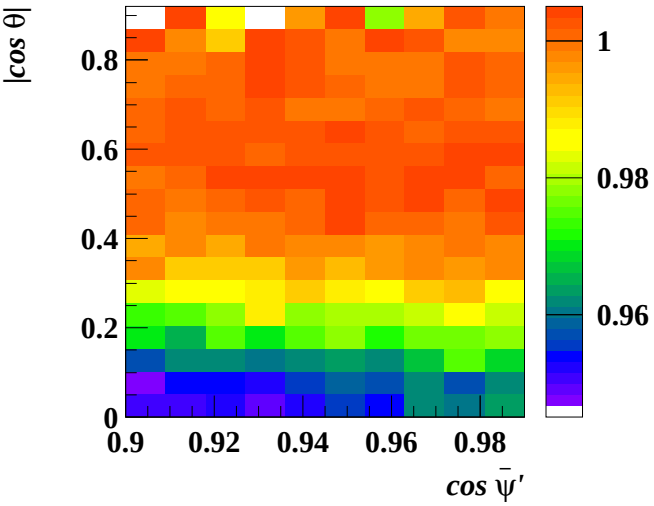

Figure 4.59: Normalised $\langle dE/dx \rangle$ in bins of $|\cos\theta|/(dE/dx_{true})$ and $\cos\overline{\psi'}/(dE/dx_{true})$. For a more detailed explanation see the text.

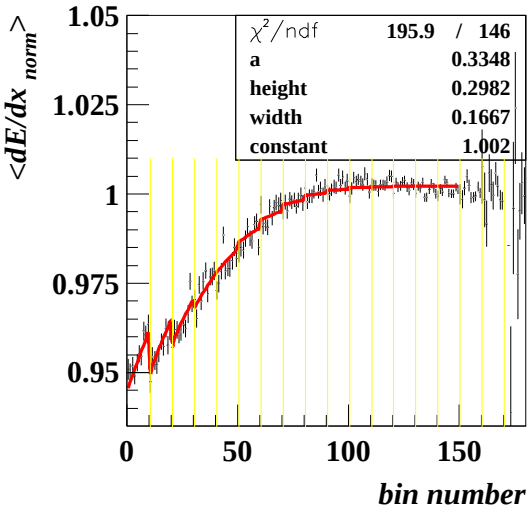

Figure 4.60: One-dimensional illustration of Fig. 4.59, including the fit. Detailed explanations are given in the text.

one-dimensionally. The bins in $|\cos\theta|$ are indicated by the vertical lines. Each 'package' in this plot represents one bin in $|\cos\theta|$, starting with the lowest bin. Within each of these packages, the bins in $\cos\overline{\psi'}$ are shown, also in ascending order. The used fit function reflects this kind of mapping.

The stronger dependence on $|\cos\theta|$ than on $\cos\overline{\psi'}$ is reflected in the fit by the mixing parameter a which is smaller than 1. The height parameter gives an upper limit on the space-charge effect of around 5%.

4.3.1.10 Drift-time-effect correction

In terms of modelling the effect and extracting a correction function from the model, the drift-time effect is the most sophisticated part of all corrections. As mentioned in Sect. 4.2.2.8, this effect depends on the time distribution of the primary electrons arriving at the sense wire. This time distribution has to be extracted from the spatial track topology. The relation between the spatial and the time distribution is given by the isochrones in Fig. 4.19. Several attempts to parameterise the isochrones using parts of ellipses have been undertaken, but the precision of these models has been too low to be used for a correction. Finally, a purely phenomenological approach is used.

This section starts by describing the method of extracting fit parameters from the data. To make it as simple as possible for the reader, in the beginning the main concepts are described. Later in this section the technicalities will be shown. In the end one can find how the extracted information is used when applying the correction. It turned out that the tuning method applied in this section works slightly better for HERA I than for HERA II data, therefore all plots shown in this section are generated with HERA II data.

It is obvious, that the main parameter to describe the drift-time effect should be the angle ψ'. Due to the same reasons as described for the space-charge effect, this single-hit-related parameter is not accessible at track level tracks. Instead, the mean value $\overline{\psi'}$ has to be

used. The effect of this approximation will be discussed later.

The velocity of the signal pulse moving along the signal wires is larger by several orders of magnitude than the velocity of free ionisation electrons in the gas of the CTD. This means, the time distribution of the signals from different primary electrons is only given by the drift-times in the gas. To take this into account, the track has to be investigated in the plane perpendicular to the signal wire. Besides on ψ' the drift-time effect depends on the density of primary electrons within the just mentioned plane, which is dE/dx divided by $\sin\theta$. Taking these ingredients into account, one ends up with the parameter 'signal density', $\overline{s_d}$, representing the number of primary electrons per time unit reaching the signal wire. To extract this signal density $\overline{s_d}$ from data, even more has to be done. A detailed description how to calculate $\overline{s_d}$ will be given later in this section (see Eqn. 4.31).

It would be self-evident to split up the data samples in bins of $1/\sin\theta$, with respect to the structure of the parameter $\overline{s_d}$, but the statistics vary strongly in this variable. A variable bin size would be necessary to end up with equally populated bins. It is simpler to split up the tuning sample into 10 equidistant bins in $|\theta - \pi/2|$. In each of these bins, the distribution of $\overline{s_d}$ versus $\overline{\psi'}$ is generated and fitted with a proper function $f_\alpha(\overline{\psi'})$. The index α represents the dependence on the combination of θ and dE/dx (one can say, the dependence on $\overline{s_d}|_{\overline{\psi'}=0}$).

A good choice of a phenomenological fit should respect the following conditions:

- The number of free parameters should be small.
- The parameters should be as orthogonal as possible.
- Known constraints to the data should be reflected in the fit function.
- The fit function should describe the data well.

As shown in Fig. 4.61, these profiles typically have a minimum at $\overline{\psi'}_0 \approx -0.5$, which is almost the same for all of them. It is suggestive to fit the data with a function, which uses $\overline{\psi'}_0$ and $p_0 = \overline{s_d}(\overline{\psi'}_0)$ as two fit parameters. The remaining part of the fit function should describe the shape of the profiles.

At this point one should reflect once more, what the signal dependence on $\overline{\psi'}$ means. If one looks at the corresponding dependence on ψ' for single hits, the searched distribution will be part of a periodic function (ψ' is an angle) with a period of 2π. For $\overline{\psi'}$ this transforms into a period of π as the mean angle for passing once through a full circle is half of the circle. This suggests to use a fit function with a period of π. The most simple function covering this condition is $1 - \cos 2(\overline{\psi'} - \overline{\psi'}_0)$. It has a period of π and its slope and value in $\overline{\psi'}_0$ are zero. But it was found, that this function alone cannot describe the shape of f_α. Taking into account also the double frequency gives a function which describes the data very well (coloured solid lines in Fig. 4.61).

This leads to the following fit function:

$$f_\alpha(\overline{\psi'}) = \tilde{a_0} \cdot \left[1 + a_2 \cdot (1 - \cos 2(\overline{\psi'} - \overline{\psi'}_0)) + a_4 \cdot (1 - \cos 4(\overline{\psi'} - \overline{\psi'}_0))\right] \quad . \qquad (4.29)$$

Using $\tilde{a_0}$ as a global scale of the function reflects, that the slope of the fitted distributions approximately scales with $\overline{s_d}$.

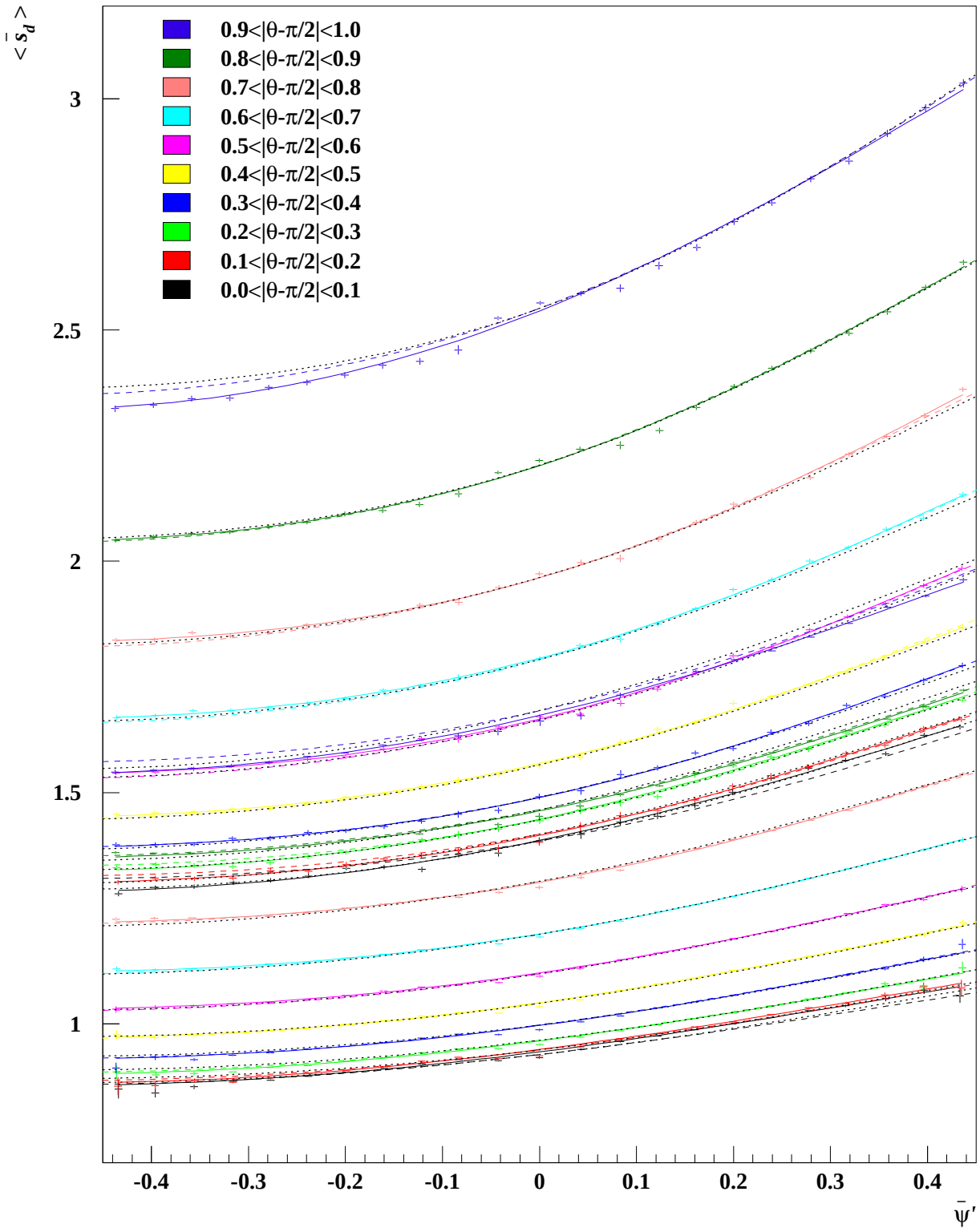

Figure 4.61: $\overline{\psi'}$-dependence of $\overline{s_d}$. The lower set of data points are given by the pion tuning sample, the upper by the electron tuning sample. Coloured solid lines are fit curves of single bins in $|\theta - \pi/2|$, coloured dashed lines are fits, still separated between pion and electron sample, the black dotted lines show the final fit (see text for details). HERA II data tuning samples.

The use of $\tilde{a_0}$ represents the symmetry of the function f_α with $\tilde{a_0} = f_\alpha(\overline{\psi'}_0)$. For reasons which will be explained later it is better, to use $a_0 = f_\alpha(0)$ as a parameter. a_0 can be easily calculated with Eqn. 4.29.

The description of the data using fits may end at this point, but this would leave a big problem. There are 2 different tuning samples, each in 10 bins of $|\theta - \pi/2|$, each of these bins fitted by a function with 4 free parameters. Summing up, one ends up with 80 fit parameters. There are many arguments against a large number of fit parameters: The fits become less stable with small tuning samples, the chance to parameterise statistical fluctuations within the test samples instead of the underlying physics increases, it becomes hard to verify the reliability of the fitting mechanism. These are enough arguments to improve the fitting method and to reduce the number of free parameters. This can be done by taking more seriously into account that one is working with a two-dimensional distribution $(\overline{\psi'}, \overline{s_d})$. To use a fit function directly in the two-dimensional plane will do the job, but the price for this is the loss of interpretability of the fit parameters and the instability of a fit with many free parameters. A better way is to fit the two dimensions in two steps as follows:

After fitting the $\overline{\psi'}$-dependence of both tuning samples in bins of $|\theta - \pi/2|$, the fit parameters are filled into histograms in bins of $|\theta - \pi/2|$. In a second step, these histograms are fitted. The parameters a_0 are fitted with a special polynomial of 3rd order, which takes into account, that the main dependence in this distribution should proceed like $\sin\theta$:

$$a_0(|\theta - \pi/2|) = \frac{1}{\sin\theta} \cdot p_{0\,-1} + p_{0\,0} + \sin\theta \cdot p_{0\,1} \tag{4.30}$$

where a_0 denotes the scale for the signal $\overline{s_d}$ at $\psi' = \overline{\psi'}_0$. The higher-order terms are normalised with this scale. The parameters a_2 are fitted with a polynomial of 2nd order. The errors of a_4 are so large, that a linear fit is reasonable (see Fig. 4.62). The angular offset $\overline{\psi'}_0$ is taken as a constant. The application of this double-fitted method is shown in Fig. 4.61 in coloured dashed lines. In the electron sample one can detect a systematic overestimation of the slope in $\overline{\psi'}$. Some remarks about this problem will be given later.

Fitting the fit parameters already leads to a reduction of the total number of parameters from 80 to 18. But this is still not the end of the game. Up to now, the electron and the pion tuning samples have been treated as completely independent of each other. But the drift-time effect itself should not differ between the different particle types. If for a given ψ' for different particles the projected $\overline{s_d}$ is the same, it should also be identical for any other ψ'. If the reference ψ' is taken at zero, the constant term in the former fits give the values of $\overline{s_d}(0)$. The remaining parameters of the former fits can now be fitted for electron and pion samples together by using histograms in which they are plotted against their $\overline{s_d}(0)$. These distributions are fitted using a polynomial of 2nd order for p_2, a linear function for p_4[8] and a constant for $\overline{\psi'}_0$. This extended method reduces the number of fit parameters further from 18 to 12.

At this point it becomes obvious, why to use $\overline{s_d}$ as the fit variable. All the work before could be done either in $\overline{s_d}$ or in an already pre-corrected dE/dx_{meas}. It may appear useless to spend extra work in removing the Phase I pre-correction on ψ' from the data. But only by going back to the density of primary ionisations in the plane perpendicular to the wire $(\overline{s_d})$ the argument holds, that both tuning samples should behave identical. So only the

[8] In fact, these polynomials are taken as functions of $\log \overline{s_d}(0)$. This gives a higher stability for extremely high signals, as the logarithm compresses this range.

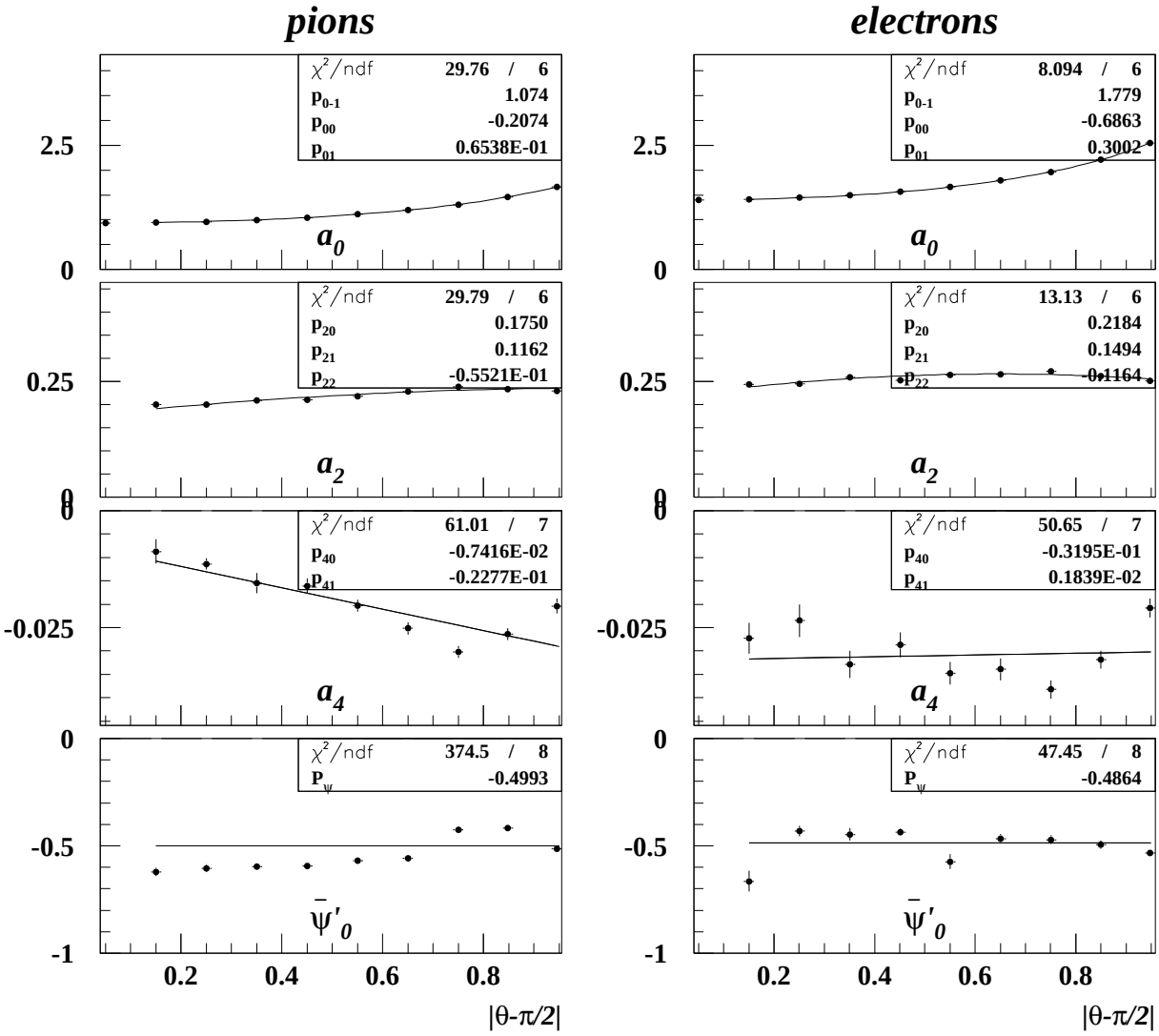

Figure 4.62: Fit of the fit parameters in Fig 4.61.

case of using distributions of $\overline{s_d}$ allows to combine the fits for both samples to reduce the number of free parameters. Furthermore, the combination of the two tuning samples in one fit reduces the dependence on the systematics within individual tuning samples.

This is a good place to focus on some technical issues for the double-fit method. The parameters of the primary $\overline{\psi'}$-fits are highly correlated. If due to statistical fluctuations or slightly different systematics one of the parameters changes in the fit, automatically the others will change, too. Figure 4.63 (a - c) shows this behaviour. If $\overline{\psi'}_0$ is fitted to be low, also the parameters a_2 and a_4 are found to be relatively low. The method of fitting fit parameters cannot ensure that such correlations are handled properly. If not, it can happen, that the data is not represented well by the double fit. One example for this is the already mentioned badly described slope in $\overline{\psi'}$ of the electron sample using the particle-separated fit (black dashed lines in Fig. 4.61).

Another issue is a proper handling of outliers. Sometimes it happens, that the fit does not find the best solution but another one (a local minimum of χ^2). In such a case the fit parameters are totally different from the 'usual' ones. In a fit of the fit parameters such

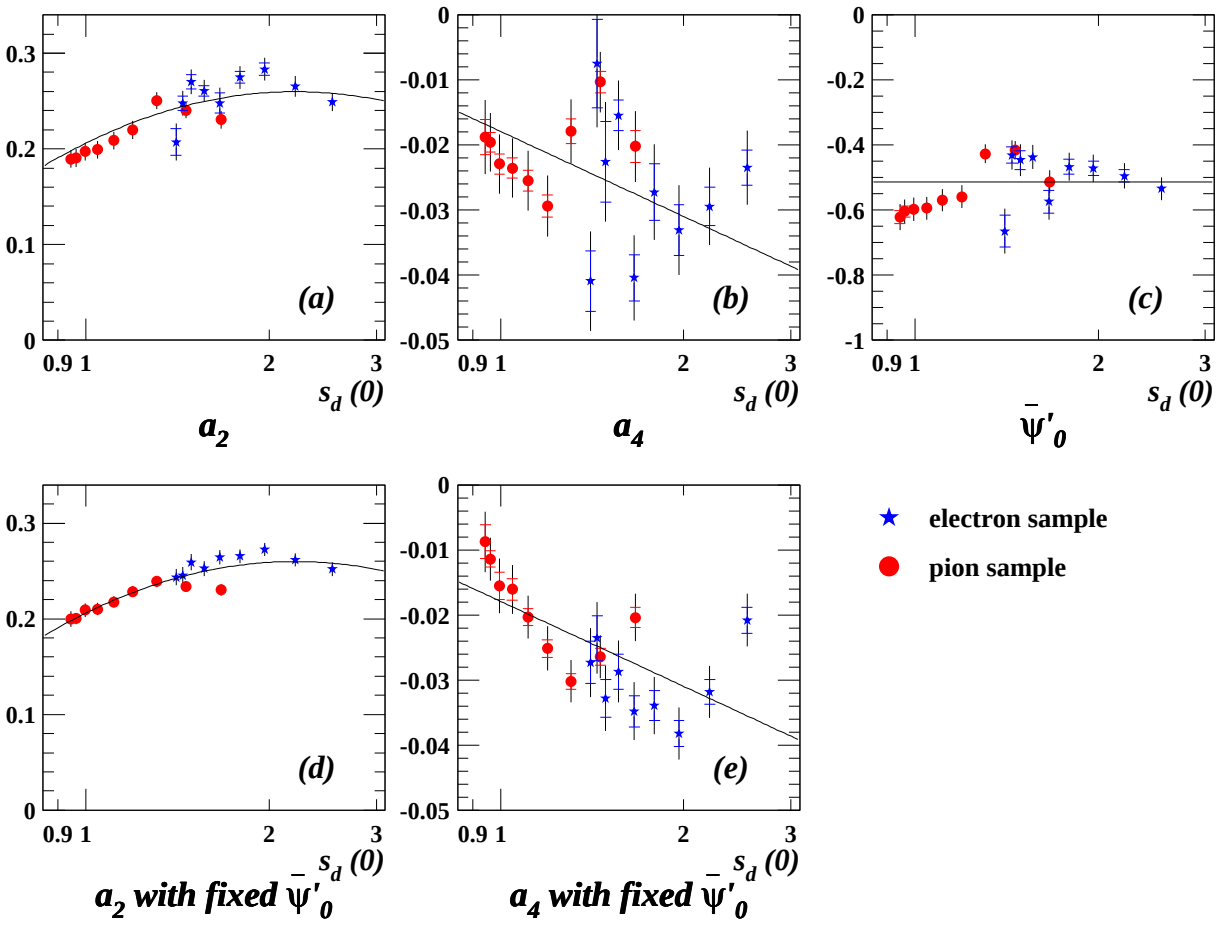

Figure 4.63: Common fit of parameters a_2, a_4 and $\overline{\psi'}_0$ for pion and electron sample. Fit of all three parameters together (a-c) and after fixing $\overline{\psi'}_0$ (d, e). The inner error bars are the errors of the parameters as found by their calculation (fit). The outer error is an additional 'systematic' error. The fits shown in this figure use the sum of both errors for the calculation of χ^2. More details about the calculation of the systematic error can be found in the text. The plots are based on HERA II tuning data.

values cause a very big χ^2 and therefore they can have a very big influence on the fit result. To get a proper result, this influence has to be reduced. This is done by increasing the errors of the fit parameters linearly by their mean value. One can understand this method as follows: adding a constant error to all errors has the effect, that the weight of all values entering the fit becomes more equal. If all errors are similar and one value out of 10 is off due to a 'bad' fit, this value cannot have a big influence to the fit of the fit parameters. One can understand this offset in the errors as adding a systematic error to the purely statistical error of the fit parameters. This leaves the question, how big this offset for the errors should be chosen. Taking the mean value of the errors of the fit parameters offers the benefit, that the mean ratio between the statistical errors and the added systematical error is always the same. This means, independently of the statistics of the used data sample (which scales the statistical error) the result of the fit of fit parameters with the combined errors stays the same. Some tests for the added systematic error with different multiples of the mean error showed, that the mean error itself is a good choice. In Fig. 4.63

the added error is shown as the outer part of the error bars.

The effect of correlated fit parameters is even more serious in the sample-combined fit. Small systematic differences between the tuning samples can cause big differences in the fit parameters. To reduce this effect, the fitting is done in two steps. First of all everything is done as already described. In the second step the parameter $\overline{\psi'}_0$ is fixed to its fit result of the first step. Figure 4.63 (d, e) show the new result for the parameters a_2 and a_4. Especially for a_2 there is a big improvement. Both tuning samples match very well and can be nicely fitted together. This is very important, as a_2 is the dominant parameter to describe the $\overline{\psi'}$-dependence. Deviations between the samples in a_2 cause big systematic effects on the results of a drift-time-effect correction.

There is also some improvement in the distribution of a_4. The jumps within a single tuning sample have disappeared. The lowest bins within each sample correspond to tracks with θ close to 90 °. These are the tracks with the biggest space-charge and threshold effect. The deviation of these bins compared to the others might indicate an incompleteness in the correction of these two effects. But even if one ignores these bins, there are obvious systematic effects left within each sample; some of the dots are off by up to 0.01 from the fit. This corresponds to deviations below 1% for the tuned dE/dx for tracks with lowest p_t (in the order of < 200 MeV), therefore this is not critical.

Figure 4.63 (e) is a good estimator for the size of remaining systematic uncertainties in the corrected dE/dx. This is a comparison of different samples at different kinematics, which should behave similarly according to their $\overline{\psi'}$ dependence of the signal height. It is almost impossible to trace back the sources for the observed difference, but one has to expect, that in the application of dE/dx measurements (data samples which are independent of the tuning samples) similar systematic uncertainties exist.

The results of the common fit can be found in Fig. 4.61 as dotted lines. The agreement with data is very good. The separated fit of a_2 and a_4 using a fixed value of $\overline{\psi'}_0$ fixes the problem of the slope in the electron data.

Up to now, the way to parameterise the measurements using the tuning samples is described, but how can this be used for correcting a single track? This is done by using the two tuning samples as references for two fixed values in dE/dx. First of all, the fits of the fit parameters are used to calculate the fit parameters in the $\overline{\psi'}$ fits for both tuning samples at the same θ as the investigated track. In a second step, the fit function in $\overline{\psi'}$ for the $\overline{\psi'}$ of the track is calculated. The result of this procedure are two reference values of $\overline{s_d}$ for tracks at 1.0 mips and at 1.4 mips. This gives two points to describe a linear relation between $\overline{s_d}$ and dE/dx_{mips}. This relation is used to transform $\overline{s_d}$ of the track into the corrected value dE/dx_{mips}.

The general concept of the drift-time-effect correction is now described. But for an easy understanding, some of the details have been skipped and still need to be discussed. One of them is the calculation of $\overline{s_d}$. It has been mentioned often, that the raw signal information is not available in processed data. During reconstruction a rough correction on ψ' is already done. To redo the drift-time-effect correction, first of all this partial correction has to be removed. This is not perfectly possible, but using the track helix the Phase I correction factor for each wire can be recalculated. The mean value of these correction factors $d_{ph1}(\overline{\psi'})$ is in first order the same as the factor for the whole track. Dividing the measured dE/dx by this mean value does the job of removing the Phase I correction at the best accessible level.

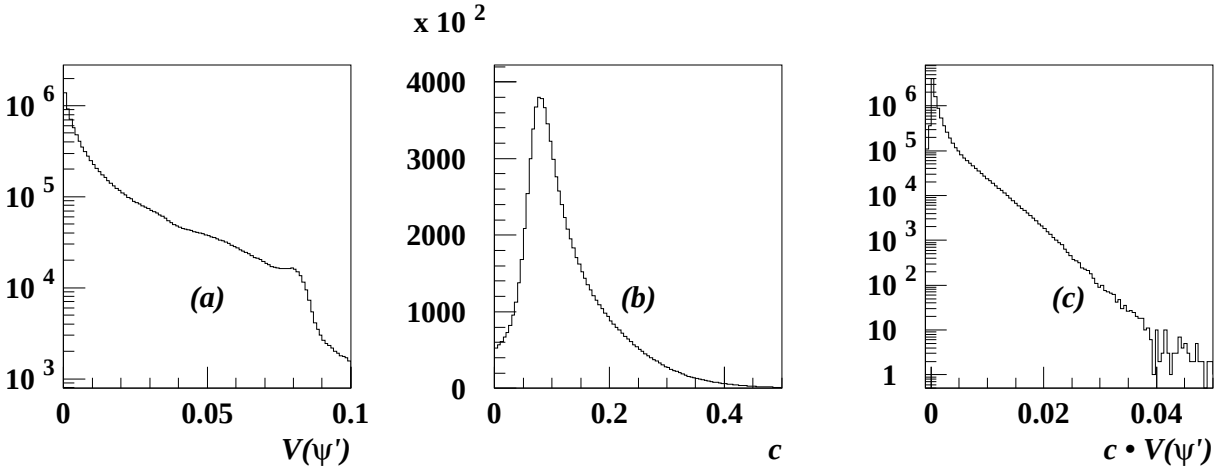

Figure 4.64: Remainder term approximation for $\overline{\psi'}$ in the drift-time-effect correction. (a) Variance of ψ', (b) quadratic term c of the ψ'-dependence in the correction function, (c) relative effect on the result.

The next extension is the idea, that the two samples represent two values of dE/dx_{mips}. In first order this is true, but in detail, the two samples cover pieces of the Bethe-Bloch curve and so they cover ranges of dE/dx_{mips}. As the position, where to find a track in the Bethe-Bloch curve, depends on p, which is correlated with p_t, which again is strongly correlated with ψ' and $\overline{\psi'}$, the deviations of the Bethe-Bloch curve from a constant are reflected systematically in the investigated distributions. To become independent of these systematics, $\overline{s_d}$ has to be normalised depending on the expected dE/dx_{exp}. Thus, the full definition of $\overline{s_d}$ is

$$\overline{s_d} = \frac{dE/dx_{meas}}{\sin\theta \cdot d_{ph1}(\overline{\psi'})} \cdot \begin{cases} \frac{1}{dE/dx_{exp}} & \text{for pion sample} \\ \frac{1.4}{dE/dx_{exp}} & \text{for electron sample} \end{cases} . \tag{4.31}$$

The disadvantage of this is that an expectation for the Bethe-Bloch curve has to be used. But as the tuning samples are selected in a range, where the Bethe-Bloch curve is almost constant, the dependence of the corrections on the expectation curve is not too strong.

The last topic of this section is the implication of using $\overline{\psi'}$ instead of ψ'. The relative effect of the remainder term can be estimated as in Sect. 4.3.1.9. This time, the correction function is evolved in $\overline{\psi'}$, so the variance $V(\psi')$ has to be taken into account. The factor of the quadratic term can be extracted from the fit function for $f_\alpha(\psi')$ by calculating its Taylor series. Figure 4.64 shows the corresponding plots. In this case, the relative effect of the remainder term is larger than 1 % in 2 % of all tracks. If this error on the measured dE/dx will be the only effect of the remainder term, its correction could be ignored and taken as systematic uncertainty. But one also has to keep in mind that the size of this effect differs depending on the track kinematics (it depends on the variance $V(\psi')$) and therefore differs for the different tuning samples. As the drift-time-effect correction searches for a common fit for pion and electron sample together, this might cause additional problems. The effect is biggest for big $|\overline{\psi'}|$ because these are typically tracks with a strong curvature. Therefore the most-affected tracks participate in the outermost ends of the $f_\alpha(\psi')$-curves;

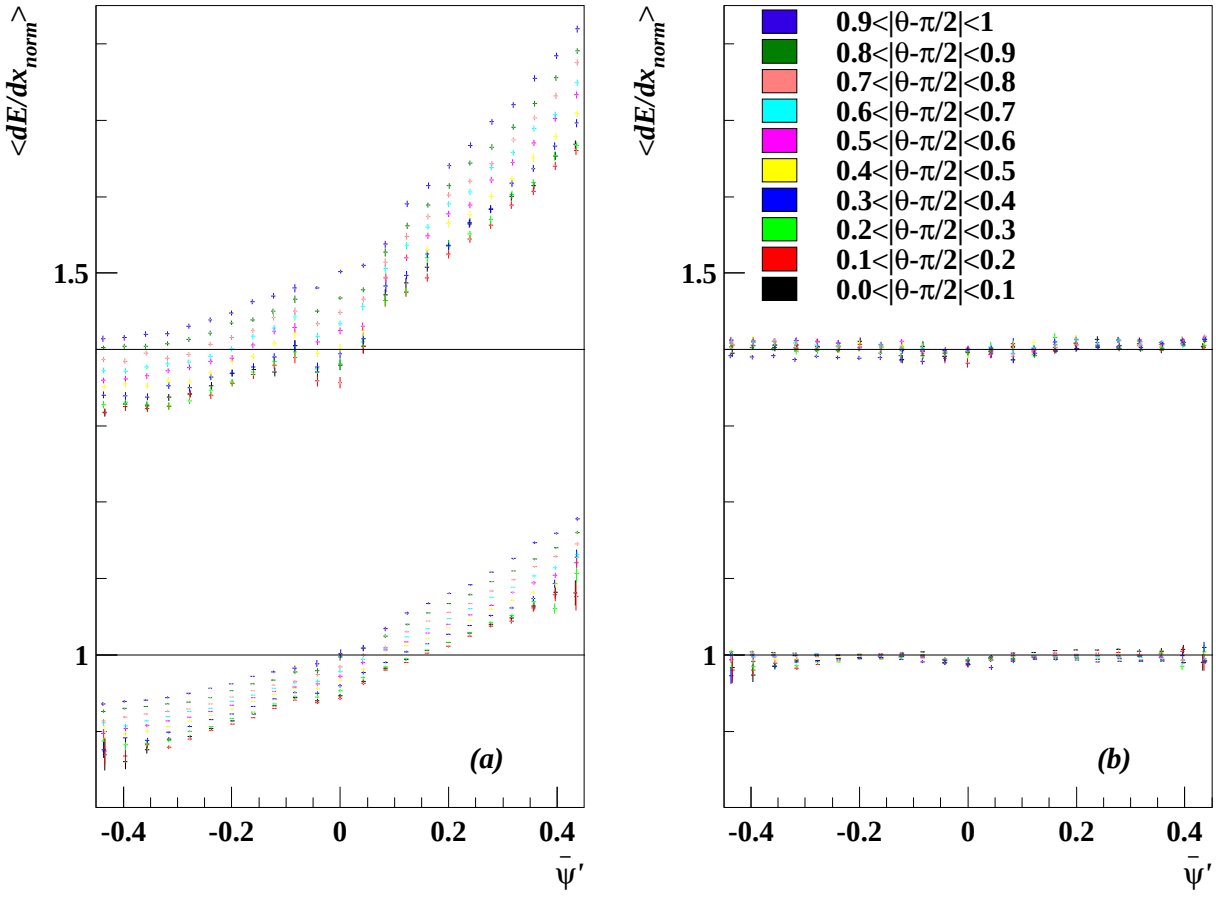

Figure 4.65: $(\overline{\psi'}, |\theta - \pi/2|)$-dependence before (a) and after (b) correction. The lower set of data points is given by the pion tuning sample, the upper by the electron tuning sample. The BETHE-BLOCH dependence is removed: Pions are normalised to 1 (the usual dE/dx_{norm}), electrons to 1.4.

they have a long lever arm to influence these fits. Even if the overall relevance of the remainder term is small, it can have a visible influence on the drift-time-effect correction. Taking this into account, for the whole correction package it is more safe to treat the remainder term properly instead of ignoring it.

Appendix F describes, how the remainder term is calculated for each track. For the profile plot in Fig. 4.61 the definition of $\overline{s_d}$ is then changed by subtracting the remainder term k (nomenclature from App. F):

$$\overline{s_d} \rightsquigarrow \overline{s_d} - k \quad .$$

Figure 4.65 shows the result of these corrections. According to Eqn. 4.31, ideally, the data points for pions should be at 1, for electrons at 1.4. This plot shows, that for almost the complete $(\overline{\psi'}, |\theta - \pi/2|)$-range the corrections are working properly.

Now we are done with the parameter extraction from the tuning samples. But how can this correction be applied to any other data?

The first step is to calculate $a_{0,i}$ with the track's θ for pions and electrons (Index i, representing $dE/dx_{mips} = 1.0$ and $dE/dx_{mips} = 1.4$) separately, using Eqn. 4.30. The common fits of the two samples depend on $\log a_{0,i}$ and allow to extract the parameters

$a_{2,i}$ and $a_{4,i}$ as the next step. Together with $\overline{\psi'}$ of the track this is all one needs to calculate $f_{\alpha,i}$ from Eqn. 4.29. Now one has the two values of $\overline{s_d}$ for the track's $(\theta, \overline{\psi'})$ representing the dE/dx_{mips}-values 1.0 and 1.4. As one has only these two points, the best one can do is to linearly interpolate $l(\overline{s_d})$ between them. Finally the corrected measurement of dE/dx_{mips} is given by $l(\overline{s_d})$ at the measured $\overline{s_d}$ of the track.

One last information is still missing in this section. Why do we use a_0 instead of $\tilde{a_0}$ in Eqn. 4.30? The first answer is, if everything will be perfect, there will be no difference between these two approaches. But reality is not so perfect which leads to systematic differences between the tuning samples. Therefore the global fit of both tuning samples together does not give exactly the same result as separated fits. The described method is using a_0 at a 'starting point' to evolve the $\overline{\psi'}$ dependence from that position. This 'starting point method' is common for the global and the separated fit, which means, for the corresponding $\overline{\psi'}$ both methods are exactly identical. The more $\overline{\psi'}$ of the investigated track differs from that point, the larger are the deviations between the two methods.

The position $\overline{\psi'}_0$ of the minimum is close to one end of the investigated distribution. Using this as a reference means, that the effect of the systematics will be minimised for negatively charged low-p_t tracks and rises with increasing $\overline{\psi'}$. Worst offenders would be the low-p_t positively charged tracks; high-p_t tracks will be in the middle. This causes a charge-dependent asymmetry in the effect of the systematics which is not wanted.

The choice of $\overline{\psi'} = 0$ as 'starting point' is much better. It is the natural symmetry point between the charges, i.e. tracks with same p_t but different charges are affected by this kind of systematics identically with opposite sign. Furthermore the typical user of dE/dx data is interested in high momentum tracks which correspond to small $|\psi'|$ ($p_t = 500\,\mathrm{MeV}$ corresponds to $|\overline{\psi'}| \approx 0.2$). With the choice of a_0 the systematic errors become smaller the larger p_t is.

4.3.1.11 Correction of run-by-run corrections

In Sect. 4.2.1.2 the method of the run-by-run corrections was shown. This kind of global correction is applied before any of the corrections shown in this section are done. Unfortunately it has turned out, that this global correction interferes with the other corrected effects (in first order with the threshold effect) in the following way:

For example, if in a run the global conditions cause very low measured signals, this will be compensated by the run-by-run correction. Anyway, the thresholds of the readout electronics do not depend on the running condition; they are always at the same level. Thus such a 'low signal run' will be more affected by the threshold effect than other runs; there are more tracks with too high measured signals than in other runs. The run-by-run correction does not take this into account, it simply searches for the mean signal in a pion enriched sample, f_r. The increased threshold effect will push this mean to a higher value. The corrected dE/dx is calculated by dividing the measured FADC counts by this mean value. For a 'low signal run' the run-by-run corrected dE/dx will therefore end up at too low values.

In other words, the run-by-run correction already does a partial correction of the threshold effect. But it only compensates for the mean threshold effect of all tracks within the same run. It cannot distinguish (like the threshold-effect correction itself) between differently strong affected tracks. To allow the threshold effect correction proper to reach its

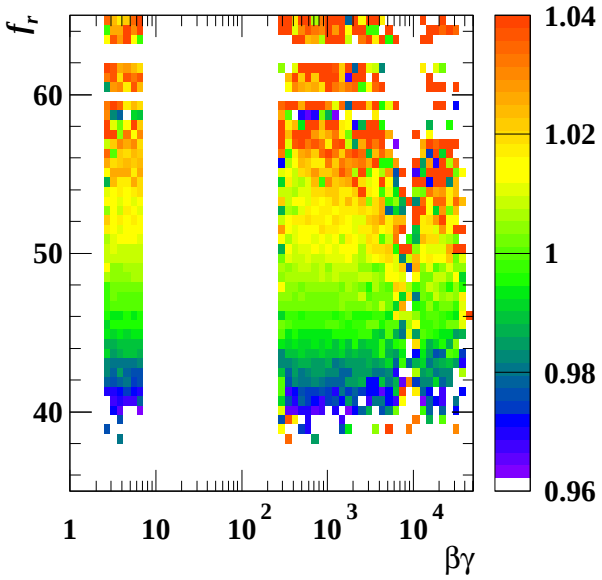

Figure 4.66: Normalised $\langle dE/dx \rangle$ in bins of the run-by-run correction factor f_r and $\beta\gamma$. For a more detailed explanation see the text.

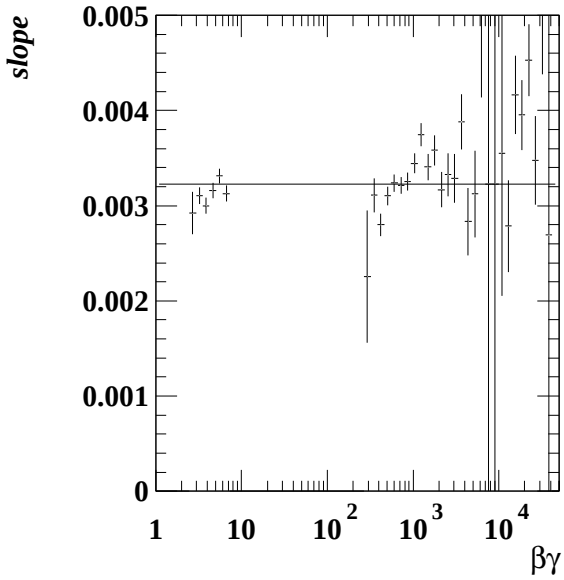

Figure 4.67: Slope of linear fits applied to the dependence of the normalised $\langle dE/dx \rangle$ (f_r) in bins of $\beta\gamma$. Detailed explanations can be found in the text.

maximum power against this single effect, first the partial correction against it must be removed from the run-by-run correction.

In Fig. 4.66 the dependence of dE/dx on f_r is shown in bins of $\beta\gamma$. The plot is filled using both tuning samples. The band at low $\beta\gamma$ is caused by the pion tuning sample, $\beta\gamma$ values between 200 and 6000 are mainly photon conversions and values beyond 10000 are reached by DIS electrons. The electrons from J/ψ decays can be found in the range between 2000 and 10000. Due to their low statistics they have almost no influence on the mean slope as shown in Fig. 4.67.

In this case one is only interested in the dependence on f_r; the $\beta\gamma$ axis is supposed to show, whether the dependence on f_r changes with $\beta\gamma$. To pronounce this, the colour code is normalised in each bin of $\beta\gamma$ to the mean value in this bin (the 'mean colour' is always green). This cancels any dependence of dE/dx on $\beta\gamma$ in this plot. It is clearly visible, that, independently of $\beta\gamma$, low f_r cause too low corrected dE/dx values. The increase of the normalised dE/dx in f_r is almost linear. Thus in each bin of $\beta\gamma$ a linear fit was applied and the resulting slopes are shown in Fig. 4.67. Except for the lowest bins in the photon conversion sample this slope is always the same. These lowest bins cover a very special kinematic range. As the photon conversion sample has a cut on the minimum p_t, the lowest $\beta\gamma$ can only be reached by tracks with $p_t \approx p$, i.e. by tracks with $\theta \approx \pi/2$. These are exactly the tracks with the highest space-charge effect. Furthermore, the space-charge effect should be strongest for high f_r. Figure 4.66 shows in the range of big f_r and small $\beta\gamma$ a slight deficiency in the normalised dE/dx. This demonstrates, that the space-charge-effect correction does not seem to cover the full effect. On the other hand, this deficiency causes smaller slopes for the afore-mentioned fit in this range of $\beta\gamma$. This explains, that the small slopes in that region have nothing to do with the run-by-run correction itself. Thus one can say, that the effect under investigation is independent of $\beta\gamma$.

HERA I

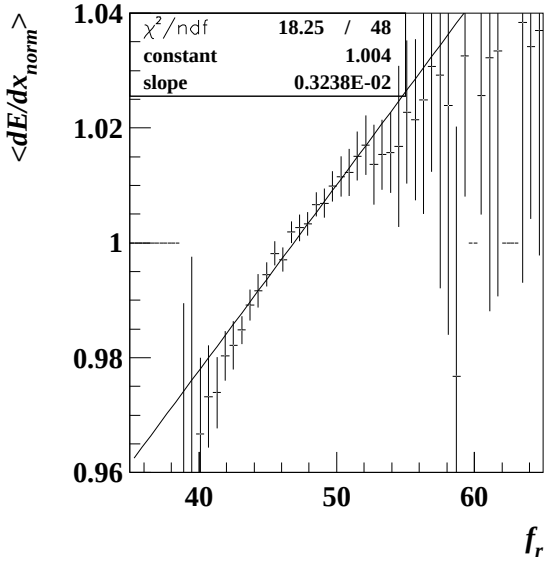

Figure 4.68: Normalised $\langle dE/dx \rangle$ in bins of f_r, using HERA I data.

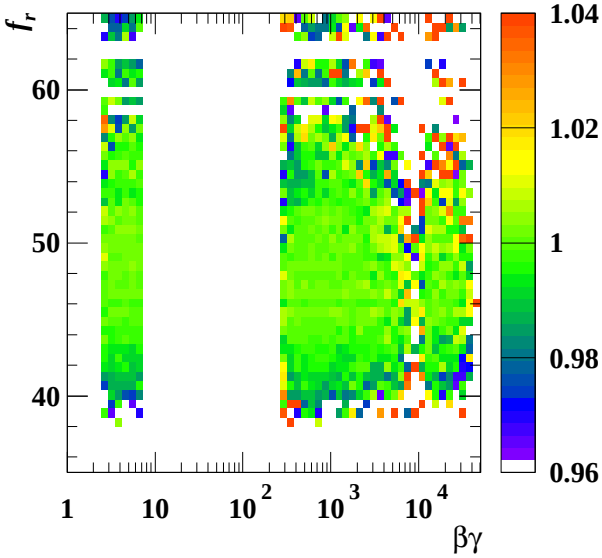

Figure 4.69: Normalised $\langle dE/dx \rangle$ in bins of the run-by-run correction factor f_r and $\beta\gamma$ after applying the correction. HERA I data.

HERA II

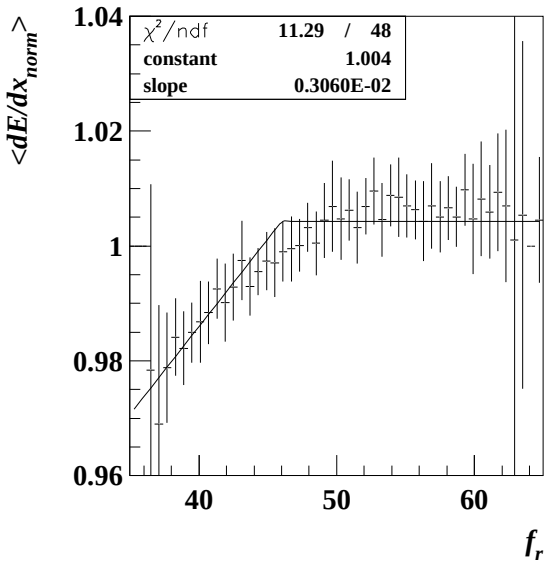

Figure 4.70: Normalised $\langle dE/dx \rangle$ in bins of f_r, using HERA II data.

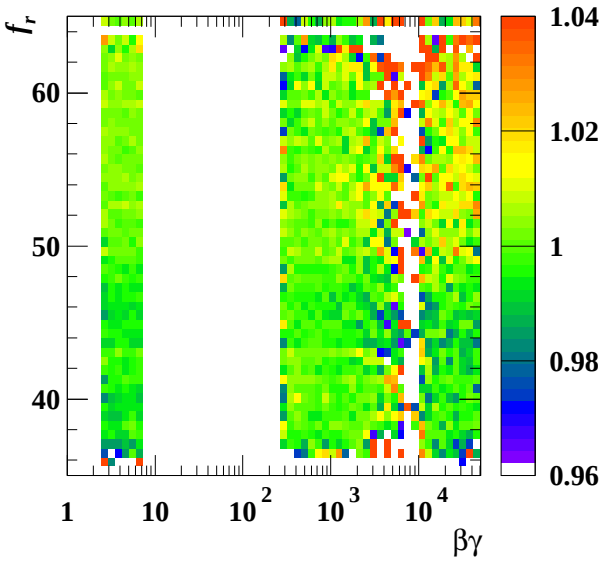

Figure 4.71: Normalised $\langle dE/dx \rangle$ in bins of the run-by-run correction factor f_r and $\beta\gamma$ after applying the correction. HERA II data.

This allows to look at the projection of Fig. 4.66 on its ordinate (Fig. 4.68, 4.70). Once more it is visible, that for small f_r the measured dE/dx is too small. To describe this distribution, for HERA I data a linear fit does a reasonable job. For HERA II data this distribution looks slightly different. Whereas for small f_r again an increase can be seen, for big f_r no change in dE/dx can be found. As the relation between the run-by-run correction and the threshold effect is found to cause the effect under investigation, this is no surprise. If the signals are very high (big f_r), the threshold effect should disappear, but if there is no threshold effect left, the run-by-run correction cannot compensate for this effect. Thus, for very high signals we expect no dependence of dE/dx on f_r.

This prompts the question, why such an endpoint of dependence on f_r cannot be seen in HERA I data. Almost all of the altered parameters for CTD-operation can have an influence on this distribution, but the largest effect seems to come from the lowered hardware threshold of the CTD. This causes the minimum signal size without threshold effect in HERA II to be much lower than it was in HERA I. In other words, in HERA II data we expect to find independence of dE/dx on f_r already at much lower values of f_r than in HERA I. Maybe in HERA I data there is also such a turnover point, but it lies at too high values of f_r to find it.

In order to react properly on this different kind of behaviour, different fit functions were applied to HERA I and HERA II data. In HERA I a linear function was used, whereas for HERA II a linearly rising function was used only for $f_r < 46$ which turns into a constant for larger f_r. The correction factor applied to all tracks of one run with a given f_r is the reciprocal value of the corresponding fit function at this f_r. The result of the correction can be seen in Figs. 4.69, 4.71.

It is worth mentioning that this is the only part of the dE/dx corrections, where different fit functions were used for HERA I and HERA II. For all other corrections shown in this chapter, the differences between the two data sets are covered in different fit parameters, using identical fit functions.

4.3.1.12 Superlayer factors

A very informative plot is the dependence of the measured dE/dx_{norm} on the radius R_{out} in ZEUS xy-coordinates, defined as the radius at which the track helix leaves the CTD through the CTD end-plate. Furthermore barrel tracks can be extrapolated to the z-position of the end-plates to calculate an artificial R_{out} for such tracks. Tracks, which turn back inwards already before reaching the z-coordinate of one of the end-plates are rejected. The dE/dx dependence on R_{out} shows several effects together, so this kind of plots needs further aid to interpretation.

As the end-plate effect is visible in this distribution, one has to spend some words on how it occurs in the R_{out} dependence. Tracks with hits close to the end-plate can occur in this distribution only in dedicated R_{out} ranges. Only if the track leaves the CTD through an end-plate within the outer half of an axial superlayer, hits close to the end-plate are taken into account for the dE/dx measurement (see Fig. 4.50). As such tracks have their last hit just next to the end-plate, their R_{out} is only slightly larger than the R-position of the last hit wire. Thus end-plate affected tracks can be found in an R_{out}-dependent distribution only in the bins around the upper limit of axial layers. In Fig. 4.72 (a, b) one can detect the end-plate effect as dips in exactly these ranges. After applying the end-plate effect

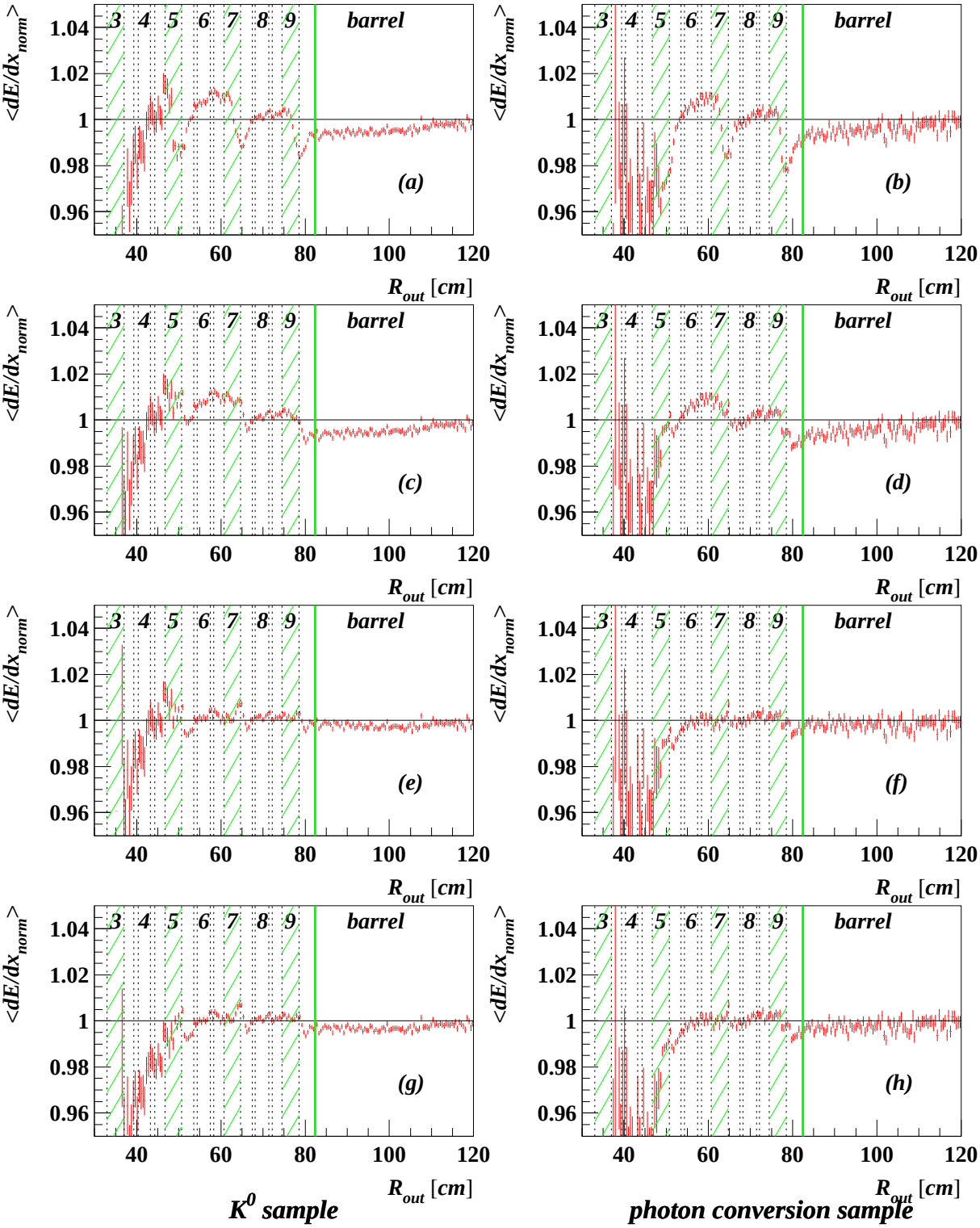

Figure 4.72: $\langle dE/dx_{norm} \rangle$ vs R_{out} for pion (a, c, e, g) and electron (b, d, f, h) samples. After applying all corrections except for the end-plate correction and the superlayer factors (a, b), after adding the end-plate correction (c, d), after all corrections (e, f) and after applying a superlayer correction extrapolated to the 3$^{\text{rd}}$ superlayer (g, h). The emphasised bands indicate the regions of the signal wires of axial layers.

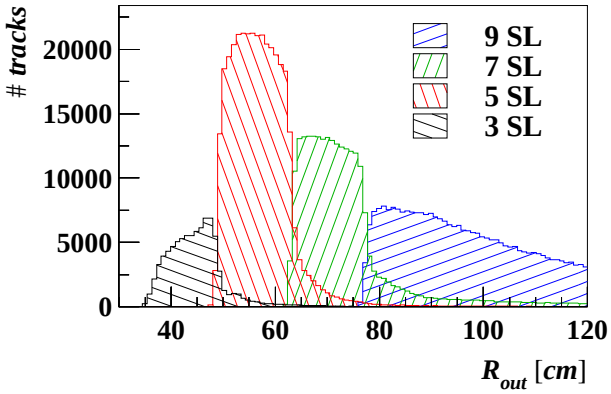

Figure 4.73: Distribution of R_{out} for different superlayer classes. Tracks ending in the 3rd superlayer are shown here for illustration reasons, even if they are not used in the tuning samples.

correction these dips disappear (Fig. 4.72 (c, d)).

Still remaining are some steps each covering the range of an axial superlayer and the innernext stereo superlayer. The distribution of R_{out} depending on the reached superlayer (Fig. 4.73) shows, that one can trace back these steps to scale factors between the different superlayers. But one has to be careful, as a dependence on R_{out} can also be a reflection of the dependence on several other variables, like θ, p_t or the number of hits. Fortunately we are in the lucky situation to have access to a very good test sample:

If CTD channels are not properly working, they are masked out for the reconstruction. It can happen, that whole groups of wires or a complete supercell has to be masked. If this happens for a supercell in the 9th superlayer, tracks which pass through that cell are reconstructed as tracks with only 7 superlayers (the outermost superlayer has to be an axial layer). This allows us to select a data sample, which contains only tracks with 7 superlayers, even if the topology of these tracks corresponds to 9-superlayer tracks. Such a test sample can be compared with another one, using exactly the same selection cuts except of the choise of a 'dead' supercell in the 9th superlayer. These two samples are identical except for the fact, that in the first one only hits up to the 7th superlayer are used whereas in the latter one all hits up to the 9th superlayer are taken into account. Therefore effects on dE/dx caused by the track topology should be identical in both samples. Differences in dE/dx of both samples can be traced back directly to the differently used superlayers.

Both samples are selected to contain tracks which start in the first superlayer and fulfil the condition $R_{out} > 85\,\text{cm}$. The track helix is used to find the supercell number in the middle of the 9th superlayer (at $R = 76.5\,\text{cm}$). Figure 4.74 shows the number of candidates found in the 1998/1999 e^- data sample, depending on the supercell index in the 9th superlayer. The left side contains tracks which are reconstructed as 7-superlayer tracks, on the right side one sees 9-superlayer tracks. For most supercells only a small number of tracks is reconstructed with 7 superlayers. This can happen if the track has a kink before reaching the 9th superlayer or if the hits in the 9th superlayer are not well reconstructed and rejected. In the range of 4 supercells most of the tracks are reconstructed only up to the 7th superlayer. Obviously the corresponding supercells in the 9th superlayer are dead. For one of them the rates of 7- and 9-superlayer tracks are almost identical. It might be, that in this supercell only about half of the wires are active, so that a track is treated as a 7-superlayer track as soon as one of the hits is rejected. It can also be, that due to hardware problems the efficiency of this supercell is reduced, but not zero. With processed data it is not possible to trace back the exact reasons for it. Figure 4.74 (a) also shows, that the rate in the supercells just besides the dead ones is increased. This is a resolution

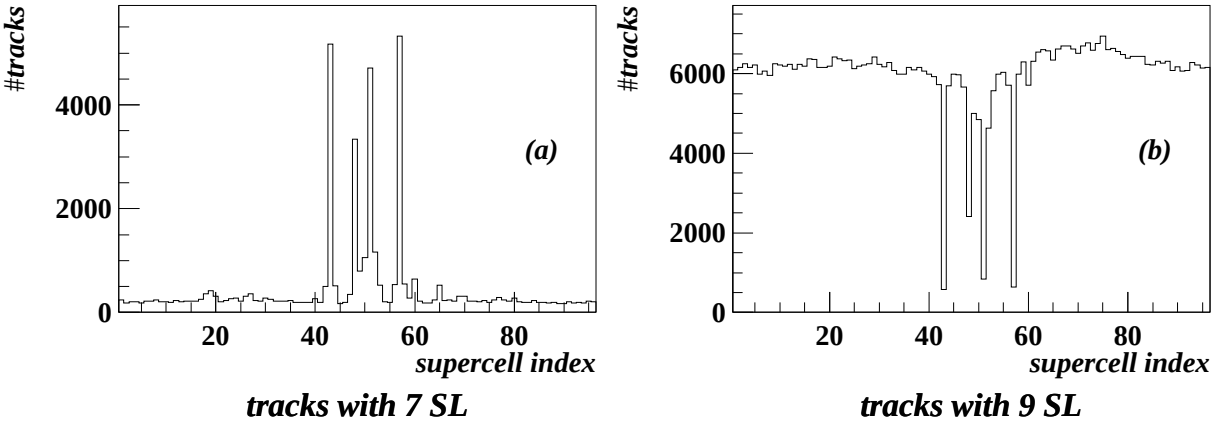

Figure 4.74: Number of tracks depending on the index of the hit supercell in the 9^{th} superlayer, reconstructed as (a) a 7-superlayer track or (b) a 9-superlayer track.

effect in this plot. Especially at the outermost end of the track the helix is not a perfect description of the real track. If a track is reconstructed to hit a dead supercell close to the border of that cell, it might be, that the real track was still in the neighbouring cell. This causes migrations between neighbouring bins. The same argument holds for Fig. 4.74 (b), where the dead supercells still contain some events.

The 7-superlayer test-sample contains only tracks passing through one of these 4 supercells, whereas the 9-superlayer test-sample is restricted to 4 other supercells close to them (supercell numbers 40, 45, 53 and 61). Using Fig. 4.74 one estimates a purity in the order of 80% for the two samples.

Based on these test samples one calculates the ratio

$$\frac{dE/dx_{norm}(7SL-tracks)}{dE/dx_{norm}(9SL-tracks)} = 1.0037 \pm 0.0063 \quad . \tag{4.32}$$

As expected from Fig. 4.72 (a, b) the mean value differs from 1 by roughly 0.4%. But to prove the need for superlayer factors one needs higher statistics than available. Nevertheless, the fact, that the found mean value matches very well with the seen 'step' in Fig. 4.72 is a good hint for the existence of a superlayer effect[9].

The next step is to extract proper superlayer factors from the data. For this, the already shown R_{out}-plots are split into different outermost superlayer classes. The 5- and 7-superlayer classes can be treated in a similar way. They cover most of their statistics in the R_{out}-range which corresponds to tracks, which leave the CTD through the endplates. For example, most of the 5-superlayer tracks leave the CTD at a radius between the outer end of the 5^{th} and the middle of the 7^{th} superlayer. Some kinky tracks can be found also at higher R_{out}-values. In addition, some tracks might be wrongly reconstructed and can correspond to even smaller R_{out}-values. For the extraction of mean values m_{sl} for these two samples one must ensure, that only well-defined tracks are used. Therefore this calculation is limited to the high statistics ranges in R_{out}. Furthermore, the low end of

[9]In order to gain as much statistics as possible for this evidence test, all samples (tuning and test samples) are used together. This is justified, as the samples for this evidence test are not used for the calibration itself.

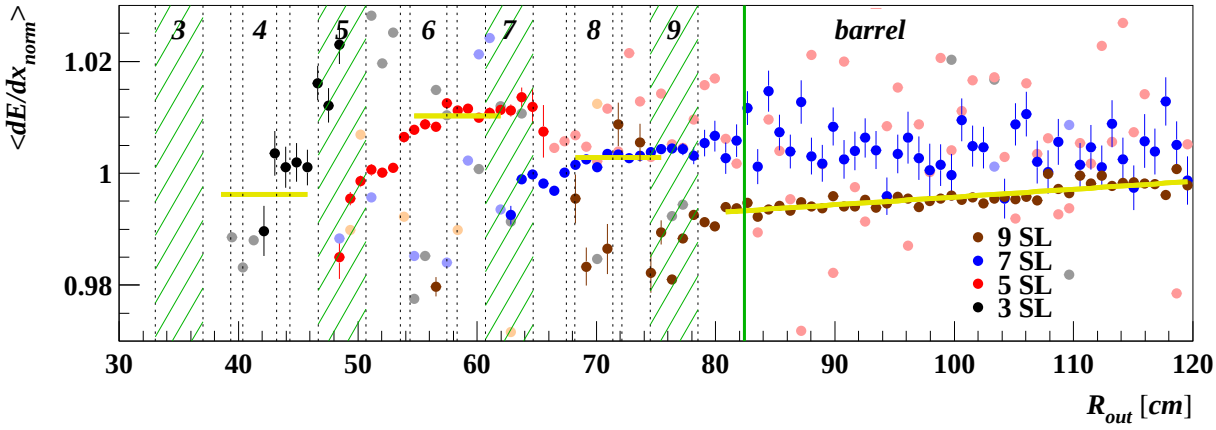

Figure 4.75: $\langle dE/dx_{norm} \rangle$ vs R_{out} separated for different outermost superlayer. For better visibility dots with small statistics are shown without error bars and in light colour. In addition to the tuning samples, tracks ending in the 3rd superlayer are shown here, too.

this range is rejected, too. This helps to minimise the bias due to the end-plate effect, as end-plate-affected tracks are clustered in the R_{out}-distribution around the outermost end of axial superlayers. The 9-superlayer tracks have a low limit in R_{out} for the same reasons as the 5- and 7-superlayer tracks. Their high-statistics range covers all R_{out} beyond the 9th superlayer. We are interested in the mean value of this track class close to the minimum of their high-statistics range. This can be found by fitting a straight line to the data and using the value of this fit at the corresponding R_{out}-position ($R_{out} = 84\,\text{cm}$).

Figure 4.75 clearly shows the steps between the superlayer classes. Tracks ending in the 3rd superlayer suffer from low statistics and the distribution falls down strongly for small R_{out}. This is caused mainly by turn-on effects in the sample selection. The cut on the minimum number of used hits rejects almost all 3-superlayer tracks. Only tracks with small signals (small number of saturated hits) can pass this selection. Thus for extracting superlayer factors the 3-superlayer tracks cannot be used.

The next task is to extract correction factors from these results. One has to keep in mind that for example a 7-superlayer track contains hits in all superlayers from the 1st up to the 7th, i.e. each mean value m_i extracted from the data sample ending in the ith superlayer contains information about all superlayers from the 1st to the ith one. To find a scale factor s_j for hits in the jth superlayer, one has to disentangle them. If one takes the 5-superlayer tracks as a reference, a simple linear transformation yields the factors $s_j,\ j = 7, 9$:

$$\begin{aligned} s_7 &= \left(\frac{7}{2} \cdot m_7 - \frac{5}{2} \cdot m_5\right) / m_5 \\ s_9 &= \left(\frac{9}{2} \cdot m_9 - \frac{7}{2} \cdot m_7\right) / m_5 \quad . \end{aligned} \tag{4.33}$$

As in this approach the first 5 superlayers are taken as a reference, hits within these superlayers are scaled by 1. Hits in the 6th and 7th superlayer are scaled by s_7, hits in the 8th and 9th superlayer by s_9. The correction factor is the inverted mean of the scale factors of all hits of the track. The result after applying superlayer factors can be found in

Fig. 4.72 (e, f). Once more one can see strong deviations from the expectation for tracks which do not reach the 5$^{\text{th}}$ superlayer. For tracks with $R_{out} > 55\,\text{cm}$ the distribution is almost flat. The steps between the superlayer classes disappear and also within the different classes the R_{out}-dependent variations are reduced. This indicates, that without a superlayer correction the other corrections partially compensate for the superlayer effect.

There are only technical reasons to start with a superlayer correction in the 7$^{\text{th}}$ superlayer and not already below. As it is not known why superlayer-factors are needed one cannot state a reason for a lower limit of the superlayer number. Therefore it is an important check to see, what happens if the superlayer correction is extended to smaller superlayers.

As one cannot trust in the measurements for tracks ending in the 3$^{\text{rd}}$ superlayer, one has to extrapolate the measurements from higher superlayer numbers downwards. One can expect that the difference in $\langle dE/dx_{norm}\rangle$ changes linearly between neighbouring axial layers:

$$m_3 := 3m_5 - 3m_7 + m_9 \quad . \tag{4.34}$$

The factors $s_j,\ j = 5, 7, 9$ can be calculated similarly to the method mentioned above:

$$\begin{aligned} s_5 &= \left(\frac{5}{2}\cdot m_5 - \frac{3}{2}\cdot m_3\right)/m_3 \\ s_7 &= \left(\frac{7}{2}\cdot m_7 - \frac{5}{2}\cdot m_5\right)/m_3 \\ s_9 &= \left(\frac{9}{2}\cdot m_9 - \frac{7}{2}\cdot m_7\right)/m_3 \quad . \end{aligned} \tag{4.35}$$

One might ask, why the same method is not extended down to the first superlayer. Several arguments are given here:

- The extrapolation from the measured 5$^{\text{th}}$ superlayer down to the first one has a very big uncertainty. Thus the scale m_1 cannot be calculated in a proper way.
- The error caused by using the 3$^{\text{rd}}$ superlayer scale down to the first one is not too big. Only hits in the first superlayer are scaled wrongly with the difference $m_3 - m_1$ whereas all other hits of the track have proper scales. Thus the mismeasurement of m_1 is strongly suppressed in the mean factor for the whole track.
- Tracks with only one superlayer are anyway useless for a proper dE/dx measurement. As long as all used tracks cover at least the first 3 superlayers, it is adequate to use a common factor for the first 3 superlayers.

The result of this extension of the correction can be found in Fig. 4.72 (g, h). Compared to the results without this extension one cannot see any improvement. Furthermore, some instabilities in the fit algorithm (Sect. 4.3.2.4) were found when applying the extended superlayer correction. The available data does not allow to gain evidence for the need of the extension. Taking all aspects into account, finally the extension of the superlayer-correction was not applied.

One has to remark, that the limited knowledge about the superlayer correction for small superlayer numbers is not very harmful. Due to their small number of hits, the dE/dx of tracks with only 3 superlayers anyway is not measured well enough to trust in it. Therefore this limitation in knowledge only affects tracks which should not be used in any analysis based on dE/dx measurements.

4.3.2 Combination of the partial corrections

In Section 4.3.1 the correction methods for several different effects were shown separately. For simplification any kind of cross relations between them were neglected; the corrections described rely on the assumption, that the data used are not affected by any of the other effects. This section will describe the combination of these separate corrections into the grand total correction also taking interdependencies into account.

4.3.2.1 Sequence of partial corrections

As the effects shown previously happen to occur at different places, they are ordered and this order has to be inverted when implying the different corrections. For example, the threshold effect occurs within the wire readout, whereas the space-charge effect already happens, when the primary electrons drift to the signal wire. Consequently the input data for the space-charge effect correction should not be affected by the threshold-effect. For the correction procedure this means, that first the threshold-effect correction has to be done using space-charge affected data, and afterwards the space-charge effect correction has to be applied to the data that have already been corrected for the threshold-effect.

The order of the different partial corrections becomes important, as soon as the input data for the correction calculation depend on the measured dE/dx. There are also corrections which use only independent input variables, like the neighbourhood correction. Therefore for the neighbourhood correction it does not matter, at which position in the queue it is calculated. Nevertheless the order of applying the corrections has an impact on the final result, as the neighbourhood effect correction is additive whereas most of the other corrections are multiplicative.

Effect	Site of occurrence	Dependence on other effects
air pressure	gas	none
drift time	gas	signal height
endplate	gas	none
space charge	gas close to wire	ionization density projected to the wire
neighbourhood	wire	none
dispersion	wire	signal height
threshold	readout	signal height
wire gain	readout	none
saturation	readout / reconstruction	none
truncation window	reconstruction	none
mean-value shift	reconstruction	none
superlayer factors	???	none

Table 4.4: Overview of the corrected effects and their site of occurrence. The last column shows direct dependences between them. The signal height as 'seen' by a certain effect depends on the other effects happening before to the signal. Thus an effect depending on the signal height, indirectly depends on all other effects occuring to the signal before, thus the dependence on the signal height is shown in the third column, too.

Table 4.4 gives an overview of the order of the investigated effects. Furthermore the table shows, which dependences are given for the corresponding calculations.

The following sections describe the data flow at the level of the track reconstruction and within the dE/dx corrections. The intention of these sections is to give a general overview of the relations between the different parts of the correction package.

Data flow in Phase I

The data flow in Phase I (Fig. 4.76) can be split into two parts: the first one deals with whole events, the second part works on single track level.

On event level, the tracking has to combine hits in order to build tracks. The outcome of the tracking are hit patterns and helix fits to describe the tracks. On the second level several corrections are applied to the raw dE/dx measurements of single hits. All of these corrections depend on the track topology, they use information from the tracking

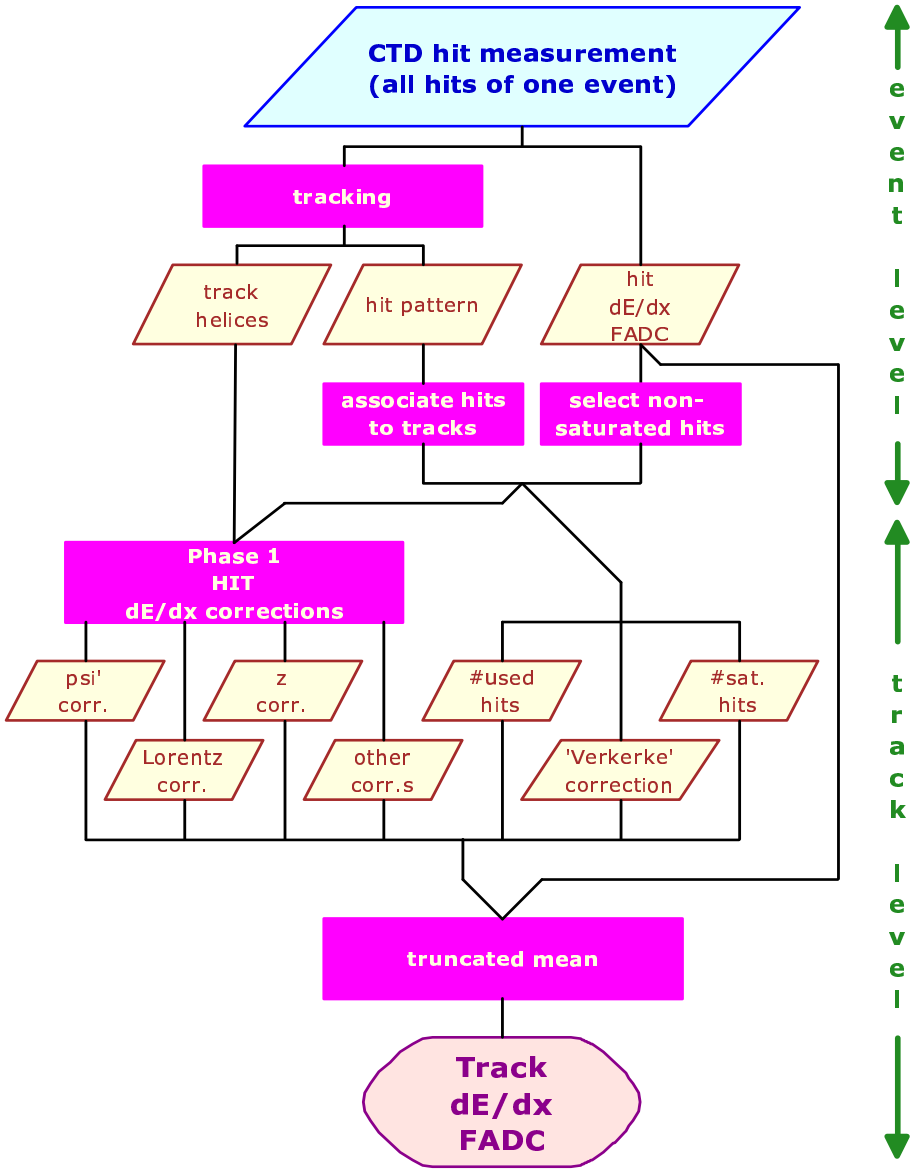

Figure 4.76: Data flow of the dE/dx corrections in Phase I.

calculated previously. In the flow chart shown in Fig. 4.76 only those corrections are named explicitly, which are of special relevance in Section 4.3.2.1. All other corrections are combined in the box 'other corr.s'. In the next step for each track the corrected single hit dE/dx values are combined to a track-dE/dx using a truncated mean method. Finally a special correction is applied to tracks with a large fraction of saturated hits (more than 30% of the highest signals have to be removed by the truncation method) to render the calculated dE/dx comparable for all tracks. In reference to the author of this correction it is called 'VERKERKE correction'.

Data flow of partial corrections

Figure 4.77 gives an overview of the data flow in the dE/dx correction code. To keep this flow chart as simple as possible it is based on special rules. The data flow always goes from left to right. Lines entering a box from the left are input variables, lines leaving a box on the right side denote the output. The lines going out of the process boxes (green, rectangular) represent variables, which are calculated in the corresponding process. The flow of the dE/dx value itself is denoted by a thick red line.

The input for the corrections, delivered from the tracking, can be split into four classes. One of them is of course the dE/dx_{FADC} itself. Besides this, the most important input is the helix of the track under examination. Only the neighbourhood correction additionally uses the other tracks of the same event, thus all track helices are needed for its calculation. Finally the run-by-run corrections (including the air-pressure corrections if available) are delivered by a separate routine.

Using these ingredients several input variables for the partial corrections can be calculated. These extracted variables only depend on the input and do not change after applying any of the corrections.

At this level it is also possible to calculate an approximation of the correction factors depending on the z-position of the hits, the angle ψ' and the Lorentz angle α_l as calculated and applied in the Phase I reconstruction. These corrections are calculated in Phase I at single hit level and affect the dE/dx of the track, as this is the (truncated) mean value of all dE/dx_{hit}. The size of these correction factors (at track level) could be calculated exactly, if one had access to the informations, which hits are used for the track reconstruction. As this information is not available for processed data one can only approximate the calculation assuming a 100% efficiency of the CTD. Thus the mean $\overline{\psi'}$, $\bar{z}$ and α_l are calculated using all hits that are geometrically possible. It is mandatory to re-calculate these factors, because some parts of the new corrections need the 'raw signal' as an input. As these raw signals are not stored in the processed ZEUS data, the only way to get an approximation for them is to use the Phase I corrected dE/dx and divide out the corrections from Phase I. Slightly different conditions are given for the dispersion correction (z-dependent) and the drift-time correction ($\overline{\psi'}$-dependent). The new corrections are more sophisticated than the ones given in Phase I and they replace the corresponding Phase I corrections. Thus it is necessary to remove these Phase I corrections from the data. To separate the removed corrections from other variables, they are shown in the flow chart in magenta.

Based on the variables mentioned so far, several correction factors can be calculated. The structure becomes more complicated when dealing with the dispersion correction and the threshold correction. They need the signal height at the end of the signal wire as an input. This signal height can only be reconstructed using the measured dE/dx_{FADC}, applying all corrections for effects which occur later in the readout chain and removing the corrections

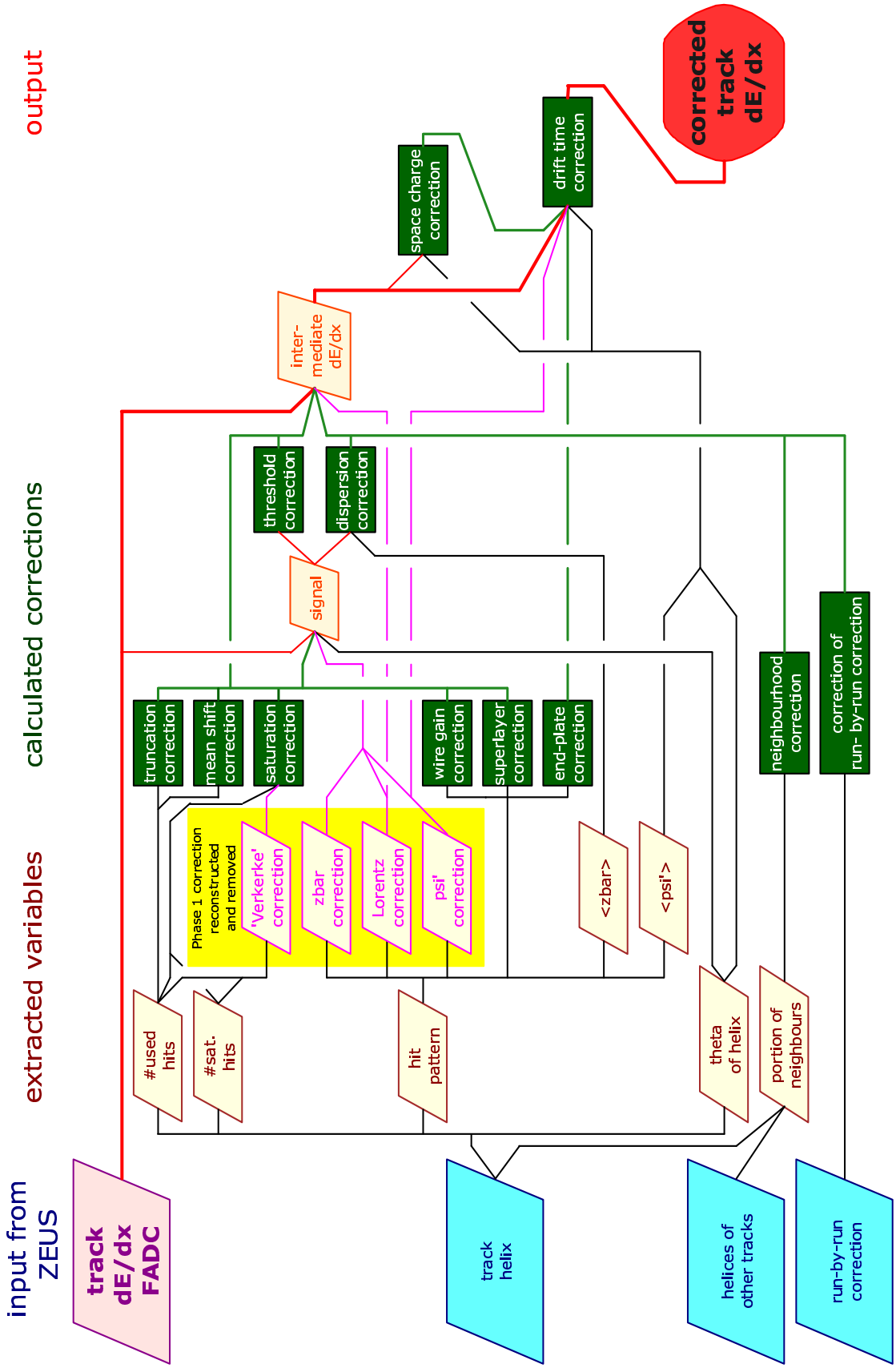

Figure 4.77: Data flow of the dE/dx corrections.

from Phase I, using the approximate correction factors mentioned previously. A similar method is used for the space-charge and the drift-time corrections, which use the dE/dx within the gas of the CTD. For the drift-time correction also the correction factor from the space-charge correction has to be applied to the input. Finally, the output of the drift-time correction is the corrected dE/dx_{mips}.

4.3.2.2 The issue of correlations

The effects described above are caused by independent sources, they occur at different places on the way from the primary ionisation in the chamber to the dE/dx value stored for each track. This legitimates the approach of applying separate corrections as shown in Section 4.3.1. However, all of them have an influence on the measured dE/dx which can eventually cause correlations between them. The most simple correlation is the global scale. Generally the scale of the uncorrected dE/dx can differ from the expected one. The fit functions have to take this into account. For example in case of the threshold correction it is obvious, that for high signals (no threshold effect) the correction factor should be 1 (no correction). However, if the (partially) uncorrected data have a different scale than the expectation, Fig. 4.43 (a) will show this scale factor for high signals to be different from 1. To provide a stable fit, it is necessary to keep this factor as a free parameter. The same is true for the space-charge effect correction. And finally the drift-time correction pulls the data towards the expected dE/dx which also contains a global scale correction. Taking all partial corrections, the global scale would be corrected three times. This is, of course, not favourable for the final combined corrections. Fully correlated parameters can never stabilise in an optimisation algorithm; only their sum can have a fixed value. In the end, the scale should be corrected only in one place. Thus the correction functions for the threshold and the space-charge effect are rescaled after fitting, forcing their scale parameter to be 1. On the other hand, the drift-time correction has to be rescaled, so that this correction compensates for the rescaling of the other two corrections. After applying this rescaling, the final result (the dE/dx value after applying all corrections) is still unchanged, but the scale parameters of the first two corrections are fixed to 1 and are therefore not free parameters anymore.

This example of correlations is quite evident and easy to handle, but there are also less obvious correlations. Probably, the most prominent example is the one between the threshold and the space-charge effect. Both are maximised for tracks with $\theta \approx \pi/2$: in case of the space-charge effect, for these tracks the primary electrons are very close together in the z-direction; for the threshold effect, the signal is proportional to $1/\sin\theta$, which has its minimum at this value. The space-charge effect decreases the measured signal whereas the threshold effect increases it. Just by chance, for pions close to minimum ionisation the amount of the two effects is roughly the same, so that they cancel each other. Consequently, both effects were not seen in the first days of dE/dx tuning at ZEUS with pion samples. If electron samples are used, the situation changes. Compared to the pion sample the space charge-effect is larger whereas the threshold effect is smaller. The effects cannot cancel anymore and a fraction of the space-charge effect remains visible.

This example shows the difficulty in combining corrections. If two (or more) effects cancel each other, it is not directly visible how large a single effect is. It is impossible to optimise the corrections for each effect sequentially. The correction factors have to be estimated simultaneously to allow each partial correction to 'take what it needs'.

The route taken to fulfil this job is an iterative procedure. In each iteration the corrections of the previous one are applied as follows: in order to estimate new fit parameters for the correction function for each effect, the corresponding histograms are filled with data, which are corrected against all effects except for the one in question. This kind of 'precorrection' is done using the fit parameters of the previous iteration. For the first iteration either no 'precorrection' or an initial correction is done.

For example, in order to calculate the correction function against the neighbourhood effect in the n^{th} iteration, the histogram in Fig. 4.47 is filled with the data after all corrections except of the neighbourhood correction, using the correction factors calculated in the $(n-1)^{\text{th}}$ iteration. After that, the fit function is calculated (in this case a linear function). The resulting fit parameters (in this case only the slope) are kept as the n^{th} iteration of a parameterisation of the correction function against the neighbourhood effect. As soon as this is done for all partial corrections, the set of parameters for the next iteration is determined.

So far, this procedure will still not manage to deal with every kind of correlations. In order to understand this, one can investigate the two most simplified scenarios:

- Two effects (partially) compensate each other.

  In the beginning, the distributions for extracting the correction functions do not show the full effect, as parts of it are compensated. Thus the calculated corrections will be too small for both effects. In the next iteration, each of the distributions will 'see' the correction of the other effect, so the interesting effect for each histogram will become more pronounced and its correction will become larger than in the first iteration. After some more iterations, the correction factors do not change anymore, when both corrections have compensated 'their' effect completely. As soon as this state is reached, the iterative procedure can be stopped.

- Two effects add up.

  This case is more difficult. In the first iteration both distributions will be over-pronounced, as they will not only show 'their' effect but in addition the second one. Consequently, the correction functions for both effects will become too large and over-correct both effects. In the next iteration each of the histograms will 'see' the data after overcorrection of the other effect. So in this iteration both effects will be underestimated. Depending on the size of each effect and the level of their correlation the effect seen may even flip its sign. In such a case, in this second iteration the calculated correction will increase the effect instead of compensating it. In any case the correction will not be large enough (or maybe even inexistent), so that the situation in the 3^{rd} iteration is similar to the first one; the iterative procedure will produce oscillations between over- and under-corrections. In the worst case these oscillations will diverge.

The examples mentioned above describe the most simple cases of correlations. In reality, twelve different corrections with various possibilities of multi-effect correlations have to be combined. These remarks may illustrate, how important a proper handling of correlations is. The following sections will show, how this is done here.

4.3.2.3 Disentangled corrections

Some of the corrections shown in Section 4.3.1 are (almost) completely disentangled from the others. For these effects, a special handling of correlations is not necessary. They can be tuned and used separately from the others. These corrections are:

- **The wire-gain correction:**

  The main reason for the wire-gain correction being independent is, that the wires (and their individual wire-gains) are localised in R and ϕ. All other previously mentioned effects do not have any ϕ dependence. As the wire-gain correction is predominantly sensitive to the azimuthal positions of the hits, it is almost totally disentangled from all other corrections. This allows to optimise the wire-gain correction almost independently of the other ones. The very small correlation due to the R-dependence (which is related to p_t and to θ) is controlled by the following approach, which can be read like a 'one iteration method':

  1. First all other corrections are optimised without wire-gain correction (gain correction factor 1 for all wires).
  2. Then the wire-gain corrections are found, using dE/dx values determined after applying all other corrections.
  3. Finally, the other corrections are generated again, this time using wire-gain corrected dE/dx values. This allows the corrections to react on the small correlations between wire-gains and the other corrected effects.

- **The truncation-window correction and the shift of the mean value:**

  The dependence on the truncation-window is purely arithmetic and has almost nothing to do with chamber physics. Input from real data is only needed to fix the width of the reference LANDAU distribution. It was shown in Fig. 4.32, that this is stable for the whole ZEUS data taking period, so it can be treated as independent of the other corrected effects. Thus the correction method itself is pure arithmetics as well as the effect corrected for. It cannot be affected by other effects and therefore is done independently.

- **The saturated-track correction:**

  Generally this correction can, of course, be correlated with the corrections of other effects. But as mentioned before, care has been taken to clean up the tuning samples in a way, that almost all tracks with a high number of saturated hits are rejected. Thus the tuning samples usually used cannot contain correlations with this effect. The opposite direction is also safe: Like the truncation-window correction, this correction only deals with arithmetics of the reference LANDAU distribution, so it cannot be affected by other corrections, which do not influence this function.

The general approach is to do these independent corrections beforehand and to use in this term partially corrected dE/dx values as input values for the following corrections.

4.3.2.4 Entangled corrections

The correlations between the remaining effects cannot be neglected. It is impossible (and by far too subjective) to identify and keep them under control manually. Instead, the

algorithm itself should offer an objective method to damp oscillations and to find the optimum in the multi-dimensional parameter space.

The chosen algorithm splits the iterations into two phases. The first phase should bring the corrections close to their optimum. When this is done, the risk to blow up oscillations is gone. The second phase can do the 'fine tuning' by following simply the method already described.

In the first phase we expect big changes in the fit parameters, which can overshoot the final result and lead to large (or growing) oscillations. The different parts of the corrections have to find 'their space'. Several mechanisms are used to damp such oscillations and to allow the different parts of corrections to occupy their space.

The first mechanism is to 'freeze' some corrections for the first iterations. This is done with the treshold and the dispersion corrections.

The threshold correction is very sensitive to oscillations. To ensure the convergence of the whole method, the threshold correction is initialised in the first iteration with parameters, which are already not far away from their final values. For the first 5 iterations the threshold correction is fixed to these parameters. After these 5 iterations, the other corrections are stable enough to allow also the threshold correction to vary.

The dispersion correction has the disadvantage to become instable if the starting conditions are not good enough. To provide the necessary conditions, for the first 10 iterations no dispersion correction is applied. After the 10^{th} iteration, the other corrections are almost stable and the dispersion correction can be turned on.

The second mechanism is not to apply the full corrections as calculated. If an effect is corrected only partially, this will still allow the corrections of other effects to take over their phase space, even if they tend in the same direction. In the first iteration only 1/3 of the calculated correction-values are applied. In the following iterations this fraction is steadily increased to full values. This method is applied to all corrections except for the ones in Section 4.3.2.3 and the neighbourhood correction. The latter is quite safe with respect to correlations, as it is the only correction which uses information of all tracks in one event.

The third mechanism is to limit the variation of the corrections between iterations. Instead of taking the latest calculated correction parameters, values between the current fit result and the parameters of the previous iteration are used. This method is extremely powerful against oscillations with a cycle of two iterations. It has turned out, that especially the threshold effect, the dispersion effect and the space-charge effect correction are very sensitive to this kind of oscillation. Therefore this damping mechanism has been used only for these three corrections. The price for this way of damping is, of course, that the number of iterations necessary to find a stable optimum blows up. Several attempts with different damping factors lead to the final choice, which uses for the threshold effect and the dispersion effect the mean value between current and previous iteration; for the space-charge effect correction 70% of the current change is taken.

The stability of this method can be judged in Fig. 4.78, which shows the evolution of the fit parameters in the 60 iterations calculated. In the first iterations some of the parameters show very strong variations. Some parameters show oscillations which disappear after about 30 iterations. Especially the dispersion correction is totally off in the first iterations, but one observes, that after about 10 iterations (when the dispersion correction starts to

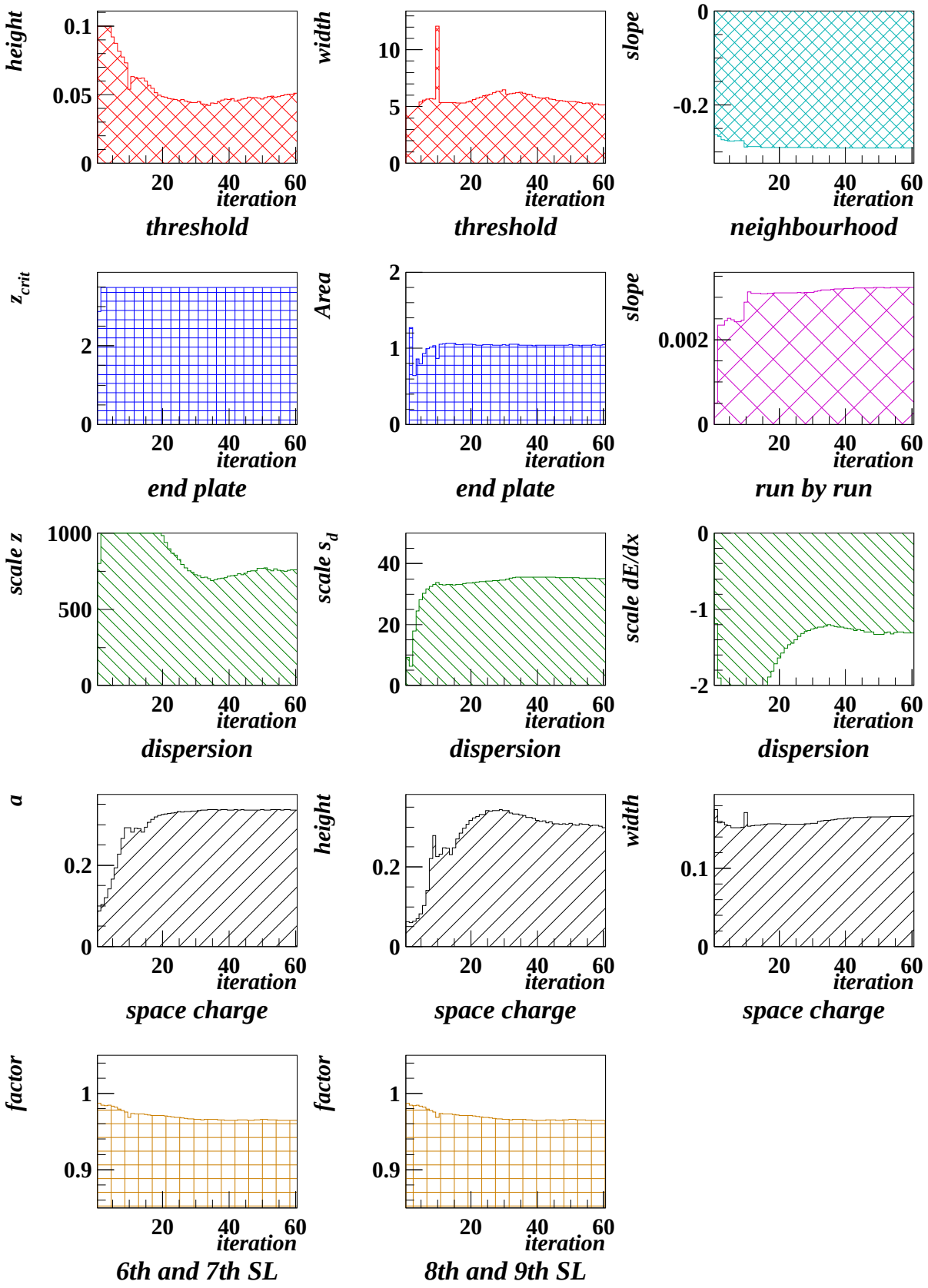

Figure 4.78: Evolution of various fit parameters. HERA I data without water.

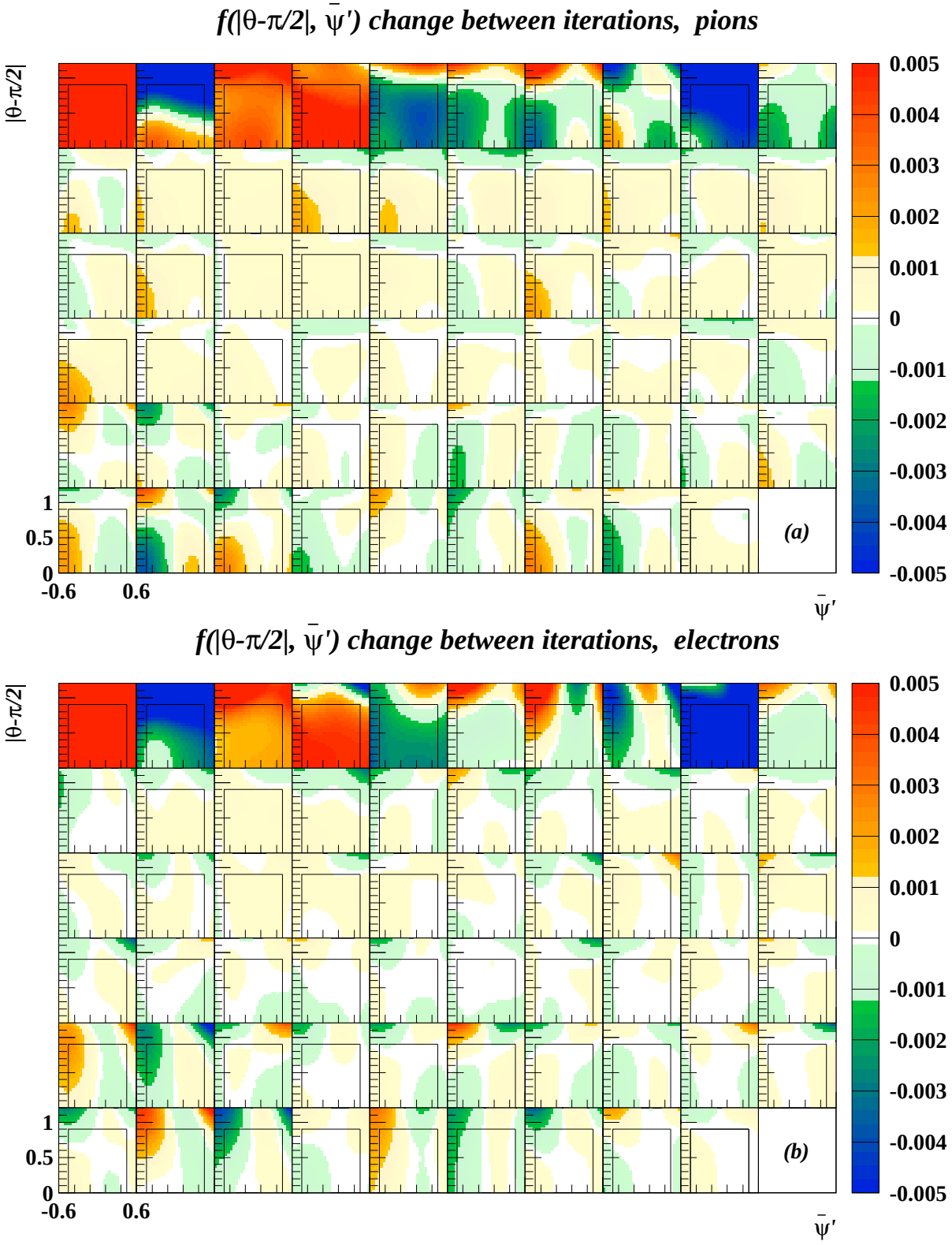

Figure 4.79: Evolution of the drift-time correction for pion (a) and electron (b) tuning sample. Each histogram shows the change of the expected signal in bins of $|\theta - \pi/2|$ and $\overline{\psi'}$ between two successive iterations. The black lines indicate the fit range. Outside of this range the expectation function is extrapolated.

be admitted) all parameters are in the same range as their final result. Anyway, between the 15$^{\text{th}}$ and the 20$^{\text{th}}$ iteration the dispersion correction is lost which also affects most of the other corrections. After the 30$^{\text{th}}$ iteration all parameters start to stabilise without serious oscillations.

The drift-time effect is parameterised in a high-dimensional parameter space. A side effect of the high dimensions are strong correlations between the parameters. These correlations render it futile to look at the evolution of single parameters. Even if single parameters show strong changes they can almost completely be compensated by the simultaneous change of other parameters of the same effect. Only the complete correction function can give information on the stability of the iterative method. In Fig. 4.79 the changes between successive iterations of the calculated expectation for the pion and electron samples are shown. As soon as the whole method has stabilised (≈ last 1/3 of the iterations) within the fitting range (black line) the expectation is stable within 1‰.

4.3.2.5 An example for correlated effects

This section offers a closer look at the (indirect) dependence of dE/dx on $\cos\theta$. Figure 4.17 has shown such a dependence of the order of 10%. It seems to be obvious, that this is caused by the space-charge effect. In contrast to this examination, Fig. 4.60 shows, that the maximum of the space-charge-effect correction is only 5%. So, where do the other 5% disappear? Or maybe they do not disappear, and the dE/dx corrections are incomplete concerning this aspect? A first cross check is given in Fig. 4.80. The $\cos\theta$-dependence is shown without any corrections, after the space-charge, threshold, drift-time, dispersion and after all corrections. For properly corrected data it is expected, that this distribution is almost flat. Only the correlation between θ and p, mainly caused by a cut on p_t for all tracks, combined with the p-dependence of the BETHE-BLOCH curve can cause slight deviations from flatness. Indeed it turns out, that the space-charge-effect correction alone

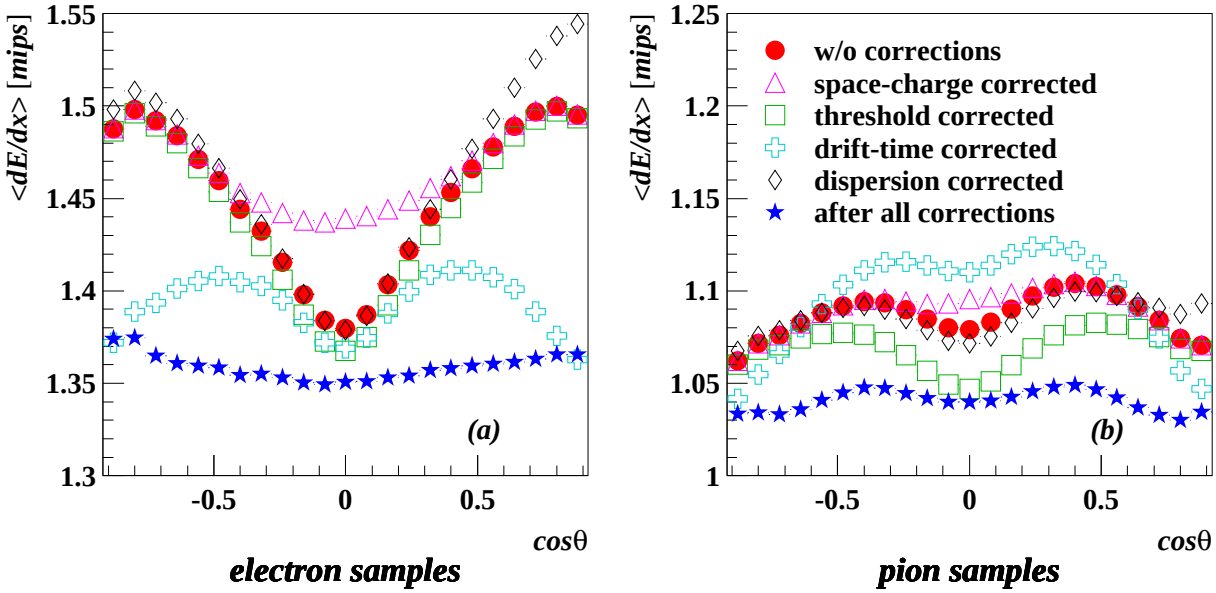

Figure 4.80: dE/dx dependence on $\cos\theta$; (a) electron samples, (b) pion samples.

does not fulfil this expectation. Only for $\cos\theta \approx 0$ the effect of the correction becomes visible. The electron sample after space-charge-effect correction alone looks by far not flat. Nevertheless, after all corrections, the dependence on $\cos\theta$ has almost disappeared.

As expected, for the pion sample the dependence on $\cos\theta$ is much smaller even without any corrections. Due to the low signals in this sample, the space-charge-effect correction has almost no effect. Except for a global shift to smaller values there is no big change visible between space-charge corrected and completely corrected values. This shows that there are other corrections which take care of the dependence of dE/dx on large values of $|\cos\theta|$. Indeed, Fig. 4.80 (b) shows, that the increase of dE/dx for $\cos\theta \approx 0$ caused by the drift-time correction is compensated by the threshold-effect correction, which is almost negligible in case of the electron samples.

This example demonstrates very clearly how complicated correlations can be and that it is likely to misinterpret single distributions, if these correlations are ignored.

4.3.2.6 Size of correlations

The preceeding sections have presented, how the different partial corrections are combined to a total correction. For some of the partial corrections arguments are given, why they can be handled separately from the others. The remaining parts are combined in an iterative procedure.

After generating several corrections it is possible to cross-check the estimations about correlations, given in the previous sections. Having all partial corrections at hand, the correlations between them can be calculated. Low correlations will indicate independence of the effects. A concise way to show correlations is to arrange the correlation coefficients in a correlation matrix. By definition this matrix has to be symmetric and the entries in the main diagonal have to be 1. Figures 4.81 and 4.82 show such matrices for the different particle types together with the variation σ of the correction factors. The bigger this variation, the higher is the probability for instabilities in the iterative procedure caused by the corresponding correction. Most of the correlations are small, but some of them need further discussion. At this point a special remark about the run-by-run correction is in order. Usually in this work the run-by-run correction is treated on the same level as the Phase I corrections. The 'uncorrected' data already contains this correction. For investigating the correlations it is interesting to see the relation of the other corrections also to this one, so here it is included in the list. As the correction of run-by-run corrections is not a self-contained correction but only an addition to the Phase I run-by-run correction, in Fig. 4.81 and Fig. 4.82 the entry named run-by-run correction stands for the combination of the correction made by the CTD group and its correction.

Most obvious are high correlations between the mean-value shift and many other corrections. As an example, the correlation with the neighbourhood correction can be explained as follows: The mean-shift is a correction which always reduces dE/dx. The reduction becomes bigger the smaller the number of hits is, especially tracks almost parallel to the beampipe will be strongly corrected. The neighbourhood correction also reduces dE/dx. As the highest probability for neighbours is given in the innermost superlayers, tracks almost parallel to the beampipe tend to be strongly corrected by the neighbourhood correction, too. In other words, tracks with a strong mean-shift in many cases also have a strong neighbourhood correction. As both corrections have the same direction, the cor-

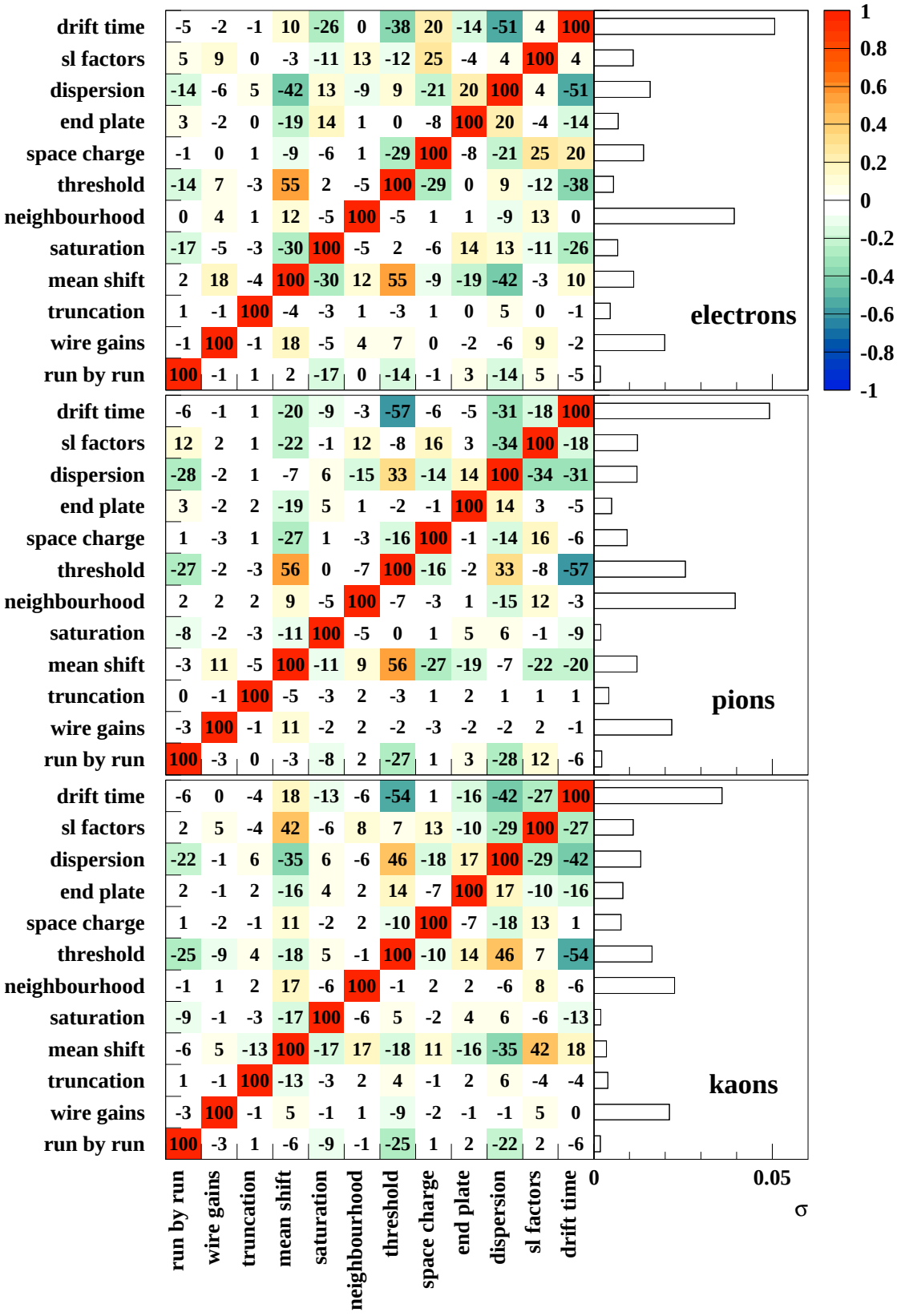

Figure 4.81: Correlation matrix for partial corrections for the electron, pion and kaon sample. The numbers are the correlation factors in %. On the right side the variation σ for each partial correction is shown.

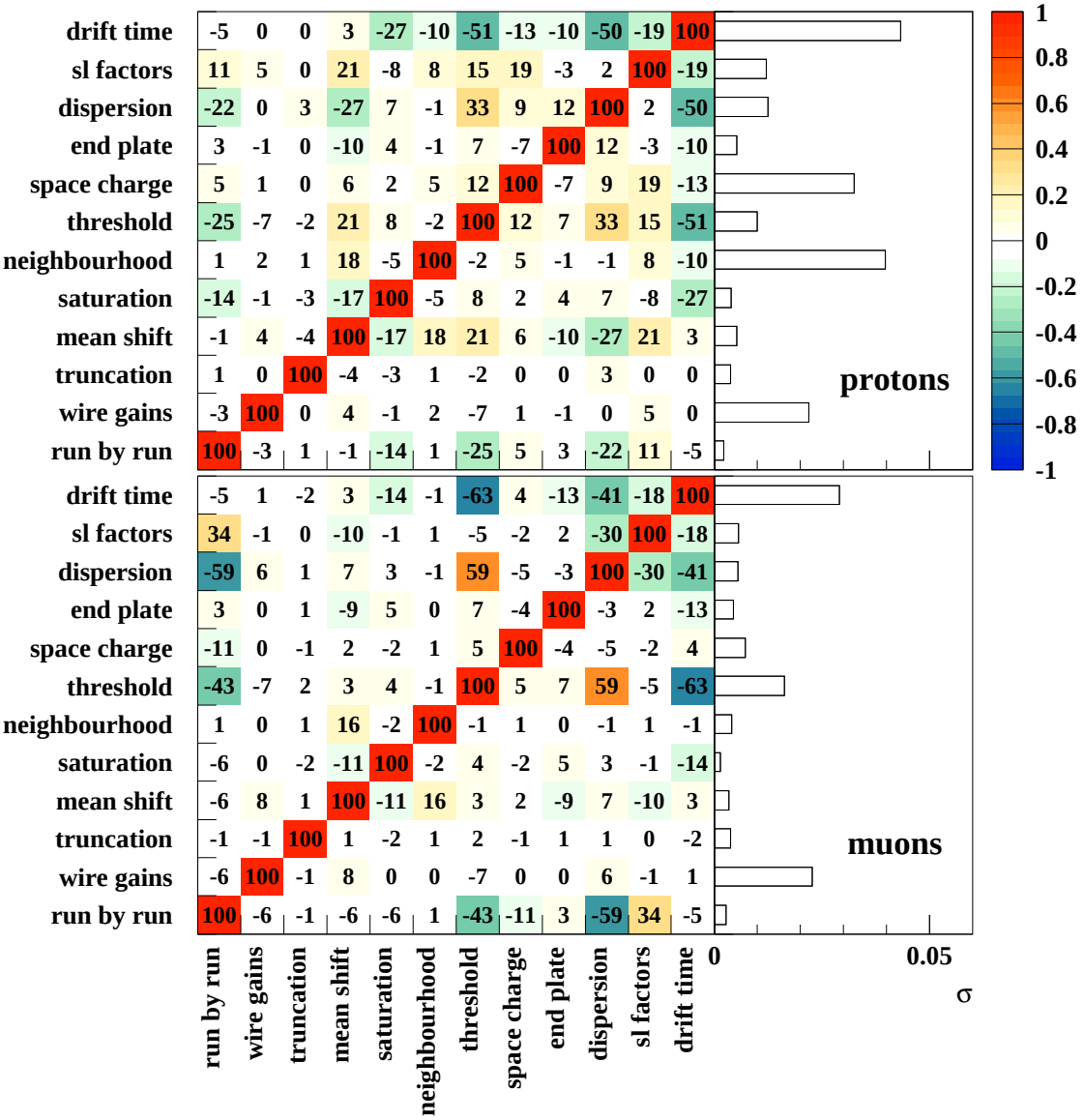

Figure 4.82: Correlation matrix for partial corrections for the proton and muon sample. The numbers are the correlation factors in %. On the right side the variation σ for each partial correction is shown.

relation is highly positive. The correlations with the superlayer factors, the dispersion-, threshold- and saturation-correction can be explained in a similar way. Anyway, one does not have to be concerned about these correlations, as the shift of the mean value is purely arithmetic and can be treated very well in the corrections. As this correction does not change between the iterations of the correction-finding algorithm, these correlations cannot cause instabilities.

Depending on the particle type the correlation between the run-by-run correction and the threshold-effect correction is measured between -43% and -14%. This anti-correlation has already been described in the introduction to the run-by-run corrections. It is not very large, which proves that the run-by-run corrections cover only a small part of the threshold effect. Therefore it was indeed useful to separate the threshold effect and to apply an independent correction to it.

The same argumentation is true for the correlation between the run-by-run correction and the dispersion correction, which uses the signal height as an input parameter and therefore is as well partially corrected by the run-by-run correction.

The saturation correction correlates with the drift time correction at a level of 13%-27%, most pronounced for high-signal samples (electrons and protons). This correlation is easily understandable. Saturation typically occurs for tracks with very high signals. Inspecting Fig. 4.61 one finds, that most of these tracks have large $\overline{\psi'}$ and $\theta - \pi/2$ values. These are exactly those tracks with the largest drift-time corrections. In other words, the strongest drift-time-corrected tracks are also the strongest saturation-effect-corrected ones and the correlation between these two corrections is obvious. Nevertheless, the saturation correction is tuned as a disentangled correction. This is possible, because the optimisation of this correction is done in a pure toy-model calculation which is not at all affected by any chamber effects. Therefore the correlation with the drift-time effect is well under control.

Except for the cases mentioned before, the disentangled corrections do not show high correlations with other corrections. This confirms their independence and validates their treatment.

The neighbourhood correction appears to be quite independent of all other ones. This is also reflected in the iterative algorithm, where the neighbourhood-effect correction is very stable: after the first three iterations it does not change anymore. The neighbourhood correction only depends on the neighbourhood ratio which is independent of the other corrected effects. Therefore no large correlations to other effects should appear. Anyway, the neighbourhood-effect correction is part of the iterative algorithm for entangled effects, as there was no strong argument beforehand to disentangle it. As it does not cause any stability problems in the algorithm, keeping it in the iterative procedure does not do any harm.

The remaining corrections (threshold, space-charge and drift-time) show larger correlations up to 60%. In Section 4.3.2.5 these correlations have been explained in more detail. Especially the high anti-correlations between the threshold effect and the space-charge and drift-time effects, respectively, are the reason for the oscillations found in the iterative method, which need the special damping methods presented above.

4.3.2.7 Estimate of remaining errors

Each correction has a limited efficiency. There are several reasons why an estimate of the remaining uncertainties of the partial corrections is crucial:

- The relative uncertainty of a correction factor estimates, how stable the correction is. It furthermore points out, how well the correction can cope with the corresponding effect.
- The size of the uncertainty of a partial correction indicates, how well this effect is under control.
- If the correction uncertainty depends on track parameters, one can use a detailed error analysis to maximise the accuracy of the calculated error of the dE/dx measurement on a single track. This error is an important figure for particle identification based on dE/dx (Section 5.3); thus an improved quality of the calculated resolution increases the accuracy of particle identification.

The different sources of uncertainties can be classified into two groups:

1. **predictable uncertainties:**
   Some uncertainties can be predicted with mathematically well defined methods. The partial errors are independent; they have to be added in quadrature:

   - **fit uncertainty:**
     All corrections are based on fits, which are applied to distributions given by the tuning data. For most of the effects, the inverted fit function is used as the correction function. Consequently, the uncertainty of the fit causes an uncertainty of the correction function. Usually, this kind of uncertainty decreases with increasing statistics in the tuning samples. As most of the data-taking periods offer high statistics, these errors are typically small. Anyway, in particular kinematic ranges, even with big tuning samples, statistics can be very limited. If the effect in question is huge in such ranges, the fit uncertainty can become substantial. Therefore the size of the fit uncertainty strongly depends on the kinematic range and can be immense for a small fraction of all track candidates.

     Furthermore, the three data-taking periods in the year 2000 with water in the CTD were not very long; for these periods the fit errors can become dominant.
   - **parameter uncertainty:**
     The correction functions depend on parameters given by the tracks. The errors of these parameters propagate into the error of the correction function. For the parameter used in the threshold-effect correction one needs the error on the dE/dx measurement itself. Section 5.2.2 will show the method of its prediction. All other parameters depend on the track helix. Their errors are calculated with error propagation of the helix (and its covariance matrix). For the histograms shown in this section these errors are calculated based on a data reference sample. The results of this sample are used as an estimate for the errors of the whole test samples. For the end-plate-effect correction a special method had to be employed to calculate the uncertainty. Details are given in App. H.
   - **hit selection for the truncated mean value and CTD-inefficiencies:**
     Some parameters used for the correction functions are mean-values of all hits corresponding to one track. As the information which hits were used for the track reconstruction is not available in processed data, these mean-parameters are calculated with all geometrically possible hits. The replacement of the mean-value of the really used hits by the one of all geometrically possible hits causes an additional uncertainty.

     For each track the number of used hits for the dE/dx calculation is known; this allows to select the same number of hits randomly from all geometrically possible ones and to calculate the parameter only with these selected hits. This random selection can be repeated several times. The width of the distribution of the parameters calculated in many such tests is an estimate for the variation of the parameter due to the truncation selection.

     For the parameters $\overline{\psi'}$ and $\bar{z}$ this uncertainty is calculated based on a test data sample. The results of these tests are parameterised for the uncertainty of $\overline{\psi'}$ as a function of the difference between the maximum and the minimum ψ' of the track and its number of hits; for $\bar{z}$ as a function of $\cos\theta$.

In case of the wire-gain correction such a parametrisation based on a test data sample is inadequate, because the gains of different wires are totally independent and therefore global parameters to describe the uncertainty of the wire-gain correction cannot exist. In addition, the wire gains show long-term variations. Therefore one would need to work with different test samples for different data taking periods. Consequently, the calculation of the uncertainty using 100 randomly selected sets of hits is done individually for each track.

The end-plate effect correction is very sensitive to the particular hit selection. Details about the proper uncertainty calculation for this effect can be found in App. H.

- **limitations of the fit function:**
  In some cases, the fit function describes the data only within a limited range of its parameters. In rare cases the parameters of a track can be outside the stable fit range. If this happens, the fit function has to be extrapolated. Of course, such an extrapolation increases the risk of deviations from correct values; therefore the uncertainty of the corresponding correction is increased. It is difficult to predict this kind of uncertainty properly.

  This kind of uncertainty is given for the neighbourhood correction for tracks with a very high number of neighbours. In case of $n_w > 0.25$ one observes a small overcorrection of the neighbourhood effect (for the definition of n_w see Eqn. 4.10). This could be compensated for by using a fit function other than a linear fit for the distribution in Fig. 4.47, but a fit with a higher degree of freedom increases the risk of fitting fluctuations in statistically lowly populated ranges. It is safer to keep the linear fit and to treat the deviation for high values of n_w as an increased uncertainty. The size of this uncertainty was assumed to be the difference between a linear and a quadratic fit to the distribution of $\Delta dE/dx(n_w)$ for the full HERA I and HERA II tuning data sets.

In this section the calculable part of the relative error of dE/dx_{meas} is named Σ_{rel}. The capital letter Σ is chosen in this section to distinguish this error from the total uncertainty σ of the track's dE/dx_{meas}; Σ_{rel} constitutes only a part of σ.

2. **unpredictable uncertainties:**
   There exist also uncertainties which cannot be predicted because the information needed for measuring their size is unavailable.

   - If for example the parameters used for a correction are correlated with the corrected effect, but do not fully describe the effect, the resulting correction can only partially compensate for the effect. It is impossible to quantise this uncertainty: as soon as one finds a distribution which shows the remaining part of an effect, one can use this distribution for an improved correction.
   - Another source of uncertainties are effects, which are yet unknown. As one is not familiar with their parameter-dependencies, one cannot provide an estimate for them.

Some of the corrections depend on identical parameters, so one has to be careful not to double-count errors. The most prominent example for this is the global scale of dE/dx. This scale is part of the fit functions for the corrections of the threshold effect, the space-charge effect, and the drift-time effect, but it is applied only for the latter; in the other two

cases, the global scale is a free fit parameter; it exists only to ensure a stable convergence of the fit. As its correction is done within the drift-time effect correction, the fit functions for the threshold effect and the space-charge effect are transformed into correction functions with the constraint not to touch the global scale. Therefore the fraction of the variance of the fits, which corresponds to their scale uncertainty, has to be removed from the correction-function uncertainty. This is done by subtracting the fit variance for parameters which represent the range of unaffected tracks[10] from the variance for the whole parameter range.

For the superlayer factor the used reference (tracks without fit error) are tracks with hits in all layers. As the nine-superlayer tracks are the dominant fraction of all tuning tracks, this is consistent with the fact, that the global scale is determined by the drift-time correction.

The user of dE/dx measurements is interested in the uncertainties of the corrections depending on commonly used track parameters, e.g. $\cos\theta$. Such distributions allow to get a feel for dangerous kinematical ranges for dE/dx measurements. The $\cos\theta$-dependence (Fig. 4.83) shows some interesting features. For tracks almost parallel to the signal wires, the saturation correction can be very huge. In this case, the uncertainty of the correction is large as well. Nevertheless, the mean uncertainty of all tracks is very small, because most of the tracks are not at all affected by this correction. Also the end-plate-effect correction shows a strong $\cos\theta$-dependence: tracks with $\cos\theta \approx 0$ cannot reach the end-plates, therefore there is no end-plate effect, no correction for this effect, and no uncertainty for the correction.

The threshold-effect and space-charge effect corrections have their biggest uncertainties for tracks with $\cos\theta \approx 0$. These tracks are affected most by these corrections. Especially for the space-charge effect one can find a large fit-uncertainty for small values of x_t (as defined in Eqn. 4.27), which causes a rather large Σ_{rel} at $cos\theta \approx 0$ for all tracks.

Some of the distributions display characteristic structures. These have two main sources:

- Different data taking periods are tuned separately, thus the uncertainties of the fits differ between different data sets. This kind of differences is very pronounced for the space-charge effect correction: The uncertainty for $\cos\theta = 0$ is almost completely given by the fit uncertainty, which differs for this range by a factor of 2 for high statistics data samples and even more so for the low statistics data sets from the year 2000 with water. The different data taking periods cause separated bands in Fig. 4.83.

  The pronounced bands in the drift-time correction can also be traced back to the different data taking periods. The well separated band with a very high uncertainty of $\approx 6\%$ corresponds to the very short first data-taking period with water in the year 2000.

- The threshold-effect correction is tuned with a distribution based on dE/dx_{exp} but applied to dE/dx_{meas} of single tracks. Consequently the dE/dx_{meas}-resolution itself propagates into the uncertainty of the threshold effect correction. As $\sigma(dE/dx_{meas})$ strongly depends on the number of used hits, this dependence is also visible in Fig. 4.83: the different bands represent different numbers of used hits.

[10] The used parameter values for unaffected tracks are $s_d = 1000$ for the threshold effect and $x_t = 10$ for the space-charge effect.

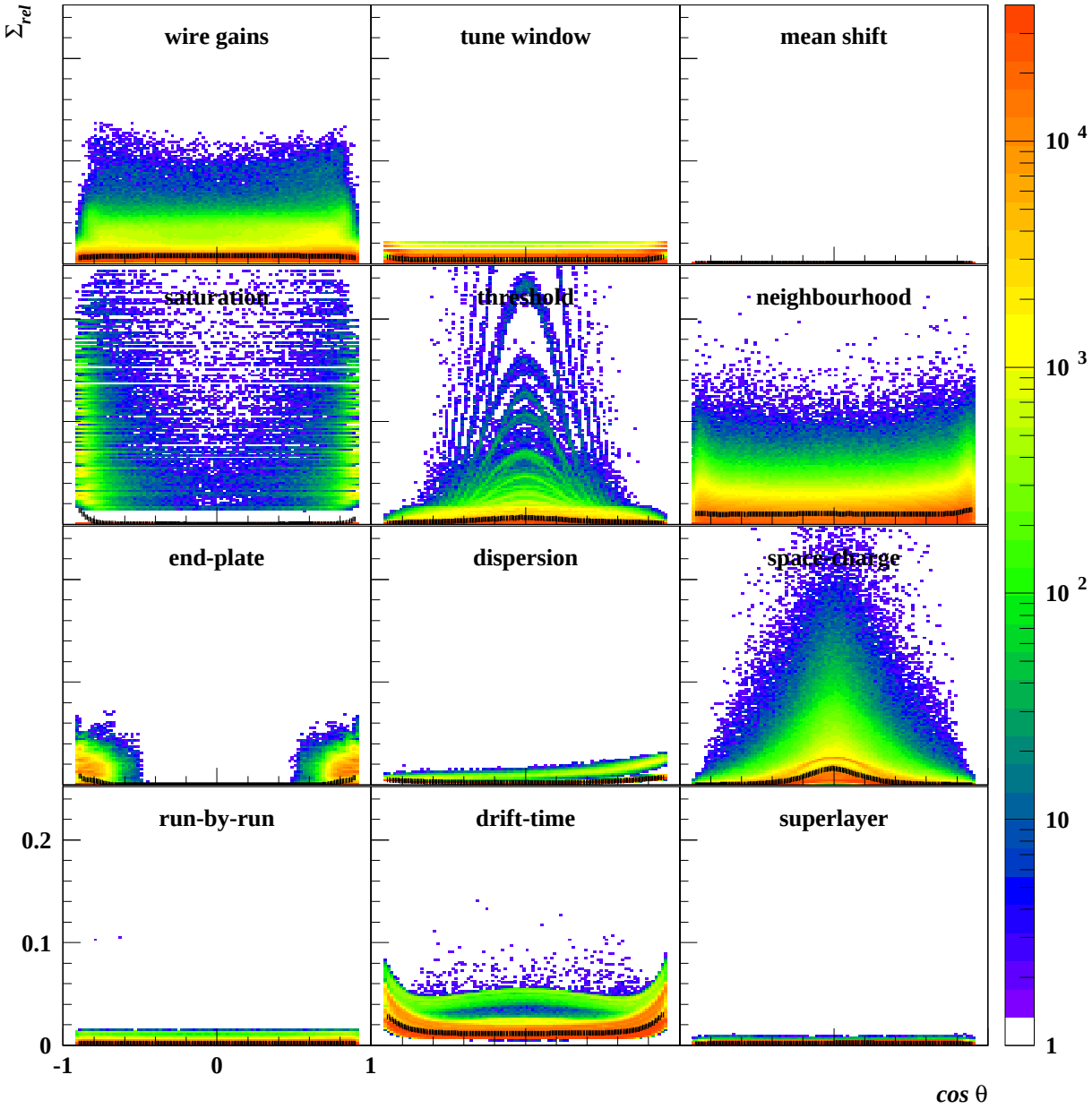

Figure 4.83: Relative uncertainties of the partial corrections versus $\cos\theta$. The colours represent the frequency, the black lines are the mean values of the distributions. All HERA I and HERA II data are shown together.

Furthermore Fig. 4.83 shows two other important features. The mean uncertainties are always small, thus for the majority of the tracks the applied correction methods are well under control. But there are some tracks with really huge uncertainties of 20% or more. For such tracks, the dE/dx measurement has to be taken with great care, in most cases one might decide to reject such tracks from the analysis.

A remark on the uncertainty of the drift-time effect correction is in order: The uncertainty is at a level of more than 1% for all tracks, because the correction of the global scale of dE/dx is part of the drift-time effect correction, which by itself already contains an error of $\approx 1\%$.

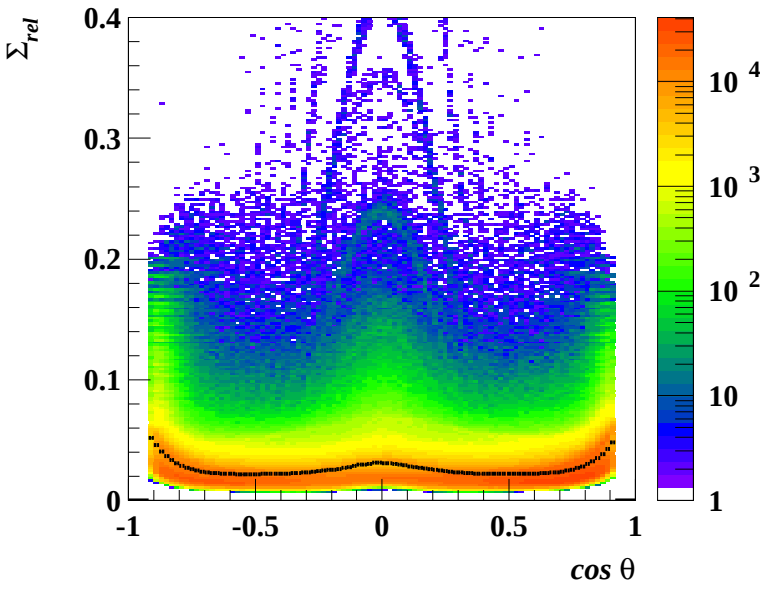

Figure 4.84: Relative uncertainty of the full correction versus $\cos\theta$. The colours represent the frequency, the black line is the mean value of the distribution. All HERA I and HERA II test data samples are shown together.

The uncertainties of the different corrections can be combined to an uncertainty of the complete correction (Fig. 4.84). As already seen for the partial corrections, the mean uncertainty is largest for forward and backward tracks and also for transversal tracks. The uncertainty of the corrections rises to a level of $\approx 4\%$ in these ranges; for the ranges inbetween the uncertainty is $\approx 2\%$. For a small fraction of all tracks the uncertainty can be much larger.

The orthogonal component to $\cos\theta$ is the transverse momentum p_t. The dependence of the uncertainty of partial corrections on p_t is shown in Fig. 4.85. For low p_t the wire gain correction suffers from a bad resolution of ϕ. An increased probability to reconstruct the track in the wrong CTD-cells also increases the uncertainty of the wire-gain correction for such tracks. Only for very low p_t the resolution improves again; these are tracks, which pass only a small number of layers. As the biggest wire-gain corrections happen for cells in the outer part of the detector (Fig. 4.27), for such tracks the correction is very stable.

The saturation correction shows a band around $p_t = 0.5\,\text{GeV}$. These are protons with very high signals and therefore very high saturation corrections. One can also find an increased mean uncertainty for $p_t \approx 6\,\text{GeV}$, caused by DIS-electrons (high dE/dx tracks predominantly in backward direction). The threshold effect correction shows its biggest uncertainty in the p_t range of pions with minimum ionisation. For low p_t, the neighbourhood effect correction has its biggest mean uncertainty, because in the innermost superlayers the probability for neighbourhoods is higher than in the outer part of the CTD.

For the space-charge-effect correction one observes some bands at different p_t with very high uncertainties. They correspond to the high dE/dx regime of different particle types. Further investigation proved, that only the 2003/2004 data set causes these high uncertainties; for the other periods similar bands stay below $\Sigma_{rel} = 0.1$. The fit for the space-charge-effect correction has a higher uncertainty for the 2003/2004 data set than for the other periods (see Sect. 5.1.3.2). The increased fit uncertainty is mostly pronounced for tracks with high dE/dx values and therefore a strong space-charge effect. Figure 4.83 offers the same conclusion: the highest uncertainties for the space-charge-effect correction can be found at $\theta = \pi/2$.

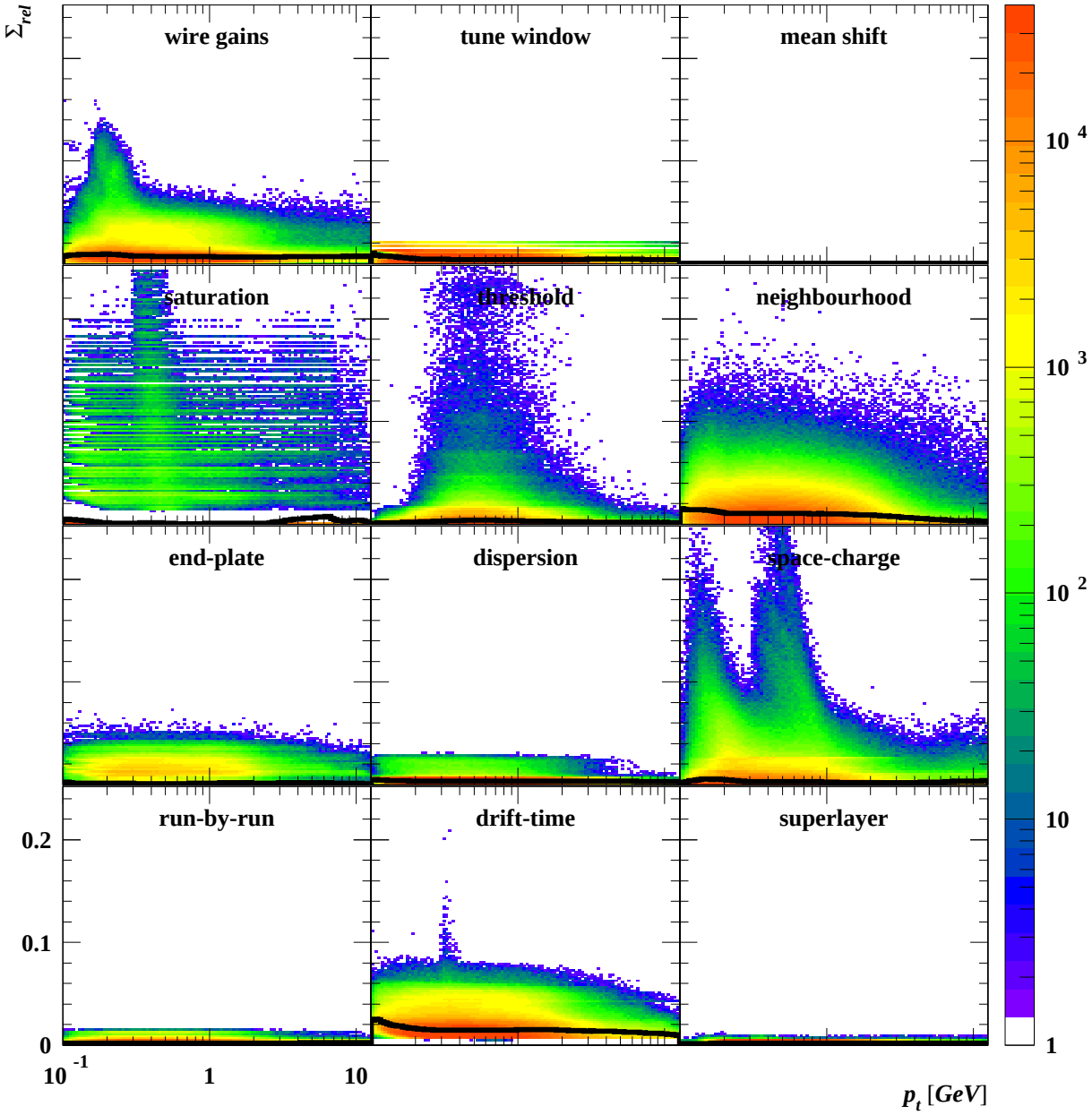

Figure 4.85: Relative uncertainties of the partial corrections versus p_t. The colours represent the frequency, the black lines are the mean values of the distributions. All HERA I and HERA II test data samples are shown together.

Also the drift-time effect correction shows slightly higher uncertainties for the lowest p_t-regime: big variations of ψ' within one track increase the uncertainty due to the truncated mean hit-selection.

The uncertainties of all corrections are summarised in Fig. 4.86. The sources for the uncertainties are separated into fit-, parameter- and truncation-hit-selection uncertainty. Large uncertainties are almost completely given by fit uncertainties. For $\approx 1\%$ of all tracks this uncertainty is larger than 10%. For the majority of all tracks a Σ_{rel} of about 2.5% is found; the fit-uncertainty and the parameter-uncertainty are of almost identical size, whereas the selection-uncertainty for the truncated mean calculation contributes with

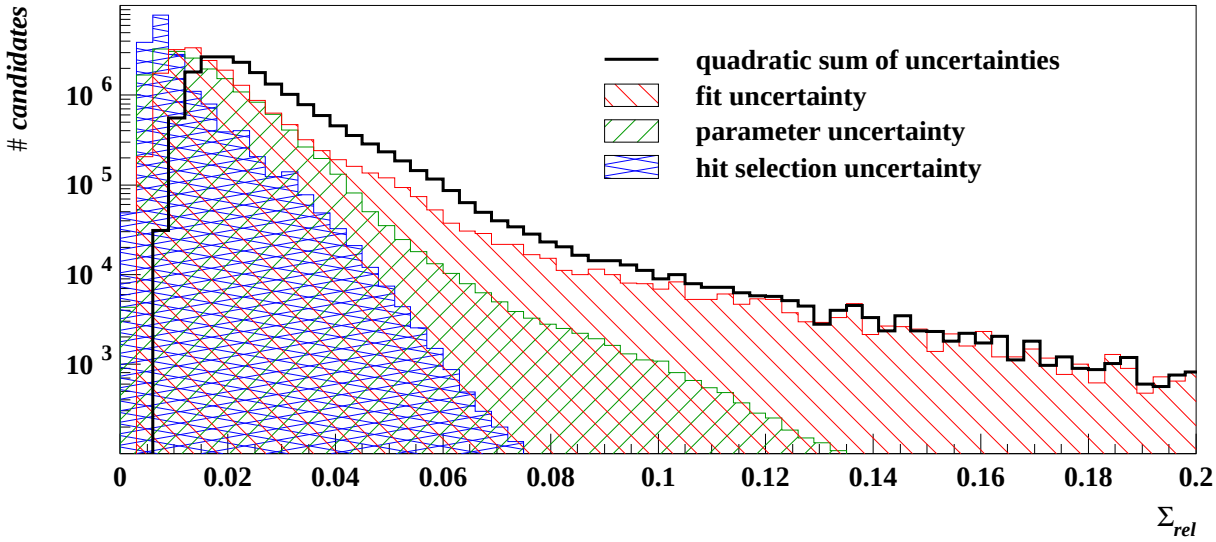

Figure 4.86: Distribution of Σ_{rel}, separated into fit-, parameter- and truncation-selection uncertainty. All HERA I and HERA II test data samples are shown together.

$\approx 1\%$. Even if the latter contribution is the smallest, one should keep in mind that this fraction of the uncertainty would completely disappear if one had access to single hit information.

4.4 The BETHE-BLOCH prediction for the ZEUS CTD

For several of the corrections introduced in Sect. 4.3.1 a prediction for the energy loss $dE/dx_{exp}(\beta\gamma)$ is mandatory. In this section the procedure to find this function will be described. Furthermore, the stability of the measurement against an inadequately identified measured dE/dx_{exp} will be determined.

The general concept to find a proper dE/dx prediction is the following:

1. First one has to use a 'starting' prediction. This is available from measurements done by OLIVER M. KIND [6] using HERA I data and ROBERT ZIMMERMANN [55] using HERA II data.

2. Based on a given dE/dx_{exp} tuning parameters as described in Chapter 4.3 are generated.

3. Applying these tuning parameters, a distribution of corrected dE/dx values versus $\beta\gamma$ is generated with test data samples. A parameterisation of this distribution according to Eqn. 3.3 is found by a fit.

4. This parameterisation of the BETHE-BLOCH curve is an improved dE/dx_{exp}.

   Then one returns to step 2.

5. After a few iterations the change between two iterations of dE/dx_{exp} becomes negligible. The result of the last fit of the BETHE-BLOCH curve is the optimum dE/dx_{exp}.

Several conditions have to be fulfilled to avoid instabilities in this iterative procedure:

- Two constraints have to be applied to the Bethe-Bloch fit: Equation 3.3 as well as the dE/dx-correction algorithm allow for linear transformations of dE/dx (a linear transformation of dE/dx in Eqn. 3.3 corresponds to a linear transformation of the parameters p_1 and p_2; the same freedom has been shown to exist for the dE/dx-corrections algorithm in Sect. 4.3.1.10). If within an iterative procedure two parts have an identical degree of freedom, the corresponding parameters can adopt any value. For example, if the dE/dx prediction and the corrections correspond well to each other, one finds exactly the same correspondence if one scales both the prediction as well as the correction, or if one adds the same offset to both. Consequently, two constraints are mandatory to cancel this freedom. The most obvious constraint is to fix the minimum of the prediction-curve to 1 mips to respect the definition of dE/dx_{mips}. The second fix-point is the value of the dE/dx prediction at the FERMI plateau. Without corrections this plateau is found to be at 1.4 mips. The same value is used for the prediction, allowing direct comparison between dE/dx measurements before and after corrections.

- In order to build up the distribution of dE/dx_{corr} versus $\beta\gamma = p/m$ one needs to know the mass of the contributing particles. The data samples as introduced in Chapter 4.1 are a good choice [11].

[11] The sample $\rho^0 \to \pi^+\pi^-$ is a sample with high statistics and low purity. To avoid systematic shifts of the fit due to wrongly identified candidates in the sample, this sample is not applied for the BETHE-BLOCH fit.

- A well-estimated fit requires data points for a huge range in $\beta\gamma$, covering all characteristic ranges of the BETHE-BLOCH curve (β^{-2}-dominated part, minimum, logarithmic rise and plateau range). The test-data samples fulfil this condition and cover the full range.

- The tuning samples should not have too much influence on the BETHE-BLOCH fit to avoid artificial shifts in the BETHE-BLOCH prediction due to systematic shifts in these samples. For example one finds a slight tendency for electrons and especially for positrons from photon-conversions to have a too high measured dE/dx value. If these candidates contribute to the BETHE-BLOCH fit, the resulting curve tends to higher values in the $\beta\gamma$-range of the photon-conversion sample compared to the dE/dx prediction used for the same iteration. Consequently, the prediction in this range will be shifted to higher values in the next iteration. The photon conversion sample will again overshoot the prediction in that iteration, causing once more a shift of the BETHE-BLOCH fit to higher values. This yields a loop-back of the photon conversion sample to its own corrected values. After several iterations the resulting BETHE-BLOCH curve will be dominated by the systematics of the photon conversion sample.

  To avoid such a loop-back, the photon-conversion sample is not used for the BETHE-BLOCH fit. The other tuning samples are not so critical and can safely be used for this fit. The pion tuning sample is located about the minimum of the BETHE-BLOCH curve. As mentioned before, this minimum is constrained to be 1 mips. Due to this constraint the pion tuning sample cannot systematically bias the fit result. For the DIS-electron sample and the ($J/\psi \rightarrow e^+e^-$)-sample the situation is similar; both samples lie close to the FERMI-plateau which is fixed to 1.4 mips.

The free choice of the plateau-level prompts the question, wether this constraint forces systematic errors for the dE/dx measurement. If one keeps the minimum of the dE/dx prediction at 1 and varies the value for the plateau, one compresses or stretches the whole dE/dx distribution of the data, i.e. one can 'tune' to any value for the mean spread (the resolution) of the data. The only application of dE/dx measurements is the separation between particle types, which is determined by the difference of mean dE/dx values for different particle types normalised to the resolution of the dE/dx measurement. As the previously mentioned 'stretching' affects nominator and denominator in the same way, the separation power is independent of the choice of the FERMI-plateau level.

As particle identification is the only application of dE/dx measurements one concludes, that the free choice of the value of the dE/dx prediction in the plateau is not critical. Therefore it is most convenient to keep the plateau level unaffected by the corrections.

The situation is different if one measures the resolution of the dE/dx measurement, calculated to be the mean dE/dx value over the spread. If one fixes the minimum of the BETHE-BLOCH curve at 1 mips and moves the FERMI-plateau level, the absolute resolution scales with the difference between the plateau-level and 1 mips. In first order the same holds for the relative resolution. As the correct plateau-level is not measurable with the given resources, the 'traditional' resolution is **not** a good variable to measure the power of the dE/dx measurement.

A much more appropriate observable for this issue is the separation power between particle

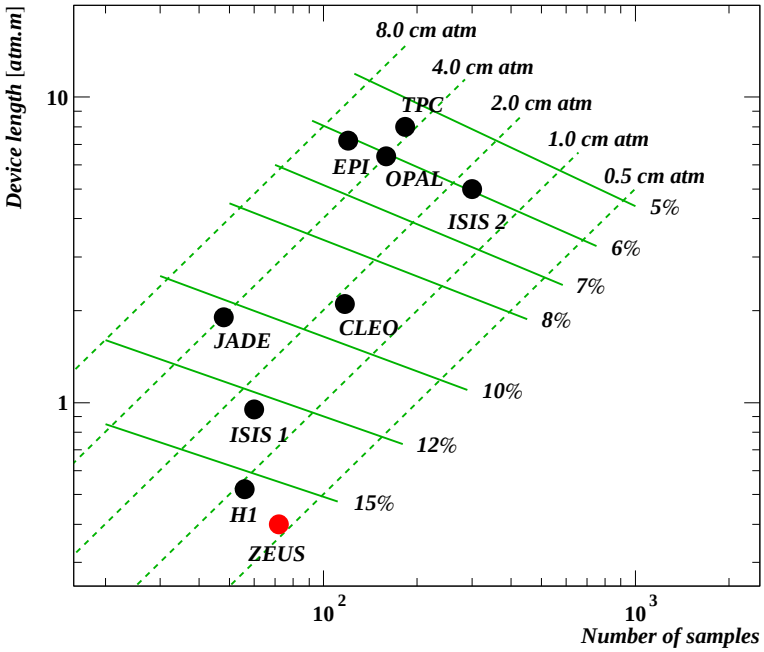

Figure 4.87: Ionisation resolution (% FWHM) contours for argon with $\beta\gamma = 100$, as calculated by ALLISON and COBB [46]. The device length per cell is indicated with dashed lines. The dots mark the expected resolution for several detectors.

species. [12]

Anyway, theoretical predictions for drift chambers comparable to the ZEUS CTD expect higher values for the FERMI-plateau than used at ZEUS. For example, ALLISON and COBB predict a FERMI-plateau at 1.55 mips for a chamber operating with 80% Argon and 20% CO_2 at normal density [46]. ALLISON and COBB also give a prediction for the expected resolution of a drift chamber depending on the number of samples (number of used hits) and the device length (distance for the ionising particle passing through the sensitive area). Taking the mean number of 55 hits for tracks passing all superlayers of the CTD and a mean track length of 50 cm for the particle passing through the sensitive volume of the CTD (the gaps between the superlayers are not counting to the sensitive volume), they predict a dE/dx resolution of 16% (see Fig. 4.87). This prediction is based on the assumption of a likelihood method to calculate dE/dx from single hit measurements. The truncated mean method as applied at ZEUS (see Sect. 2.5) is expected to yield a worse resolution. Furthermore, the theoretical prediction only takes into account the uncertainty due to the ionisation process within the sensitive medium. In a real measurement there are several other sources contributing to the total uncertainty, like the limited resolution of the readout chain or all the effects which have been introduced in Sect. 4.2. Nevertheless, the measured dE/dx resolution at ZEUS for tracks passing all 9 superlayers is of the order of 11-12% even without applying the dE/dx corrections introduced in this thesis. If one would fix the FERMI-plateau at 1.55 mips, the measured resolution of the ZEUS CTD would be of the order of 16%, which matches with the prediction in [46]. One concludes, that there are clear hints to find the correct FERMI-plateau for the ZEUS CTD around 1.55 mips.

The procedure of dE/dx tuning permits any value for the plateau; for the issue of particle

[12] For the H1 detector the situation is similar to ZEUS. The jet chambers of H1 are operating at atmospheric pressure using a mixture of equal amounts of Argon and Ethan with a 0.5% admixture of water, which leads to similar conditions for the BETHE-BLOCH curve as for ZEUS. The parameterisation used for the BETHE-BLOCH curve in the H1-collaboration leads to a FERMI-plateau at 1.3 mips. For comparing the commonly used resolution of the dE/dx measurement between these two detectors, one consequently has to multiply the H1-value by a factor of 4/3.

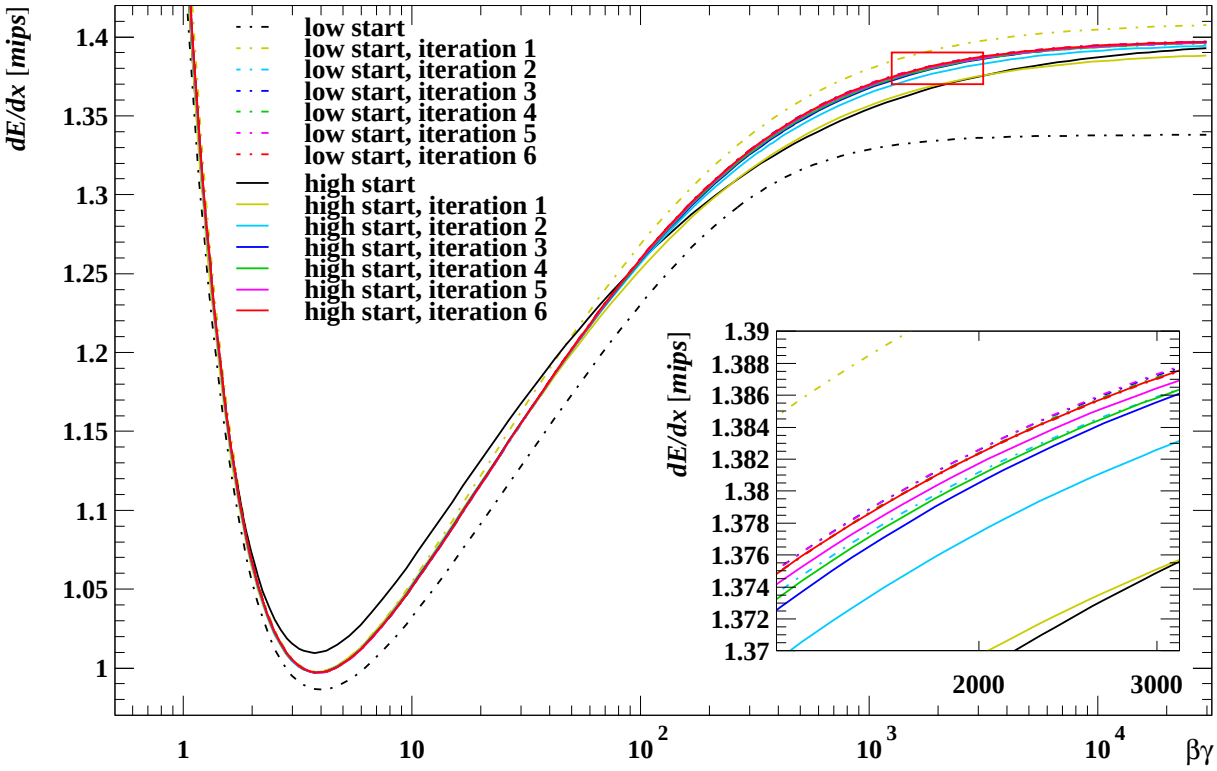

Figure 4.88: Iterations of fitted BETHE-BLOCH parameterisations. The high and low starting curves are intermediate results from [6] and [55]. The boxed area is shown enlarged in the insert plot. The shown curves are **not** normalised to a minimum of 1 mips and a plateau-level of 1.4 mips.

identification the choice of this value is irrelevant. As it is difficult to prove the reliability of the theoretical models (for example there are no predictions for the same gas mixture as used in the ZEUS CTD), it was decided to tune the dE/dx measurement without changing the plateau with respect to the status before corrections (at 1.4 mips).

In terms of the application of dE/dx measurements there are two different types of differences between the applied dE/dx prediction and the correct BETHE-BLOCH curve. The uncritical type are linear transformations, which have no effect at all on the particle identification. Transformations, which change the shape of the BETHE-BLOCH curve can also affect the particle identification. Therefore it is mandatory to find a proper function $dE/dx_{exp}(\beta\gamma)$ using the iterative method as mentioned in the beginning of this chapter.

The resulting BETHE-BLOCH curves are shown in Fig. 4.88. The curves are shown before normalisation to 1 mips and 1.4 mips in their minimum and plateau. The level and position of the minimum stabilises already after one iteration. Only the transition region between the logarithmic rise and the plateau shows changes of the order of 1% in the first iterations. Within 3 iterations also the shape and the plateau-level converges. Finally the 6^{th} iteration of the higher start parameterisation is used as the reference curve dE/dx_{exp}.

Investigating the changes of the BETHE-BLOCH curve between iterations convey this result to be correct at a level of a few tenth of a percent. In terms of particle identification this accuracy is even less critical: one compares the measured, corrected dE/dx value with

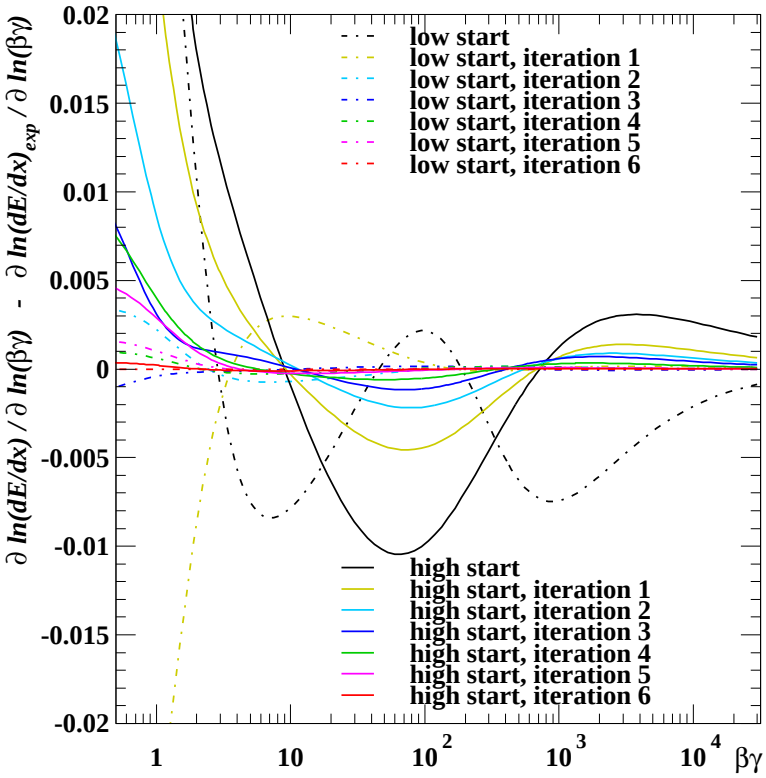

Figure 4.89: Logarithmic derivative of $dE/dx(\beta\gamma)$ minus the same quantity for the finally used dE/dx_{exp}.

the prediction. The correction algorithm itself forces the measurements to correspond to the prediction applied in the correction algorithm. Therefore in first order deviations between the applied dE/dx_{exp} and the correct BETHE-BLOCH curve are compensated. The remaining uncertainty due to the error of the applied dE/dx_{exp} scales with the difference of the slope in $\ln\beta\gamma$ between dE/dx_{exp} and the correct BETHE-BLOCH curve; the relative uncertainty scales with this slope divided by dE/dx. As the correct BETHE-BLOCH curve is not known the best accessible choice is to compare the slopes of the iterations with the finally used dE/dx_{exp}. The $\ln\beta\gamma$-related slope is given as the derivative $\partial(dE/dx)/\partial(\ln\beta\gamma)$, leading to the logarithmic derivative for estimating the relative uncertainty:

$$\frac{\partial\frac{dE}{dx}}{\partial(\ln\beta\gamma)} \Big/ \frac{dE}{dx} = \frac{\partial\ln\frac{dE}{dx}}{\partial(\ln\beta\gamma)} \quad . \tag{4.36}$$

In Fig. 4.89 the differences between the derivatives for the different iterations and the one for the optimum dE/dx_{exp} are shown. One finds big improvements with each iteration. In the range $\beta\gamma > 1$ the deviations for the last iterations are less than 0.1%, for $\beta\gamma > 2$ even less than 0.02%.

This final deviation has to be transformed into an estimate for the systematic uncertainty of the measured dE/dx in relation to dE/dx_{exp}. In a very conservative approach one can expect a coverage of 3 orders of magnitude in the momentum range for tracks measurable with the ZEUS CTD, corresponding to a coverage of ± 3.5 in $\beta\gamma$ for a fixed particle type (fixed mass). Assuming that the mean dE/dx of a whole sample is estimated well (at this point only the systematic influence of wrongly shaped dE/dx predictions on the result of the measurements is under investigation), the biggest expected systematic effect (for the highest and lowest achievable particle momenta) is expected to be 3.5 times the previously mentioned deviations of 0.1% and 0.02% respectively. One concludes, that this contributes neglibibly to the total uncertainty.

For $\beta\gamma < 1$ the deviations increase. Such small $\beta\gamma$ correspond to $dE/dx_{exp} > 1.5$ mips, a range, where the separation of particles due to their dE/dx is very clear, so that an increased uncertainty does not harm.

The quality of the iteratively fitted Bethe-Bloch curves is investigated in the direct comparison of the fit curves and the data samples. In Fig. 4.90 it is visible, that after the first iterations the data points are located closer to the prediction curve. Already after 2 iterations one cannot see any further changes.

The distributions shown in Fig. 4.90 only show that the mean dE/dx values for whole data samples do not change after some iterations. These plots do not test if the corrections react on the changed dE/dx prediction with instabilities, but keeping the mean values constant. This possibility is disproved by Fig. 4.91. For a subsample of all data the distribution of the correction factor c_i is shown versus the same factor for the finally used correction c_{final}. One observes this distribution to be very narrow already in the 2$^{\text{nd}}$ iteration, i.e. slight changes in the Bethe-Bloch curve for high iteration numbers systematically shift the corrections without causing big changes in the relative order (in dE/dx) between the tracks. This behaviour is also reflected by the numbers shown in the scatter plots (left column), which are the ratio of the RMS of the distribution projected to the main diagonal (fully correlated axes) divided by the RMS of the orthogonal projection (fully anticorrelated axes). This ratio quantises the size of the redistribution of the data samples due to the change of the prediction curve compared to the total size of dE/dx corrections. Small numbers for this ratio indicate, that changes in the prediction do not cause strong fluctuations within the correction algorithm. From the 3$^{\text{rd}}$ iteration on this ratio stays stable between 0.5% and 1%. The right column of Fig. 4.91 leads to the same conclusions. The ratio of the correction factors c_i/c_{final} is shown separately for the iterations. For the first iteration this ratio is still widely distributed with an RMS of 0.6%. For higher iterations this distribution is very narrow with an RMS less than 0.1%.

These test distributions show, that the iterative procedure to find the proper parameterisation of the Bethe-Bloch curve converges fast. The dE/dx corrections reproduce the applied prediction dE/dx_{exp} and react robustly on slight changes of this prediction function.

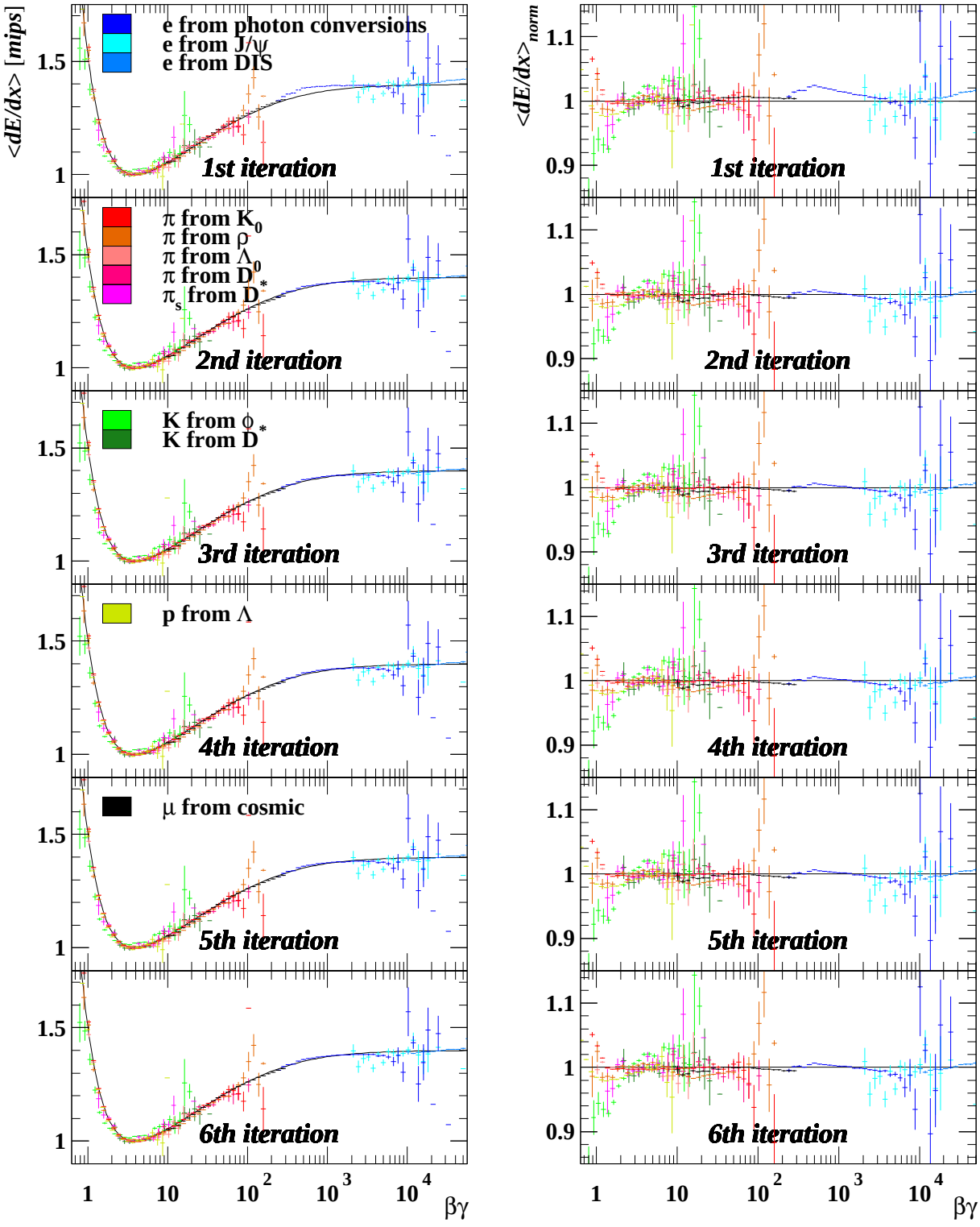

Figure 4.90: The profiles of dE/dx (left column) and dE/dx_{norm} (right column) of the data samples for the first 6 iterations of the BETHE-BLOCH fit, using the 'low start' as the initial BETHE-BLOCH curve. The fit functions are shown as curves, the different data samples are illstrated as data points. The samples not used for the fit (photon conversions and $\rho^0 \to \pi^+\pi^-$) are shown, as well.

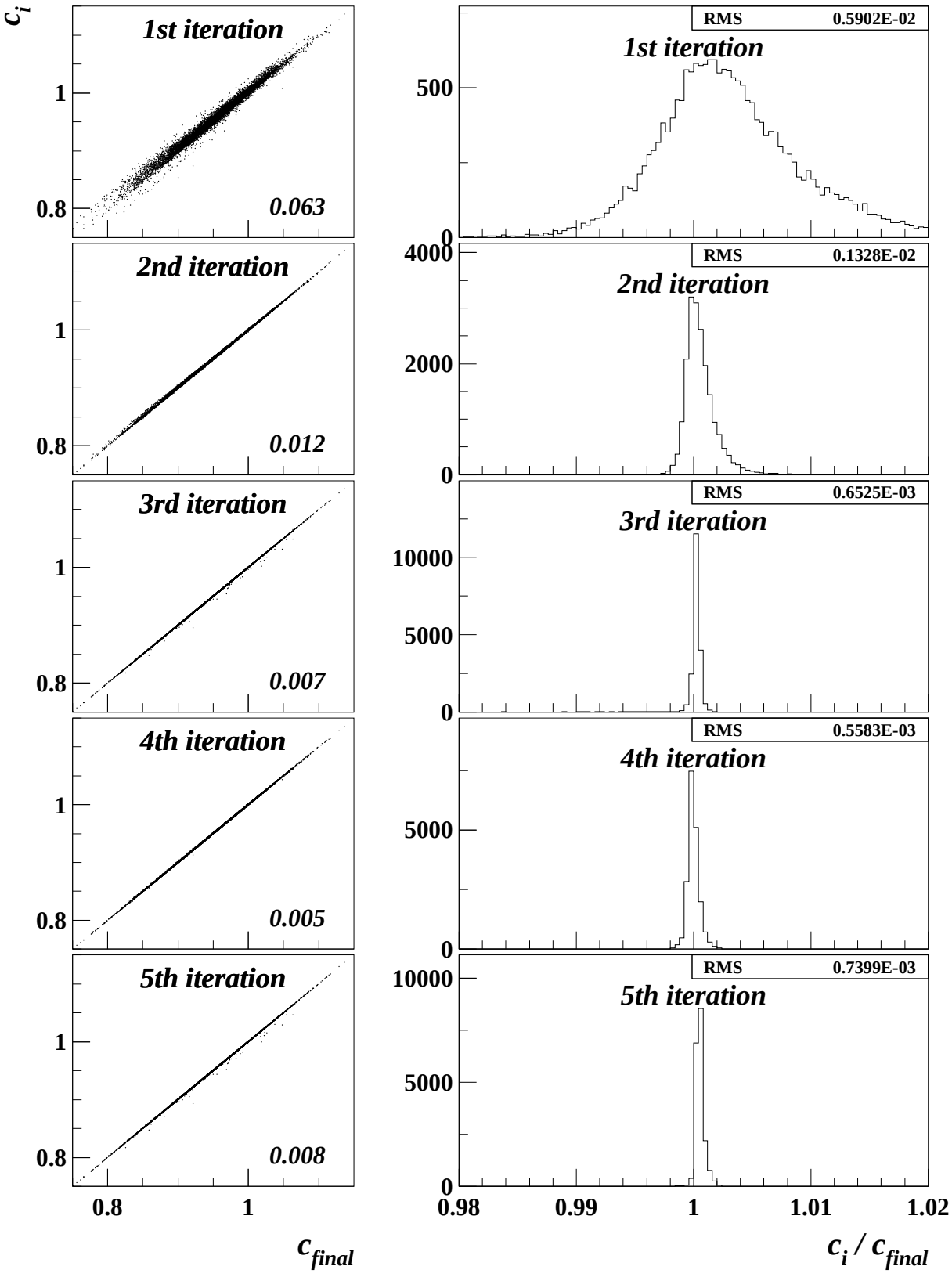

Figure 4.91: Left column: The correction factor c_i (combination of all partial corrections) versus the same factor calculated with the finally applied Bethe-Bloch curve dE/dx_{exp} separated for the iterations i of the Bethe-Bloch fit, using the 'low start' as the initial prediction curve. The numbers shown in the plots are the ratio of the RMS along the main diagonal (correlated axes) over the RMS in the orthogonal projection (anticorrelated axes). Right column: The ratio of the correction factors c_i/c_{final}. All data samples of a sub-period of 2005 data are shown in these plots.

Chapter 5

Results and discussion

With the full set of corrections now on hand their impact on the physics analysis of data will be explored. This investigation separates into three main tasks.

In the first section mean dE/dx values of tracks will be verified. Their systematic dependence on the particles species and its charge will be discussed. Differences between HERA I and HERA II data will be under investigation. The dependence on the data-taking periods will be checked in more detail.

The second section will focus on the dE/dx resolution. Its measurement as well as its improvement due to the dE/dx corrections will be shown. The sources for uncertainties are investigated and the total uncertainty is split into its main contributions.

In the third section a method how to use the dE/dx measurement for particle identification, based on a likelihood ratio method, is shown. This allows to estimate the achievable separation power of an identification method based on dE/dx values. Furthermore, tools for the scrutiny of likelihood ratios will be presented.

5.1 Properties of corrected data

To investigate the full set of corrections, besides the tuning samples also the other data samples (listed in Sect. 4.1.2) become important. They are not used for optimising the corrections themselves, and therefore offer an independent test for the correction procedures. As they differ in their kinematics and several other parameters, they also offer a testing tool for different parameters separately. Pions from K^0 decays are only used for tuning, if their momentum is in the range $400\,\mathrm{MeV} < p < 1000\,\mathrm{MeV}$. Therefore, the rest of this sample can be used as a test sample, too.

To properly compare plots before and after corrections, it is necessary to define, what is meant by 'before corrections'. It does not make sense to use FADC counts, because then the plots will be dominated by slowly changing parameters like the air pressure. Comparing different data taking periods based on FADC counts will be a weather report more than anything else.

The focus of this thesis are corrections of effects, which depend on parameters of single events or tracks. Therefore one does not want to get any reflection of slowly changing effects in the investigated distributions. Thus the status 'before correction' should already

contain the run-by-run corrections.

Furthermore, the comparison should show the amount of improvement gained by using the new corrections. The starting point for these corrections is the dE/dx measurement as given in the ADAMO table VCTRHL. Therefore the 'before correction' state has to contain the Phase I corrections.

We define:

- *before correction*
  dE/dx after Phase I reconstruction and with run-by-run corrections applied;
- *after correction*
  dE/dx after all shown corrections;

These definitions will be used throughout this chapter.

5.1.1 The $\beta\gamma$ dependence

The business of dealing with dE/dx is based on the assumption, that its $\beta\gamma$ dependence is given by a Bethe-Bloch curve. Figure 5.1 shows this dependence before and after corrections. In the upper plots all samples are shown together. It is hard to distinguish between them, but comparing Fig. 5.1 (a) and (b) gives the impression, that after correction all profiles are much closer together and also closer to the expected values than before. It is hard to see details in these plots because they contain many separate distributions. Thus it is necessary to reduce the contents of the plots to a manageable amount. This is done in different ways to emphasise different topics.

5.1.1.1 Combining samples of identical particles

One possible check is to combine the profiles of all samples for the same particle species in one profile. According to $\beta\gamma = p/m$ this way of combining preserves the relation between $\beta\gamma$ and p, i.e. the momentum dependence is kept in this combination whereas other influences on the samples are partially gone by using the mean values. This makes sense as many of the corrections shown in chapter 4.3 depend on the momentum of the tracks. The resulting plots (Fig. 5.1 (c, d)) pronounce the dependence of the corrected dE/dx on particle species and momentum.

Most obviously, before correction low-momentum electrons are too high in dE/dx and their $\beta\gamma$ dependence is rather different from the expected one. After correction this looks by far better. Few deviations remain, but to first order the data matches the expectation.

The largest deviations after correction are observed in the kaon samples for low momenta. The kaon samples suffer from reduced purity for low-momentum tracks. For example, taking $\beta\gamma \approx 1$ the expected dE/dx_{mips} is around 1.5. For kaons, the corresponding momentum is $\approx 500\,\mathrm{MeV}$. The background is dominated by pions. At the given momentum, they can be found at $\beta\gamma \approx 3.5$, which is almost in the minimum of the Bethe-Bloch curve: $dE/dx_{mips} \approx 1$. The background-contaminated profile then shows a mixture of signal at $dE/dx \approx 1.5$ and background at $dE/dx \approx 1.0$, which of course ends up somewhere in-between. Thus the deviations of the kaon samples for low $\beta\gamma$ do not indicate problems in the corrected dE/dx, but can be traced back to impurities in the test samples.

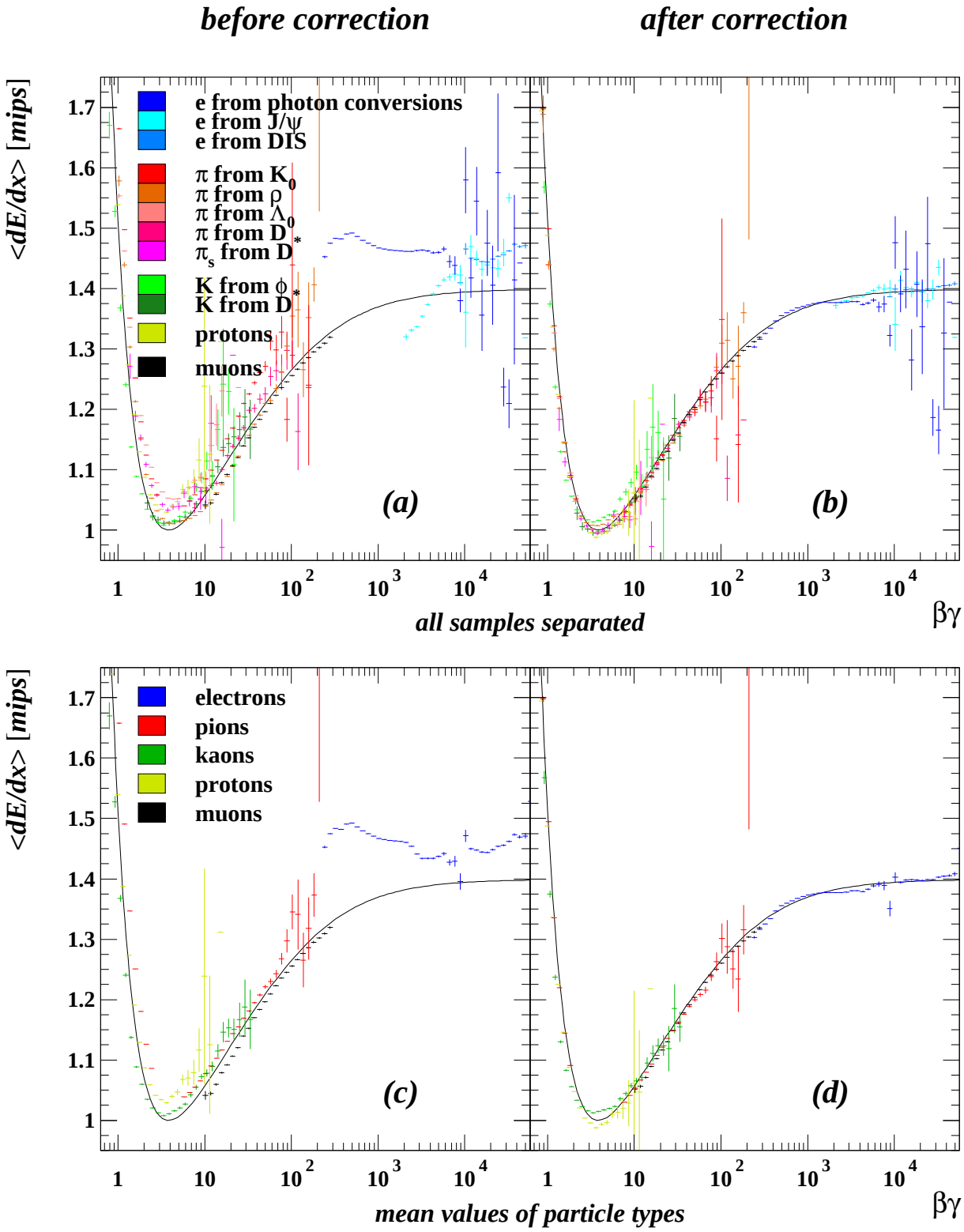

Figure 5.1: Profiles of dE/dx in bins of $\beta\gamma$ before (a, c) and after (b, d) correction. The upper plots (a, b) show all samples together, whereas in the lower ones (c, d) for the sake of clarity the profiles of identical particles are combined into one profile. The curve in the histograms illustrates the expected Bethe-Bloch curve.

5.1.1.2 Pions in the minimum of the Bethe-Bloch curve

A very interesting part of Fig. 5.1 (a, b) is the area close to the minimum of the Bethe-Bloch curve. Restricted to the pion samples this is shown in Fig. 5.2 (a, b). The restriction to the pion samples ensures, that for a given $\beta\gamma$ all samples are taken with the same track momentum. Therefore any momentum dependence should show up in all samples simultaneously.

Before correction, all other samples have a higher dE/dx than the $\rho \to \pi^+\pi^-$ sample. This can be traced back to the neighbourhood effect. As the ρ-decay sample is an exclusive one, it is not at all affected by neighbourhoods whereas the other samples suffer from this effect. The neighbourhood effect in terms of a pile-up effect typically increases the measured dE/dx, so all other samples end up at too high values. After correction, these differences are gone and the samples lie almost perfectly on top of each other. This is a really stringent test for the quality of the applied corrections. Remember, that only the pions from K^0 decays in a small range about the minimum of the Bethe-Bloch curve were used for tuning. So almost all data points shown in this plot are independent test data.

The plots also show, that for momenta below the minimum of the Bethe-Bloch curve, the expectation does not perfectly describe the data. The data points are clearly below the expected Bethe-Bloch curve.

About the ρ-sample one should remark, that close to the minimum it shows a kind of bump. Its source has not been investigated in detail. Most probable it is caused by the admixture of wrongly identified particles in the sample (the contamination is $\approx 1.8\%$). In this momentum range, particles from other species have a higher dE/dx than pions, leading to an increase of the mean dE/dx of the sample.

5.1.1.3 Electron samples

The electron samples are shown in Fig. 5.2 (c, d). They are of special interest, as they are used for tuning. Furthermore, without corrections the photon conversion sample shows the strongest deviations from the Bethe-Bloch curve and the mismatch between the different electron samples is much larger than for the other samples.

Before corrections, first of all the electrons from photon conversions show much too high dE/dx values and a $\beta\gamma$ dependence very different from the expectation. A possible source for this is the neighbourhood effect, as the two electrons from a conversion typically are their own neighbours for the innermost layers. Furthermore, photon conversions prefer to happen in busy events, as they need a photon most often generated in a π^0 decay. In high multiplicity events low momenta (for which the excess compared to the expectation is biggest) are more probable as more particles have to share the total momentum available.

Even after applying the corrections, in the lowest accessible momentum range a bump is left in the photon conversion distribution. Several studies were conducted to find its origin and to keep it under control [54]. The reason for the existence of this bump is not fully understood; but there are hints, that it is related to very small transverse momenta. The range of this bump corresponds to lowest transverse momenta, which are so small, that the tracks cannot leave the CTD in radial direction due to their curvature. It cannot be tested, if this problem only exists for electrons. Other particles with such small momenta

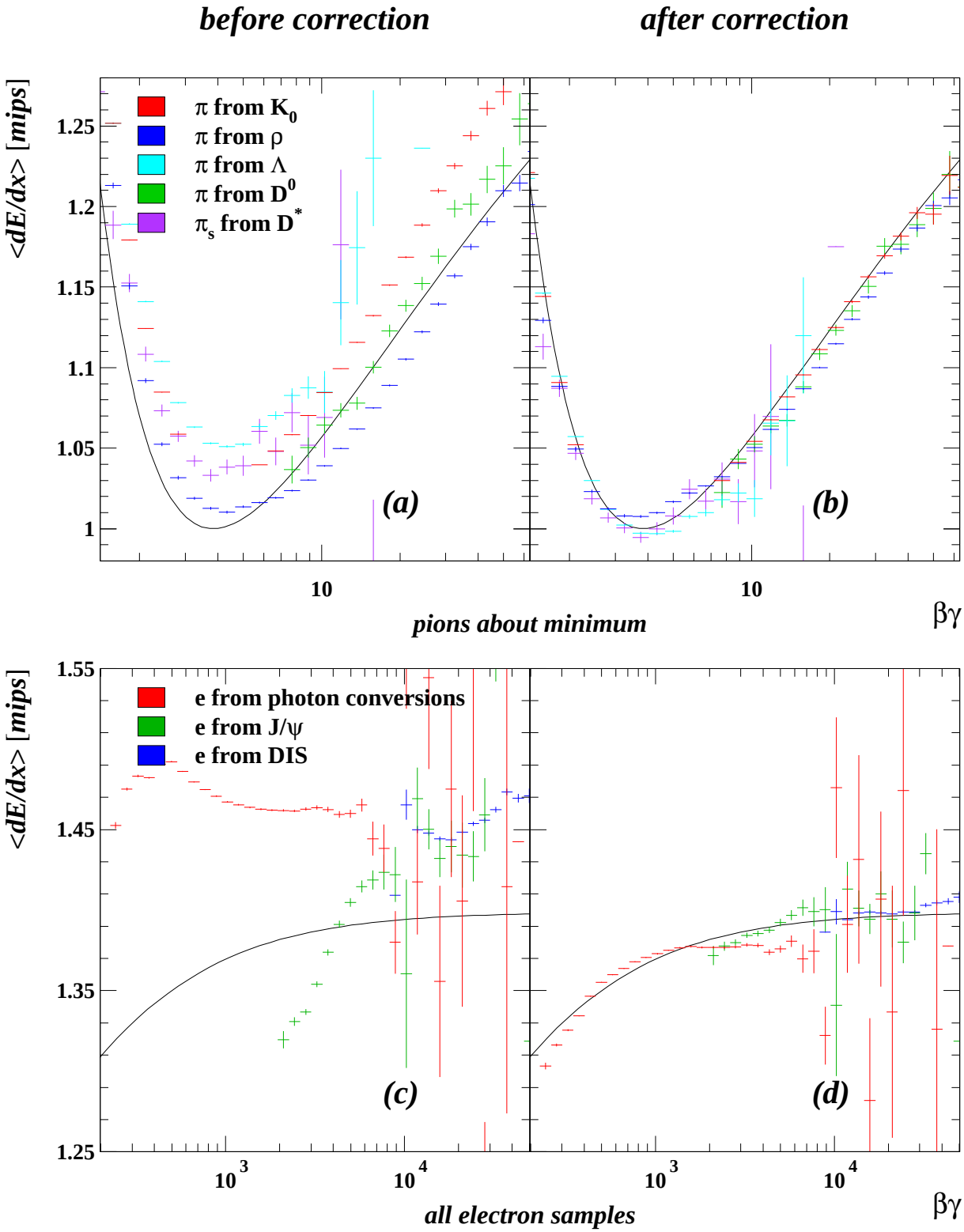

Figure 5.2: Profiles of dE/dx in bins of $\beta\gamma$ before (a, c) and after (b, d) correction. In the upper plots (a, b) only the pion samples close to the minimum of the BETHE-BLOCH curve are shown, whereas the lower ones (c, d) show the electron samples. The curve in the histograms illustrates the expected BETHE-BLOCH curve. In the pion samples, the K^0 candidates in the range $400\,\text{MeV} < p < 1000\,\text{MeV}$ corresponding to $2.9 < \beta\gamma < 7.2$ are used for tuning. The other data points shown are test samples. The electron samples are used for tuning, too.

end up on the strongly falling part of the BETHE-BLOCH curve. It has already turned out, that in this range the expectation curve is not so well settled. Nevertheless, this deviation shows, that the low transverse momentum range contains problems which are not understood. Consequently, for tracks with $p_t < 180\,\mathrm{MeV}$ the dE/dx measurement can only be used conditionally.

Before corrections, the $J/\psi \to e^+e^-$ sample shows a much too strong slope for the lowest accessible momenta. This is traced back to the combination of the space-charge effect and the way of selecting this sample. One of the selection cuts was a minimum on the transverse momentum of the electron tracks of $p_t > 900\,\mathrm{MeV}$. The lowest accessible momentum therefore is $p = p_t = 900\,\mathrm{MeV}$, which corresponds to $\theta = \pi/2$. This is the θ range, for which the space-charge effect has its maximum. So the lowest J/ψ bins in Fig. 5.2 (c) are filled only with tracks with a very high space-charge effect, which always reduces the measured dE/dx. With increasing $\beta\gamma$ the accessible θ range increases and therefore the influence of the space-charge effect on the profile mean value decreases. As Fig. 5.2 (d) shows, after correction the J/ψ data points follow the expectation very well.

At this point it should also be remarked, that the bump in the electron profile around $\beta\gamma \approx 6000$ in Fig. 5.1 (c) is caused by the combination of different samples. In this range, the photon conversion sample dies out and the profile is dominated by the J/ψ sample, which without correction lies at much lower dE/dx values.

5.1.1.4 Summary of the $\beta\gamma$ dependence

After corrections the dE/dx measurements confirm the $\beta\gamma$ dependence. This is not the case before corrections (see the photon conversion sample). The most important result is, that **after corrections the profiles of all test samples lie on top of the expectation with an accuracy of 1%**. This shows, that systematic uncertainties due to different track and event topologies in the different test samples are almost completely removed. This result is of extremely high importance in the application of dE/dx measurements in a physics analysis.

As an example take the search for semileptonic electrons. In a typical approach, first of all some cuts are tuned using electron-enriched and electron-depleted samples. Such distributions will also be used for efficiency and acceptance studies. In a second step the final selection will be done. The acceptance will be used to extract cross sections. Now the problem shows up: if the typical kinematics or event topology of the final sample differs from the sample, which is used to calculate the acceptance, the systematic dependence of dE/dx on kinematics and topology will also be reflected in the calculated acceptance. This means, the acceptance used to calculate the cross section is systematically wrong. It is almost impossible to quantise this systematic effect as long as it is not understood in detail, on which parameters the systematics in the dE/dx measurements depend and what this dependence looks like. However, if the dependence is gone, there is no risk left in such an application.

This is exactly what this section shows: after correction, in the $\langle dE/dx \rangle$ measurement no dependence on the different test samples (different topologies) is left. In other words, the dE/dx corrections offer the possibility to use dE/dx measurements for physics analyses.

5.1.2 Charge dependence

Several former analyses found a difference in the measured dE/dx between positively and negatively charged tracks [25, 5, 56]. In Section 4.3.1.10 this was traced back to a dependence of the dE/dx measurement on ψ'. It is the main task of the drift-time correction to compensate this dependence, so one should expect, that after applying these corrections, the charge dependence is gone or at least strongly reduced. Figure 5.3 shows, that before corrections positively charged tracks typically end up at higher dE/dx values than negatively charged ones. This difference is biggest for small track momenta. Especially for photon-conversion electrons one can find differences of more than 0.1 mips. After corrections, the differences have mostly disappeared. Only for very low-momentum tracks a difference of up to 0.02 mips is left. Figure 5.3 (f) shows, that this difference is really momentum dependent and not $\beta\gamma$-dependent, as it can be found for each particle type at its lowest $\beta\gamma$- ($\sim$ lowest p) range.

Another interesting check is the relation between the charge dependence of the dE/dx measurement and the $\bar{z}$ of the track. To first order this checks the dispersion correction, which depends strongly on $\bar{z}$. This correction depends on the signal height, which is correlated with the charge of the particle. Furthermore, this relation is affected by any other correction, that depends on the signal height, as there are the space-charge-effect correction, the threshold-effect correction and the drift-time-effect correction.

A possible way to check this relation is to inspect the difference $\Delta_\pm$ of the measured $\langle dE/dx_{norm}\rangle$ for positively and negatively charged tracks in bins of $\bar{z}$ as displayed in Fig. 5.4. The advantage of the variable $\Delta_\pm$ is the cancellation of all charge-independent influences on dE/dx_{norm}.

Before correction one finds a strong $\bar{z}$ dependence of $\Delta_\pm$. It is small in the centre of the CTD and rises towards the end-plates. In the range, where the composition of the data samples changes from barrel- to end-plate-tracks, $\Delta_\pm$ becomes smaller again. Once more one can see, that the measurement for positively charged tracks typically creates higher signals than for negatively charged tracks and $\Delta_\pm$ is larger for the electron sample than for the pions. The charge-dependent difference in $\langle dE/dx\rangle$ amounts up to 7%; it varies by $\sim 4\%$ depending on $\bar{z}$.

After correction, $\Delta_\pm$ is at 0 with a variation of up to 1% in all cases. This means, the sample dependence, the $\bar{z}$ dependence and the charge dependence are reduced to the 1% level.

5.1.3 Variation within different data-taking periods

Investigating the variation of the dE/dx-measurement corrections with time allows to estimate the stability and reliability of the correction algorithm. One has to distinguish between two different 'time scales': The modifications of the ZEUS-detector between HERA I and HERA II are so immense, that it is a difficult task for the dE/dx corrections to yield comparable results for these two main periods. Section 5.1.3.1 will briefly touch on this. In Section 5.1.3.2 the dependence of the partial corrections on the different data-taking periods used for the tuning will be investigated.

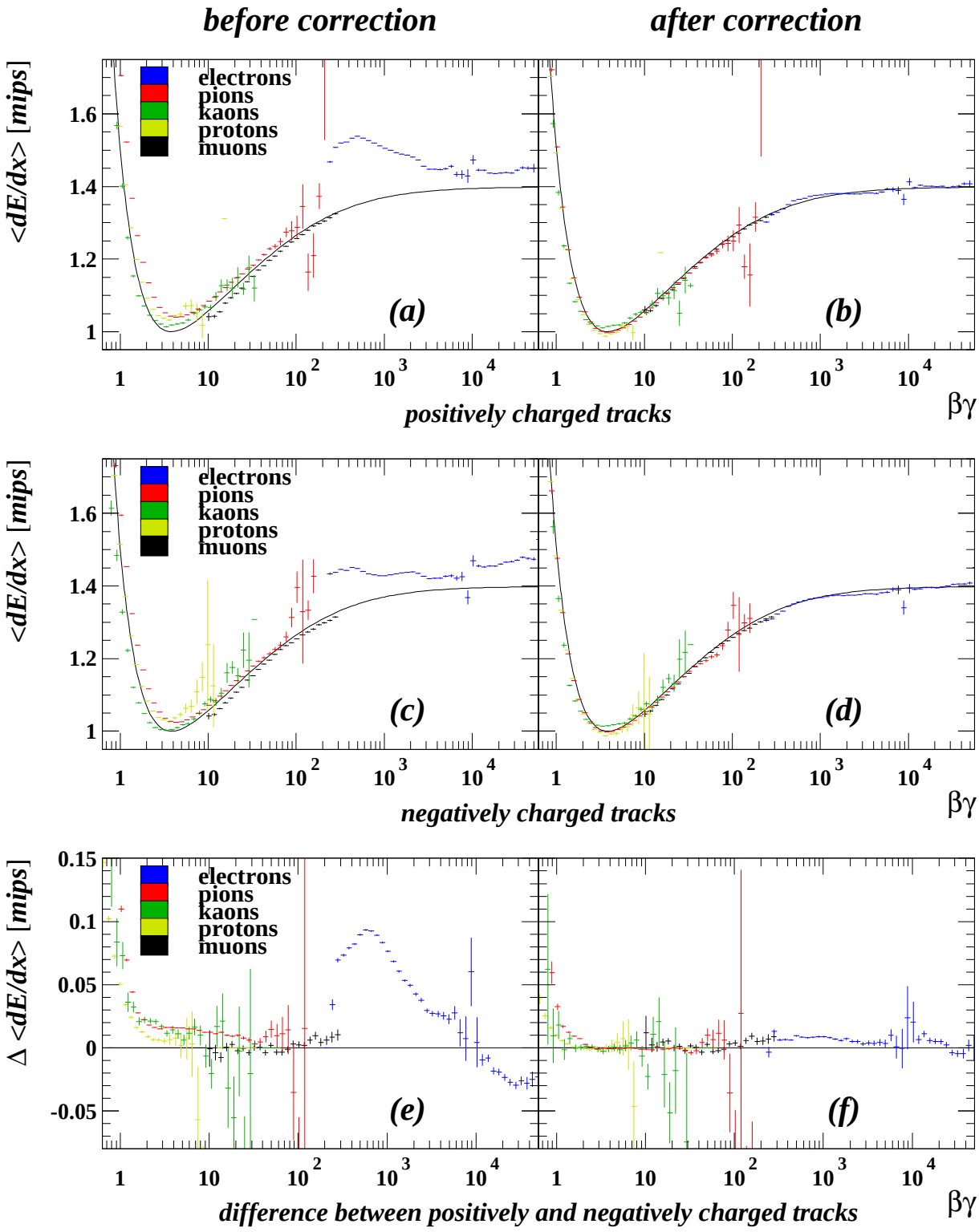

Figure 5.3: Profiles of dE/dx in bins of $\beta\gamma$ before (a, c, e) and after (b, d, f) correction. The first row (a, b) shows positively charged tracks only, the second (c, d) covers the negatively charged tracks. In the third row (e, f), the difference of the profiles between positively and negatively charged tracks is shown. The curve in the histograms illustrates the expected Bethe-Bloch curve.

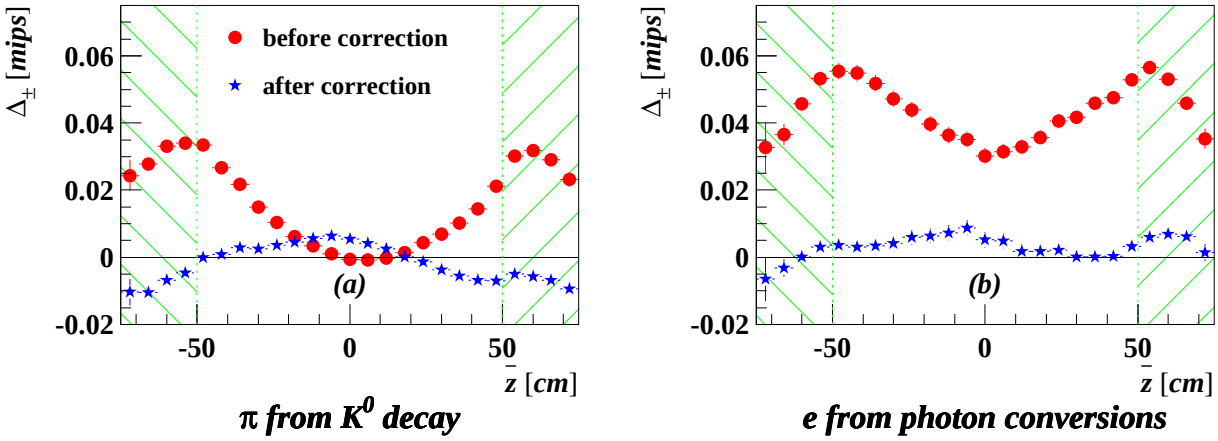

Figure 5.4: Difference $\Delta_\pm = \langle dE/dx_{norm}\rangle_+ - \langle dE/dx_{norm}\rangle_-$ between positively and negatively charged tracks in bins of $\bar{z}$. The hatched areas indicate the $\bar{z}$-range, which is dominated by tracks passing trough the end-plates.

5.1.3.1 Comparison between HERA I and HERA II

As the operation parameters of the CTD as well as the tracking itself changed between HERA I and HERA II, also for the dE/dx measurement changes are expected. The idea of a commonly usable correction package is to compensate such changes and to deliver corrected dE/dx measurements, which are independent of the running period.

Before corrections, Fig. 5.5 (a, c) clearly shows differences between the two data-taking periods. Most obviously, from HERA I to HERA II the difference between the pion and the muon samples increased significantly and the electrons cause higher uncorrected dE/dx values in HERA II data than in the older data. After corrections, these differences have disappeared. Only in the electron samples one might diagnose a remaining difference at the level of 1%.

5.1.3.2 Separation into tuning periods

The comparison of partial corrections for different data-taking periods is important for two reasons: If a correction method and the extraction of the parameters needed for this correction work properly, the results for different data sets should be similar. Therefore such a comparison tests the stability of the method. On the other hand, the operating conditions for the CTD can change with time; the chamber is ageing, the beam conditions for HERA change. Especially between HERA I and HERA II as well as with switching between e^+- and e^--running one has to expect serious changes. Therefore it is indeed not surprising, that the effects corrected for change between different data taking periods. In order to handle this properly, the partial corrections are tuned with separate data sets for separate running periods, as listed in Tab. 4.3.

Several effects corrected for depend only on a small number (≤ 3) of fit parameters. For these corrections one can directly compare the fit parameters for different data-taking periods as depicted in Fig. 5.6. The parameter Δz_{lim} for the end-plate effect has only a second order influence on the correction result, therefore it is not shown in Fig. 5.6. Even if the dispersion-effect correction depends only on 3 parameters, their correlations

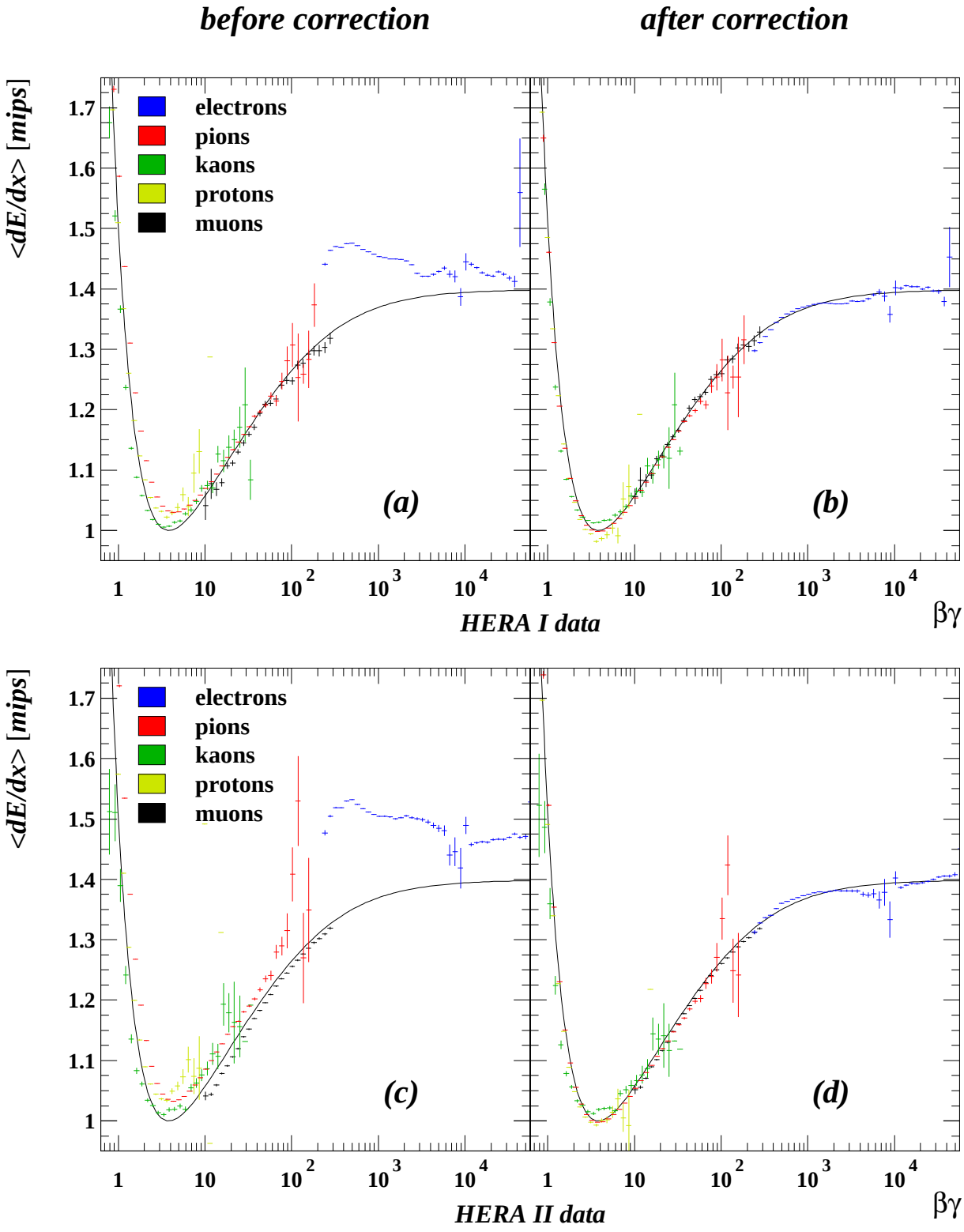

Figure 5.5: Profiles of dE/dx in bins of $\beta\gamma$ before (a, c) and after (b, d) correction. Comparison of HERA I- (a, b) and HERA II- (c, d) data. Different particle types are shown in different colours. The samples of same particles but different sources are combined into one profile.

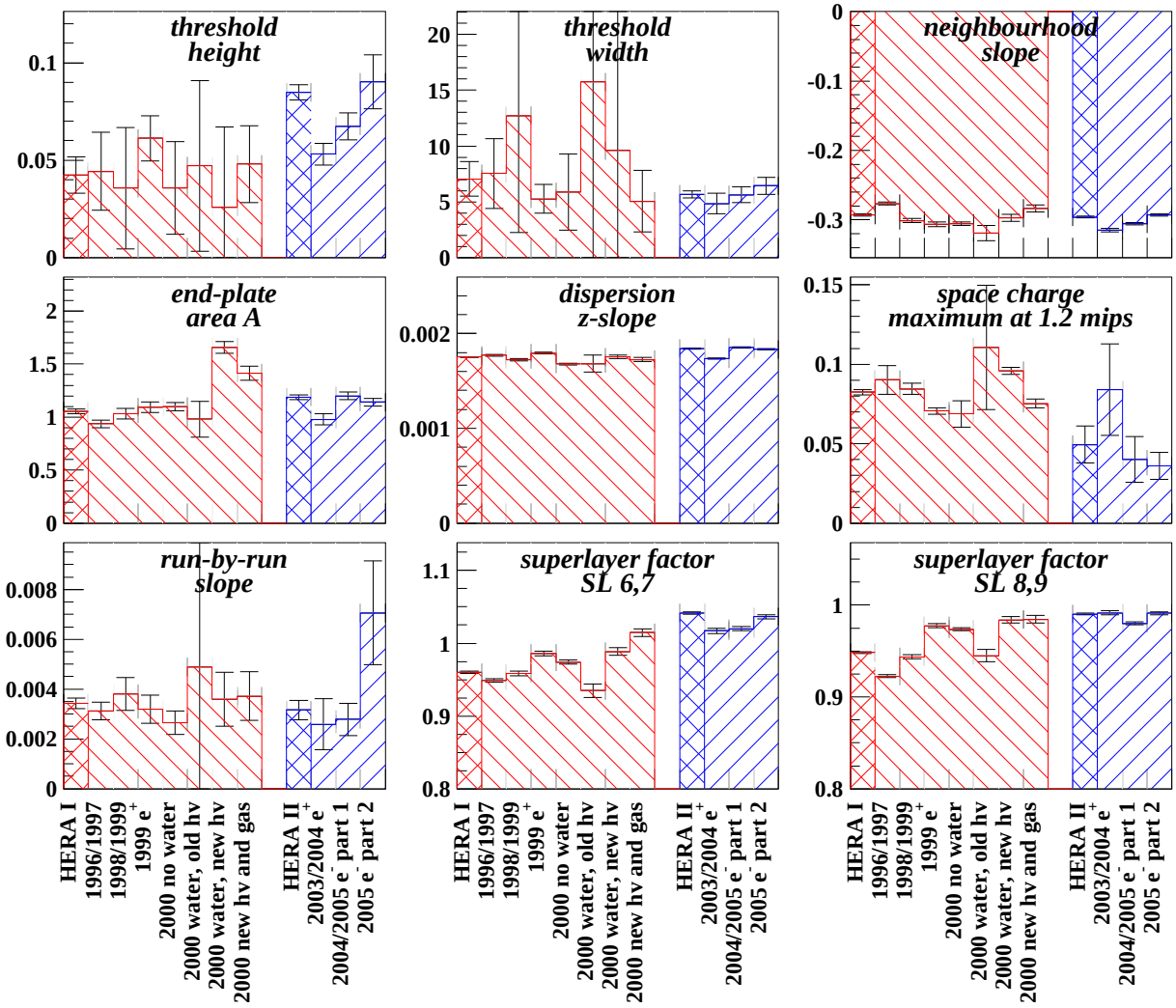

Figure 5.6: Parameters of correction functions separated by tuning-periods. For comparison, the fit results for the complete period of HERA I without water and for HERA II are also shown.

are very high. It is not useful to compare these parameters for the different running periods. Figure 5.6 contains a histogram of the z-slope of the dispersion-effect correction, calculated as the slope of the correction function in the direction of $\bar{z}$ at $\bar{z} = 0$. This is an informative quantity, as the size of the dispersion-effect correction dominantly depends on $\bar{z}$. A more detailed investigation of the dispersion-effect correction in its multi-dimensional parameter space will be given later in this chapter.

Even if the space-charge-effect correction has 4 fit parameters, one histogram for it is shown in Fig. 5.6: For typical tracks (with $dE/dx = 1.2\,\text{mips}$) the relative size of the correction is shown for high p_t-tracks with $\theta = \pi/2$. This represents a well defined point in the kinematical plane, where one expects almost the maximum of the space-charge effect. This maximum correction is a quantity, which does not suffer strongly from the correlations between the 4 fit parameters of the space-charge-effect correction. Therefore it allows a meaningful comparison between different data-taking periods (which is not possible for the fit parameters themselves).

The histograms of the z-slope and the maximum of the space-charge-effect are the only ones in Fig. 5.6, which do not show a particular fit parameter as obtained by the correction algorithm itself, but a quantity derived from such fit parameters.

Several parameters display huge error-bars for the data-taking periods with water in the year 2000, especially for the first one (added water with old high-voltage and old gas mixture). These periods are short and therefore the uncertainty of the fits is high.

For the second part of the 2005 data the correction of run-by-run corrections is obviously stronger than for all other periods. This is related to a broken argon flow-meter during parts of that period. The gas mixture changed steadily for about 2 months and caused a continuous rise of the ionisation rate as shown in Fig. 5.7. As the correction of the run-by-run correction is sensitive to the mean ionisation rate, it is no surprise to find it changed for that period.

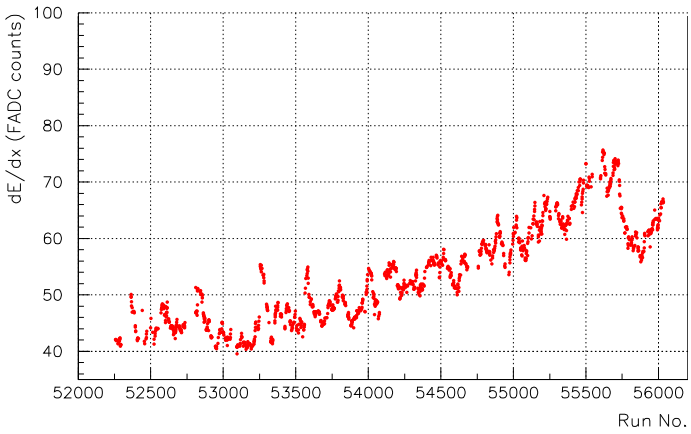

Figure 5.7: Mean dE/dx_{FADC} vs run number for year 2005 data. An argon flow-meter was broken and caused a rising ionisation rate for the run range 53500-55600. This histogram is taken from [57].

Several corrections reveal general changes between HERA I and HERA II data. For example the height-parameter of the threshold correction slightly increased. The height of the space-charge-effect correction also changed from HERA I to HERA II to lower values. This corresponds to the result of the investigation for the threshold effect. Both changes were expected, because the mean signal height became lower. Only for the 2003/2004 data-taking period the space-charge-effect correction is measured with high uncertainty at a similar level to the HERA I data. Within its big error the measurement is still compatible with the other periods of HERA II.

An interesting behaviour was found for the superlayer factors: they are steadily increasing. The reason for this is as yet unknown.

Except for the above mentioned cases all parameters are stable within their errors.

For the dispersion-effect correction it is not very enlighting to compare the fit parameters of different tuning periods. It is much more suggestive to compare the correction functions calculated with these parameters. As the emphasis is on the differences between the different tuning periods, one should normalise the correction function to its 'general shape'. This is implemented by extracting the fit functions for all tuning periods separately and in addition globally for the complete HERA I (without water) and HERA II periods. In a second step the separate correction functions are divided by the global one for the corresponding time.

For the periods without water the changes in the shape of the correction function are smaller than 1% (Fig. 5.8), but a global shift between the periods was found; the 1999 data is shifted by about +0.5%, the 2000 data without water by approximately −1%.

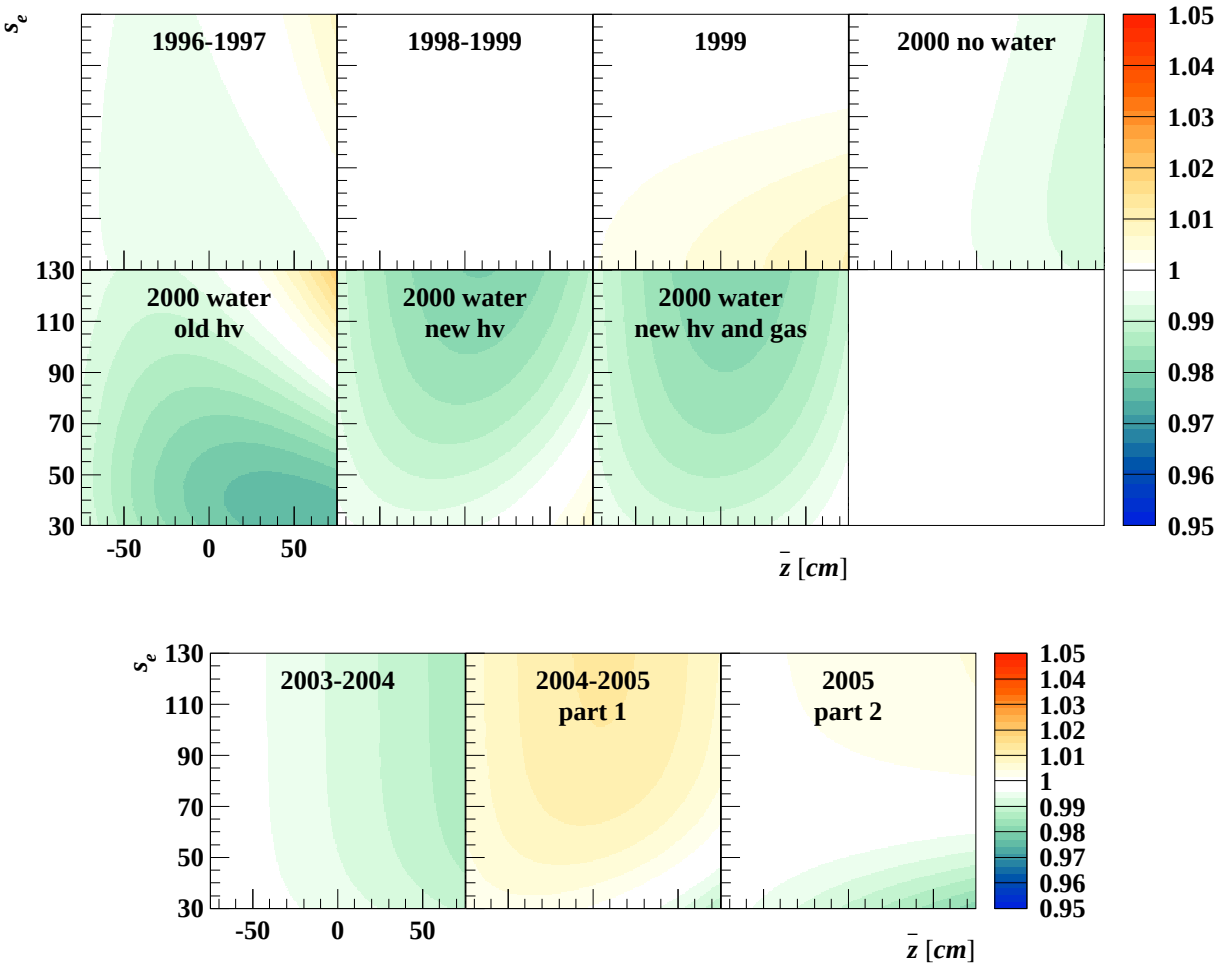

Figure 5.8: Correction factors for the dispersion correction for separate tuning periods, normalised to the global correction factor for the full HERA I or HERA II tuning data set.

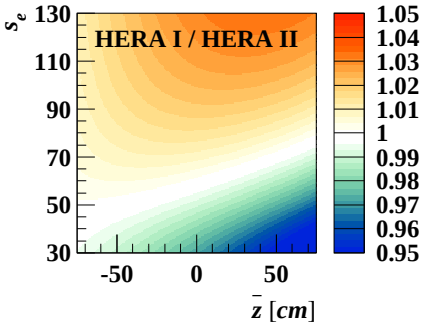

Figure 5.9: Correction factors for the dispersion correction; ratio between HERA I and HERA II.

This can happen if the slope of the z-dependence has changed: the reference point for the correction is at the position of the readout, i.e. $\bar{z} = -105\,\text{cm}$. The dispersion correction for the data taking periods with water in the CTD has a different shape. This motivates once more, that it is mandatory to handle these periods separately from the others.

The different periods of HERA II are also consistent at a level of 1% as shown in Fig. 5.8. Like for HERA I data one observes a global shift. Such shifts behave like a global scale, which is compensated by the drift-time-effect correction. Therefore they must not be reacted upon; they simply reflect the correlations between the corrections of the dispersion

effect and the drift-time effect, which are taken care of by construction of the iterative method.

In Fig. 5.9 the relation between the two references, the global correction functions for HERA I and for HERA II data, is shown. Differences of up to 5% can be found, which reflect the different behaviour of HERA I and HERA II data. These differences are ≈ 5 times larger than the ones within the two main data-taking periods.

The correction of the space-charge effect depends on 3 main parameters: θ, dE/dx and $\overline{\psi'}$. The dependence on $\overline{\psi'}$ is of minor importance. For large $|\cos\theta|$ it disappears almost completely, for $\theta = \pi/2$ a variation of $\overline{\psi'}$ within its accessible range causes only variations of less than 10% for the parameter x_t (see Eqn. 4.28). Consequently, $\cos\overline{\psi'}$ was fixed to 0.98, corresponding to tracks with $p_t \approx 0.4\,\text{GeV}$. Plots similar to the ones shown for the dispersion effect are given in Fig. 5.10. The remaining parameters $\cos\theta$ and dE/dx are displayed at the two axes. Differences of several % can be found between the different data-taking periods, especially in the range of strongest space-charge corrections (low $\cos\theta$ and high $\cos\overline{\psi'}$). Figure 5.10 also contains iso-lines of s_d. This is the most important parameter for the drift-time effect correction to constitute the global scale of the dE/dx measurement (see Sect. 4.3.1.10). For very small $|\cos\theta|$ one observes the gradient of the normalised space-charge-effect correction orthogonally to these iso-s_d-lines, which indicates high correlations between the space-charge-effect correction and the drift-time-effect correction. Therefore, the huge variations in the space-charge-effect correction between the different samples can be compensated by the drift-time-effect correction. In the range of large $|\cos\theta|$ the space-charge-effect correction varies parallel to the iso-lines of s_d, which means the two corrections are well disentangled.

Furthermore Fig. 5.10 shows, that the space-charge-effect correction for the 2003/2004 data set differs strongly from that of the other HERA II data sets. This corresponds to the investigations reported earlier in this section and to the observations according to Fig. 4.83 and Fig. 4.85. The comparison between HERA I and HERA II (Fig. 5.11) confirms the conclusions found with the separate data-taking periods. The two main periods differ in the space-charge effect on the order of 5%.

The changes for the drift-time-effect correction can be investigated in a similar way as the ones for the dispersion effect. There is, however, an additional technical problem; this correction depends on 3 parameters $\overline{\psi'}$, θ and dE/dx_{meas}. To visualise the correction factor in a 2-dimensional histogram, one has to integrate over the third dimension. Figure 5.12 contains distributions of $\cos\theta$ and $\overline{\psi'}$. For each bin the mean correction factors for dE/dx_{meas}-values between 0.6 mips and 1.6 mips are calculated. The colour of the bin represents the ratio of these mean correction factors for the single tuning periods over the corresponding global factor for the whole HERA I or HERA II tuning.

Ignoring the general scale for the different samples the corrections for HERA I without water and for HERA II vary by 1-2%. This range has to be compared with variations of $\approx 15\%$ without normalisation to the global correction factors for HERA I or HERA II. In conclusion, the drift-time-effect for different periods is quite similar. Only for the periods in 2000 with water in the CTD the shape differs significantly.

Besides the slope of the correction function its scale is another interesting feature. As it is a task of the drift-time-effect correction to compensate the different scales for the different data-taking periods, one expects to find such factors in Fig. 5.12. This scale factor is most pronounced for the 2000 data without water. In case of the 1999 data both corrections

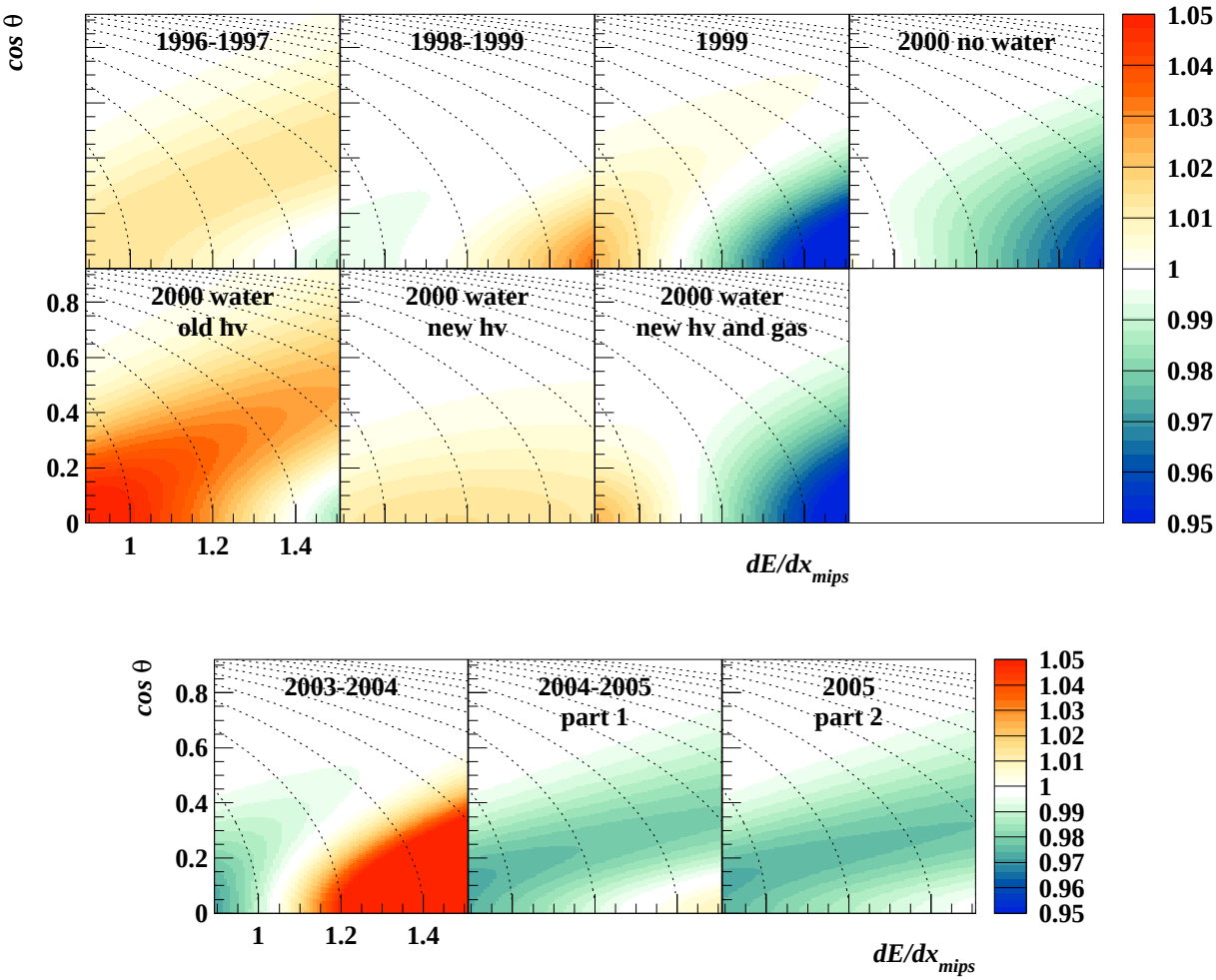

Figure 5.10: Correction factors for the space-charge-effect correction for separate tuning periods, normalised to the global correction factor for the full HERA I or HERA II tuning data set. The displayed lines are iso-lines of s_d as used for the drift-time effect correction. Details can be found in the text.

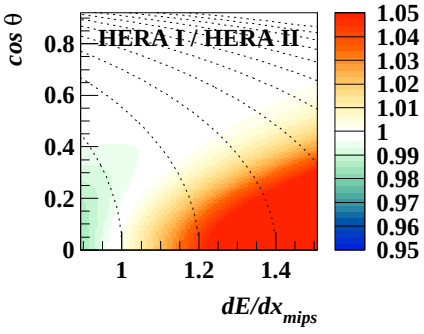

Figure 5.11: Correction factors for the space-charge-effect correction; ratio between HERA I and HERA II.

slightly increase the dE/dx value; the resulting scale is higher than for the year 2000 without water data. The origin of these differences lies in different scales caused by the superlayer factors. More details will be given later in this section.

The comparison of the global correction for HERA I with HERA II (Fig. 5.13) shows, that the drift-time corrections for these two main periods differ strongly on the order of 10%. These differences are much larger than the ones within each of the two main periods.

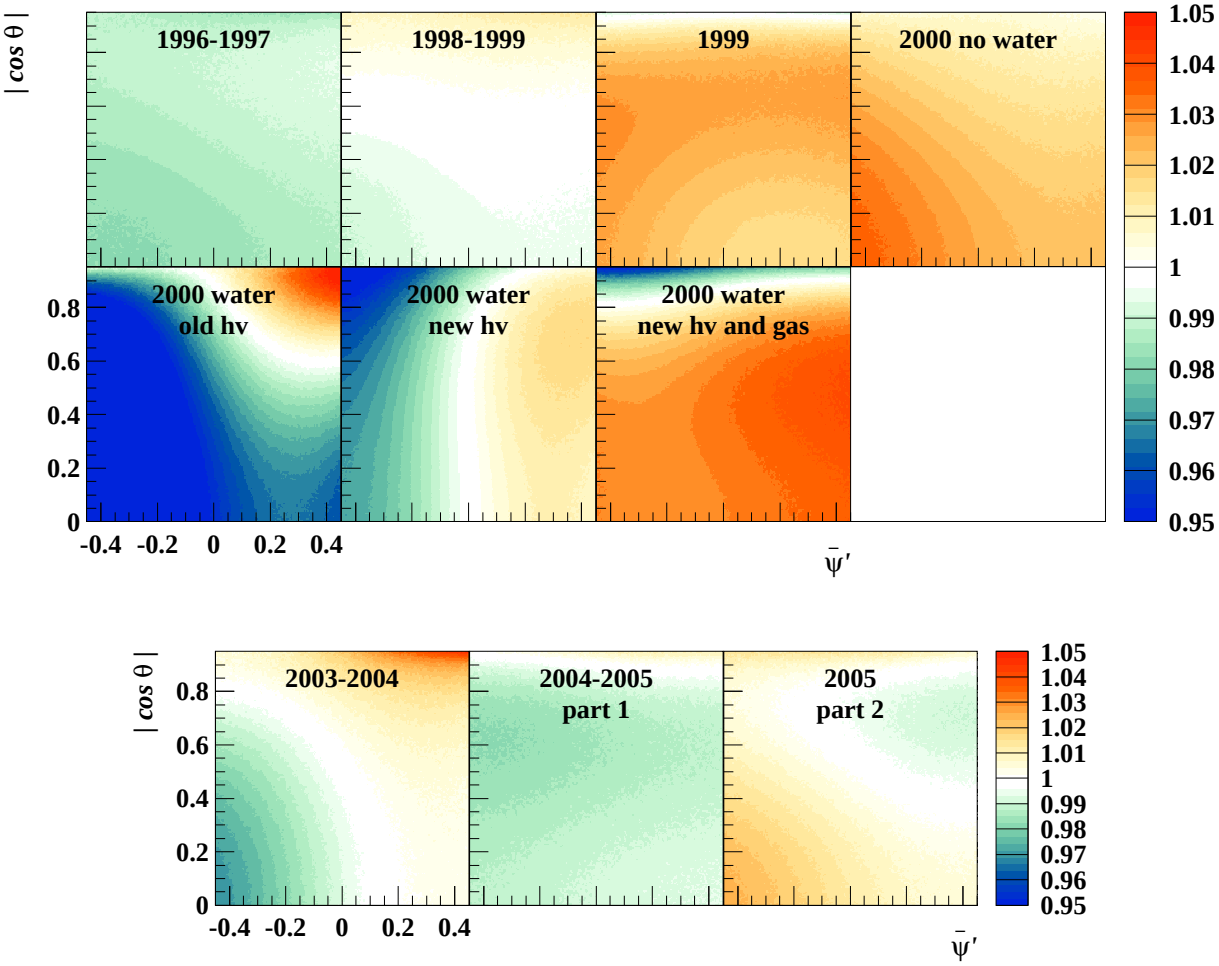

Figure 5.12: Correction factors for the drift-time-effect correction for separate tuning periods, normalised to the global correction factor for the full HERA I or HERA II tuning data set. Details can be found in the text.

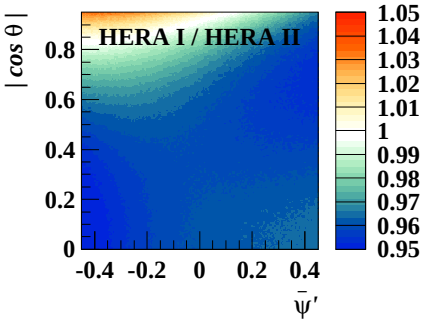

Figure 5.13: Correction factors for the drift-time-effect correction; ratio between HERA I and HERA II.

Up to now, only the changes of the fit functions between different data-taking periods were discussed. Another more goal-oriented approach to investigate long-term changes in the corrections is to compare the distributions of correction factors as applied to real tracks between different data-taking periods. The remaining part of this section will focus on this issue.

In Fig. 5.14 the histograms for the partial corrections are shown separately. For each partial correction the data is split into the different data-taking periods. To distinguish between the two main periods different line styles are used. The short data-taking periods

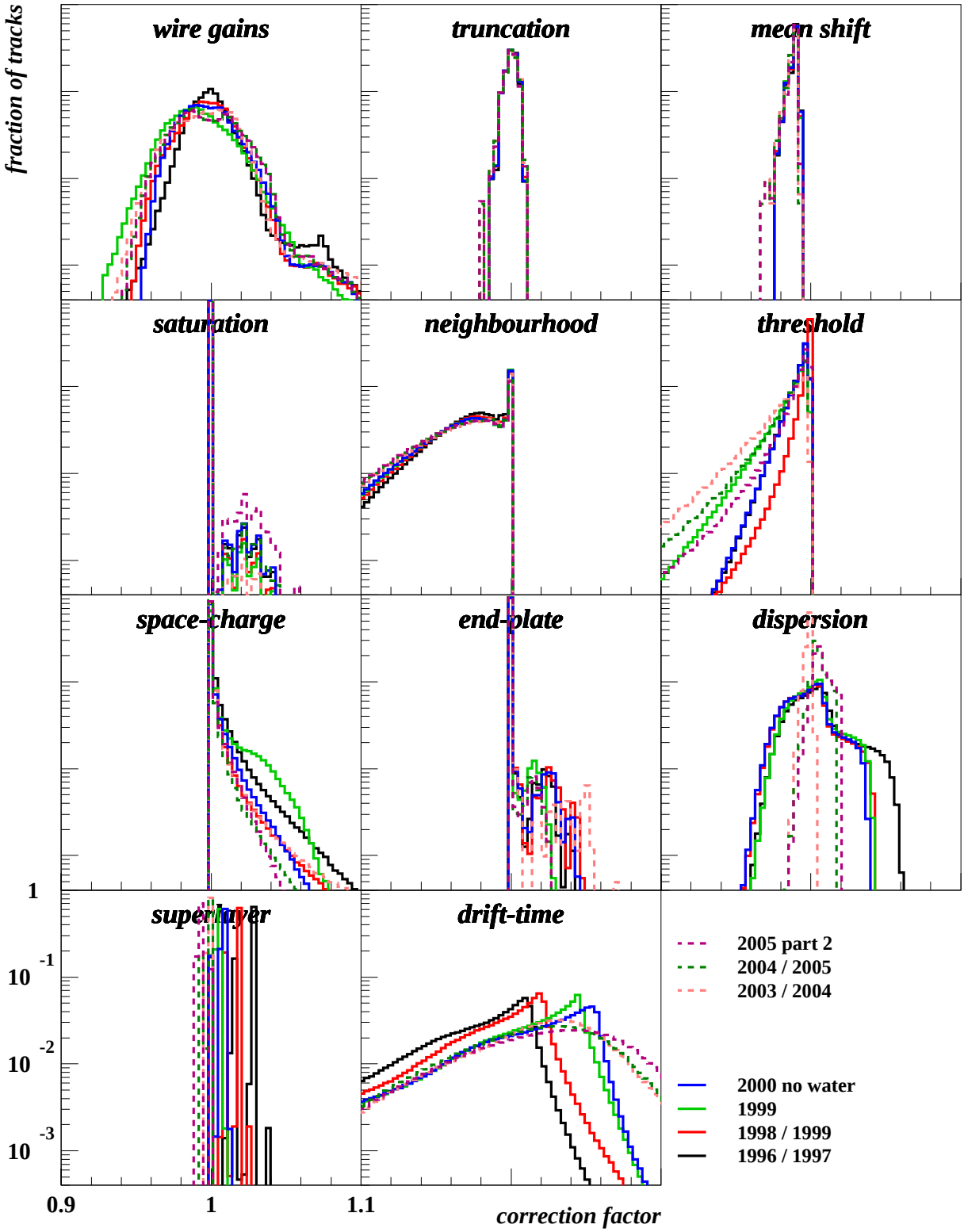

Figure 5.14: Histograms for all test data samples of correction factors for different data-taking periods, separated in partial corrections. All histograms are normalised to 1. HERA I data is shown in solid lines, HERA II data in dashed lines. The short data-taking periods with water in the year 2000 are not shown for clarity reasons.

with water in the year 2000 are not very trustworthy due to low statistics; they ignored in the following interpretation.

The histogram of the wire-gain correction for 1996/1997 data has more pronounced structures (like the peak at 1.07) than for the other periods. Furthermore, this distribution is more narrow than the others. This corresponds to the already mentioned observation, that just after the last calibration of the CTD the need of further calibration was much smaller than a couple of years later. Anyway, even for the first data-taking period this distribution is quite wide, which indicates, that using tuning samples for the calibration, which are already corrected for other effects, offers the chance for a more precise calibration than done early in the year 1996 with uncorrected data and low statistics.

The truncation window and mean-shift correction are identical for all data-taking periods. This has to be expected, as these corrections are independent of the data-taking period. One can also see, that the range of possible correction factors for these corrections is very small.

The saturation-effect correction is sample-independent, too. However, the 2^{nd} part of 2005 data shows a higher fraction of tracks to be corrected than the other periods. This happens due to the very high signals during the time, when the argon flow meter was broken.

The neighbourhood effect is found to be a very big effect, which did not change with time.

Compared to HERA I data one observes a stronger threshold effect for HERA II data. This is in accordance with the reduced high voltage and the already mentioned lower number of used hits. Only the data from 1999 does not match the expectation; they appear like HERA II data.

For the same reasons the space-charge effect is reduced from HERA I to HERA II. The shape of the histogram for the data from 1999 differs from the other periods. This is correlated to the difference in the threshold effect, the 1999 data shows compared to other data-taking periods.

The shape of the distributions for the end-plate-effect correction reflects the classification of the tracks into two groups. On the one hand there are tracks which are not affected by the end-plates, causing a high spike at 1. For the tracks affected, the distribution has a peak at higher values, passing a minimum half way between this peak and 1. The shapes of the distributions are rather similar, only the 2003/2004 data set is distributed more widely than the others. The peak position for the 1999 data is lower than for the other HERA I data. Similar to the threshold effect these data look more like HERA II distributions.

The dispersion effect shows the same characteristics as mentioned before: within the main periods it does not change, but from HERA I to HERA II the change is significant. Furthermore, one can find again the different scale factors caused by this correction between the HERA II data-taking periods.

The superlayer factors mainly cause different scale factors for the different periods.

These artificial scale factors caused by the superlayer correction and the dispersion correction are taken care of by the drift-time correction. Except for these different scales, the periods of HERA I data look rather similar but differ strongly from the HERA II data-taking periods. The distribution of the 2^{nd} part of 2005 data is wider than the others, which might once more be a reflection of the broken argon flow-meter.

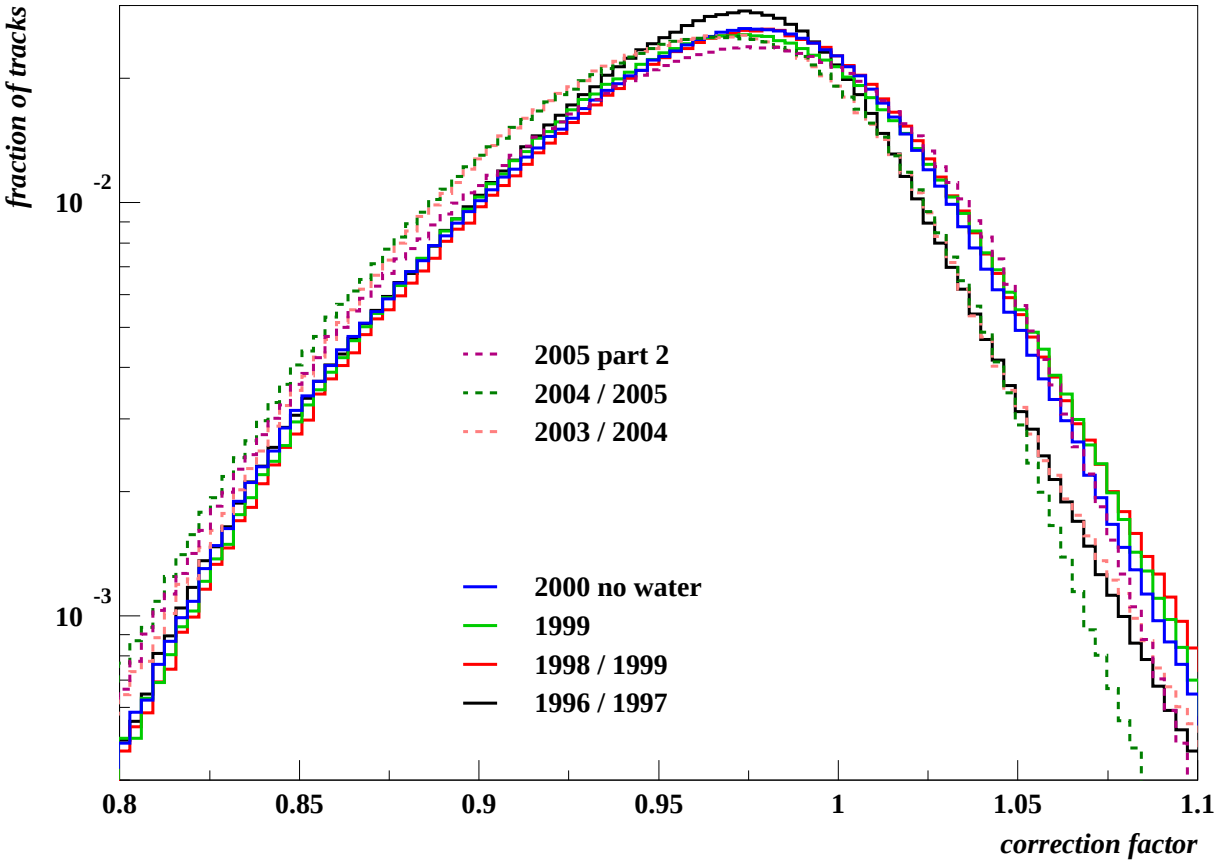

Figure 5.15: Histograms of the total correction factors for all test data samples for different data-taking periods. All histograms are normalised to 1. HERA I data is shown in solid lines, HERA II data in dashed lines.

Finally, one can compare the overall correction factor combined from all corrections between the different data-taking periods (Fig. 5.15). The differences are much smaller than for some of the partial corrections. The separation between different effects has only limited relevance. It can happen, that one partial correction 'robs' from another effect. With slightly different conditions between separate periods the amount of this 'robbing' can vary. Consequently the partial corrections can differ between separate data-taking periods more than their corresponding effects. Anyway, within the iterative procedure for finding the best correction parameters, the other partial corrections can react on such 'robbing'. In the end the combination of all corrections has to yield a proper result; in their combination any 'robbing' has to be compensated. Thus only the distribution of the combined correction factors can show real differences between the data-taking periods.

In the combination of all partial corrections the different data-taking periods behave very similar. Only small differences between HERA I and HERA II were found. Even the distributions for the low statistics periods in the year 2000 with water in the CTD behave rather similar to the other ones. Within the HERA I datasets the distribution of the 1996/1997 data is slightly narrower than the later ones; the reason for this difference can be found in the better calibrated wire gains just after their calculation.

Overall one concludes, that the corrections are well under control.

5.1.3.3 Summary of the variation within data-taking periods

The investigation of long-term variations covers two different kinds of changes:

The upgrade of the ZEUS-Detector between HERA I and HERA II caused many modifications in equipment and operation which induces changes in the reactions of the CTD. The task for the dE/dx corrections is successful, when they compensate for such changes and deliver values for the measured dE/dx which are common for all HERA-data.

The two main data-taking periods are split into shorter ones and correction parameters are extracted for them separately. This allows the corrections to react on medium-term changes of the detector reactions due to ageing effects or changes of the running conditions. As this kind of changes is expected to be small, a comparison between the tuning-periods is a good test for the stability of the optimisation algorithm used to extract the correction parameters. The small data sets with water in the year 2000 show several differences to the other data sets. One cannot decide, whether these differences are due to statistical fluctuations or if they are caused by the different running conditions. For the partial corrections the 1999 data set shows slight differences to the other HERA I data sets; some of its distributions look more like HERA II data. Even if 2003/2004 data suffers from very bad data taking conditions in the beginning of HERA II, the distributions of its partial corrections are similar to the other HERA II data.

This investigation shows correlations between the space-charge-effect correction, the superlayer factors and the drift-time correction. Except for these differences, the stability of the partial corrections was found to be very high.

The distributions of the combined correction factors are very similar for the different periods. The small remaining differences are mostly understood and the corrections in their combination are well under control.

5.1.4 Example demonstrating the power of corrected dE/dx measurements

In this section parts of the analysis from 1999 of the semileptonic decay of charmed mesons to electrons as given in [5] will be presented as an example for the application of dE/dx measurements. When this analysis was carried out, the tools presented in this thesis were not available yet. Here the focus will be on the potential of improvements for that analysis when using the new tools within the framework of the old analysis.

The main challenge in [5] after a proper preselection of the data sample was the correct measurement of the number of electron tracks in the data sample. The only way to account for the background in a signal-enriched data sample selected with dE/dx measurements was the statistical subtraction, using a background-enriched sample to describe the shape of the background in the distribution of dE/dx. The background-enriched sample was normalised to the signal-enriched sample in a range, where one expects no signal (see Fig. 5.16). In the signal region, statistical subtraction was applied to extract the number of signal events. In order to reduce the systematics due to track kinematics, this procedure was carried out separately in bins of p_t and η[1]. This method suffers from big uncertainties in the extracted number of events.

[1] The pseudorapidity η is defined as follows: $\eta = -\ln(\tan(\theta/2))$

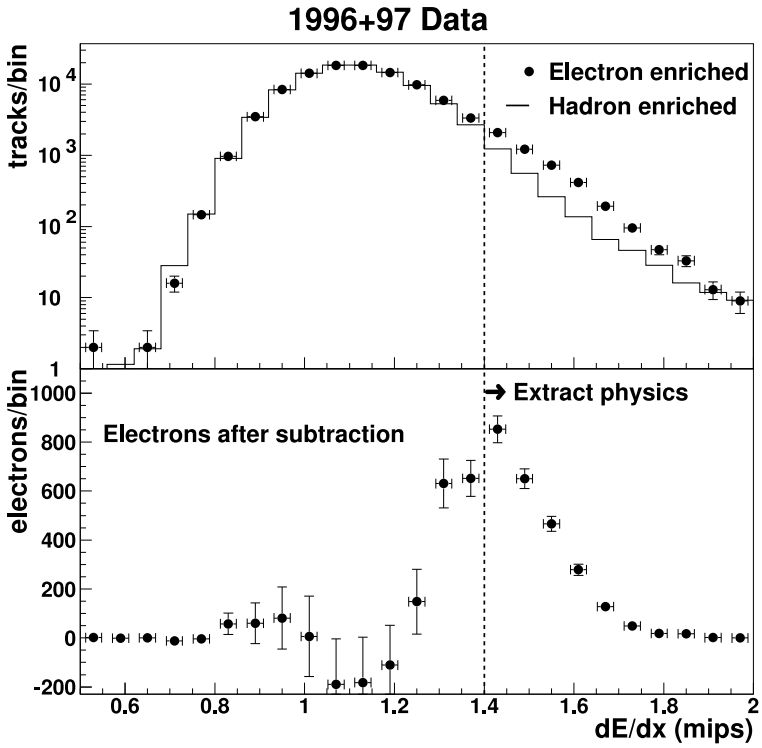

Figure 5.16: Extraction of the number of signal events (electrons) in a statistical subtraction method, from [5]. The hadron-enriched sample was normalised to the electron-enriched sample within the range 0.5 mips $< dE/dx <$ 1.1 mips, separately in 4 bins of p_t and η respectively. The difference of the two distributions for $dE/dx >$ 1.4 mips was treated as the number of electron events.

The most relevant uncertainties and their improvements due to dE/dx corrections are:

- Differences in the selection of the signal-enriched and the background-enriched sample (for example in their kinematic range) are unavoidable. These differences can cause different shapes of the distribution of the background-enriched sample and the background in the signal-enriched sample, leading to a systematic error in the statistical subtraction. As one can observe in Fig. 5.16, the background ratio in the signal-enriched sample is quite high or even dominant. Subtracting a high background measured with a big systematic error from a signal-enriched sample renders the result dominated by this systematic error.

  It has been shown, that the corrections introduced in this work reduce this kind of systematic uncertainty by about an order of magnitude.

- In order to reduce the statistical error of the calculated difference, the signal extraction in the mentioned method has to be restricted to a range in dE/dx, where the background contamination is not too big. One finds in Fig. 5.16, that in the range $dE/dx <$ 1.4 mips the difference distribution shows very big errors, leading to a high uncertainty in the result, if one uses this range for the calculation. The way out was to extract physics only for $dE/dx >$ 1.4 mips and to argue, that 1.4 mips is the mean value for dE/dx of electrons and therefore 50% of all electrons are counted with this method. As one can see in Fig. 5.3 (a, c), this argument is only approxi-

matively true and furthermore different for electrons and positrons, leading to an additional systematic error.

An important effect of the dE/dx corrections is, that the mean corrected dE/dx matches with the BETHE-BLOCH prediction. If one replaces the previously mentioned cut $dE/dx_{meas} > 1.4\,\text{mips}$ by a cut $dE/dx_{meas} > dE/dx_{exp}$, the systematic error caused by this selection method will be reduced dramatically.

This example shows, that had the new dE/dx corrections been on hand the accuracy of the analysis would have been strongly improved, even if the method of the analysis will be kept unaltered. Furthermore, the improved understanding of the dE/dx measurements allow for modified analysis methods, like for example the useage of likelihoods, opening the access to not yet applied analysis methods at ZEUS with the potential of further improved accuracy.

5.2 Resolution

The most common estimator for the precision of a measurement is its resolution. There are many possibilities how to define 'resolution', but all of them have in common, that the resolution describes the width of the distribution of measurements around their expectation value. A precise definition of 'resolution' will be given later in this section. Several independent quantities contribute to the total resolution. In this section the main contributions to the resolution are discussed.

The statistics of the number of used hits is a main parameter for the resolution and will be discussed in Sect. 5.2.1. Section 5.2.2 will focus on the question, how resolution has to be defined. In Sect. 5.2.4 the measured resolution will be split into different parts, like the 'intrinsic' resolution due to the LANDAU-shaped single-hit ionisation distribution, the calculable uncertainty of the dE/dx corrections and the remaining part. Separating the resolution into its different contributions is the most powerful approach to reach highest possible precision for estimating the resolution of a single track measurement. This estimate is one out of two ingredients for the particle identification based on dE/dx measurements; therefore profound knowledge about the single track resolution is mandatory for a reliable particle identification. An overview of the amount of the different parts of the resolution is given in the Sect. 5.2.5. Section 5.2.6 will summarise this section about the resolution of dE/dx measurements.

5.2.1 Resolution dependence on n_h

The measurement of dE/dx is given by a (truncated) mean of the measurements of several independent hits. Therefore one expects, that the dependence of the resolution $\mathcal{R}$ on the number of used hits n_h is given by

$$\mathcal{R}(n_h) \sim \frac{1}{\sqrt{n_h}} \quad . \tag{5.1}$$

There might be deviations from this law due to the truncation method: even if the removed hits are not taken into account in the calculation of the mean value, they can influence the resolution of the result. This is possible, because only the highest and the lowest signals

are removed. Sorting (and afterwards selecting) the single hits by their height means, that for the calculation they are not independent anymore. Thus the mathematics for the variance of a mean value is not applicable in this case. One can expect, that the resolution for high numbers of used hits is better than expected from Eqn. 5.1.

The truncated mean calculation also has an influence on the measured resolution. As for this method the biggest and the smallest values are ignored, the variance of the truncated mean is smaller than for a mean value without truncation. The size of this effect can be shown with a small Monte Carlo simulation. This simulation is done twice: once using standard gaussian-distributed single-hit measurements to see the basics of the truncation effect, then with a LANDAU distribution using the parameters from Sect. 4.3.1.2 to have a proper simulation of the real conditions for the ZEUS CTD. In order to unfold the n_h-dependence of the resolution it is helpful to look at the standard derivation σ_{track} of the mean value for the simulated track, multiplied by $\sqrt{n_h}$. As long as no truncation is applied, this value σ_{int}^{hit} is exactly the standard derivation for single hits. [2] In the gaussian case one expects σ_{int}^{hit} to be equal to 1 for any number of used hits. After truncation, σ_{int}^{hit} reduces to ~ 0.67 (Fig. 5.17 (a)). Furthermore, one can see a periodic dependence on n_h, caused by integer effects of the truncation. The period of these oscillations can easily be calculated: 10 hits is the smallest number for which the truncation limits (10% and 30%) can be selected without any variation due to integer effects. Thus the effect of integer-caused variations of the truncation-window should repeat for every 10^{th} hit. As Fig. 5.17 does not show the number before but after truncation, this number has to be multiplied by the size of the truncation-window; one calculates a period of $10 \cdot 0.6 = 6$ hits.

In order to see the dependence without these oscillations, Fig. 5.17 also shows the dependence of σ_{int}^{hit} on n_h using a binning of $\Delta n_h = 6$ to cover one complete period. This distribution is almost flat. For reasonable hit numbers (> 15) the variation of the standard derivation is less than 1%.

In case of the LANDAU-distributed density function, the oscillations are even smaller, therefore they are not observable in real data. On the other hand one observes, that the resolution improves a little bit with rising n_h. This global dependence of the resolution on n_h is of the order of 2% and can be neglected for the moment. Thus looking at data one can extract the single hit resolution measured with the width of the LANDAU-distribution by multiplying the corresponding track resolution by $\sqrt{n_h}$:

$$\sigma_{int}^{hit} \approx 0.415 \quad . \tag{5.2}$$

In order to describe the resolution of the dE/dx measurement one has to investigate the width of the dE/dx_{norm} distribution. This can be done separately for different numbers of used hits. The dependence on the number of used hits can be confirmed by using the same approach as in Fig. 5.17.

The simplest way to quantise the width of a distribution is to take its root mean square (RMS). Alternatively one can fit the distribution with a proper function and extract the width from that fit. Both approaches will be shown here.

For finding a proper fit function one has to keep in mind, that the measured dE/dx for a track is the mean value of independent measurements for several hits. According to the

[2] The index *int* for the single hit resolution σ_{int}^{hit} stands for 'intrinsic resolution'. The corresponding nomenclature will be introduced in Sect. 5.2.4.

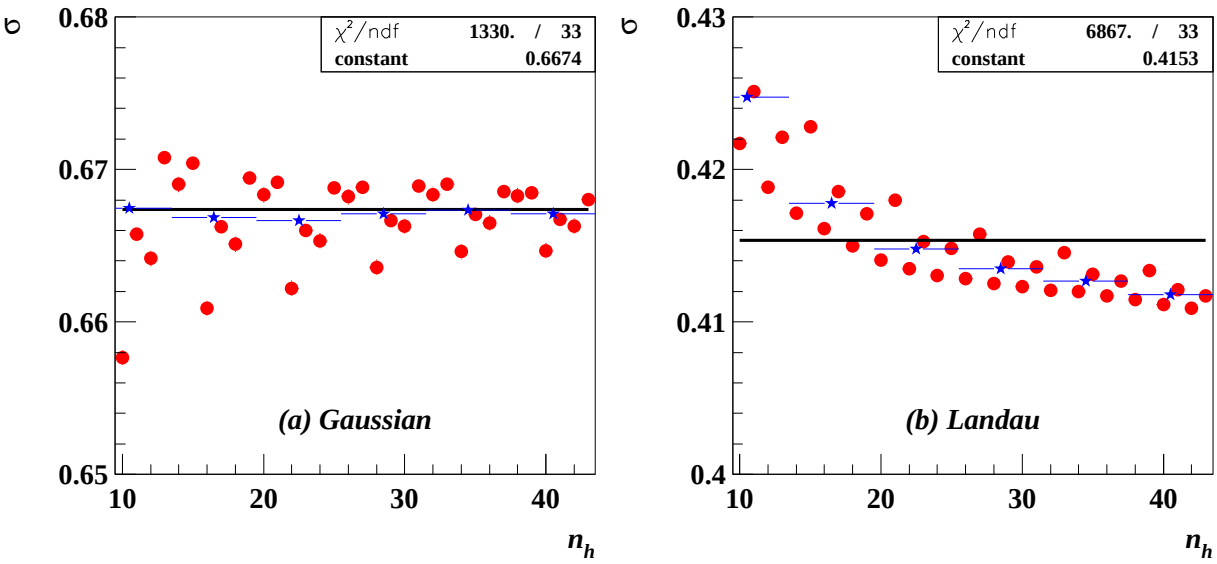

Figure 5.17: The influence of the truncated mean calculation on the standard derivation of the calculated variable. Monte Carlo simulation with (a) Gaussian- and (b) LANDAU-distributed probability density for single measurements. The truncation window corresponds to the one used for the dE/dx measurement. Red dots are the standard variation in bins of the number of used hits n_h. To compensate integer effects of the truncation method, the blue stars show mean values in bins of $\Delta n_h = 6$. In (b) the width of the LANDAU distribution is the same as extracted from data in Section 4.3.1.2. Therefore this plot shows the expected resolution due to the single hit resolution.

central-limit theorem for a large number of hits these measurements should be gaussian-like distributed. However, we are also investigating tracks with too small n_h to expect pure gaussian distributions. As the probability density for the signal of a single hit is asymmetric with a long tail towards high values (LANDAU-distributed), one also expects a small asymmetry for the distribution of dE/dx_{norm}.

The remaining asymmetry is covered by fitting a Gaussian to the distribution of $\ln(dE/dx_{norm})$. This 'Log-Gaussian-fit' is placed somewhere between phenomenology and physics arguments. The phenomenological part is a good description of the data by such a fit. The physics argument can be found if one thinks about the kind of errors on the measurements, which cause the resolution. Most of the effects shown in Sect. 4.2 cause some factors for the measured dE/dx. According to $\ln(f \cdot dE/dx) = \ln f + \ln(dE/dx)$ the logarithm transforms such factors into offsets, which are symmetric around the mean value. In most cases symmetric errors can be described well by a gaussian distribution. The weakness of this argument is of course the fact, that systematic errors very often are not gaussian. The 'real' error therefore is a mixture of Log-Gaussian and other distributed fractions. Therefore this argumentation points in the right direction, but finally the fit used should rather be treated as a phenomenological fit.

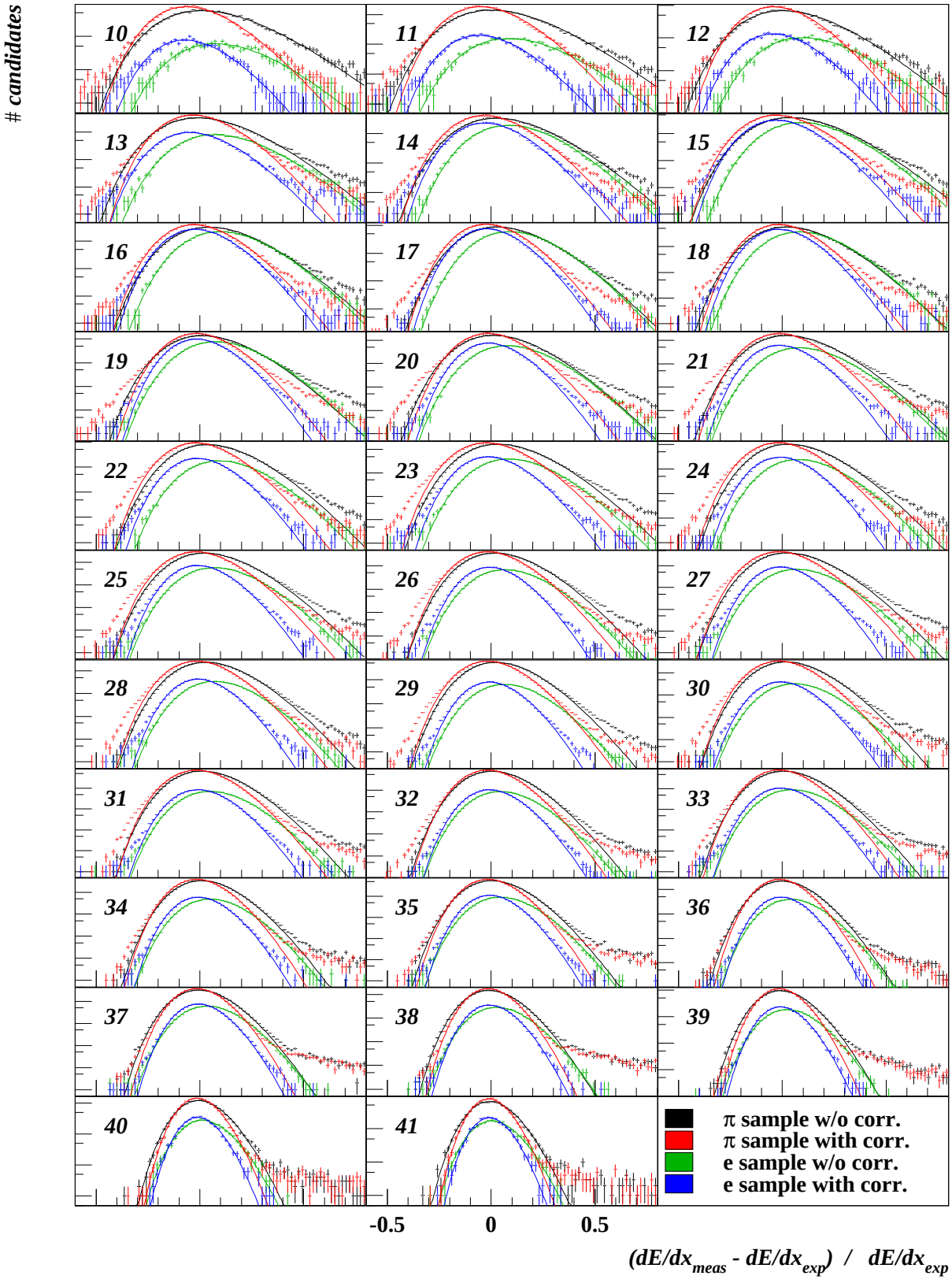

Figure 5.18: Residuals $\frac{dE/dx_{meas}-dE/dx_{exp}}{dE/dx_{exp}}$ separated by n_h (indicated by numbers in the histograms). Pion and electron samples before and after dE/dx corrections. Details about the fit can be found in the text.

The fit function for the residual $r = \frac{dE/dx_{meas} - dE/dx_{exp}}{dE/dx_{exp}} = dE/dx_{norm} - 1$ is given by

$$\mathcal{R}(r) = A \cdot \exp\left(-\frac{1}{2} \cdot \left(\frac{\ln(r+1) - \mu}{\sigma}\right)^2\right) \quad . \tag{5.3}$$

The histograms in logarithmic scale as given in Fig. 5.18 show, that the data overshoot the fit in the tails. This can be caused by the admixture of wrongly identified candidates in the test samples. For example in the electron distributions, the upper tail is described quite well by the fit function, as most of the background candidates for the electron sample have a lower dE/dx_{exp} than the electrons themselves. On the other hand, most of the candidates in the pion sample are located around the minimum of the Bethe-Bloch curve, thus most of the background should be located in the high range of the residuals, where indeed too many candidates are found. As a cross check the ratio of found candidates over the area of the fit curves was measured to be $\approx 1\%$, which matches with

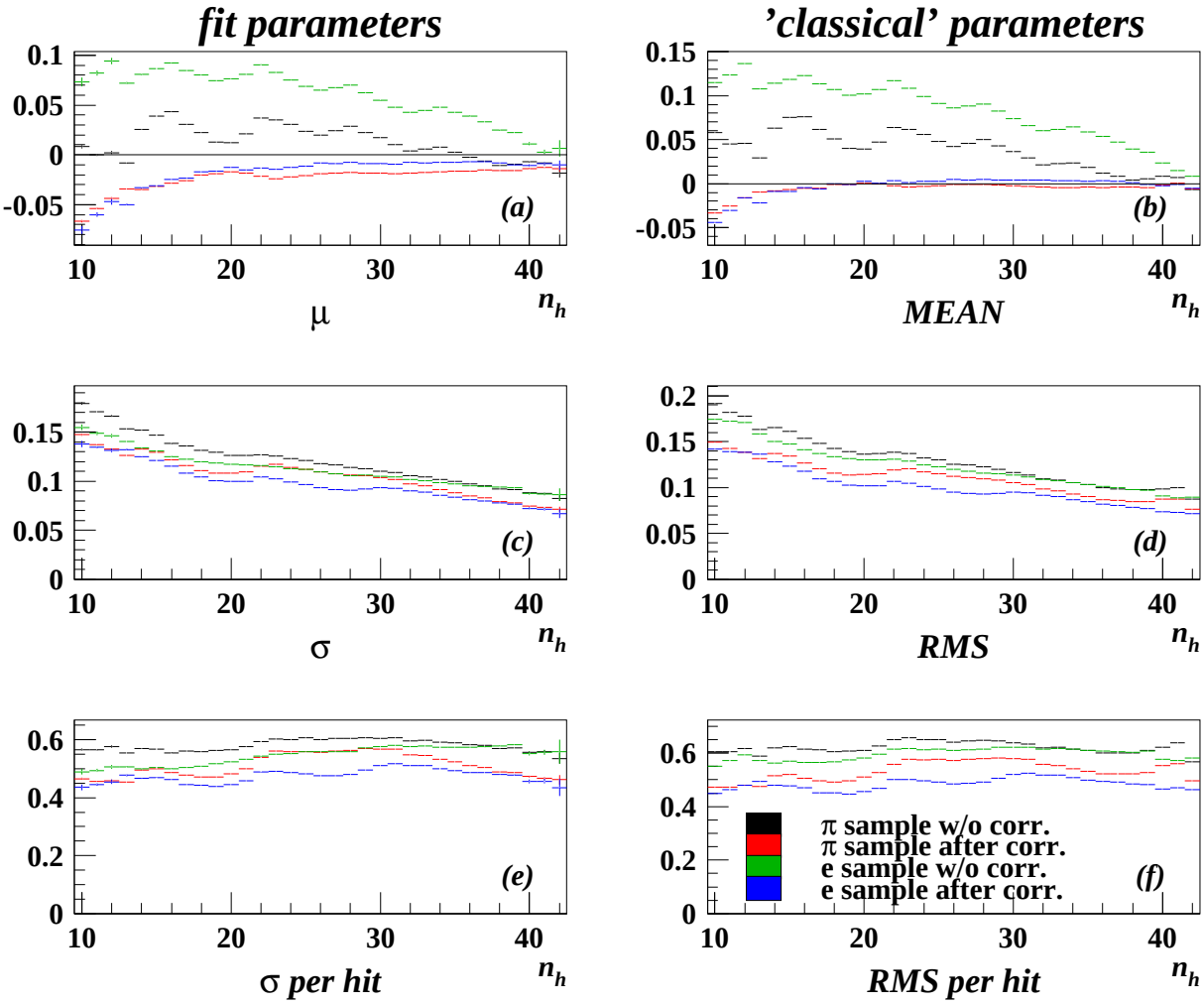

Figure 5.19: Dependence of the normalised residuals on n_h. The left column presents the parameters of the fits shown in Fig. 5.18, in the right column the 'classical' mean value and RMS are shown. In the 3rd row the shown points are normalised by $\sqrt{n_h}$.

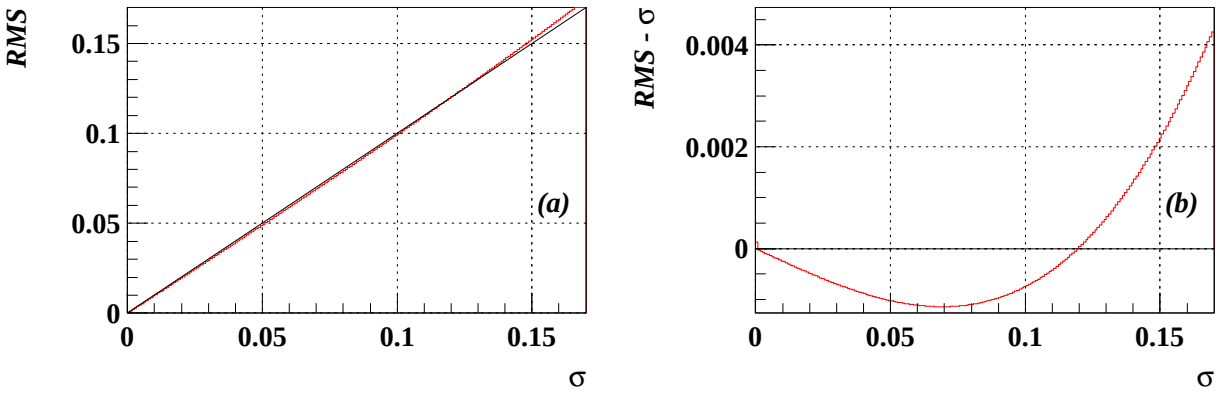

Figure 5.20: Relation between the RMS and the parameter σ in Eqn. 5.3. Direct comparison (a) and the deviation of the RMS from σ (b) in bins of σ.

the expected signal/background ratio in the test samples. One can conclude, that within the achievable accuracy the fit describes the data very well.

Based on these fits (and alternatively on the 'classical' RMS-calculation) one can investigate the n_h-dependence of the measured resolution (Fig. 5.19). One finds a similar behaviour in the shape of the fit parameters and the classical mean and RMS values. The absolute values are not directly compatible as the fit parameters describe the mean and width of the $\ln(dE/dx_{meas})$-distribution. Especially for the mean value one can find a shift of ≈ 0.015 between the two methods. The RMS and σ are very similar. This is confirmed by comparing the RMS and σ of distributions according to Eqn. 5.3 as shown in Fig. 5.20. In the range of interest the difference between the RMS and σ is smaller than 0.005 and therefore negligible. The visible difference between Fig. 5.19 (c) and (d) can be explained by the admixture of wrongly identified particles in the samples. This will be discussed in detail in Sect. 5.2.2.

The mean values (Fig. 5.19 (a, b)) for uncorrected data are far off and oscillate with a period of $\Delta n_h = 6$. These oscillations are caused by integer effects as described earlier in this section for the n_h dependence of the resolution. The corrections remove these oscillations very well and for high n_h the mean value is perfectly at zero whereas for very small n_h the mean value decreases to lower values. The same effect has been seen in Fig. 4.72 for small values of R_{out} and can be explained by turn-on effects in the selected data sample.

As expected, σ and the RMS are falling with n_h (Fig. 5.19 (c, d)). After normalisation to single hits (Fig. 5.19 (e, f)) the global n_h-dependence disappears. Nevertheless there are wiggles of order 10% left. They exist in all samples and they are more pronounced after corrections than before. Comparing with the coverage of n_h by different superlayer-classes (Fig. 4.5) one observes, that the resolution is worsened in the ranges, where different superlayer-classes overlap. This is yet another indication for a deeper (not yet found and corrected) cause for the factors between superlayers.

According to Fig. 5.19 (f) the correction improves the resolution at single hit level by $\approx$ 15%. One might be surprised, that already before correction the resolution for the electron sample seems to be better than the one for the pion sample. Many plots shown here suggest the opposite; the Phase I corrections were tuned for pions and therefore they

should work better for pions than for electrons. The reason for this unexpected behaviour is given in the definition of (relative) resolution used and will be discussed in Sect. 5.2.4.

It is remarkable, that the $\sqrt{n_h}$-normalised resolution is (almost) flat. This proves, that the dominant contributions to the resolution are uncorrelated for single hits. Any contributions affecting the whole track, like the dependence on the air pressure, should cause an offset in the RMS at track level. Therefore such contributions should have a $\sqrt{n_h}$-shape in the hit-resolution plots. Unfortunately, the most probably superlayer-related fluctuations in Fig. 5.19 (f) make it impossible to extract from data the track- and hit-related fractions of the spread. Within the achievable accuracy a track-related contribution cannot be observed.

5.2.2 A proper method to measure the resolution

There are several possibilities to define a 'resolution'. Most common is to use the relative resolution, based on the residual r

$$r = \frac{dE/dx_{meas} - dE/dx_{exp}}{dE/dx_{exp}} \quad . \tag{5.4}$$

The width of the distribution of r defines the relative resolution. But what happens if the prediction dE/dx_{exp} is wrong for a certain fraction of all tracks? In that case the residual r will get a bias and its distribution using all tracks will be widened artifically. This is not a desired effect as one wants to keep systematic errors on dE/dx_{exp} and the resolution separated. One has to find a way to measure the resolution without being sensitive to the errors of dE/dx_{exp}. The desired result can be achieved by looking at the residuals in bins of $\beta\gamma$, the variable on which dE/dx_{exp} depends. As long as the binning is fine enough one can expect, that within one bin the difference between the 'wrong' dE/dx_{exp} and its correct value is almost constant. Therefore, only the mean value of the distribution of r within this bin is affected; the width stays unchanged. The contribution V_{track} of each track to the variance of the residual is given by

$$V_{track} = \left(x_{track} - \left\langle x_{\beta\gamma-\mathrm{bin}} \right\rangle \right)^2 \quad .$$

This can be transformed to the mean variance of each hit in the track using

$$V_{hit} = n_h \cdot V_{track}$$

and finally the spread and its error are given by

$$s = \sqrt{\frac{\sum\limits_{tracks} n_h(track) \cdot V_{hit}(track)}{\sum\limits_{tracks} n_h(track)}} \quad , \quad \Delta(s) = \frac{s}{\sqrt{\#tracks - 1}} \quad . \tag{5.5}$$

The error calculation takes into account, that for each track only the mean value of the variance of its hits is given. Therefore the number of degrees of freedom is not given by the total number of hits but by the number of tracks taken into account.

In this calculation the spread s is given as the RMS of a distribution. Unfortunately the RMS is very sensitive to the admixture of misidentified particles in the investigated data

samples. In case of a misidentification (wrong mass assumption) the residual can become very big. As its square enters the RMS, even a small admixture of wrongly identified particles can have a visible effect in the calculated RMS. Therefore it is necessary to reject such tracks from the resolution measurement. As these tracks cannot be identified (otherwise they would not be in the test samples), only a statistical method can be applied. The tool needed for it is given in Sect. 5.2.1: a fit of the distribution of r is dominated by the 'proper' tracks which cover the range around 0 with high statistics. Wrongly identified tracks cause a much wider distribution of r which is reflected in long tails with low statistics in the distribution of r. Such bins with low statistics have almost no influence on the fit. Therefore the RMS of the fit function is much less burdened by misidentified particles than the RMS of the residuum-distribution itself.

Anyway, to fit a distribution high statistics are mandatory. In Sect. 5.2.4 residuals are investigated in bins of $\beta\gamma$. To allow fits within such bins in the test samples one needs higher statistics; only the RMS is properly calculable. A first step out of this misery is to combine the n_h-separated distributions as shown in Fig. 5.18 into a residual for single hits, which is the distribution of $r \cdot \sqrt{n_h}$, each track weighted with n_h, as already described for the calculation of the spread s. The second step is to fit the r-distributions of the full samples (without $\beta\gamma$-binning) and to compare the RMS of such distributions with the fit parameter σ. In Sect. 5.2.1 it has been shown, that this σ is the same as the RMS of a 'clean' distribution, which is represented by the fit function. The ratio RMS/σ is a correction factor which transforms the RMS of the full sample (including wrongly identified particles) into an RMS of a pure sample (correctly identified particles only). This factor has to be applied to the spread in Eqn. 5.5.

Unfortunately one gets into trouble when applying the fit function from Eqn. 5.3 to the residual distribution of single hits. As the single hit resolution is very wide, the argument of the logarithm can become negative and then the function is not defined. However, for this task it does not make a big difference if one replaces the logarithmic gaussian by a 'usual' gaussian function.

The residuals of the investigated test samples and their gaussian fits are shown in Fig. 5.21. As mentioned before, the shape and height of the tails depend strongly on the sample, which clearly indicates, that these tails are not caused by the resolution of the dE/dx measurement, but by an impurity in the samples. This indicates, that rejecting the tails from the resolution calculation is advisable indeed.

The method shown is only able to exclude the long tails in the residual distribution caused by misidentified particles, if their 'real' dE/dx_{exp} differs a lot from dE/dx_{exp} of the investigated particle type. If the two values are close together, this background will appear in the shoulder of the 'correct' part of the distribution. In such cases it is impossible to separate such tracks from the others. The width of the fitted function is increased by such tracks. A toy model was used to quantise this effect. For 'typical' tracks $\sigma = 0.12$ was set in Eqn. 5.3 to generate the density distribution for the residuals. The width of a gaussian fit to this function was used as a reference for the width of 'typical' tracks. If a real residual distribution is contaminated by wrong particles, they will contribute to the residual distribution at another mean value. For fixed momentum this mean value is given by the difference of dE/dx_{exp} for the involved particle types. The residual distribution of the contaminated sample is the sum of the one of the correct particle and the (shifted) contamination. The height of the contamination part is given by the fraction of wrongly identified particles in the sample. One can apply a gaussian fit to the contaminated dis-

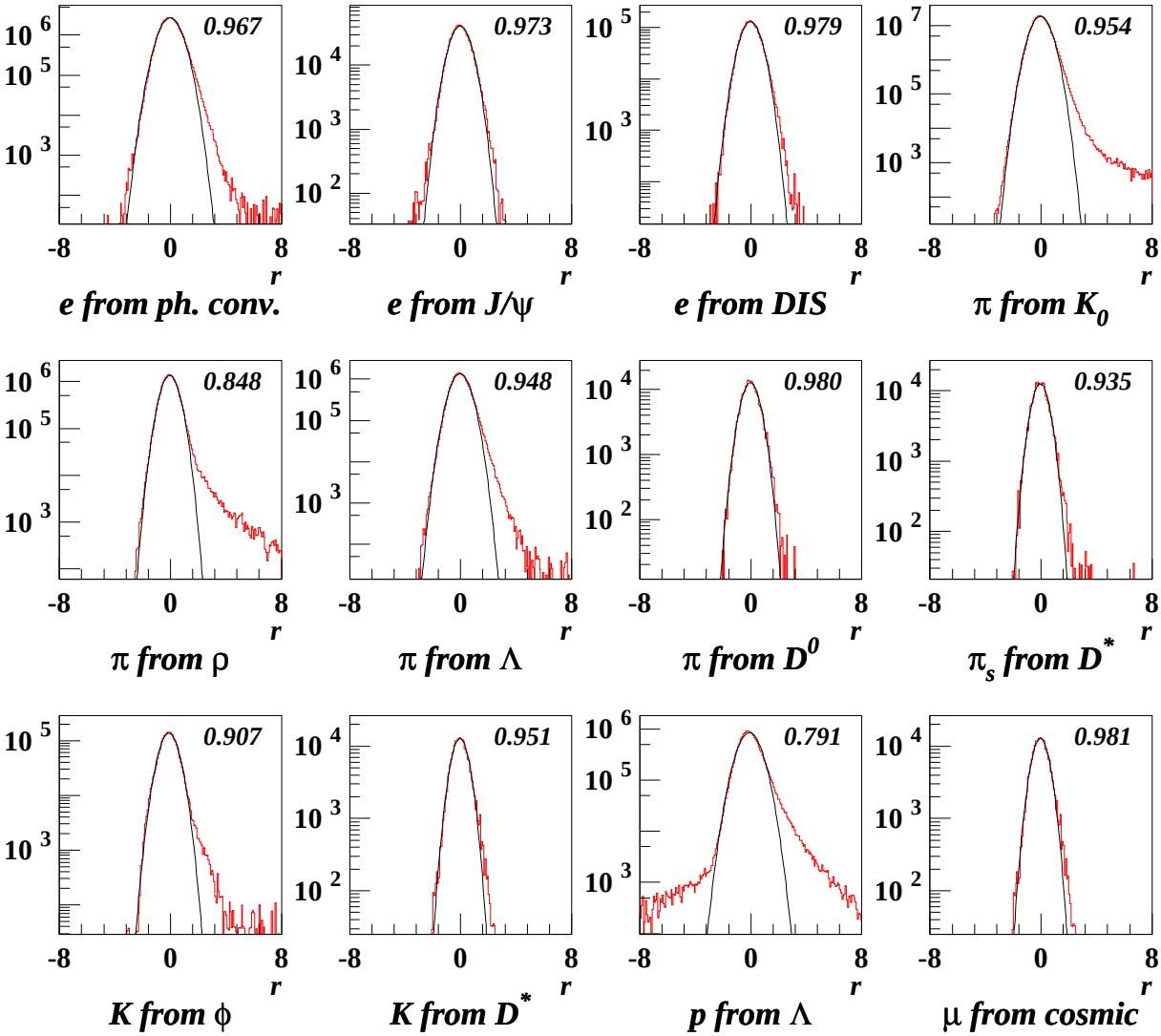

Figure 5.21: Distributions of the residual r for all test samples. Gaussian fits are shown, too. The numbers in the plots are the correction factors for the resolution measurement, given as the ratio of σ from the fit over the RMS. Details can be found in the text.

tribution to extract its width. Comparing this width to the previously measured reference width allows to quantise the effect of misidentified particles on the measured resolution.

This method was applied with an expected pion fraction of 1% in the samples. The effect on the measured resolution was $\approx 1.5\%$. As this number is only a rough estimate and not a measurement no corresponding correction was applied to the measured resolution.

Another source of a possibly wrong measurement of the resolution is the prediction dE/dx_{exp} itself. As the figures in Sect. 5.1 show, there are systematic differences left between the expectation and the mean dE/dx of the data samples. These differences vary depending on the momentum. As the residuals are calculated with respect to dE/dx_{exp}, they are widened by such variations. The size of this effect was measured with a Monte Carlo simulation for the photon conversion sample. On the one hand the 'usual' residuals were simulated as deviations from dE/dx_{exp}; on the other hand a phenomenological fit of

the dE/dx data in bins of $\beta\gamma$ was used to extract the 'real' expectation of this sample. The difference between this expectation and dE/dx_{exp} was added to the residuals. Finally one obtains two simulated distributions for the residuals: the one based on dE/dx_{exp} and another one containing the effect of systematic shifts between expectation and data. Comparing the width of these two distributions gives an estimate of the size of this effect.

The influence of the deviation of $\langle dE/dx_{meas}\rangle$ from dE/dx_{exp} in the photon conversion sample on the measured width of the residuals was found to be of the order of 0.5%. For most samples one expects an even smaller effect. Only for very small $\beta\gamma$ the data differs quite a lot from dE/dx_{exp}. For such samples this effect can be slightly larger. As the measurement based on a Monte Carlo simulation only gives an estimate of the size of the effect, and as this value was found to be small, it is not taken into account for the resolution measurement.

Finally one has to consider a disadvantage of this method: It provides only correction factors for whole samples, but the effect of misidentified particles on the measured RMS is strongly momentum-dependent. The larger the difference between the values of the BETHE-BLOCH curve for the two involved masses, the larger is the effect on the RMS. Consequently, results from strongly affected samples like $\rho \to \pi^+\pi^-$ have to be treated with great care.

5.2.3 Impact of the corrections on the resolution

For a proper measurement of the resolution one has to ensure, that the influence of the dE/dx-corrections on the resolution is treated correctly. This section does **not** treat the influence on the resolution of effects corrected for. Obviously, an effect influencing the dE/dx-measurement 'blows up' the spread if no correction is applied for it. The focus of this section is the direct influence of a correction function on the resolution. For example, a correction factor multiplied to all measurements changes their mean value as well as their spread.

The neighbourhood-effect correction is an additive correction. This implies, the spread of the dE/dx-measurements is not touched by this correction.

Most other corrections lead to factors applied to the measured dE/dx. Such factors do not affect the relative resolution: the measurement values are scaled and so is their spread.

Special care has to be taken for the drift-time-effect correction. In this correction the expected signal is calculated in the $(\overline{\psi'}, \theta)$-plane for tracks with the reference dE/dx values of 1 mips and 1.4 mips. A linear transformation from the measured signal $\overline{s_d}$ to dE/dx_{corr} is applied using these two reference points. Therefore, the slope of this linear transformation is the proper factor to transform the absolute resolution of $\overline{s_d}$ into the absolute resolution of dE/dx_{corr}. For the treatment of relative errors it is more convenient to investigate this correction as a transformation from the partially uncorrected dE/dx_{uncorr} (after Phase I corrections) to the corrected one. In this case one exploits the fact, that the correction is small: $dE/dx_{uncorr} \approx dE/dx_{corr}$. With a linear transformation $dE/dx_{corr} = a \cdot dE/dx_{uncorr} + b$ one finds:

$$\frac{\Delta dE/dx_{corr}}{dE/dx_{corr}} = \frac{a \cdot \Delta dE/dx_{uncorr}}{a \cdot dE/dx_{uncorr} + b} = a \cdot \frac{\Delta dE/dx_{uncorr}}{dE/dx_{uncorr}} \frac{dE/dx_{uncorr}}{dE/dx_{corr}} \approx a \cdot \frac{\Delta dE/dx_{uncorr}}{dE/dx_{uncorr}} :$$

The relative uncertainty scales with the slope a.

5.2.4 Splitting into 'intrinsic' and 'detector-side' resolution

In data one finds a $\beta\gamma$-dependence of the relative resolution (Fig 5.22 (a)). Focusing on the $\beta\gamma$-range where the BETHE-BLOCH curve is rising, the relative resolution falls. In the same range of $\beta\gamma$ the absolute resolution ((Fig 5.22 (b), based on the residual $r = dE/dx_{meas} - dE/dx_{exp}$) is rising. It seems that the realistic resolution is somewhere between the absolute and the relative case. To understand this, one has to look more closely on the ingredients which cause the resolution.

There are many independent sources contributing to the total resolution. The sources can be split into two classes: one is given by the variation of the probability for primary ionisations in the CTD gas, i.e. the variation of the ionisation per path length (intrinsic resolution), the other is given by the CTD components and the reconstruction code due to their limited accuracy in transforming the 'real' ionisation into a dE/dx_{meas}-value (referred to as 'detector-side resolution' in this section).

The intrinsic resolution has been described theoretically by LANDAU. It depends on the gas mixture, the pressure and the detector dimensions only. In terms of dE/dx-measurement corrections, the variations thereof already happen before the level, which can be controlled by corrections. They are part of the intrinsic statistical behaviour of gas ionisations (therefore the name 'intrinsic'). There is no chance to improve this part of the resolution by corrections.

At least some parts of the detector-side variations offer the chance for improvements, as some of them depend on measurable quantities, like e.g. the track topology. This work deals with the reduction of such variations. Most of the effects introduced in this work scale with dE/dx (only the neighbourhood-effect causes offsets in dE/dx). Therefore the dominant parts of the detector-side variations contribute relatively to the resolution.

The situation is different for the intrinsic resolution. In LANDAU's approach the probability density of the energy loss of high-energetic ionising particles is given by

$$d = L_s \left(\frac{E - E_{mp}}{\xi} \right) \quad , \quad \xi = \frac{cx}{\beta^2} \quad . \tag{5.6}$$

In this equation E_{mp} represents the most probable energy loss, x is the thickness of the sensitive area and c is a constant containing the detector-specific parameters. Thus LANDAU's description expects the resolution to be proportional to

$$\beta^{-2} = 1 + (\beta\gamma)^{-2} = 1 + (p/m_i)^{-2} \quad .$$

As one can see in Fig. 5.23, for high $\beta\gamma$ this factor is 1; the width of the LANDAU distribution, and therefore the absolute resolution of dE/dx_{meas}, is independent of the mean value dE/dx_{exp}. Only for small $\beta\gamma$ this factor becomes important. In order to investigate the resolution independently of the β^{-2} dependence, one has to divide the measured resolution by β^{-2} as shown in Fig. 5.22 (c).

One can use the result of Eqn. 5.2 to split up the measured resolution in its intrinsic and detector-side parts. One might object, that the width of the single-hit LANDAU curve as extracted from data in Sect. 4.3.1.2 is based on dE/dx_{norm} and therefore a relative quantity. However, the sample used for that calculation is the pion tuning sample which populates only the minimum of the BETHE-BLOCH curve. For such a sample, the difference between relative and absolute values is negligibly small.

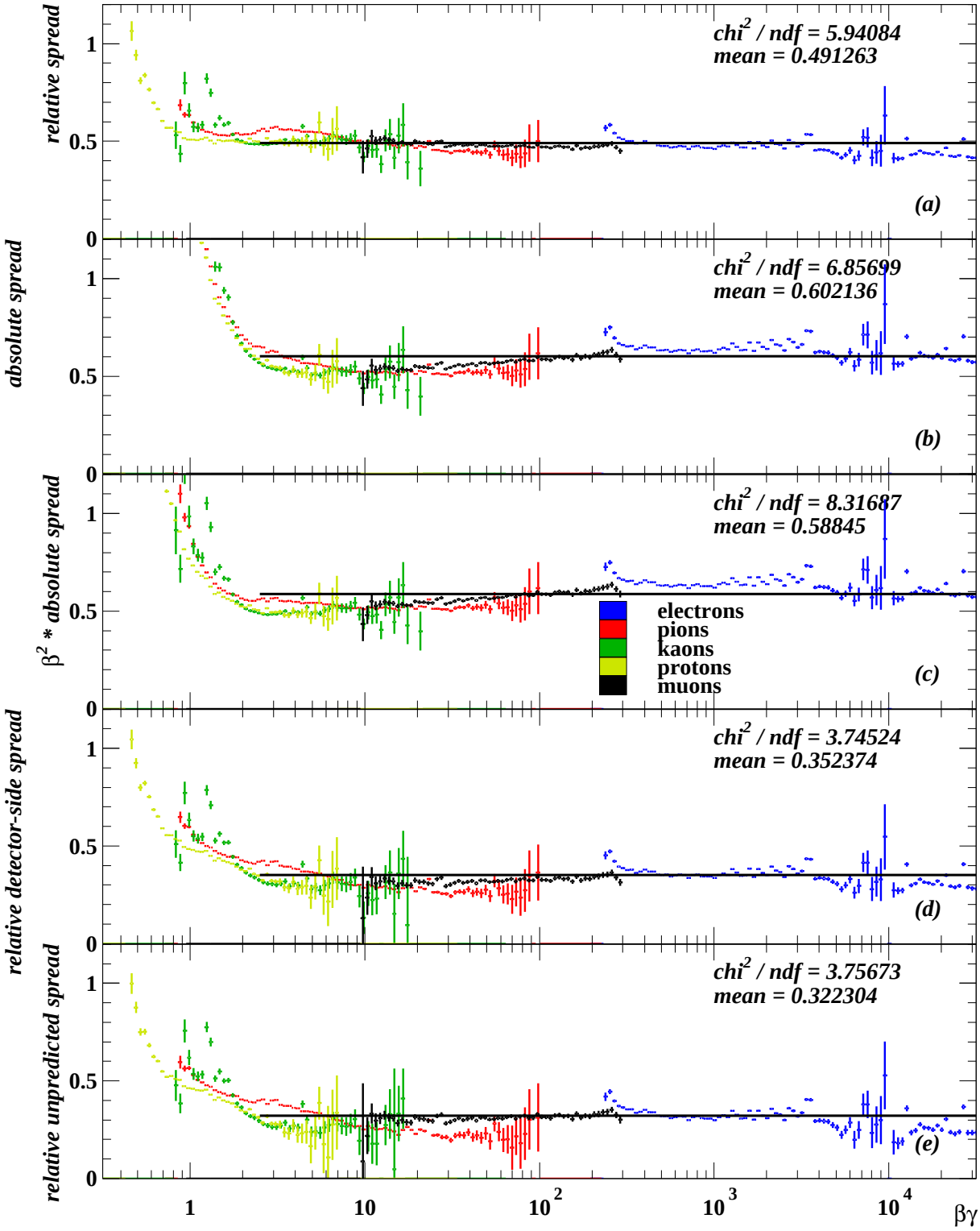

Figure 5.22: Single hit RMS after dE/dx corrections vs $\beta\gamma$ calculated as (a) relative resolution, (b) absolute resolution, (c) absolute resolution normalised to $\beta = 1$, (d) relative detector-side resolution (after subtracting the intrinsic resolution) and (e) relative resolution after subtraction of intrinsic and corrections resolution. The fitted mean value for $\beta\gamma > 2.5$ is shown as a line. Details can be found in the text.

As the intrinsic and detector-side resolutions are independent one can calculate the detector-side resolution as follows:

$$R_{det} = R_{overall} \ominus R_{intrinsic} \quad . \tag{5.7}$$

Figure 5.22 (d) shows the relative detector-side spread. Compared to the plots shown before, the $\beta\gamma$-dependence for the muon-sample disappears, but a rather more pronounced $\beta\gamma$-dependence for the pion-sample appears. After subtracting the measured uncertainty of the corrections as specified in Sect. 4.3.2.7 this dependence still remains (Fig. 5.22 (e)). More details about the treatment of the pion samples for the spread calculation will be given below in this section.

Down to $\beta\gamma \approx 2.5$ the relative 'unpredicted' spread is rather independent of $\beta\gamma$. For smaller values of $\beta\gamma$ the spread is still rising. There are many arguments to explain this. Most important is the fact, that the LANDAU-approximation is restricted to energies far above the atomic binding energies; in the low $\beta\gamma$-regime one leaves the validity range for this approximation. Another reason is related to the ZEUS CTD itself. In the low $\beta\gamma$-range one has to deal with very high dE/dx_{exp}-values. In this regime the probability for saturation is strongly increased. As mentioned in Sect. 4.3.1.4 for tracks with a very high number of saturated hits the factor to transform the truncated mean to a value compatible with the 'standard truncated mean' is very big, which implies, that uncertainties in this factor have a strong influence on the corrected dE/dx. Therefore tracks with very high dE/dx_{exp} are expected to have a bad dE/dx resolution.

Other contributions to the total resolution exist which do not fit into the scheme of intrinsic and detector-side resolution. The BETHE-BLOCH curve depends on p/m, therefore a mismeasurement of the momentum p causes an uncertainty in dE/dx_{exp} and contributes to the measured dE/dx_{meas}-resolution. In order to quantify this part of the resolution, a parametrisation of the momentum resolution for non-vertex-tracks was used [33]:

$$\sigma(p)/p = 0.005p \oplus 0.007 \oplus 0.001/p \quad . \tag{5.8}$$

For a given particle mass one can calculate the momentum-dependent variation $\widetilde{\sigma_p}$ of dE/dx_{pred} within the momentum resolution (Eqn. 5.8) as shown in Fig. 5.24. Depending on the mass of each particle, $\widetilde{\sigma_p}(p)$ has a minimum for the momentum at which the

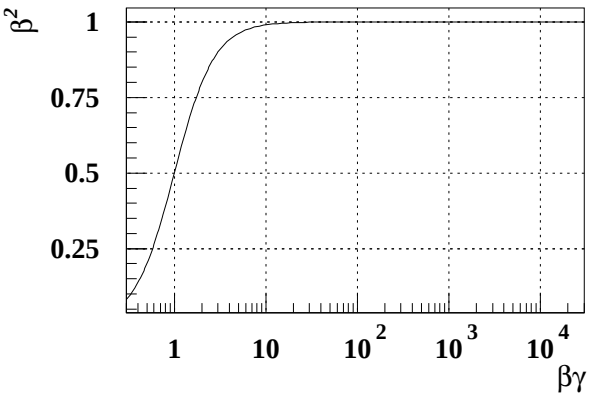

Figure 5.23: β^2 vs $\beta\gamma$.

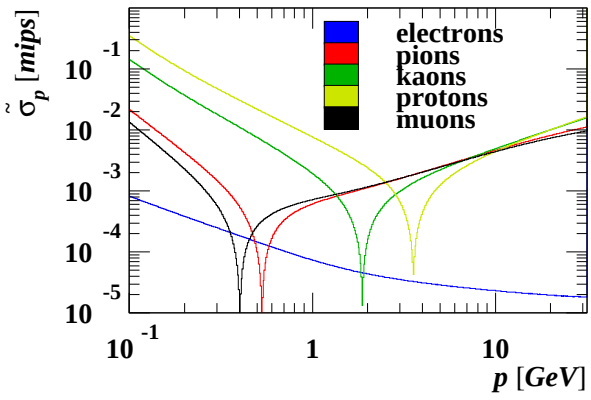

Figure 5.24: Resolution $\widetilde{\sigma_p}$ of dE/dx_{meas} due to the limited momentum resolution.

BETHE-BLOCH curve passes through its minimum (zero slope). For lower momenta the rising error is dominated by the big slope of the BETHE-BLOCH curve; for higher momenta the increasingly bad momentum resolution dominates $\widetilde{\sigma_p}$. Only for tracks with very high $\beta\gamma$ (plateau region) the vanishing rise of the BETHE-BLOCH curve can compensate for the bad momentum resolution: for electrons $\widetilde{\sigma_p}$ is extremely small.

Except for tracks with $p < 200\,\text{MeV}$ this part of the resolution is less than 0.01 mips and therefore negligible. For the distributions in Fig. 5.22 one has to be careful in handling this part of the resolution. The momentum p is a track variable and therefore its error is the same for all hits of the track. The applied method of unfolding the single hit resolution expects independent hit measurements, i.e. uncorrelated errors. The identical (correlated) inherited error based on the track-momentum measurement error is overestimated by a factor $\sqrt{n_h}$ in Eqn. 5.5. Nevertheless, compared to the overall variance the fraction coming from $\widetilde{\sigma_p}$ is far below 1‰ and therefore can be neglected.

Another source of uncertainty that has been investigated is the BETHE-BLOCH fit itself. The relative error of the fit is plotted in Fig. 5.25. For almost the whole accessible $\beta\gamma$-range this uncertainty is smaller than 2‰. In order to compare this quantity with the single-hit uncertainties as shown in Fig. 5.22 one has to scale this value with $\sqrt{n_h}$ as it is a correlated effect for all hits of the same track. One ends up with an effect of 1% compared to an unpredicted mean spread of 32%; the uncertainty of the BETHE-BLOCH fit is responsible for only $\approx$ 1‰ of the variance of the data and therefore can be neglected.

Comparing the detector-side resolution before and after dE/dx corrections (Fig. 5.26) one finds an overall improvement from 46% to 35%, which corresponds to a reduction of the variance by $\approx$ 40%. The slight change of χ^2/ndf from 4.4 to 3.7 documents, that also the $\beta\gamma$-dependent variation of the spread is reduced. One has to be rather careful with the interpretation of these numbers. As described in the case of the propagation of the momentum resolution into the dE/dx_{meas} resolution for single hits, any track-wide component is overestimated by a factor of $\sqrt{n_h}$. Even if such track-wide components were found to be small, such a factor of typically > 5 renders them non-negligible. The numbers given have to be treated as upper limits for the single hit spread; the real spread is expected to be much smaller.

The $(\rho \rightarrow \pi^+\pi^-)$-sample shows a very large spread for $1.5 < \beta\gamma < 6$. This is most probably caused by wrongly identified particles. In the corresponding momentum range the difference between dE/dx_{exp} for pions and kaons or protons is very big; already a small admixture of such particles in the sample can screw up the spread significantly. One can also see a very small spread in the $(\rho \rightarrow \pi^+\pi^-)$-sample for higher $\beta\gamma$. This is caused

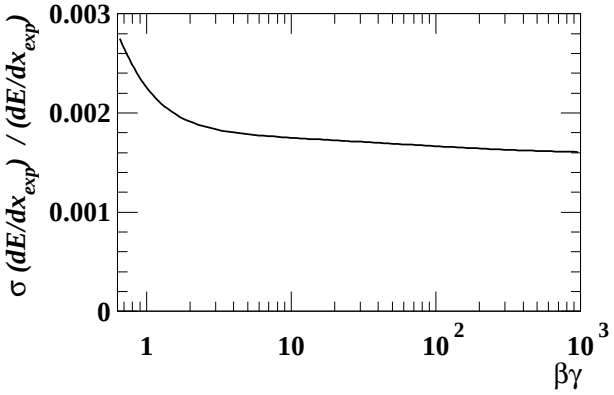

Figure 5.25: Relative uncertainty of the BETHE-BLOCH fit.

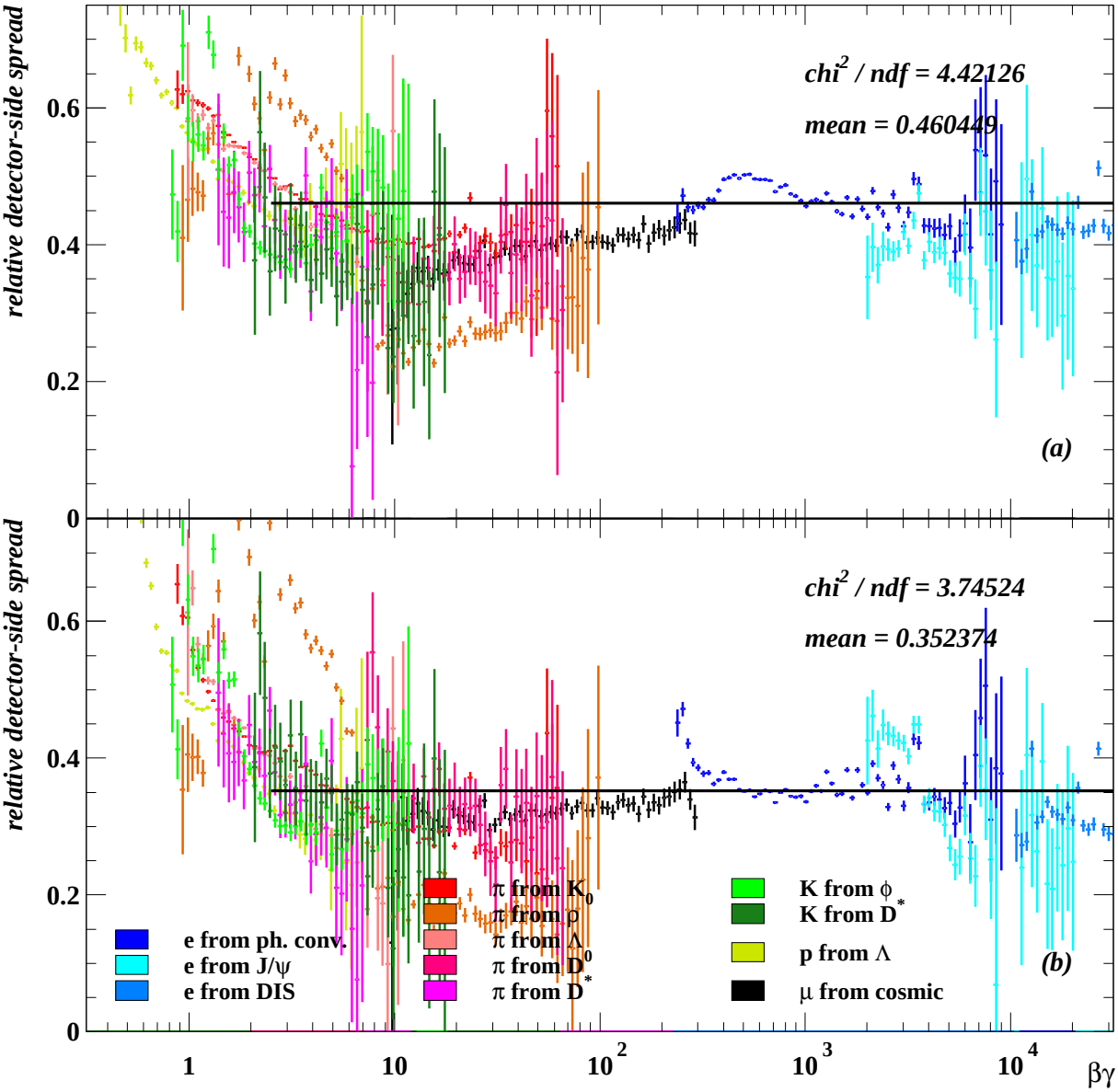

Figure 5.26: Single hit RMS after quadratic subtraction of the intrinsic resolution vs $\beta\gamma$, (a) before and (b) after corrections. The mean value for $\beta\gamma > 2.5$ is shown as a line.

by an overcorrection of the 'wrong particle effect' as described in Sect. 5.2.2. The mean value of the RMS of the whole sample is shifted properly. In this case of a strongly $\beta\gamma$-dependent effect, for low $\beta\gamma$ this leads to an undercorrection and in the high $\beta\gamma$-range to an overcorrection. Consequently the ρ-sample is not used for the calculation of the mean spread. Furthermore, all pion-samples suffer from the same disease. A similar behaviour (though less pronounced) is observed in the K^0-sample. To take this additional uncertainty into account, all pion samples are treated in the mean spread calculation only with half weights. One should also remark, that electrons from photon conversions ($\beta\gamma < 10000$) have a significantly worse resolution than other particles. This is not surprising as the topology of photon conversions nurture difficulties for a good measurement of dE/dx.

Comparing the different samples in Fig. 5.26 allows to estimate systematic differences in the dE/dx resolution due to sample-specific variations of the order of 10% of the resolution.

5.2.5 Overall dE/dx resolution

The previous sections documented, that the resolution of the measured dE/dx value depends on many parameters. For single tracks one can calculate proper values for the resolution based on their specific track parameters. Anyway, for comparison with other tracking detectors the reader might prefer to have a single global number for the resolution on hand, which is integrated over all tracks. Therefore such numbers are calculated here, using the full data from test-samples.

Before correction (i.e. after Phase I and run-by-run corrections) the overall resolution is 12.0%. [3]

After corrections this value shrinks to 10.8%.

In order to investigate the fractions of the uncertainties, which are removed by the corrections or which have identified sources, the proper quantity is the variance of the normalised dE/dx measurement. The partition of the total variance before corrections into the contributing fractions is:

43%	intrinsic variance of LANDAU distribution,
19%	removed by the corrections,
10%	measured variance from corrections,
≈ 3%	contamination of the samples with misidentified particles,
26%	remaining variance from unknown sources.

A part of the remaining variance can be observed in differences of the mean dE/dx between different data samples in Fig. 5.1 (b). These differences are responsible for a very big χ^2/ndf in the BETHE-BLOCH fit on the order of 100. As the fit uncertainty is dominated by the differences between samples one can take the quantity

$$\sigma_s = \sqrt{\chi^2} \cdot \sigma \left(\frac{dE}{dx}_{exp} \right) / \frac{dE}{dx}_{exp} \tag{5.9}$$

as a rough estimate of this part. This calculation leads to 2% remaining variance visible in sample differences, whereas the complementary 24% affect the investigated data samples simultaneously.

[3] The reader might be used to a much smaller value stated in other publications. The numbers given here are based on a real data sample, including tracks with unfavourable topology. In many cases published numbers for the dE/dx resolution are limited to ideal tracks with high p_t to insure uniform behaviour for the whole sample and to reject tracks with very high dE/dx, which suffer from the saturation effect and therefore worsen the resolution. Furthermore, such samples are restricted to tracks passing through the whole CTD, delivering the maximum available number of samples for the dE/dx measurement.

5.2.6 Summary of the resolution measurements

The findings about the dE/dx resolution are summarised as follows:

- The resolution scales with $\frac{1}{\sqrt{n_h}}$. This shows, that the dominant contribution to the track resolution is given by the single hit resolution. With the achievable accuracy the existence of correlated 'track-wide' contributions cannot be confirmed.
- Oscillations in the spread depending on n_h point to a dependence of dE/dx_{meas} on a parameter, which is reflected in the superlayer class of tracks. The size of these oscillations indicate an undigged potential for improvement.
- The 'intrinsic' resolution scales with β^{-2}. As for most tracks of interest β is almost 1, this resolution behaves like an absolute resolution.
- The 'detector-side' resolution dominantly scales with dE/dx; it can be treated as a relative resolution.
- The component caused by the limited momentum resolution is negligible.
- The different test samples vary in their single-hit spread of the order of 10%. One has to expect this number as a typical variation due to the sample selection.
- The 'detector-side' spread comprises that part of the total spread, which can be improved by corrections on the dE/dx measurement. Upper limits on this spread for single hits have been measured to be $\approx 46\%$ before and $\approx 35\%$ after corrections. Subtracting in addition the variance due to known uncertainties of the correction procedure itself, a spread of $\approx 32\%$ remains. Taking into account the estimate of the influence of wrongly identified particles in the test samples, all these numbers are reduced by $\approx 2\%$.
- Summing up all test samples and ignoring the dependence of the dE/dx resolution on track parameters (like the number of used hits or the kinematics), one measures a track-dE/dx resolution of 12.0% before and 10.8% after corrections. Almost half of the variance is caused by the ionisation process itself (intrinsic resolution), i.e. at least this fraction of the variance can never be corrected for. About 1/3 of the remaining variance vanishes thanks to the dE/dx corrections, 1/5 can be explained as the uncertainty of the correction method itself, $\approx 1/20$ can be traced back to be fake variance due to the contamination of the samples with misidentified particles, and a bit less than 1/2 remains without identified sources.

5.3 Separation power between particle types

The main application of the dE/dx measurement is the identification of particles. Therefore it is an important task to investigate the separation power between different particle types provided by the dE/dx measurement. This is not the same as investigating the resolution of the dE/dx measurement, as corrections to the measurement affect not only the resolution but also the expected dE/dx. If, for example, the resolution is improved, but the difference of dE/dx_{exp} for two particle types is reduced at the same time, it might happen, that the separation power is still unchanged or even worsened.

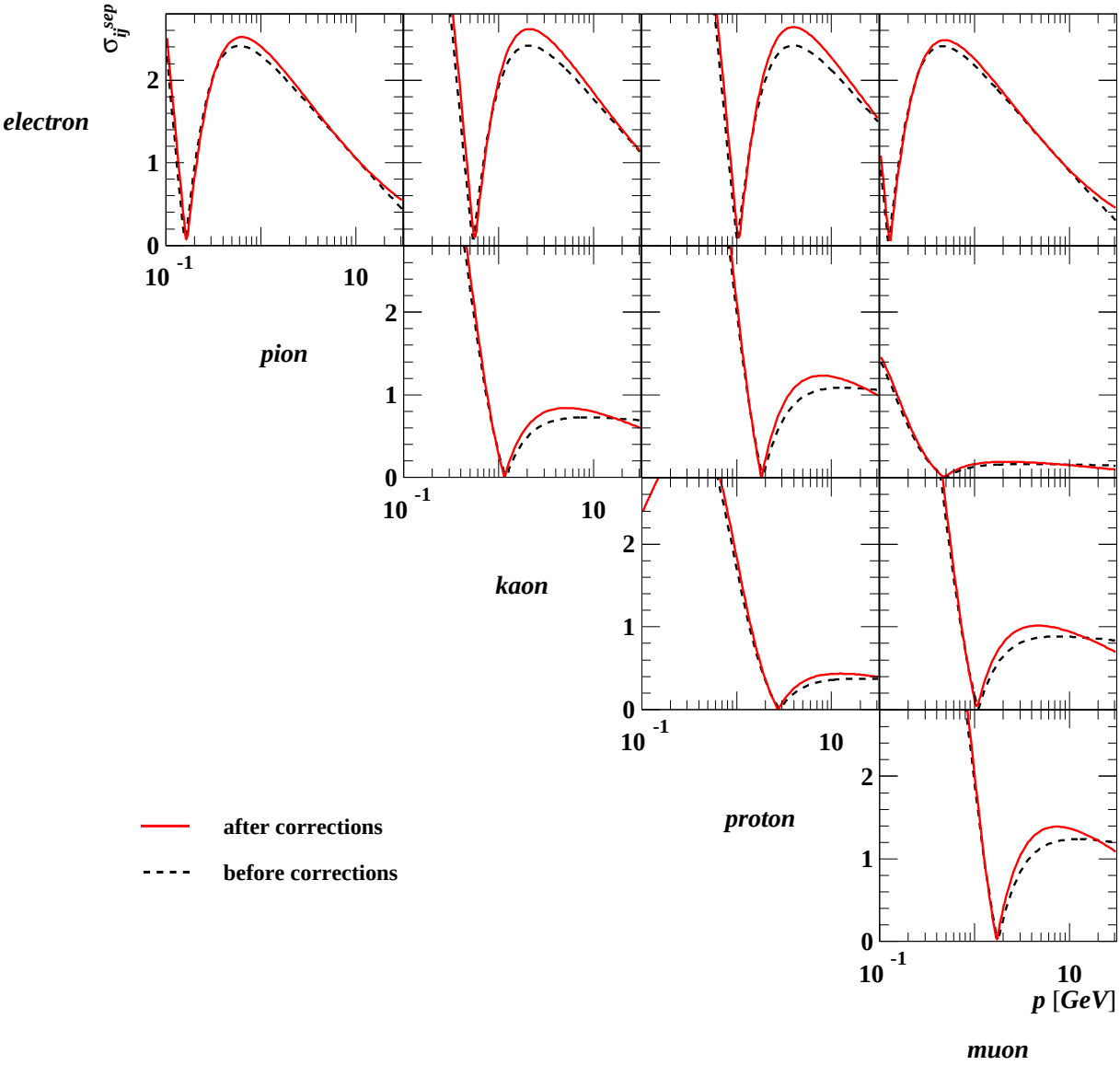

Figure 5.27: Separation power σ_{ij}^{sep} between different particle species calculated for tracks with 31 used hits. The resolution as measured in Sect. 5.2 was applied.

The most common visualisation of the separation power is to plot the difference of the predicted dE/dx for two particle types normalised to the quadratic sum of the two resolutions versus the track momentum: [4]

$$\sigma_{ij}^{sep}(p) = \frac{|dE/dx_{pred,\,i} - dE/dx_{pred,\,j}|}{\sigma\left(dE/dx_{pred,\,i}\right) \oplus \sigma\left(dE/dx_{pred,\,j}\right)} \quad (p) \quad . \tag{5.10}$$

As shown in Sect. 5.2, the resolution of the dE/dx measurement depends on many parameters. Nevertheless, for a fixed number of hits n_h one can use the measured intrinsic resolution in Eqn. 5.2 and the mean detector-side resolution as shown in Fig. 5.22 (d) in

[4] In the literature one often finds σ_{ij}^{sep} normalised to the resolution of one of the two particle species, i.e. one measures not the separation between the two species but the separation of one species to the mean expectation value of the other one. As in first order both resolutions are identical, such a σ_{ij}^{sep} is larger by a factor of $\sqrt{2}$ compared to the values given in this thesis.

order to calculate an estimate of the typical resolution. The corresponding curves for each combination ij of particle species are shown in Fig. 5.27, calculated for the mean number of hits for tracks passing all 9 superlayers, $n_h = 31$. For each combination of species there exists a momentum p_x, for which the corresponding BETHE-BLOCH curves cross each other. For that momentum σ_{ij}^{sep} falls to 0. The same happens for $p \to \infty$. For most particle combinations one finds an improvement due to the corrections in the momentum range between 1 GeV and 10 GeV.

The shown method of investigating the separation power does not take into account any properties of the investigated data. A more sophisticated and much more powerful estimator is the likelihood ratio which will be introduced and investigated in this section.

After an introduction to the computation of likelihood ratios in Sect. 5.3.1, their consistency will be proven in Sect. 5.3.2. There are various possibilities to apply likelihood ratios for particle identification. The most simple approach is to use the likelihood ratio for the particle hypothesis under investigation as a discriminator and to apply a cut on it. In this case one has to find proper cut limits by examining the distribution of likelihood ratios as shown in Sect. 5.3.3. Whenever applying selection cuts one has to keep under control their effect on sample purity and selection efficiency. The relation between these two quantities is the best indicator for the quality of any selection. Section 5.3.4 deals with this topic. In a more sophisticated approach one wants to look not only at single likelihood ratios, but at the whole set of likelihood ratios for all possible particle hypotheses. Only such a multi-dimensional approach allows to see correlations between different hypotheses and to react properly on these correlations. Special methods are required to visualise such high-dimensional distributions. Section 5.3.5 will focus on such visualisations and their interpretation.

5.3.1 Computation of likelihood ratios

Particle identification is based on the comparison of likelihoods for the possible particle hypotheses. Based on the results of Sect. 5.2 the most accurate way to compute these likelihoods (for particles i with known mass m_i) is given as follows:

1. The 'intrinsic' part σ_{int}^{hit} of the RMS of the residual for a single hit is computed based on the results of Sect. 5.2 as a function of β^{-2}. It therefore depends on p and m_i.

2. The calculable uncertainty Σ_{rel} as introduced in Sect. 4.3.2.7 is calculated.

3. The remaining 'detector side' part of the RMS is taken as the mean value from Fig. 5.26 (e). To transform it into an absolute width, it is multiplied by dE/dx_{meas}.

4. The RMS of the track dE/dx is defined as the squared sum of these three parts, divided by $\sqrt{n_h}$ and the 'slope factor' coming from the drift-time-effect correction (see Sect. 5.2.3).

5. According to Fig. 5.20 the RMS can be interpreted as σ in Eqn. 5.3.

6. According to Fig. 5.18 (a) the mean value μ of the fit is fixed to $\mu = -0.015$.

7. The height parameter A in Eqn. 5.3 is computed by

$$A^{-1} = \int_{-\infty}^{\infty} dr \exp\left(-\frac{1}{2}\cdot\left(\frac{\ln(r+1)-\mu}{\sigma}\right)^2\right)$$

   in order to obtain an area-normalised probability density function $f_\sigma(r)$.

8. The residual $r = dE/dx_{meas} - dE/dx_{exp}$ is computed.

9. The likelihood for a particle $i \in e, \pi, K, p, \mu, ...$[5] with mass m_i is given by

$$L_{m_i}(n_h,\ p,\ dE/dx_{meas}) = f_{\sigma(n_h,\ p,\ m_i)}(r) \quad . \tag{5.11}$$

To enable a comparison of the power of particle identification after applying the methods of this work with the status before (after applying the Phase I corrections and run-by-run corrections), one also has to compute likelihoods at uncorrected level. The methods applied to do this must be based on the notion as it was available in the past. The most important ingredient for the likelihood calculation is the expected dE/dx value. Depending on the kind of analysis there are three different approaches for this:

- Electrons measurable at ZEUS always have a very large $\beta\gamma$-value. They are all in the plateau-range of the Bethe-Bloch curve, therefore their dE/dx_{exp} was fixed to 1.4 mips.
- In the distribution of dE/dx versus p particles with very small $\beta\gamma$ (very high dE/dx) are clearly separated. In this case one can localise them by eye and describe them by phenomenological functions.
- In some cases a proton sample from Λ-decays has been used to extract an expectation value for dE/dx for small $\beta\gamma$. Compared to the method mentioned before this allows to describe a larger range in $\beta\gamma$ accepting systematic errors due to the sample selection.

The drawback of all three approaches is, that they only access limited $\beta\gamma$-ranges. Especially the middle part of the Bethe-Bloch curve cannot be described by them. Only clearly separable candidates can be identified by these methods. This is based on a totally different philosophy than a likelihood method.

Anyway, one wants to find a common basis to compare the status 'before' and 'after' corrections. Thus a huge effort has been spend for the uncorrected case by extracting a Bethe-Bloch fit to the dE/dx^{before} of the used test samples to extract the dE/dx^{before}_{exp}. This is much more precise than what was done in the past. Much more effort has to be put into the analysis than needed for the 'classical' approaches, as one needs to generate and understand the test-samples at first. This provides the reliable basis to do a 'before-after' comparison. Anyway one should keep in mind, that for this approach the state 'before

[5] Any long-lived charged particle which produces a track in the CTD can be in this list. This section deals only with the 5 explicitly named particle types, because the available test samples are restricted to these types. The deuteron is known to be visible in ZEUS, too. If one is interested in its likelihood, one has to add it to the list.

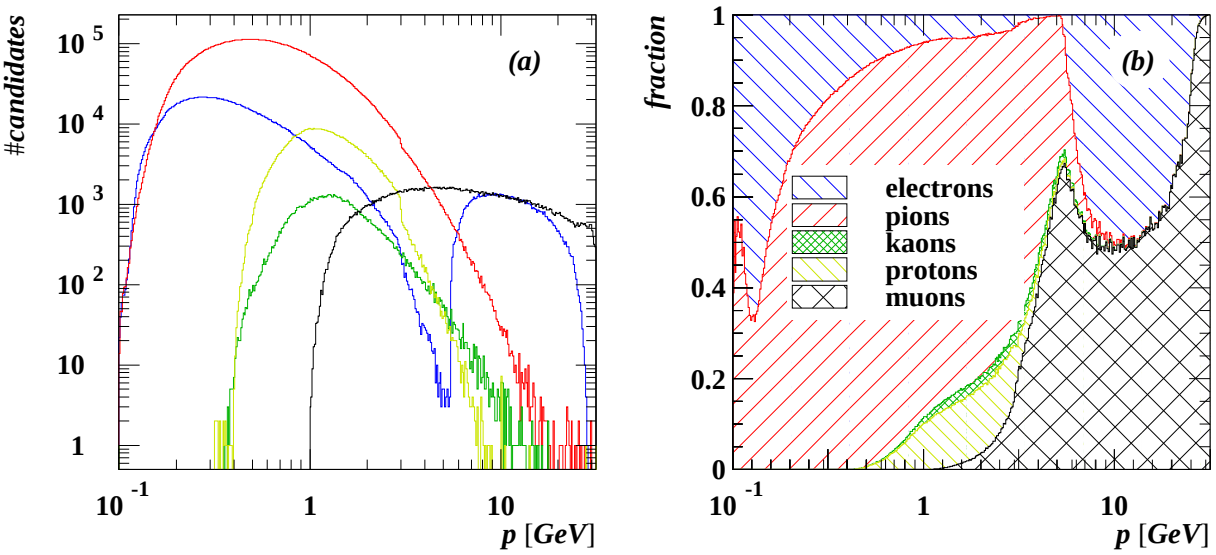

Figure 5.28: (a) Number of candidates in the test samples for each particle type in bins of the momentum. (b) A-priori probabilities for the particle types.

correction' is already much more sophisticated and precise than the level of using dE/dx measurement in 'classical' physics analyses.

The second ingredient for a likelihood is the residual. Most common and therefore also used here is a gaussian-shaped residual. Its width is taken from a measurement using again the test samples. Based on dE/dx_{exp}^{before} and a gaussian-shaped residual one can compute likelihoods for all particle types in the same way as for corrected data.

For a particle hypothesis one has to combine the likelihood values for all particle types in a proper way. For a given hypothesis, the estimator should give the probability, that this hypothesis is true. Such an estimator needs information on the composition of the sample before using the dE/dx measurement, which means, one needs to know the a-priori probabilities $a_i(p)$ for all particle types $i \in e, \pi, K, p, \mu$. These probabilities should be measured depending on the momentum p, as the likelihood for a particle hypothesis depends strongly on p. If one focuses on tracks with $\theta \approx 0$ or $\theta \approx \pi$ one also has to take care of the dependence on the number of used hits n_h, which is related to θ. This dependence is by far less important than the p-dependence: if the number of hits changes, the width of the residuals changes simultaneously for all hypotheses. If one relates these likelihoods to each other, to first order such a dependence cancels. In this section only the momentum dependence is considered for the a-priori probabilities. For the test samples the momentum-dependent candidate numbers and a-priori probabilities are shown in Fig. 5.28. These histograms show, that the mixture of the test samples varies strongly depending on the momentum of the tracks.

The last step is to compute the likelihood-ratio $L_r(i)$ for a particle hypothesis i:

$$L_r(i) = \frac{a_i \cdot L_{m_i}}{\sum_j a_j \cdot L_{m_j}} \quad . \tag{5.12}$$

A big benefit of the likelihood-ratio is its easy extension to more independent estimators than only the measured dE/dx: The combined likelihood from several estimators is the

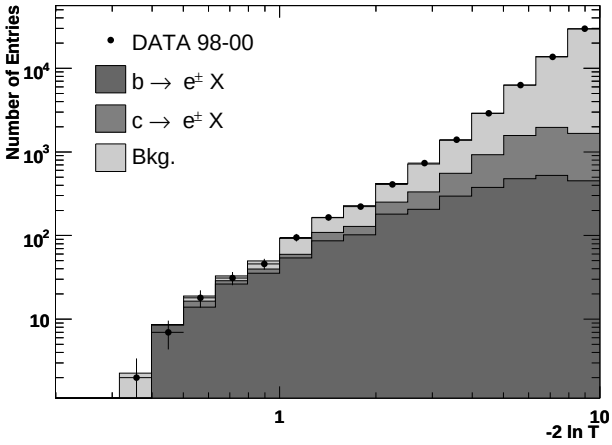

Figure 5.29: An example for the application of likelihood ratios, using the corrected dE/dx measurement. The Monte-Carlo-distributions for beauty, charm and background are fitted to data in the distribution of the likelihood ratio $-2 \ln L_r(e)$ (the variable T in the plot corresponds to $L_r(e)$ in this thesis) in order to measure the beauty and charm fractions. This measurement can be found in [6].

product of the partial likelihood values. Due to the limited separation power of the dE/dx measurement alone, for many applications such a combination is mandatory. An example, can be found in [6], where the likelihood using the measurement and corrections of dE/dx was combined with other likelihoods in order to achieve a proper separation of electrons from semileptonic decays of mesons with heavy-quark content (see Fig. 5.29).

5.3.2 Consistency check on the likelihood ratios

If the expectation dE/dx_{exp}, the residual, and the a-priori probabilities are described perfectly, the following interpretation of the likelihood ratio is satisfied: if the likelihood ratio for a hypothesis i has a value x, the ratio of tracks, which fulfil this hypothesis (the purity), is x too. This property can be tested in the following way: one can separate a test sample in bins of $L_r(i)$. For each of these bins the ratio of correctly identified candidates over all candidates is computed. For test samples this is possible because one knows, which of the track candidates really fulfil a hypothesis. According to the relation mentioned before, this ratio has to be the same as $L_r(i)$. The histogram of this ratio versus $L_r(i)$ should be a straight line along the main diagonal.

Figure 5.30 shows, that the data tends to follow the expectation, but there are obvious deviations. Especially before corrections one finds big differences between HERA I- and HERA II-data. These differences are strongly reduced by the dE/dx corrections and the more sophisticated calculation of the likelihoods.

Figure 5.30 also reveals, that except for very small L_r the kaons do not fulfil the expectation at all. This demonstrates the limitations of the accuracy of likelihood ratios. The kaon test samples are very small, they account only for $\approx 0.5\%$ of all test samples. Furthermore it is a feature of the test samples not to find kaons in the low momentum range, where their dE/dx is well separated from other particles. Thus large likelihood ratios for the kaon hypothesis can only be found for tracks with $p \approx 2\,\text{GeV}$ (dE/dx_{exp} for kaons is smaller than for any other particle type in this momentum range) and very small dE/dx_{meas}. Such candidates have a high probability to be mismeasured (a mismeasurement can cause an artifically small dE/dx_{meas}), thus the very low purity for high L_r in case of the kaon hypothesis should not be taken seriously. By the way, these candidates do not show up in the plots before correction. As the dE/dx resolution before correction is much worse, large likelihood ratios for the kaon hypothesis cannot be reached in the

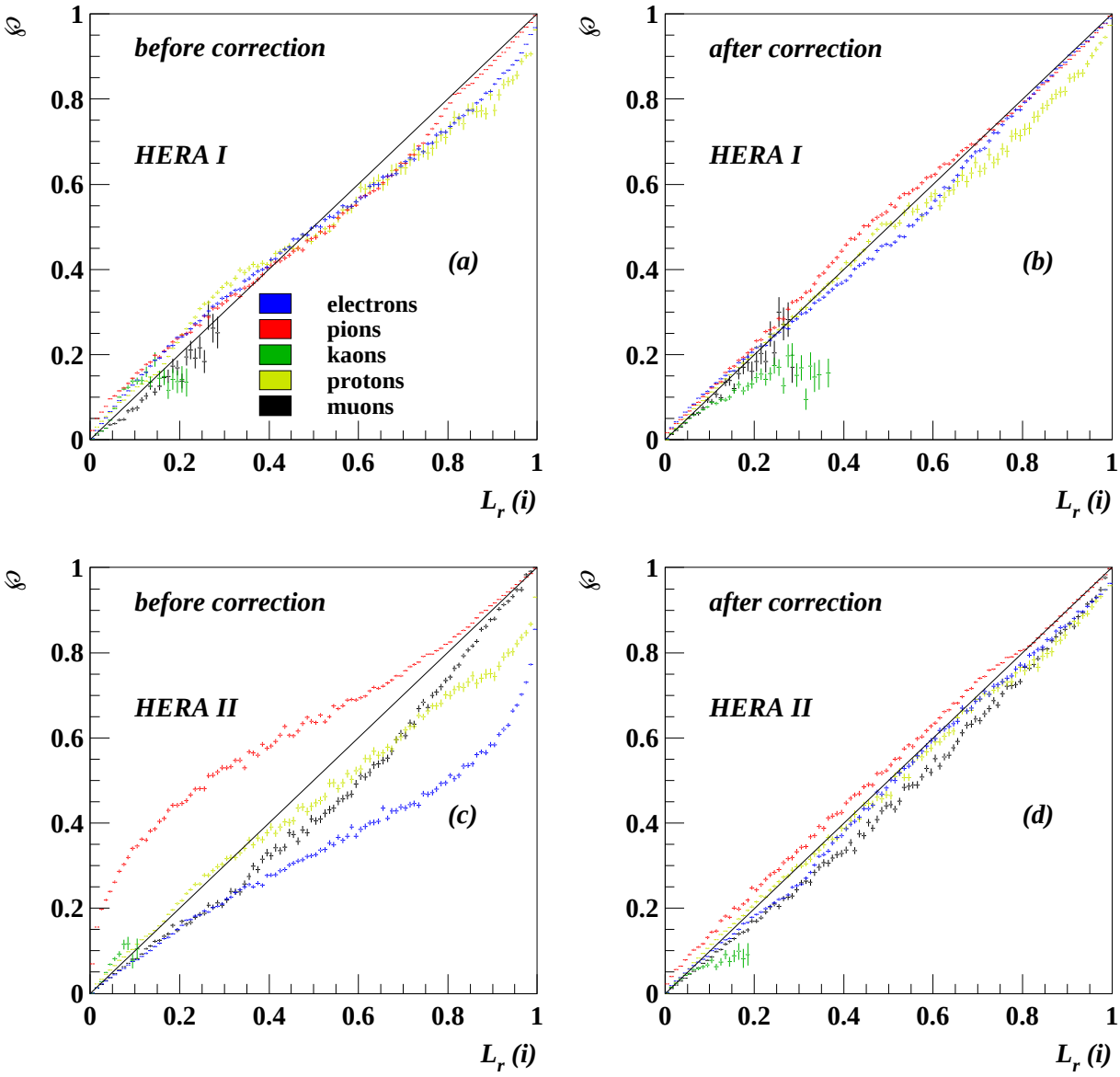

Figure 5.30: Ratio of correctly identified particles (purity $\mathcal{P}$) over all particles in bins of $L_r(i)$, $i \in e, \pi, K, p, \mu$. HERA I (a, b) and HERA II (c, d) are shown separately. All test samples are included in the plots. Results before correction (a, c), and after correction (b, d). Data points are only shown if they contain at least 100 tracks.

relevant momentum range.

5.3.3 Distribution of likelihood ratios

The likelihood ratio L_r depends strongly on the track momentum. Therefore it is informative to look at L_r-distributions in bins of momentum as shown in Fig. 5.31. In all these plots one finds dips in the L_r-distribution in the range of momenta, for which the BETHE-BLOCH curves for different particle types cross each other. In such crossing areas L_r is given by the a-priori probabilities of the two involved particle types. As these prob-

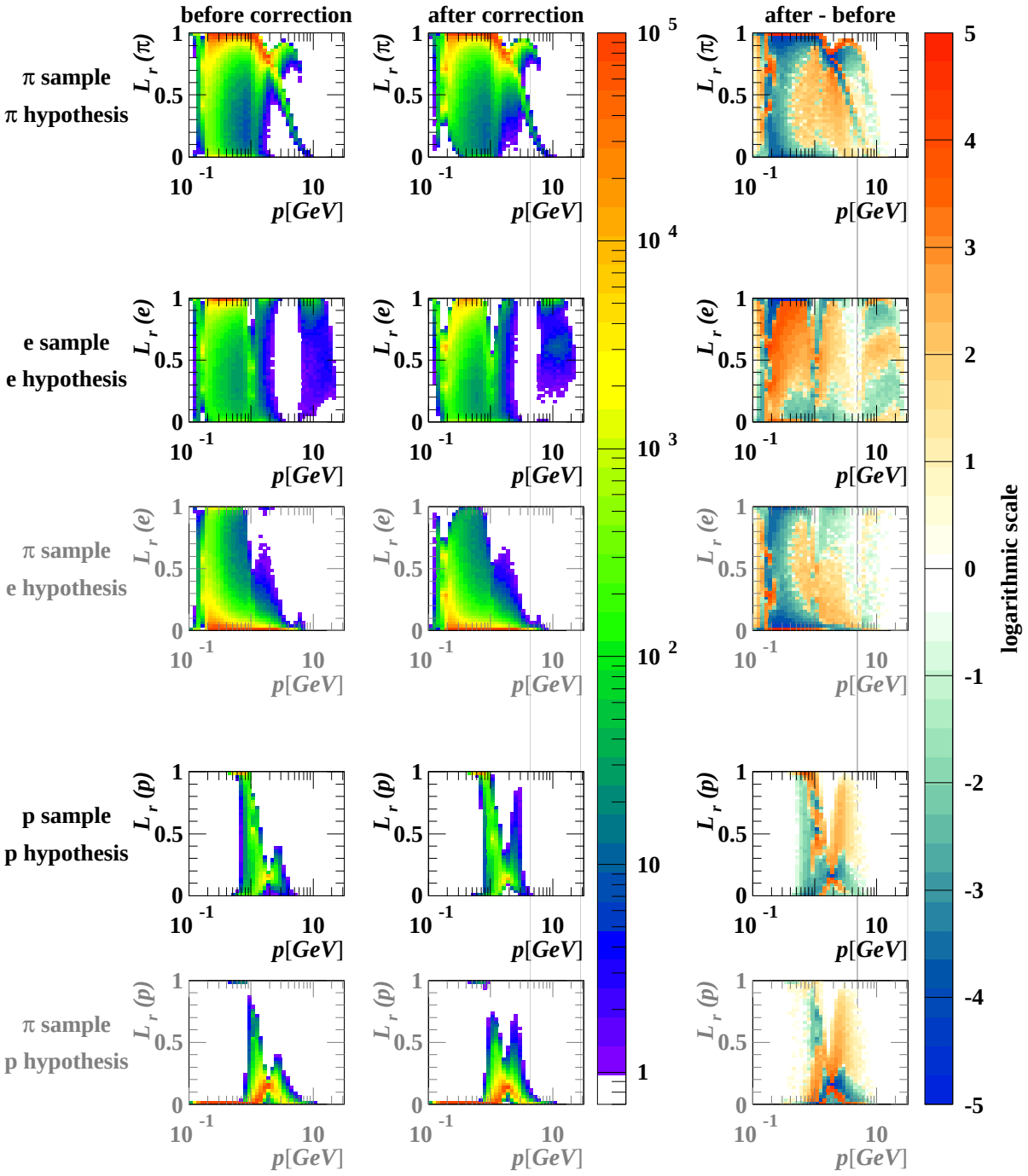

Figure 5.31: Likelihood ratio versus momentum. In the columns one can find the distribution before correction, after correction, and the difference of the histograms after and before correction to emphasise the changes. The colour code in the third column is a logarithmic scale; negative values are standing for $-\log_{10}(-(\#\text{after} - \#\text{before}))$. The rows are grouped for the likelihood hypotheses of pions, electrons and protons. The data in the plots are the corresponding test samples for the hypotheses. In case of the electron and the proton hypotheses also the pion samples as the biggest background source are shown. The full test samples for HERA I and II are used.

abilities differ between HERA I and HERA II data, two different values for L_r are highly populated in these crossing points.

In the pion sample (first row) already before corrections $L_r(\pi)$ is very large for most of the tracks. This reflects the high a-priori probability for pions. Comparison of the distributions before and after correction shows a slight improvement. The number of candidates ending up in the highest bin of L_r increases significantly.

For electrons one finds a less fortunate picture. For highest $L_r(e)$ the rate decreases. This reflects what one can already see in Fig. 5.1: before corrections electrons from photon-conversions are reconstructed with too high dE/dx values. As within the investigated momentum range the expectation dE/dx_{exp} for electrons is higher than for pions (the main background), the likelihood ratio 'wins' before dE/dx corrections. After corrections the distributions are much more realistic, so the apparent reduction of separation power due to dE/dx corrections is only a fake. The distribution of the pion sample with electron hypothesis shows, that also for electrons the separation is in fact improved. The number of pions with $L_r(e) \approx 0$ increased a lot, i.e. after correction many more pions are clearly separated from electrons than before.

The situation for protons is a bit complicated. First of all one finds much smaller typical values for $L_r(p)$ than in case of the pion or electron hypotheses, which is caused by the small a-priori probability for protons. In the crossing ranges of the proton band with the electron band ($\approx 1\,\mathrm{GeV}$) and with the pion band ($\approx 2\,\mathrm{GeV}$) one finds a reduction of $L_r(p)$ due to the corrections. This is related to slightly moved crossing points before and after corrections: in both cases the Bethe-Bloch curve is extracted from data; therefore the Bethe-Bloch curves before and after corrections are not exactly the same. Another interesting feature of the proton sample can be found in the low momentum range ($< 800\,\mathrm{MeV}$). The protons are well separated from other particles which is reflected by very high values of $L_r(p)$. Anyway, there are also candidates with $L_r(p) \approx 0$ in the sample. This shows, that the test sample is not totally clean; those entries are most probably pions in the proton sample. One finds something similar in the pion sample with the proton hypothesis. For most of the low momentum tracks, as expected, $L_r(p)$ is very close to zero. But there are also some tracks in the sample, which look like protons in the $L_r(p)$ versus p-distribution, which indicates, that they are indeed protons.

One concludes, that the investigation of the likelihood ratios offers a vague picture. On the one hand hints for improvements can be found, but on the other hand there are many parameters like the change of the Bethe-Bloch curve, which affect these distributions. It is not easy to distinguish between real improvements and 'fake' changes in these distributions. Furthermore, these plots show the strong dependence of the likelihood ratios on the a-priori probabilities.

5.3.4 Purity versus efficiency

A way to do particle identification is to apply a hard cut on the likelihood ratio for a certain particle hypothesis. Tracks with a value beyond the cut limit are declared as identified. Using this method, one is interested in the quality of the selection, represented

by purity $\mathcal{P}$ versus efficiency ϵ, defined as:

$$\mathcal{P} = \frac{\#\text{correctly selected candidates}}{\#\text{all selected candidates}} ,$$
$$\epsilon = \frac{\#\text{correctly selected candidates}}{\#\text{all available candidates of the proper type}} .$$

Depending on the kind of analysis one might be more interested either in high purity or in high efficiency. This consideration decides about the cut value for the likelihood ratio. The higher the cut level, the lower the efficiency and the higher the purity of the result.

As a-priori probabilities have a large influence on the likelihood ratio, purity and efficiency strongly depend on the preselection of the samples. A typical approach for a physics analysis is to investigate these numbers based on a Monte Carlo simulation. At this point one can also do a test based on the data coming from the test samples.

One can investigate purity and efficiency for all available particle types. Unfortunately, the kaon test sample is almost completely located in a kinematic range where its members cannot be distinguished from pions. Furthermore the kaon samples are extremely small. As already shown in Fig. 5.30 the kaons in the test samples cannot be separated from other particles using the dE/dx measurement. Consequently their purity and efficiency are not investigated. For muons one observes a similar situation. Their mass is almost the same as the pion mass, therefore a separation from pions is not possible with dE/dx methods. They appear in Fig. 5.30 as expected mainly due to the a-priori probabilities.

The electron, proton and pion samples are shown in Fig. 5.32. For all samples one can see, that a very weak cut in the likelihood ratio can improve the purity a lot without any efficiency loss. Such a cut removes only clearly separable background candidates. For the remaining tracks a clear separation is impossible; one can only search for a proper balance between purity and efficiency. For the electrons one finds a clear improvement after applying the dE/dx corrections. For instance with a purity of 90% one achieves an efficiency of 39% before correction and 60% after correction. At this point one has to remember, that such absolute numbers are strongly dependent on the investigated samples. Anyway, their ratio is much less sample-dependent, so one can say that for electrons the improvement in efficiency at a fixed high purity is of the order of 50%. The improvement in purity with a fixed efficiency is significant, as well. With a fixed efficiency of 50% the purity improved from 86% to 94%; more than half of the wrongly identified candidates are rejected by using the corrected dE/dx-measurement.

The proton sample benefits a lot from the corrections. With an efficiency of 30% one can improve the purity from 70% to 84%. Especially the highest purity range is worth to be mentioned. The plateau in the purity ranges up to an efficiency of 15% after corrections. For analyses needing highest purity, this is a very important improvement.

The pion sample is a very special case as anyway most of all tracks are pions. Even without any selection cut one reaches a pion purity of $\approx 80\%$. Consequently for the pions another way of presentation is used in Fig. 5.32 (c): the 'contamination' $1 - \mathcal{P}$ is shown versus ϵ in a logarithmic plot. One finds almost no change due to the corrections.

The conclusion is, that except for special cases (like proton identification) the improvement of particle identification is not the main result of the dE/dx corrections. The ZEUS CTD was not designed for a very good dE/dx measurement and that limits its performance in this field.

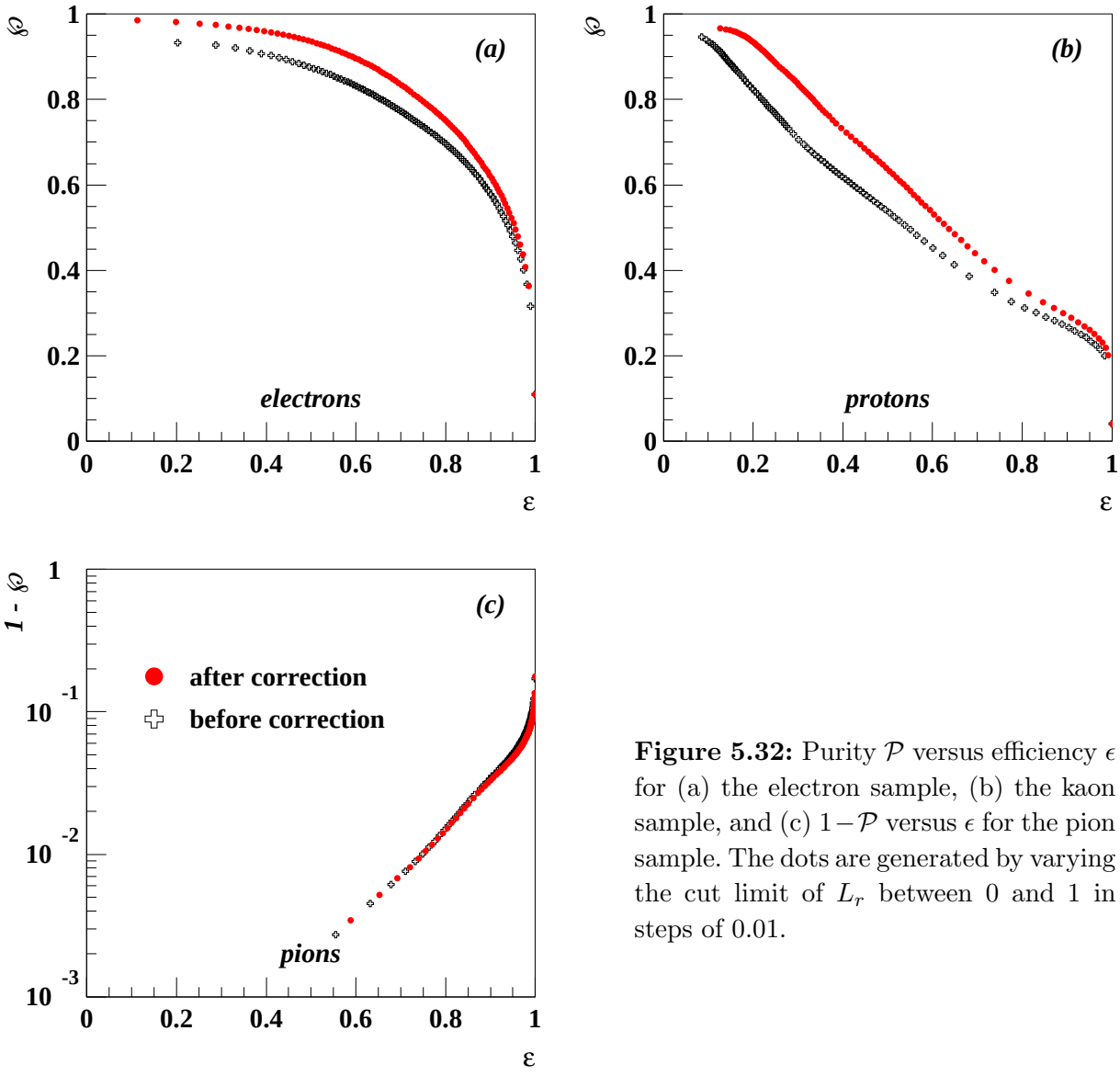

Figure 5.32: Purity $\mathcal{P}$ versus efficiency ϵ for (a) the electron sample, (b) the kaon sample, and (c) $1-\mathcal{P}$ versus ϵ for the pion sample. The dots are generated by varying the cut limit of L_r between 0 and 1 in steps of 0.01.

5.3.5 Multi-dimensional distributions of likelihood ratios

In Section 5.3.3 likelihood ratios were shown for single hypotheses. As there is the constraint on the sum of the likelihood ratios ($\sum_i L_r(i) = 1$), the single likelihood ratios are not independent. To get a feeling for the interdependence of the different likelihood ratios one wants to find a way to visualise them all together at the same time. As the space of all $L_r(i)$ is multi-dimensional one has to find a method to project the data onto the two dimensions of a sheet of paper without loosing too much information. This section deals with such projections. As they are technically complicated and one needs some practice for their interpretation, the projection method will be introduced step-by-step. Anyway, the information content of the plots in this section is high enough to be worth the trouble of reading and understanding them.

A straight-forward approach for showing the relations between the likelihood ratios is to generate a 5-dimensional scatter plot with $L_r(i),\ i \in e, \pi, K, p, \mu$ on each axis. As such high-dimensional plots cannot be presented in a proper way, one has to reduce its dimensionality. To start with, one can cancel the muon-hypothesis. As the mass of muons is

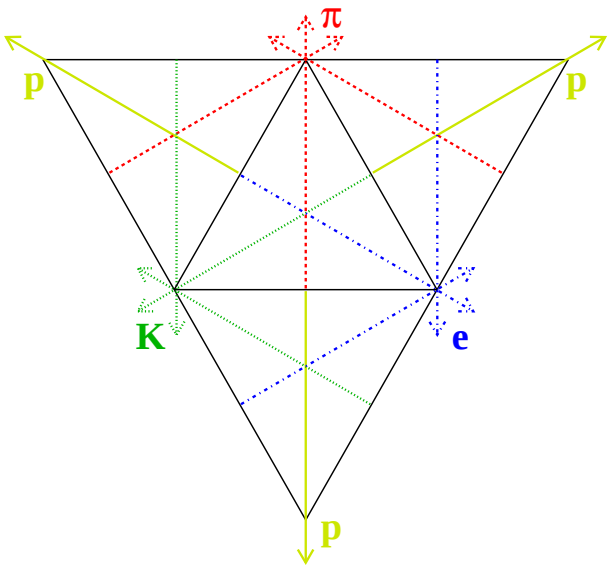

Figure 5.33: Schematic view of the 'flattened' tetrahedron. The axes of the four likelihood ratios $L_r(i),\ i \in e, \pi, K, p$ are shown.

very close to the mass of pions, these two particle types are almost undistinguishable; thus muons should be excluded from this kind of analysis. The constraint, that the sum of all probabilities has to be 1, cancels another dimension, so one ends up with a 3-dimensional scatter plot. To be more explicit, one can arrange the 4 axes for the 4 particle types in a 3-dimensional tetrahedron. Each track corresponds to one point inside this tetrahedron. One still has to reduce the dimensionality of this plot by one to be able to print it. One way to do this is to project all points within the tetrahedron to all four surfaces of the tetrahedron. The surfaces can then be shown in 'flat' two-dimensional plots.

This is a quite tricky way to show relations between likelihood ratios. It needs some further discussion to make the reader more familiar with the interpretation of such plots:

The surface of the tetrahedron consists of four triangles. Each triangle represents the distribution of L_r between three particle types. The edges of the triangles represent the probability $L_r = 0$, in the corners one has $L_r = 1$. The four triangles which make up the surface of the tetrahedron represents all possible combinations of three particles. Figure 5.33 shows the axes of the four possible $L_r(i)$ in such a 'flattened tetrahedron'. For each particle type there is one corner where all corresponding axes are crossing. These corners, representing clearly identified particles, are labelled with the particle name. The same arrangement is kept for all plots of this type (in the following named 'tetrahedron plots').

This chapter deals with the visualisation and interpretation of tetrahedron plots. In the Sect. 5.3.5.1 different projections will be introduced, focusing on different aspects of the visualised distribution (direct interpretable distributions, emphasing the ranges with highest statistics using a fish-eye view, investigation of the changes due to dE/dx corrections). Sect. 5.3.5.2 presents an introduction to migration plots, showing differences of likelihood ratio before and after dE/dx corrections. Both sections make use of the knowledge about the true particle type within the test data samples. In Sections 5.3.5.3 and 5.3.5.4 the momentum dependence and hit-number dependence of the likelihood ratios will be inspected. These distributions are important tools for an analysis framework, as they are related to the data sample only via the a-priori probabilities. Section 5.3.5.5 will give a short summary of this chapter.

5.3.5.1 Visualisation of likelihood ratios in tetrahedron plots

The projection of entries within a tetrahedron onto its surface can be carried out in two different ways; it can be parallel or focused to a point. Both projection methods have their specific benefits. Details about their difference, using the pion data sample as an example, are discussed in App. I. In that appendix it is also shown, that most of the entries are located close to one of the surfaces of the tetrahedron. This implies that the differences between the two possible projection methods are small. Furthermore, it motivates to limit the projection depth to a certain limit. Such a limitation works as if the tetrahedron is opaque: if one looks onto one of its surfaces one can only see the entries close to this surface.

All tetrahedron plots in this chapter are using the point projection and the limitation of the projection to entries close to the surface.

For the electron sample three tetrahedron plots were chosen to be shown in Fig. 5.34. Most of the entries are very close to the edges of the tetrahedron. In order to visualise this range in more detail, an inverted fish-eye view was applied for each triangle. Inverted fish-eye means, the areas close to the edges are stretched whereas the centre of the triangle is shown in a condensed way. The transformation between the linear projection and the inverted fish-eye-view represents an area-density transformation in a triangle. In order to keep the colour-code unchanged, the entries in the histogram have to be reweighted with the reciprocal area-density. The result of this transformed view is found in Fig. 5.34 (b). Some level lines for the electron hypothesis are added to the plot. Especially the outermost ranges are very strongly expanded; the outermost level lines shown in this plot indicate likelihood ratios of 0.1% and 99.9%. For the other hypotheses one should visualise similar level lines; showing all of them would render the plot less concise. In the range close to the edges of the triangles one observes ranges in red colour, indicating a very high number of entries. Before applying the inverted fish-eye transformation, these entries were located so close to the border of the triangles, that they were hidden by the lines surrounding the triangles. The aim of this transformation is obviously fulfilled: one sees many more details in the ranges of almost zero and almost 100% probabilities. For example, in this visualisation one finds no entries in the e-p-π-triangle close to the e-p-edge: due to the very high a-priori probability for pions the probability $L_r(\pi)$ only goes down to zero, if the candidate is very well identified as an electron (it appears in the electron corner in the tetrahedron).

The same kind of plot can be filled with likelihood ratios before dE/dx correction (Fig. 5.34 (c)). The general shape is similar to that after correction, the most obvious difference is found along the edges for $L_r(\pi) = 0$. Before correction there are entries in this range, which disappear after correction. This reflects the badly described resolution before correction. As an example one may focus on the entries close to $L_r(K) = 1$. There is a small (but existing) number of candidates in this range before correction, which totally disappear after correction. Very high kaon probabilities (especially with the constraint of small kaon a-priori probabilities) are only possible, if the measured dE/dx value matches very well with the kaon hypothesis and is far off the bands of any other particle type. Such entries disappear after correction, because these are tracks with a bad resolution, which is found correctly by the more sophisticated calculation of residuals after correction. Therefore these candidates pick up some probability for other particle types and move away from the kaon corner.

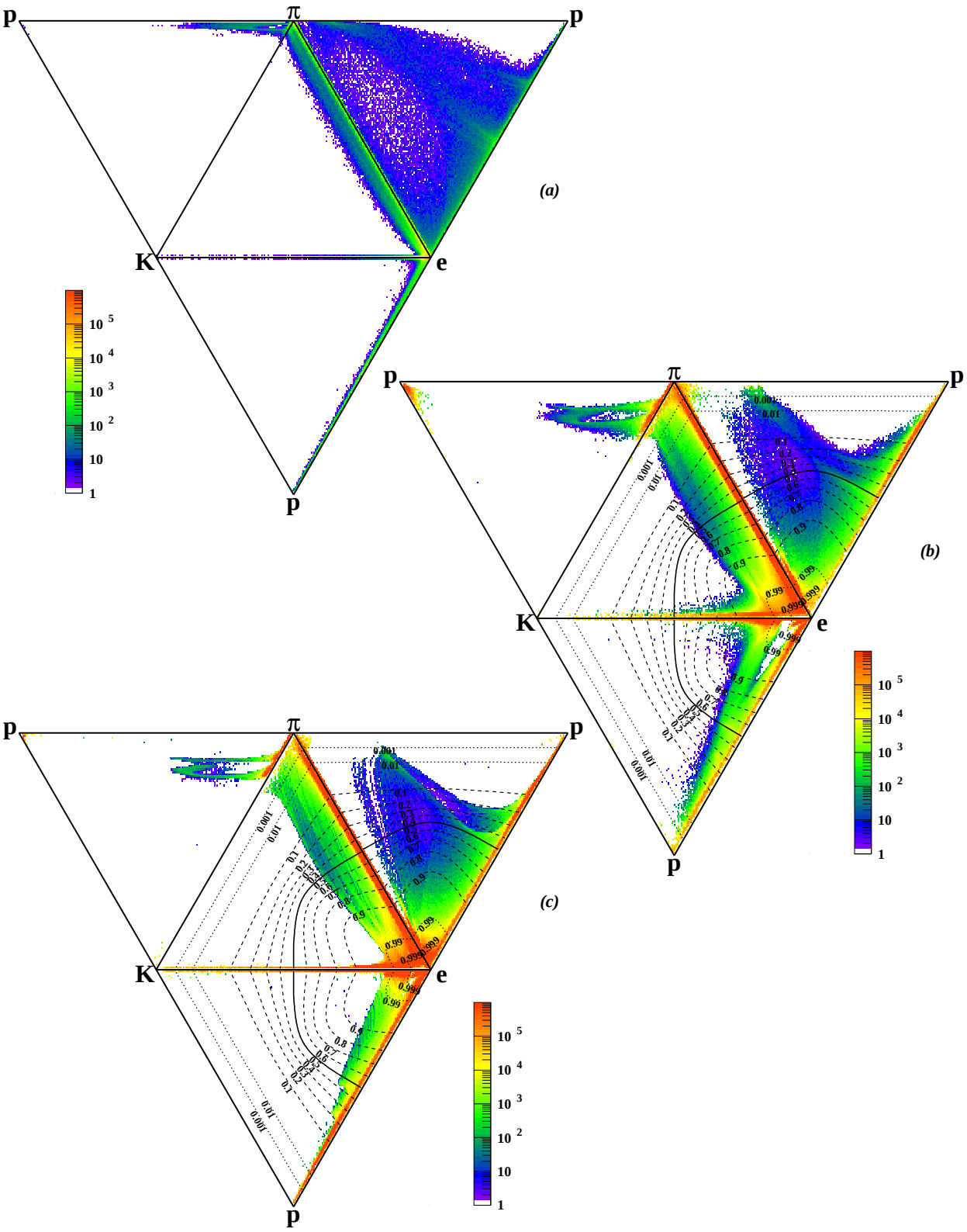

Figure 5.34: Likelihood ratios of the preselected electron sample point projected to the surface of the accessible tetrahedron. (a) corrected data in standard view, (b) corrected data in inverted fish-eye view, (c) uncorrected data in inverted fish-eye view. In case of the inverted fish-eye view contour lines for constant probability for the electron hypothesis are shown.

Comparing the situation before and after correction one finds a reduction of the number of candidates very close to $L_r(e) = 1$. One might assume, that the dE/dx correction make the electron identification worse than it was before correction. This is not true! The very high probabilities for the electron hypothesis are fake. As Fig. 5.2 shows, the dE/dx of electrons from photon-conversions is reconstructed as much too high before correction. Just by chance in the corresponding momentum range the BETHE-BLOCH curve for electrons is higher than for any other particle type. As the shape of the residuals is falling very steeply, the electron hypothesis 'wins' for candidates with such mismeasured dE/dx values. Therefore the successful electron identification is artificially increased before correction.

A detailed comparison of the likelihood ratios before and after dE/dx correction for the proton sample is given in Fig. 5.35. Before correction one finds many protons with an electron probability of more than 50%. The separation from pions is even worse. The latter problem is not solved by the corrections. For high momenta ($> 1.5\,\mathrm{GeV}$) the pion and proton bands are too close together to allow an efficient separation. But the separation from electrons improves a lot. There are only a few protons left with $L_r(e) > 0.5$. This matches with the result mentioned earlier, that the proton-finding efficiency improves due to the dE/dx correction. The improvement is also investigated by looking at the difference of the histograms 'after-minus-before correction' (Fig. 5.35 (c)). One can clearly see a reduction of the number of candidates close to the electron corner.

This plot also shows an interesting structure. There are bands of reduced numbers of candidates next to bands of increased candidate numbers. Such migrations happen, when the predicted BETHE-BLOCH curve or the resolution changes. One has to be very careful with the interpretation of this plot. For example in the K-p-e-triangle for $L_r(p) > 0.5$ the entries have moved a little bit towards the kaon corner ($L_r(K)$ slightly increased by less than 0.01). The value of $L_r(p)$ is almost unchanged, so even if the plot suggests strong changes, in terms of proton identification the changes are negligible.

Close to the edges of the triangles one observes in Figure 5.35 (a) several clearly separated entries with high counting rates. This is an artefact of the visualisation in the inverted fish-eye view. Close to the edges the weight for single entries is very high. One should read this like a histogram with very finely binning and a small number of entries: a few bins are far higher than the expectation whereas the neighbouring bins remain empty. A proper interpretation is to 'smear' the rare entries over all bins.

5.3.5.2 Migration of likelihood ratios

Another way to investigate the change of likelihood ratios due to the corrections is to look at the distribution of the change of likelihood ratios $\Delta L_r(i) = L_r(i)_{after} - L_r(i)_{before}$. These migrations can be shown in a way similar to the tetrahedron. Restricting to one surface of the tetrahedron one finds, that the values ΔL_r are distributed within a hexagon: the axes for the different hypotheses are the same as for the tetrahedron with the bounding condition $-1 \leq L_r(i) \leq 1$. A schematic view of the hexagons is given in Fig. 5.36. If the likelihood ratios for a candidate do not change at all, the candidate will appear in the centre of a hexagon.

The corresponding plot for the proton sample is shown in Fig. 5.37. For most of the entries the likelihood ratios are almost unchanged; they appear in the centre of the hexagons. In many cases only two likelihood ratios are changed whereas the other hypotheses stay

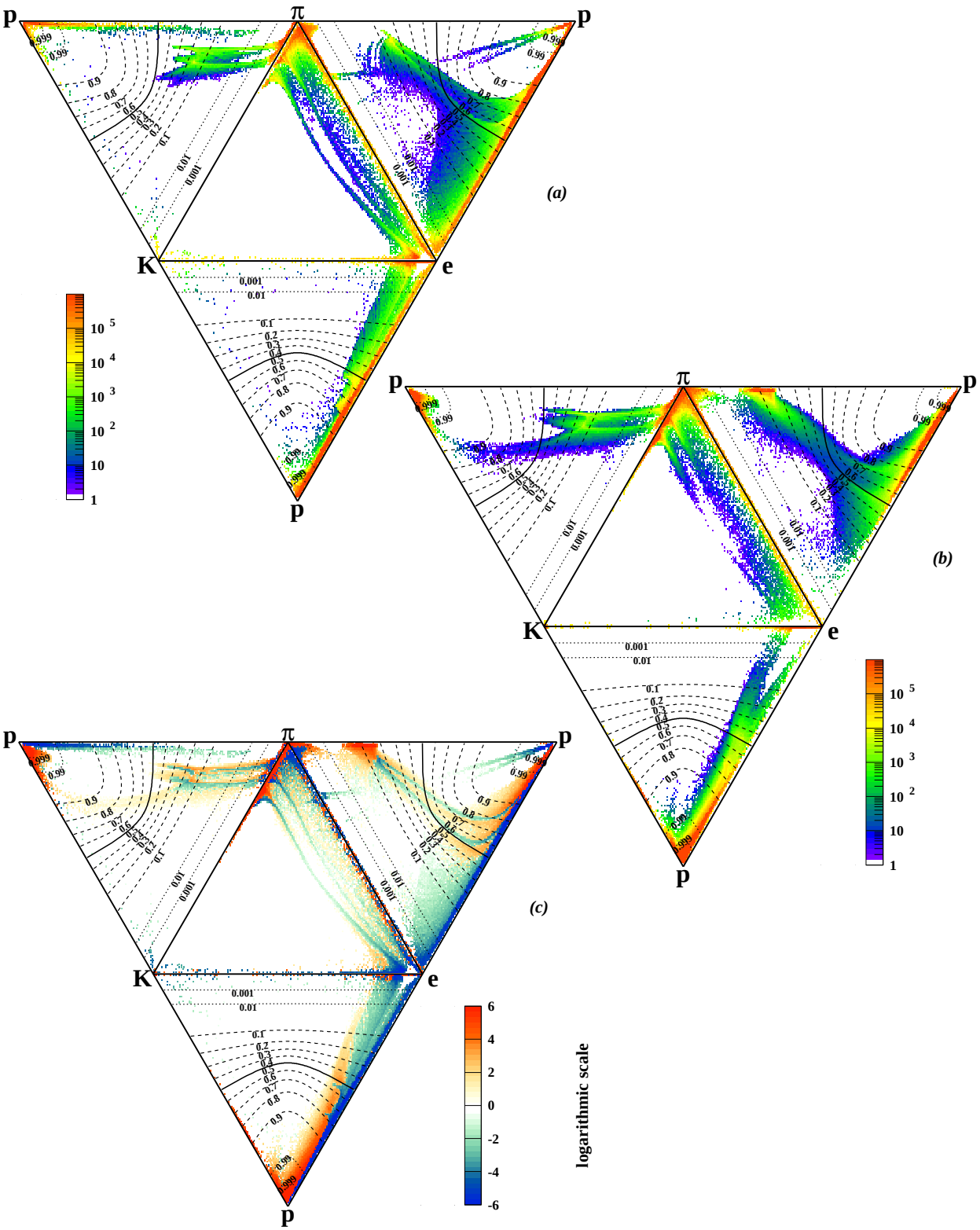

Figure 5.35: Likelihood ratios of the preselected proton sample point-projected to the surface of the accessible tetrahedron, using the inverted fish-eye view. The contour lines for constant $L_r(p)$ are shown. (a) uncorrected data, (b) corrected data, (c) difference corrected - uncorrected rate, using a logarithmic scale. Negative values stand for a higher number before correction.

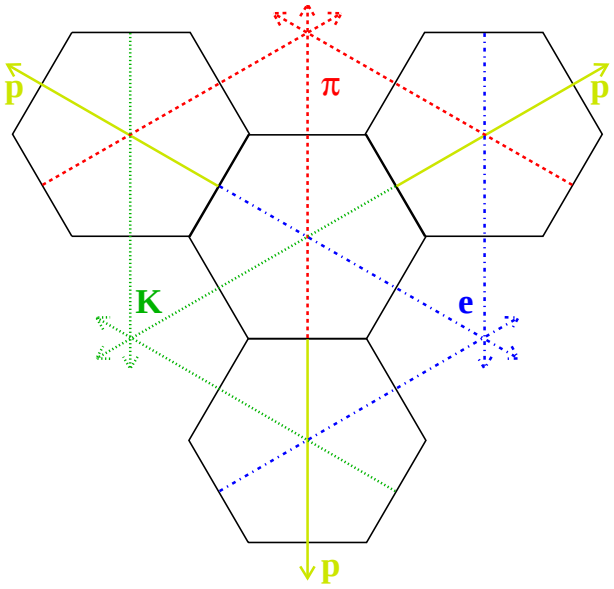

Figure 5.36: Schematic view of the range of values for migrations of L_r. The axes of the four likelihood ratios $L_r(i),\ i \in e, \pi, K, p$ are shown.

the same. These kinds of candidates appear on a straight line between the centre of a hexagon and one of its corners. Figure 5.37 (a) and (b) both show the same distribution, once with a linear scale and once using the same inverted fish-eye view for the sub-triangles of the hexagons as used in previous figures. For the hexagons this kind of view enlarges the ranges around the three axes connecting oppositely placed edges of the hexagon. As these three axes are crossing in the centre of the hexagon, the enlargement in that range is maximised. The enlarged ranges are exactly the ranges, where most of the statistics cumulate. Therefore this view is optimised for the given histograms. The price one has to pay for it are strangely shaped and not even differentiable level lines. So both views have their characteristic benefits: whereas the linear plot gives a good feel for absolute changes, the inverted fish-eye view allows to see the details of the mostly populated ranges.

In case of an increase of $L_r(p)$, the corresponding entry in the histogram appears in one of the hexagons in the positive half according to the p-axis (in that half, where the label p is written to one of the edges). Figure 5.37 shows, that such an increase happens more often than a decrease; the dE/dx corrections improve the proton identification. This result was already found before with much simpler approaches. However, the migration plots offer more details about the change of the $L_r(i)$. For example in the p-K-π-hexagon one can find a cloud of candidates at the lower-left side of the centre. This direction shows, that these candidates reduced their $L_r(\pi)$ in favour of $L_r(p)$ together with a slight increase of $L_r(K)$. This is a correlated effect (the sum of the likelihood ratios within the projection has to be 1). One can see in this hexagon that for the majority of candidates most of the changes happen between the pion and the proton hypotheses, whereas the change of the kaon hypothesis is small. But there is also a smaller subclass of candidates with almost unchanged $L_r(\pi)$ and (strongly) increased $L_r(p)$. This means, some of the protons were clearly misidentified as kaons before correction, after correction the identification is correct.

The plots also show that the biggest changes are happening in the p-π-e-triangle. These are the three particle types with the best separation of the Bethe-Bloch curves, thus changes in the resolution are very pronounced in this subsystem. Most important is the improvement in the proton-electron separation (the entries between the centre and the upper right corner). High statistics can be found in the whole range of possible migra-

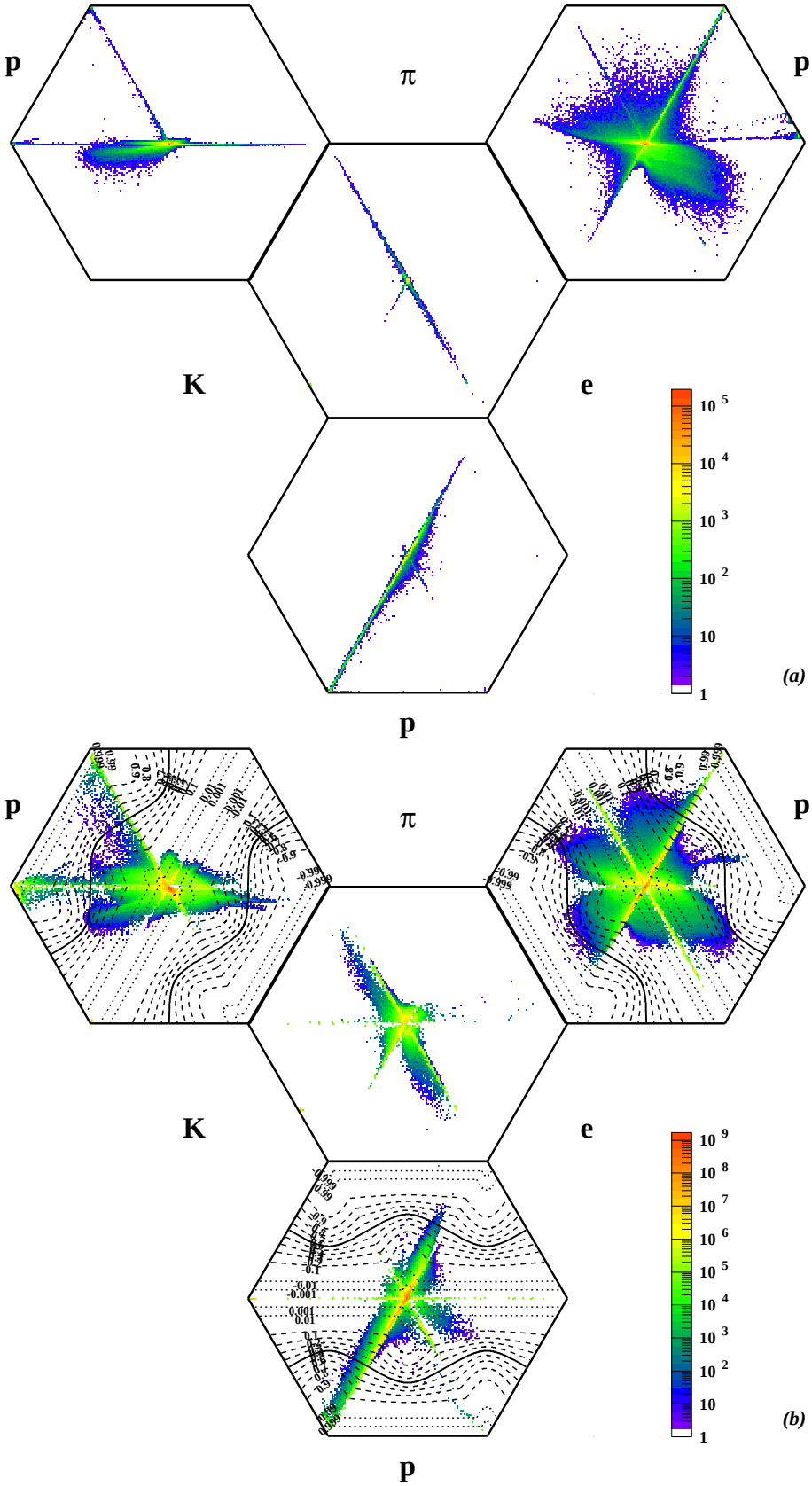

Figure 5.37: Migrations due to dE/dx corrections of L_r in the proton sample in (a) linear view and (b) fish-eye view.

tions (between no migration and the change from $L_r(p) = 0$ to $L_r(p) = 1$). This means, independently of a cut level in $L_r(p)$ one benefits from the dE/dx corrections.

5.3.5.3 Momentum-dependence of likelihood ratios

Both the a-priori probabilities and the dE/dx prediction depend on the momentum of the track. Therefore one expects a strong momentum dependence in the likelihood ratios. Figure 5.38 shows this dependence. The plot is similar to the tetrahedron plots, but the colour code is not a histogram (the number of entries found in a bin) but the mean momentum of all entries in a bin.

One has to distinguish between two different ways, a tetrahedron histogram can depend on data. One way is the dependence via the a-priori probabilities of the particle types. These a-priori probabilities anyway have to be found before any particle identification can be done, because they are needed in the calculation of the likelihood ratios. The difference between the two histograms in Fig. 5.38 is given by the different a-priori probabilities corresponding to the test samples for HERA I and HERA II.

The tetrahedron plots in the previous sections are frequency distributions of the data samples. Mandatory for these plots is preceding knowledge about the particle types of the shown candidates. Consequently these plots can only be generated using test samples, whereas in an analysis environment only the combination of all particle types can be shown in one plot. The expressiveness of such plots will be strongly reduced.

For Figures 5.38 and 5.39 the conditions are different. For any point in the dE/dx-p-plane one can calculate a unique set of likelihood ratios $L_r(i)$ which determines where this point has to appear in the tetrahedron. The colour in the plot represents the p-component of this point. These plots are filled by calculating such entries for a lattice in the dE/dx-p-plane. One can read these plots as a transformation of the dE/dx-p-plane onto the tetrahedron, independent of the distribution of real data in the dE/dx-p-plane. Only one complication has to be kept in mind: different, separated areas of the dE/dx-p-plane can overlap in the tetrahedron view. In such cases the mean momentum of the overlapping parts is shown in the colour code. Examples for this behaviour will be discussed later.

The independence of these plots from the data sample is very profitable. After establishing the a-priori probabilities for a particular physics analysis they can be filled. Therefore such plots are a useful tool to investigate the effect of selection cuts in the likelihood ratio on the selected momentum range of the final data samples. This kind of 'hidden' cut on the momentum range can be an important information to decide on proper cut limits.

The interpretation of Fig. 5.38 will be shown now with some examples. Focusing on the high momentum ranges in Fig. 5.38 (a) one can inspect two separate areas. One of them is located at high electron probabilities, visible in all three triangles related to electrons. For high momenta ($> 1.5\,\mathrm{GeV}$) the expected dE/dx for electrons is higher than for any other particle type. Particles in this momentum range with a dE/dx higher than the expectation for electrons are closer to the electron expectation than to any other particle expectation. Therefore their $L_r(e)$ is very high. For even higher momenta the expectations for particles other than electrons rise to the Bethe-Bloch plateau, too. Especially the pion prediction is already close to the electron prediction for highest momenta ($> 10\,\mathrm{GeV}$), thus the high-momentum area in Fig. 5.38 (a) extends from the electron corner towards higher pion probabilities.

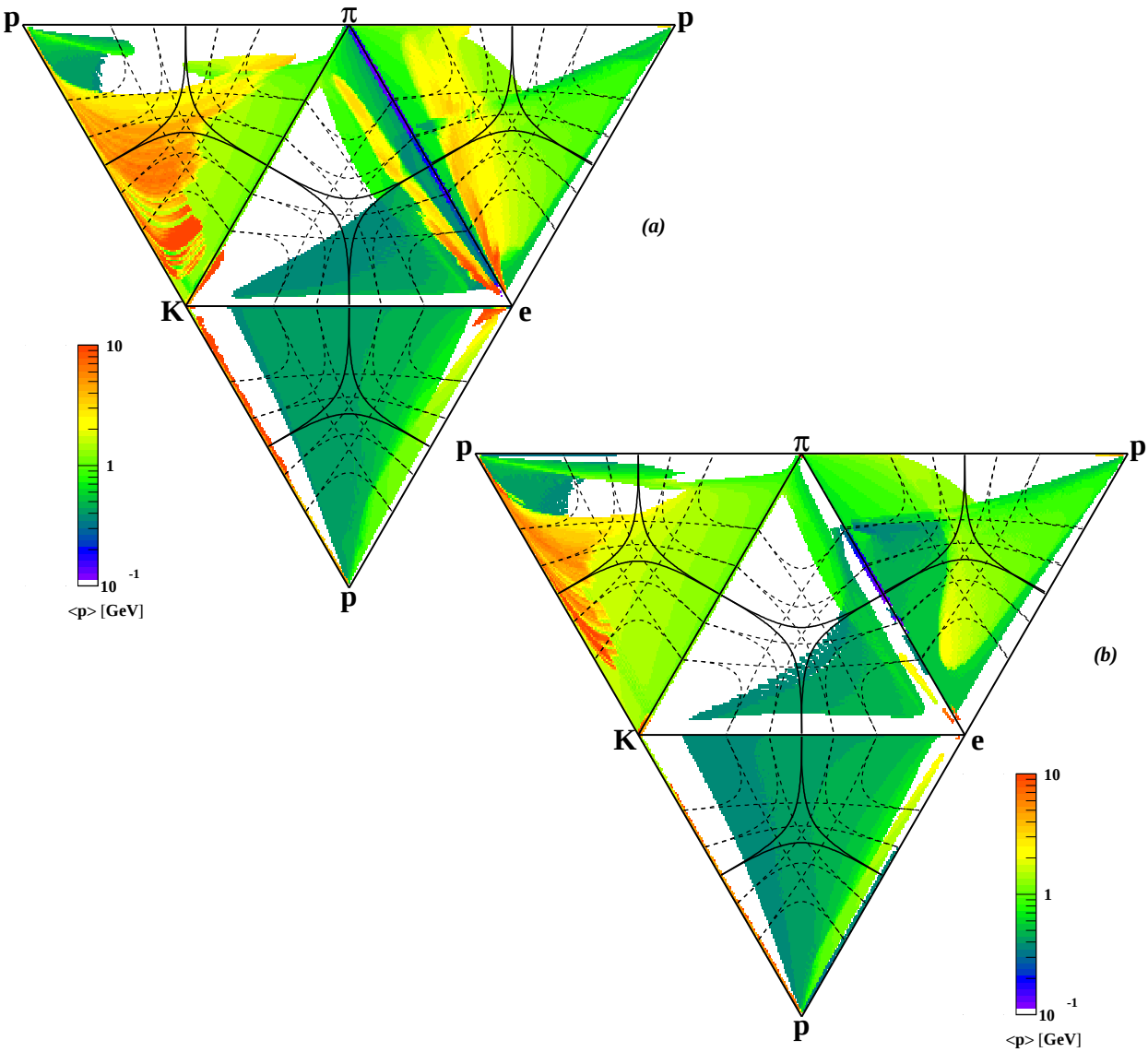

Figure 5.38: Momentum-dependence of likelihood ratios, using the inverted fish-eye view based on a-priori probabilities for (a) HERA I and (b) HERA II test samples. The level lines for all hypotheses are shown for the values 0.1, 0.3, 0.5, 0.7 and 0.9.

Similar things happen for very low dE/dx values in the high-momentum regime. In this case, the proton expectation is closest to the measurement, but the proton- and the kaon-expectation are very close together. Therefore the likelihood ratios are typically shared between the proton and the kaon hypotheses; the entries appear along the edge between proton and kaon corners in the tetrahedron plot. In the K-p-e-triangle the entries are very close to $L_r(e) = 0$: the electron expectation for dE/dx is so far away from the dE/dx_{exp} for kaons or protons, that the electron likelihood ratio is almost zero. In the p-K-π-triangle the high-momentum range also covers pion probabilities of 10% and more. This has two reasons: dE/dx_{exp} for pions is much closer to the expectatios for kaons and protons than the electron expectation. Thus the pion likelihood for such candidates is higher than the electron likelihood. The second reason is the high a-priori probability for pions, which

favours high pion probabilities.

For the high-momentum range in the p-K-π-triangle one observes stripes. This is an artefact of the calculation on a lattice. The change of likelihood ratios between neighbouring bins in the lattice is larger than the binning of the tetrahedron plot.

The effect of cuts in the likelihood ratio on the kinematics of the selected sample may be illustrated using the kaon hypothesis. In the K-e-π-triangle one can see that even an extremely loose cut of $L_r(K) > 0.1$ rejects most candidates. The remaining candidates are only the high-momentum, low-dE/dx candidates, which were already mentioned above, and the ones with very low momenta, which are well separated from other particles in the expected dE/dx. The medium-momentum range will be rejected completely. In a physics analysis this might be a very important information.

Figure 5.38 (b) is shown to remind the reader of the sensitivity of likelihood ratios to a-priori probabilities. The plot contains exactly the same as Fig. 5.38 (a); the only difference are the slightly changed a-priori probabilities between HERA I and HERA II test samples. Even such small changes cause obvious differences in the distribution of the likelihood ratios. This shows once more how important it is to define the a-priori probabilities properly.

5.3.5.4 Number-of-hits-dependence of likelihood ratios

The previous section have described the dependence of the likelihood ratios on their interplay with the momentum of the investigated tracks. Besides this, the number of used hits is the most important parameter for the likelihood ratios. The dependence on this number can be presented in a similar way as the momentum dependence in Section 5.3.5.3, the only difference is to replace the mean momentum by the mean number of used hits in the colour code. The corresponding plots are displayed in Fig. 5.39, which shows, that the coverage of the tetrahedron is strongly dependent on the number of used hits.

As there is a strong correlation between the azimuthal angle θ and the number of hits, the relation between the likelihood ratios and the number of hits has to be considered when data is selected by cuts on the likelihood ratios. Cuts in the likelihood ratio might imply a hidden cut for the track kinematics.

The comparison in Fig. 5.39 between HERA I and HERA II reveals strong differences, similar to the momentum distributions in Sect. 5.3.5.3. This is another proof for the importance of well defined a-priori probabilities.

5.3.5.5 Summary of 'tetrahedron plots'

This section has shown, that the 'likelihood-ratio tetrahedron' is very convenient to depict and investigate the separation power of dE/dx measurements for particle identification. Based on the general concept of 'tetrahedron plots' there is a large variety of distributions that could be shown. Tetrahedron plots offer a visualisation of correlations between different likelihood ratios, they are a helpful tool to find proper cut limits for likelihood ratios.

Nevertheless one has to be careful when using these plots. Such a high information density always contains the risk of misinterpretation. This becomes most obvious for Fig. 5.35 (c):

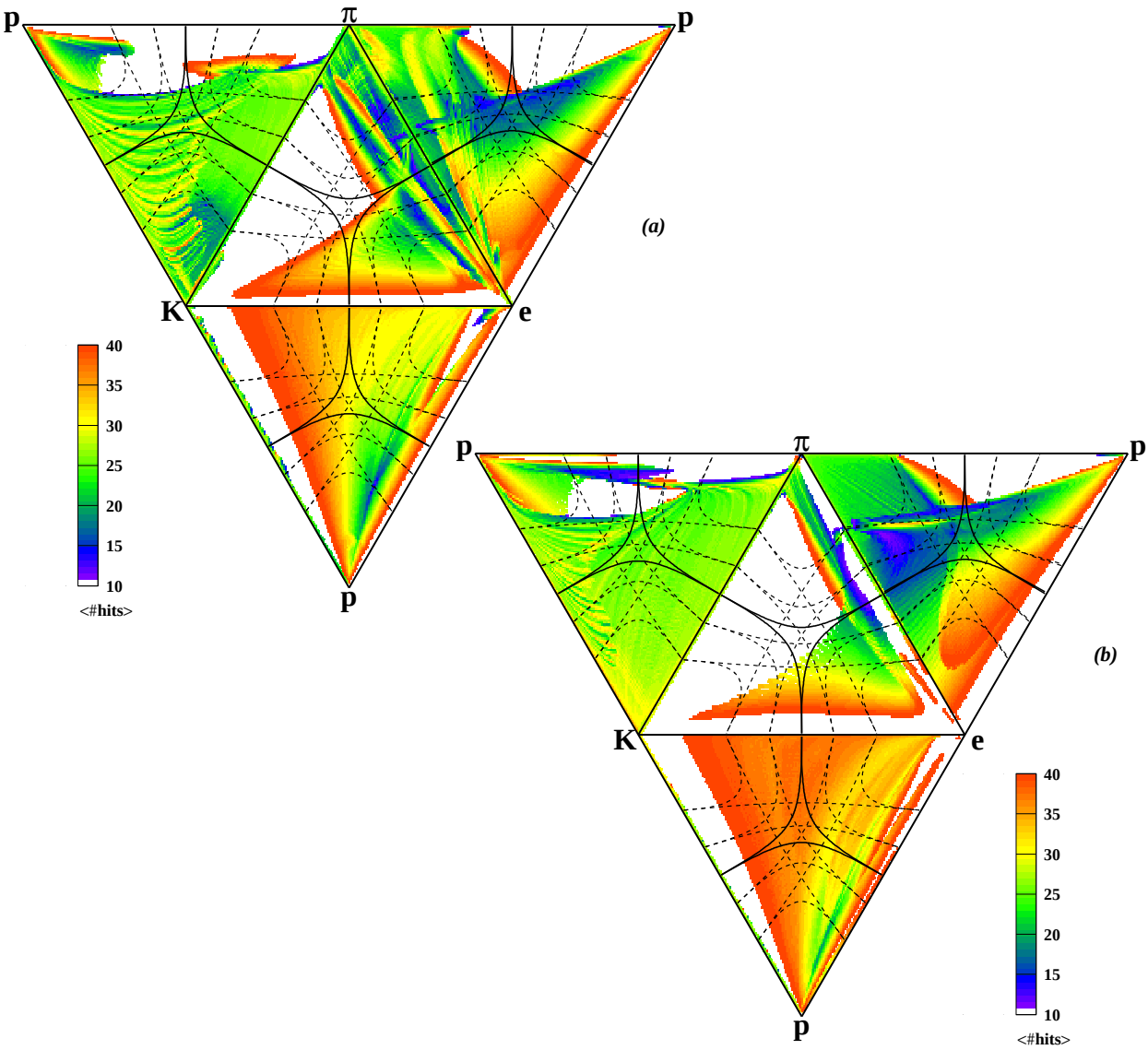

Figure 5.39: Number-of-hits dependence of likelihood ratios, using the inverted fish-eye view based on a-priori probabilities for (a) HERA I and (b) HERA II test samples. The level lines for all hypotheses are shown for the values 0.1, 0.3, 0.5, 0.7 and 0.9.

changes in the BETHE-BLOCH curve can cause migrations which dominate the tetrahedron plot, even if they are of minor relevance.

Most of the plots shown previously make use of the notion about the true particle that produced the track. This can only be done for test samples. If one wants to use the distributions in the likelihood-ratio tetrahedron to find proper cut values, one can only investigate plots filled with all data. As the resolution of the dE/dx measurement is not high enough for a clear separation between different particle species the tetrahedron plots will not show a clear separation, either. Nevertheless, the tetrahedron plots offer an important tool to search for a good separation with the best achievable visualisation of the high-dimensional correlations between different particle hypotheses.

The tetrahedron plots showing the mean momentum or mean hit number are of special

interest for analyses using dE/dx measurements. These plots only depend on the a-priori probabilities, thus they can be generated for any analysis environment. They illustrate important correlations between track kinematics and likelihood ratios, therefore they are a very efficient tool to discover hidden cuts on the kinematics caused by likelihood-ratio cuts.

Several examples have been presented to illustrate the strong dependence of likelihood ratios on the a-priori probabilities. It is essential for a physics analysis using particle identification with likelihood ratios, to measure the a-priori probabilities as precisely as possible.

Chapter 6

Summary

Several physics analyses at ZEUS require and rely on the identification of particles. For charged particles with momenta below $\approx 10\,\mathrm{GeV}$ the most powerful tool for particle identification with the ZEUS detector is the measurement of the ionisation energy loss dE/dx. In order to achieve a high separation power between particle species as well as a proper Monte Carlo simulation an thorough understanding of the dE/dx measurement including all detector-specific peculiarities is mandatory.

It is the task of this thesis to satisfy this goal and to deliver a well-tested and reliable tool for dE/dx measurements with the ZEUS CTD with best possible performance, applicable to (re)processed data, that no longer contains information on hit level. Most of the effects analysed here are not just specific for the ZEUS CTD, but are present in every drift chamber. Therefore, for usage beyond the ZEUS experiment, this thesis describes a generally applicable concept for the optimisation of the dE/dx measurement with a drift chamber.

The mean energy loss, dE/dx, depends on the velocity or $\beta\gamma$ of the traversing particle. In the early years of ZEUS data-taking the dE/dx measurements were calibrated using tracks close to minimum ionisation only. These tracks were selected in a momentum range corresponding to the minimum ionisation of pions. The sample was treated as a pion sample, building on the fact, that most of the measured tracks are caused by pions. The benefit of this method is a large tuning sample using only a small amount of collected data. This allowed multi-dimensional investigations already in the early stage of ZEUS. A serious deficit is the strongly limited purity of the sample. The most critical deficiency is the restriction of the tuning to a single value in dE/dx (the minimum of the Bethe-Bloch curve). Such a correction cannot compensate for effects depending on $\beta\gamma$ or dE/dx itself. The dE/dx measurement with the Phase I corrections and run-by-run corrections, based on the sample mentioned above, was the starting point for this thesis.

Meanwhile a lot of data has been collected by ZEUS, allowing the selection of data samples with well-identified contents. Ten independent data samples of known particle content have been produced by selecting tracks in well-identifiable channels. With this method samples for all long-lived particle species have been selected with very low contamination, of the order of 1%. Some of these samples have been used for the dE/dx tuning, the remaining ones have served for tuning-independent tests of the results of the tuning procedure.

From this data, in a grand iterative procedure, a universal parameterisation of the CTD-

specific Bethe-Bloch curve valid for all particle species have been tuned as well as a set of corrections to the dE/dx measurement have been extracted.

The optimised Bethe-Bloch curve has been employed to tune the dE/dx measurement, such that the mean corrected dE/dx measurement reproduces this prediction. For tuning issues it is mandatory to know the mass, i.e. the species, of the particles in order to calculate their $\beta\gamma = p/m$. The selected data samples fulfil this condition and are well suited for comparison with the predicted dE/dx.

Twelve independent effects influencing the dE/dx measurement have been identified. One of these is the compensation of the over-correction of the threshold effect occurring in the run-by-run correction which was available already before this work started. Another effect results in scale factors for different superlayers, which are apparently needed, though the reason for their existence has not been diagnosed. For the remaining ten effects the sources have been identified and understood, and appropriate corrections have been developed and applied.

A big effort has been made to disentangle the twelve different effects and to properly handle the correlations between the partial corrections, using an iterative algorithm for optimisation. The robustness and reliability of the method to combine partial corrections has been proven.

The reliability of the corrected dE/dx measurement has been investigated by means of distributions showing inconsistencies before correction, using test data samples, which have no influence on the tuning itself. Critical parameters are, for example, the charge dependence, the dependence on the sample selection, or on different data taking periods. After applying all corrections most of the deviations are reduced by about an order of magnitude. Systematic uncertainties are determined and reduced to about 1%.

The composition of the remaining measurement uncertainty has been investigated in detail. A decomposition into separate contributions as well as an analysis of the dependence of these contributions on the track parameters has been carried out. This approach yields the best achievable prediction for the resolution of the dE/dx measurement on each individual track. This knowledge of the resolution at single-track level is an essential basis for the realistic simulation of dE/dx values for Monte Carlo data as well as for the calculation of a meaningful estimator for the particle identification in data.

The separation power of the particle identification by the dE/dx measurement has been studied using a likelihood ratio method. Due to the measurement corrections an improvement of the separation power has been achieved. A visualisation of the tetrahedron-shaped multi-dimensional space of likelihood ratios for different particle hypotheses has been introduced and the potential of this visualisation is presented.

The main accomplishment of this work is the minimisation of systematic uncertainties in the dE/dx measurement. This is a matter of particular importance when it comes to typical applications of dE/dx measurements. As soon as background of a measurement (cross section) has to be subtracted statistically from the measured signal, the sensitivity to systematic differences between the signal sample and a background estimator easily becomes the biggest uncertainty. It is a crucial task for the reliability of any measurement using dE/dx to keep these systematic uncertainties small and well under control. In this sense, and exploiting the readily available reconstructed data, the results of this thesis enable the optimum use of dE/dx measurements with the CTD for physics analyses in ZEUS.

Appendix A

Glossary

Several of the variables used in this thesis appear at several locations. In order to help the reader, such variables are listed in this appendix. References to the section or equation of their introduction and a short description of the variable are given here, too.

Additional information about nomenclature rules can be found in Sect. 3.3.

A	Eqn. 4.15	parameter representing the size of the end-plate-effect correction
α_l	Sect. 4.2.3	LORENTZ angle
dE/dx_{exp}	Sect. 3.3	expected dE/dx (value of BETHE-BLOCH curve for given $\beta\gamma$)
dE/dx_{FADC}	Sect. 3.3	track's dE/dx in FADC counts after Phase I corrections, before run-by-run and other corrections
dE/dx_{hit}	Sect. 3.3	dE/dx of single hit
dE/dx_{meas}	Sect. 3.3	measured dE/dx after all corrections except of the one shown in the plot
dE/dx_{mips}	Sect. 3.3	$:= \frac{dE/dx_{FADC}}{f_r}$ track's dE/dx after run-by-run corrections
dE/dx_{norm}	Sect. 3.3	$:= \frac{dE/dx_{meas}}{dE/dx_{exp}}$ normalised dE/dx without dependence on $\beta\gamma$ (no momentum dependence)
Δz_{last}	Sect. 4.2.2.5	distance of the outermost hit of a track to the closest CTD end-plate
$f_m(n_h)$	Eqn. 4.6	deviation of dE/dx_{norm} due to the truncated mean calculation of a sample, based on an assymetric probability density
f_r	Sect. 4.2.1.2	mean value of the gaussian fit in the run-by-run correction (1/correction factor)

h	Eqn. 4.7	$:= \frac{\#\text{all hits}-\#\text{all saturated}}{\#\text{all hits}}$ parameter in the correction for tracks with too many saturated hits by Wouter Verkerke
L_h	Sect. 4.3.1.2	reference Landau distribution: the probability density for a single hit with $\langle dE/dx_{mips}\rangle = 1$
L_{m_i}	Eqn. 5.11	likelihood for particle hypothesis $i \in e, \pi, K, p, \mu, ...$
$L_r(i)$	Eqn.5.12	likelihood ratio for particle hypothesis $i \in e, \pi, K, p, \mu, ...$
L_s	Sect. 4.3.1.2	$:= \frac{1}{2\pi\imath}\int_{c-\imath\infty}^{c+\imath\infty} \exp(s\log s + xs)ds$ standard Landau distribution
n_h		number of hits after truncation
n_w	Eqn. 4.13	neighbour rate for neighbourhood correction
ϕ		azimuthal angle of the track
ψ'	Sect. 4.2.2.8	angle in the xy-plane between the tangent to the track and the radial axis of the CTD
r	Eqn. 5.4	residual; can be defined differently, for example in Sect. 5.3.1 the absolute residual is used
$\mathcal{R}$	Eqn. 5.3	resolution function, describing the shape of the residual
R_{out}	Sect. 4.3.1.12	radius in xy, where the track helix passes through the CTD end plate (extrapolated end-plate for barrel tracks)
s_d	Eqn. 4.31	$:= \frac{dE/dx_{meas}}{d_{ph1}(\overline{\psi'})\cdot\sin\theta}$ + higher order term signal used for the drift time correction
s_e	Sect. 4.3.1.8	$:= f_r \cdot dE/dx_{exp}$ expected signal
σ_{int}^{hit}	Eqn. 5.2	intrinsic single hit resolution
Σ_{rel}	Sect. 4.3.2.7	calculable part of the relative uncertainty of a single track dE/dx measurement
θ		polar angle of the track
w	Eqn. 4.5	slope of the transformation $L_s \rightarrow L_h$ fixes the width of the Landau distribution for single hits
x_t	Eqn. 4.27	parameter for the space-charge-effect correction, representing the density of clusters (in z and ϕ) where they reach the sense wire
z		z coordinate of a hit

Appendix B

Data sample selection

The work dokumented in this thesis would not have been possible without large data, or rather track, samples on hand for each of teh particle species. The selection cuts for all tuning data samples will be listed in Sect. B.1. The test data samples and their selection cuts will be shown in the Sect. B.2.

High purity in the data samples (especially the tuning samples) is the most important requirement for the samples. In this appendix the measurement of the purity or upper limits on the purity will be shown. HERA I and HERA II data are separated to investigate differences between these data taking periods. Similar amounts of data were used for the two periods[1], therefore the sizes of the samples are directly comparable.

B.1 Tuning samples

The tuning samples are the most important samples for this analysis work. The quality of the corrections depend significantly on their purity, therefore stringent requirements had to be applied.

B.1.1 Photon conversions

The photon conversion sample is basically selected with the ZEUS software package CONVERT2 (see App. C.3) used in the high purity mode. For the application of dE/dx tuning even higher requirements are requested for the purity of the sample. Therefore the selection cuts are tightened and cuts on more variables than the distance parameter D are applied:

- no trigger requirement;
- $D < 2.5$
  D as defined in Equation C.1;

[1] The data sets contain $103.6\,\mathrm{pb}^{-1}$ for HERA I and $150.2\,\mathrm{pb}^{-1}$ for HERA II. Due to changes in the trigger configuration the number of events per luminosity has decreased. The number of events in the data samples for both periods are almost identical: 8.9M for HERA I and 9.4M for HERA II

- $D_z < 0.7\,\text{cm}$
  distance in z between the two helices at their point of closest approach;
- point of closest approach between the two helices in (x, y)-plane within matter:
  - ◇ HERA I:
    ring with radius between 6 cm and 8 cm around $(-1.4\,\text{cm}, +0.6\,\text{cm})$
    (beam pipe) or
    ring with radius between 16 cm and 18 cm around $(0\,\text{cm}, 0\,\text{cm})$
    (CTD inner cylinder (also called 'inner wall'));
  - ◇ HERA II
    ring with radius between 14 cm and 18 cm around $(0\,\text{cm}, 0\,\text{cm})$;
- invariant mass of the reconstructed parent particle $m < 7\,\text{MeV}$;
- extrapolated photon is coming from nominal interaction region:
  $D_H < 0.5\,\text{cm}, D_z < 40\,\text{cm}$;
  D_H is the distance in (x, y) between the primary vertex and the reconstructed photon. Taking the corresponding point of the photon trajectory, its z position can be calculated. D_z is the distance between this point and z_{vtx}.

As shown in Fig. 4.3, most of the photon conversions occur within the inner wall of the CTD. The location of the conversions is strongly correlated to the density of matter. This dependence was used to measure an upper limit for the sample contamination. The number of photon conversions occurring in an area of low matter density like within the active volume of the CTD was extrapolated to the areas used for the sample generation to give an upper limit for the background in these areas. This is of course a very conservative estimate for an upper background limit, because the 'tuning area' consists of a mixture of background and photon conversions.

During the HERA II upgrade big changes were made in the matter distribution in the ZEUS detector. Therefore the sample selection as well as the background estimation differ between the two periods.

In HERA I data photon conversions were selected in a ring corresponding to the beam-pipe and another ring corresponding to the CTD inner wall. Figure 4.3 shows, that in the lower half of the detector some cables are located in the gap between beam pipe and CTD inner wall. In order to obtain a good estimation of the 'low matter density' case in this area, the background estimation was limited to candidates in the upper half of the detector. Figure B.1 (a) shows the frequency distribution of candidates versus their radial position (the distance to the centre of the circle, described by the CTD inner wall). A linear fit was applied to the 'low matter density' areas between the beam pipe and the CTD inner wall as well as within the gas volume of the CTD. The extrapolation of this fit to the CTD inner wall range was used as an estimate for the background in this range.

A similar approach was used to estimate the background in the beam pipe wall (Fig. B.1 (b)). Only the range between beam pipe and CTD was used for the fit.

In the HERA II data set photon conversions were selected only in the range of the CTD inner wall. The gap between the beam pipe and the CTD was filled by the MVD, therefore no point to support the background fit are available in this range; the fit is limited to the CTD volume (Fig. B.2).

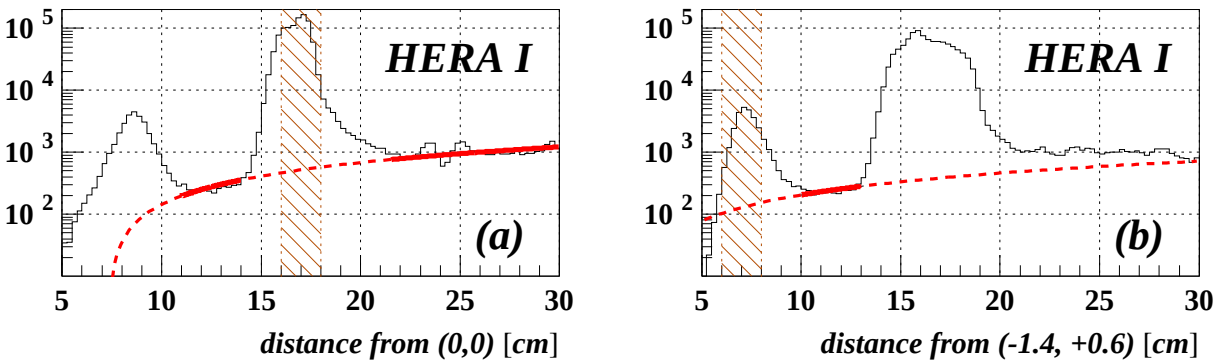

Figure B.1: Abundance distribution of photon conversion candidates in HERA I data in the upper half of the detector in bins of (a) the distance to the centre of the CTD inner wall and (b) the distance to the centre of the beam pipe. The hashed bands indicate the range for the sample selection. The solid lines are linear fit-curves, the dashed lines their extrapolation.

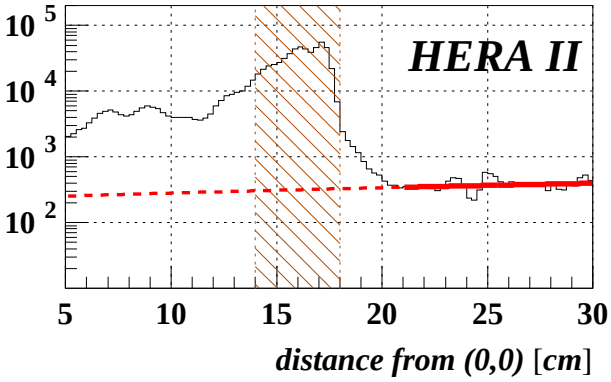

Figure B.2: Abundance distribution of photon conversion candidates in HERA II data in bins of the distance to the centre of the CTD inner wall. The hashed band indicates the range for the sample selection. The solid line is a linear fit-curve, the dashed lines their extrapolation.

For both data sets the contamination of the sample by fake identified photon conversions is less than 0.4%. As this is a very conservatively calculated limit, the real contamination is even smaller.

B.1.2 $J/\Psi \rightarrow e^+e^-$

Exclusive J/Ψ-decays can be selected with high purity, especially if one restricts the selection to exclusive decays. Unfortunately, this sample suffers from low statistics. The main goal of this sample is to fill the gap in the momentum range between the photon conversion electrons and the DIS electrons. The selection cuts are:

- Trigger requirements:
  - ◇ for HERA I data:
    DST bit 83 = HFL06 (elastic J/ψ) or DST bit 84 (inelastic J/ψ)
  - ◇ for HERA II data:
    no trigger (J/ψ-triggers were cancelled);
- Requirement for the event (restriction to exclusive events to minimise combinatorial background):

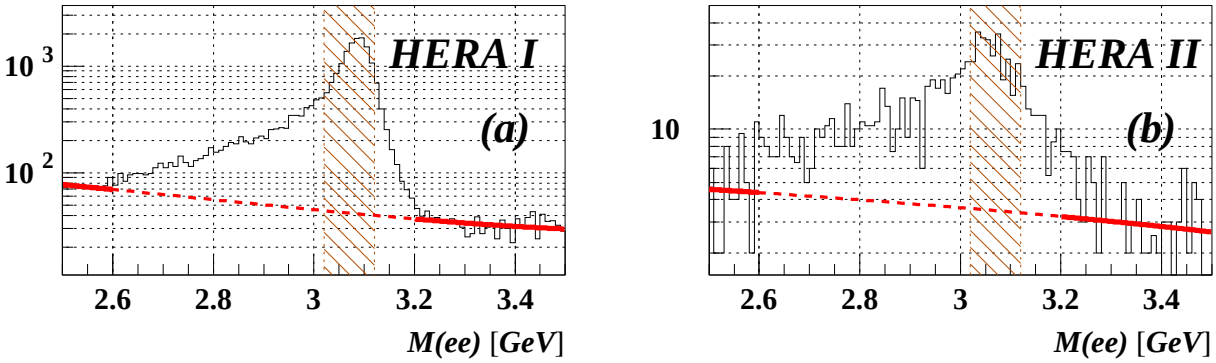

Figure B.3: Invariant mass distribution of J/ψ-candidates for (a) HERA I data and (b) HERA II data. The hashed band indicates the range for the sample selection. The solid line is a fit-curve (quadratic for HERA I, linear for HERA II), the dashed lines their extrapolation.

  - ◇ # of tracks = 2;

- Requirements for each of the tracks:
  - ◇ $p_t > 1\,\text{GeV}$;
  - ◇ $|\eta| < 1.4$;
  - ◇ track corresponds to a ZUFO (see App. C.1);
  - ◇ distance between end position of swim[2] and calorimeter island $< 20\,\text{cm}$;
  - ◇ ZUFO is purely electromagnetic[3];
- $3.02\,\text{GeV} < M(J/\Psi) < 3.12\,\text{GeV}$.

The invariant mass spectrum of the J/ψ-candidates is used for background estimation. For high masses ($> 3.2\,\text{GeV}$) the sample contains only combinatorial background. On the low momentum side a long tail in the data distribution is caused by the radiative energy loss of electrons from J/ψ decays. The background estimate is given by a linear fit using all data points below 2.6 GeV and above 3.2 GeV. As at the low-mass-side the fit still catches parts of the signal, the resulting background estimate is very conservative. Figure B.3 shows the results separated for HERA I and HERA II. As for HERA II no J/ψ trigger is active, the number of candidates is about 2 orders of magnitude smaller than for HERA I data. This affects also the sample purity; the contamination has increased from 1.7% to 6.5%.

B.1.3 DIS electrons

The highest momentum range for electrons is covered by DIS electrons. For high purity, only candidates found by both ZEUS DIS-electron finders, SINISTRA and EM (see App. C.2), are used. As most of the DIS electrons are scattered in backward direction, the

[2]Stepwise extrapolation of the track coordinates beyond the end of the sensitive area of the CTD, taking the local magnetic field of the solenoid into account.

[3]The whole energy deposit is measured in the EMC-part of the calorimeter.

geometrical coverage of the CTD is not very good in this sample. The following selection cuts are applied:

- requirement for the event:
  - ◇ no trigger selection;
  - ◇ $E - p_z > 40\,\mathrm{GeV}$;
- requirements for the track:
  - ◇ $p > 5.5\,\mathrm{GeV}$;
  - ◇ $|cos(\theta)| < 0.75$;
  - ◇ matching ZUFO found;
  - ◇ $|E_{cal} - p|/E_{cal} < 0.15$;
  - ◇ SINISTRA candidate with $\mathcal{P} > 0.985$ and
  - ◇ EM candidate with $\mathcal{P} > 0.3$.

The cuts on the electron probabilities for the two electron finders are much harder than usually applied for the identification of DIS events ($\mathcal{P} > 0.9$ for SINISTRA and $\mathcal{P} > 10^{-4}$ for EM). The 'standard' cut levels are designed for high efficiency, whereas here only high purity is important. As a consequence of these strong requirements, the DIS-electron sample is rather small. This does not matter, because the DIS-electrons lie within the plateau range of the Bethe-Bloch curve. The level of the plateau is determined well exploiting the available statistics; due to their high $\beta\gamma$ they cannot be used to describe the shape of the Bethe-Bloch curve (which would require higher statistics).

Testing a sample of DIS-electron candidates for its purity is a bit tricky. In contrast to all other samples these candidates are not found by the identification of track pairs from special sources. Such pairs allow to test correlations between the two tracks to measure the background contamination (like searching the distribution under an invariant mass peak). For DIS-electrons one can use the event kinematics for an efficient background study, i.e. one uses the DIS-electron candidate as one track and the whole rest of the event as 'the second track'. The calculation is based on the assumption, that the electron candidate is correctly identified.

1. The kinematics variable y is calculated using the Σ-method [58]:

$$y_\Sigma = \frac{(E - p_z)_h}{E - p_z} \quad , \tag{B.1}$$

   E and p_z measured with the calorimeter; the index h stands for the hadronic system (all deposits except of the one from the DIS-electron). This method is used, because it offers the best resolution for y [59].

2. The electron method is used to calculate the energy of the scattered DIS-electron E'_e with its initial energy E_e, its scattering angle θ_e and the previously calculated kinematic variable y:

$$E'_e = 2E_e \cdot \frac{1 - y_e}{1 - \cos\theta_e} \quad . \tag{B.2}$$

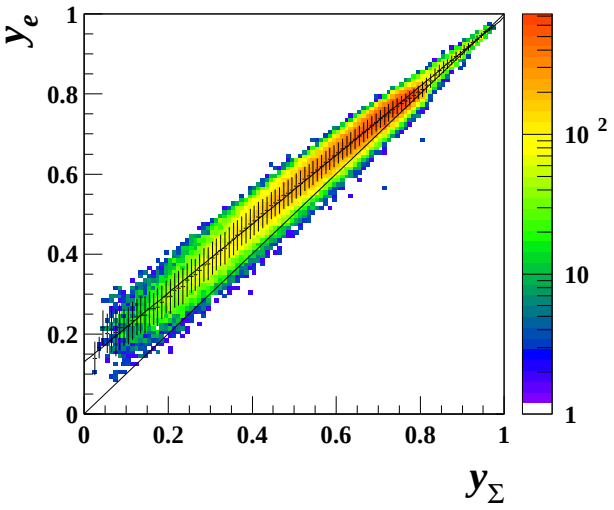

Figure B.4: Distribution of y_e versus y_Σ for the DIS-electron-candidates sample for all data taking periods. A linear fit is applied to this distribution.

3. Taking the resolution into account the calculated energy E'_e has to be the same as the momentum p_{track} of the track of the DIS-electron.

An additional step has to be applied to this approach: The electron method tends to measure too high values for y whereas the Σ-method tends to slightly too low values for y. Figure B.4 shows the distribution of these two variables, calculated for the DIS candidates sample (which is assumed to be almost clean). A linear function was fitted to the distribution and is used to transform y_Σ into y_e. As no difference between HERA I and HERA II data was found, all plots according to DIS-electrons in this section show both periods together.

The resulting distributions (see Fig. B.5 (a, b)) have to be compared with the same distributions for a background sample (Fig. B.5 (c, d)), which is generated using similar selection cuts as for the signal sample. ZUFOs matching one track with one calorimeter island, passing all selection cuts for DIS-electron candidates except of the cuts on the probabilities of the electron finders SINISTRA and EM were investigated. An additional veto on DIS electrons was applied: all ZUFOs with an island closer than 40 cm to any SINISTRA candidate were rejected. This background sample is assumed to be dominated by non-DIS-electrons, but some signal events can remain (if SINISTRA did not identify the electron candidate).

The signal sample behaves as expected: within a certain resolution E'_e and p_{track} are the same. In the background sample there are many entries with much higher E'_e than p_{track}. One should fit the shape of the background sample to the signal sample to extract its contamination. As there is no tail at all in the signal sample to high values of $E'_e - p_{track}$ one concludes, that the background contamination is unmeasurable small.

B.1.4 $K^0 \rightarrow \pi^+\pi^-$ sample

The mean lifetime of the K^0 is high enough to reconstruct the location of its decay separated from the primary vertex. This property enables a very clean sample selection.

Applied cuts:

- DST bit 9 (electron found) and DST bit 10 (vertex found).
  These cuts are not mandatory for this channel, but they increase the purity of the

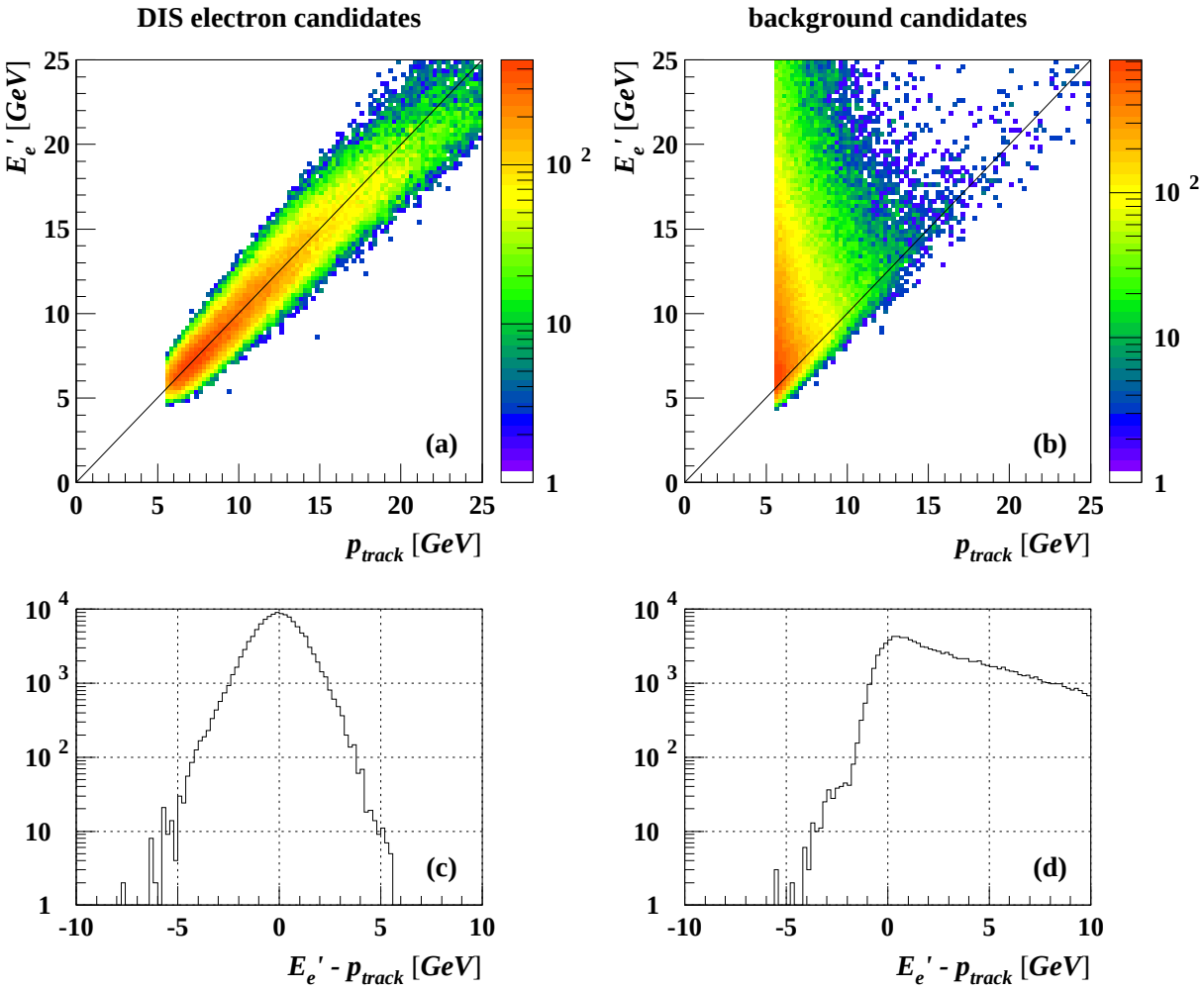

Figure B.5: Comparison of E_e' versus p_{track} between DIS-electron sample (a, c) and background enriched sample (b, d). Combined HERA I and HERA II data.

primary vertex identification and the separation of secondary vertices;

- two tracks pointing to the same secondary vertex;
- distance between primary and secondary vertex in xy-plane $< 21\,\text{cm}$ to ensure that the candidate tracks pass the innermost CTD layers;
- $p_t > 120\,\text{MeV}$ for each track to suppress badly reconstructed tracks;
- $0.4925\,\text{GeV} < M(K^0) < 0.5035\,\text{GeV}$;
- $M(p\pi) > 1.125\,\text{GeV}$ to suppress misidentified Λ-decays;
- $M(ee) > 50\,\text{MeV}$ to suppress photon conversions;
- the reconstructed K^0 trajectory points back to the primary vertex:
  - ◇ 2D-distance between K^0 track and primary vertex in xy-plane $< 4\,\text{mm}$;
  - ◇ 3D-distance between K^0 track and primary vertex $< 10\,\text{mm}$;

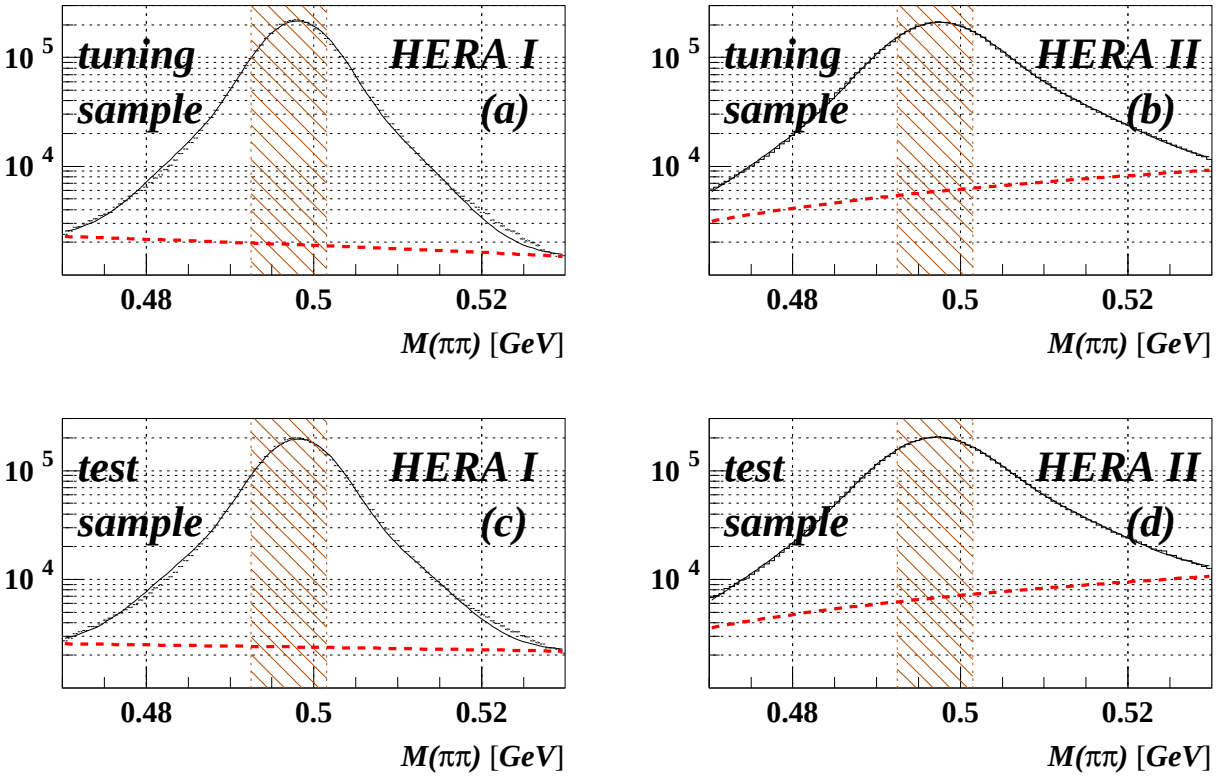

Figure B.6: Invariant mass distribution of K^0-candidates for (a, c) HERA I data and (b, d) HERA II data. (a, b) shows the distribution for candidates which contain at least one track used for the tuning sample, in (c, d) candidates with at least one track not used for the tuning sample are shown. The hashed band indicates the range for the sample selection. The dashed line shows the background estimation based on a fit.

- ◇ azimuthal distance between K^0 track and vector between primary and secondary vertex < 0.1 rad;
- ◇ angular distance between K^0 track and vector between primary and secondary vertex < 0.15 rad.

For the tuning sample an additional cut was applied, limiting the sample to a range close to the minimum of the Bethe-Bloch curve:

- $400\,\text{MeV} < p < 1000\,\text{MeV}$

Candidates outside of this momentum range are used as a test sample.

The invariant mass spectrum was used to quantise the background contribution to the data sample. The sum of two functions describing the signal peak and the background contribution was fitted to the data distribution. These fit functions are used to calculate the sample contamination.

In the K^0-sample the background is described by a linear function. A double gaussian distribution with a common mean value fits the signal. For HERA II data an additional problem occurred: The CTD-only track reconstruction suffers from a bad description

of the dead material in the MVD-area with the consequence of too low reconstructed momenta. Especially for low momentum tracks this error becomes big. One consequence is a 'running' reconstructed invariant K^0 mass, depending on the momentum of the K^0. This problem could be solved by using another tracking algorithm or by applying an additional correction on the reconstructed momentum, but for the issue here, there is no need for a precise calculation; one only needs a good description of signal and background to extract their ratio. Using a double gaussian distribution with independent mean values describes the data well.

The plots for the invariant mass of K^0-candidates appear for the two cases: K^0-candidates with at least one track in the momentum range for the tuning sample are shown in Fig. B.6 (a, b), and candidates with at least one track not matching this momentum range are used to fill Fig. B.6 (c, d). These plots represent the cases of tuning sample tracks and test sample tracks, even if they have some overlap (candidates with one track in the selected momentum range and one track outside this range). As expected, no big difference was found between tuning and test samples. The distribution of the test sample is slightly wider than the other one. The mass range shown in these plots ends within the tails of the signal peak. The preselection of the K^0-data sample was limited to the shown mass range due to unavoidable limitations on the size of ntuple files. This has no effect on the quality of the selected samples, only the estimation of the remaining background is a bit difficult. The applied fit renders a too high background, thus the results have to be treated as conservative limits. One finds for HERA I data a contamination of 1.3% in the signal sample and 1.7% in the test sample; for HERA II data the numbers are 2.1% and 2.5%. Most of the background is expected to be combinatorial. About 80% of all tracks are pion tracks, therefore only about 1/5 of the background in the pion data samples are other particles. Therefore in terms of other particles than pions all K^0-samples are contaminated much less than 1%.

B.2 Test samples

The applied cuts are listed for each test sample. The cut positions are optimised for high purity. Cuts on other parameters like the decay angle β [4] in two-body decays have also been investigated. Finally a cut on β has not been applied in any of the investigated decay channels, because depending on the cut level the gain for the sample purity has only been marginal or the loss in statistics has been too high.

B.2.1 $K^0 \to \pi^+\pi^-$ sample

Depending on the momentum of the tracks, this sample is split into a tuning sample and a test sample. Its general selection criteria have been introduced in Sect. B.1.4 and will not be repeated here. In addition, the test sample fulfils:

- $p < 400\,\mathrm{MeV}$ or $p > 1000\,\mathrm{MeV}$.

[4] The decay angle β in a two-body decay of a neutral particle is the angle between the momentum vector of an outgoing particle, measured in the rest frame of the decaying particle, and the direction of the ingoing particle measured in the laboratory frame.

B.2.2 $\rho^0 \rightarrow \pi^+\pi^-$ decays

- trigger requirements:
  - ◇ for HERA I data:
    DST bit 13 = DIS05 = DIFF15 (vector meson) or
    DST bit 58 = PHP11 (44m 2trk high pt or high mass (or) 44m 2 track VM);
  - ◇ for HERA II:
    DST bit 52 = SPP05 (vector meson);
- $\#tracks = 2$ or $\#tracks = 3$;
- both used tracks pointing to the primary vertex;
- at least one of the tracks with $p_t > 0.5\,\text{GeV}$;
- $P_t(\rho^0) > 1\,\text{GeV}$;
- $0.65\,\text{GeV} < M(\rho^0) < 0.88\,\text{GeV}$;
- veto against Φ decays:
  no good $\Phi \rightarrow K^+K^-$ candidate which shares at least one track with this candidate;
- in case of $\#tracks = 3$ the third track has to be the one with the lowest momentum;
- if SINISTRA found a DIS-electron e_{DIS}:
  $(p(\rho^0) - p(e_{DIS}))_t < 0.6\,\text{GeV}$.

The ρ-resonance is very wide and covers a big range in invariant mass. Therefore the probability for combinatorial background and for reflections of other resonances within the signal range is very high. Furthermore, the kinematical constraints in the sample selection are strongly invariant-mass-dependent and have a strong influence on the shape of the data distribution; as mostly candidates with low invariant mass are rejected, the signal peak becomes artifically sharpened. These complications strongly reduce the accuracy of any fit of the signal peak. As shown in Fig. B.7 (a, b) a Breit-Wigner distribution has been applied for the signal combined with a quadratic function for the background. The fit has been limited to $M(\pi\pi) > 0.6\,\text{GeV}$ to avoid confusion due to the resonances at lower masses. A strong hint for the effect of the sample selection on the signal shape is indicated by the fit result. The width of the resonance, already containing the detector resolution, has been measured to be 100 MeV; the corresponding literature value (149.5 MeV [60]) is much larger. Nevertheless, the fit gives a rough estimate of the background contamination of 9.2% for HERA I and 9.3% for HERA II.

B.2.3 $\Phi \rightarrow K^+K^-$ decays

- trigger requirements:
  - ◇ for HERA I data:
    DST bit 13 = DIS05 = DIFF15 (vector meson) or
    DST bit 58 = PHP11 (44m 2trk high pt or high mass (or) 44m 2 track VM);

  - ◇ for HERA II:
    DST bit 52 = SPP05 (vector meson);

- $\#tracks = 2$ or $\#tracks = 3$;
- both used tracks pointing to the primary vertex;
- at least one of the tracks with $p_t > 0.65\,\text{GeV}$;
- $P_t(\Phi) > 1.1\,\text{GeV}$;
- $1.015\,\text{GeV} < M(\Phi) < 1.024\,\text{GeV}$;
- veto against ρ^0 decays:
  no good $\rho^0 \to \pi^+\pi^-$ candidate which shares at least one track with this candidate;
- in case of $\#tracks = 3$ the third track has to be the one with the lowest momentum.
- if SINISTRA found a DIS-electron e_{DIS}:
  $(p(\Phi) - p(e_{DIS}))_t < 0.6\,\text{GeV}$.

The decay $\Phi \to K^+K^-$ happens very close to its kinematical limit. Therefore it is not sufficient to expect a linear background shape; the function to describe the combinatorial background has to reflect the phase space:

$$f_{BG}(KK) = a_1 \cdot (M(KK) - 2M_K)^{a_2} \quad .$$

The signal is described by a gaussian distribution (see Fig. B.7 (c,d). One measures a sample contamination of 12.8% for HERA I and 14.3% for HERA II.

Both vector meson samples (ρ and Φ) suffer from the cancellation of the vector meson trigger for HERA II. The statistics in these samples decreased by a factor of 10.

B.2.4 $\Lambda \to p\pi$ decays

- no trigger requirements;
- two tracks pointing to the same secondary vertex;
- $3\,\text{cm} <$ distance between primary and secondary vertex in xy-plane $< 21\,\text{cm}$;
- $P_t(\Lambda) > 0.6\,\text{GeV}$;
- $p_t(\pi) > 140\,\text{MeV}$;
- $p_t(p) > 400\,\text{MeV}$;
- $1.114\,\text{GeV} < M(\Lambda) < 1.118\,\text{GeV}$;
- $M(\pi\pi) < 0.48\,\text{GeV}$ or $M(\pi\pi) > 0.52\,\text{GeV}$ to suppress misidentified K^0-decays;
- $M(ee) > 50\,\text{MeV}$ to suppress photon conversions;
- using the reconstructed Λ trajectory:

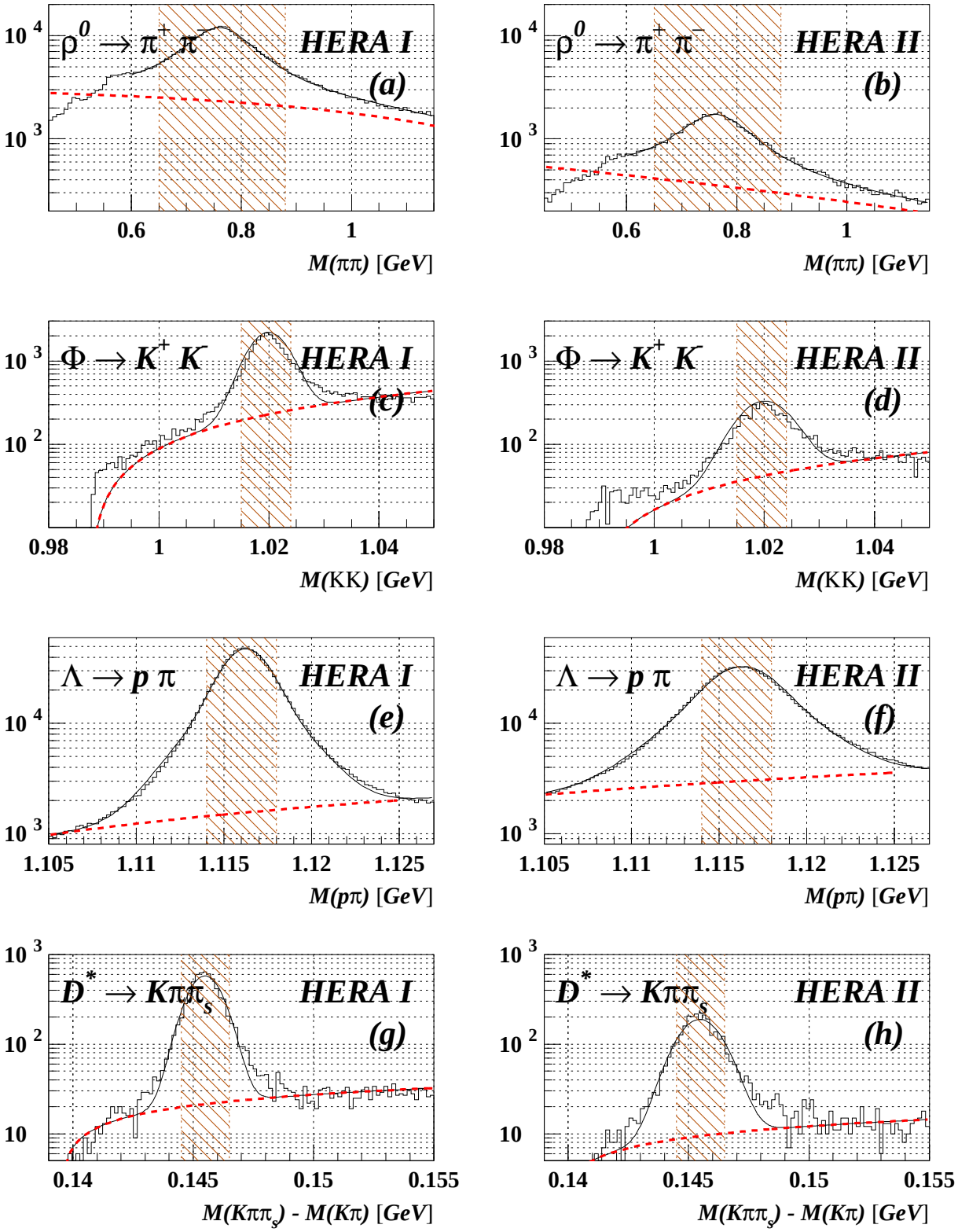

Figure B.7: Invariant mass distribution of (a, b) ρ-candidates, (c, d) Φ-candidates, (e, f) Λ-candidates and (g, h) D^*-candidates. The hashed band indicates the range for the sample selection. The dashed line shows the background estimation based on a fit.

- ◇ 2D distance between Λ track and primary vertex in xy-plane $< 4\,\mathrm{mm}$;
- ◇ 3D distance between Λ track and primary vertex $< 10\,\mathrm{mm}$;
- ◇ azimuthal distance between Λ track and vector between primary and secondary vertex $< 0.1\,\mathrm{rad}$;
- ◇ angular distance between Λ track and vector between primary and secondary vertex $< 0.15\,\mathrm{rad}$.

For the Λ-resonance in Fig. B.7 (e, f) a double gaussian distribution with common mean values and a linear background have been applied. The HERA II candidates suffer from the worsened momentum resolution of low momentum tracks (half of them have a momentum below 280 MeV) causing a worsened invariant mass resolution. Consequently, the purity of these samples also decreased. The contaminations are 4.2% for HERA I and 10.3% for HERA II.

B.2.5 $D^* \rightarrow K\pi\pi_s$ decays

- trigger requirements:
  - ◇ for HERA I data:
    DST bit 27 ($D^* \rightarrow K\pi\pi$)
  - ◇ for HERA II data:
    DST bit 23 ($D^* \rightarrow K\pi\pi$)
- $\#tracks < 20$;
- $1.82\,\mathrm{GeV} < M(D^0) < 1.9\,\mathrm{GeV}$;
- $144.5\,\mathrm{MeV} < \Delta M < 146.5\,\mathrm{MeV}$;
- $P_t(D^*) > 3.4\,\mathrm{GeV}$;
- $p_t(K) > 1\,\mathrm{GeV}$;
- $p_t(\pi) > 1\,\mathrm{GeV}$;
- $p_t(\pi_s) > 170\,\mathrm{MeV}$.

The best distribution to investigate the decay $D^* \rightarrow K\pi\pi$ is the difference $\Delta M = M(K\pi\pi) - M(K\pi)$ as shown in Fig B.7 (g,h). As well as in case of the Φ-resonance, the decay $D^* \rightarrow K\pi\pi$ is close to the kinematical limit, demanding a similar description of the combinatorial background:

$$f_{BG}(\Delta M) = a_1 \cdot (\Delta M - M_\pi)^{a_2} \quad .$$

The signal is approximated with a gaussian shape, measuring a contamination of 4.9% for HERA I and 5,9% for HERA II. The HERA II sample suffers from reduced statistics due to worsened resolution and reduced single track efficiency.

B.2.6 Cosmic muons

In order to obtain high purity, the sample is restricted to events, which contain nothing else but a single muon. The ZEUS tracking algorithm assumes a track to start from the centre of ZEUS going outwards. If a muon passes through the whole detector, its track will be split into two reconstructed tracks. As for the second half of the track the propagation direction of the particle is assumed wrongly, the two reconstructed tracks have different charges.

- trigger requirements:
  - ◇ for HERA I data:
    DST bit 24 (B/R muon)
  - ◇ for HERA II data:
    DST bit 114 (CAL cosmics)
- event with exactly 2 tracks with opposite charge;
- $p > 1\,\text{GeV}$ for each track;
- $\frac{\vec{p_1} \cdot \vec{p_2}}{|p_1| \cdot |p_2|} < -0.95$ (coplanarity);
- $|\Delta p_t| < 250\,\text{MeV}$;
- $\Delta\theta < 0.03$;
- $|\phi_1 - \phi_2 - \pi| < 0.025$;
- $|z_{H1} - z_{H2}| < 2\,\text{cm}$.

Muons from cosmics are identified by their back-to-back topology. The helix parameter D_H (see Chapter 2.4), which is the distance of the helix in the xy-plane to $(0,0)$, is left out in this selection. This allows to use the distribution of D_H to extract the background contribution in the sample. For cosmics one expects identical D_H for both tracks, whereas for fake track combinations the two D_H should be uncorrelated.

A typical background sample was generated, using only events with 2 reconstructed tracks, both with a momentum $p > 1\,\text{GeV}$, which are not back-to-back to avoid admixture from cosmics: a coplanarity larger than -0.9 was requested. Figure B.8 displays the distributions of the two parameters D_H and of their difference ΔD_H. As expected the two values of D_H are identical for the cosmics sample. In the background sample these two values are uncorrelated and for HERA I data most of the candidates are found close to $D_H = 0$, which corresponds to primary vertex tracks. For HERA II data the distribution of the expected background is box-shaped. This is an artefact due to the shift of the collision point of the two beams in xy. As the reference point of the helix reconstruction does not match with the primary vertex, the parameter D_H for primary vertex tracks depends on the helix angle Θ_H (see Fig. 2.10). The upper limit of D_H is the distance between (x, y) of the primary vertex and $(0,0)$. Most of the tracks will be found with D_H close to this limit. The resulting shape is exactly what Fig. B.8 (d) shows. One finds two boxes of different size, because the collision position changed between e^+- and e^--running.

These histograms prove, that there is no measurable background contamination in the cosmic-muon sample.

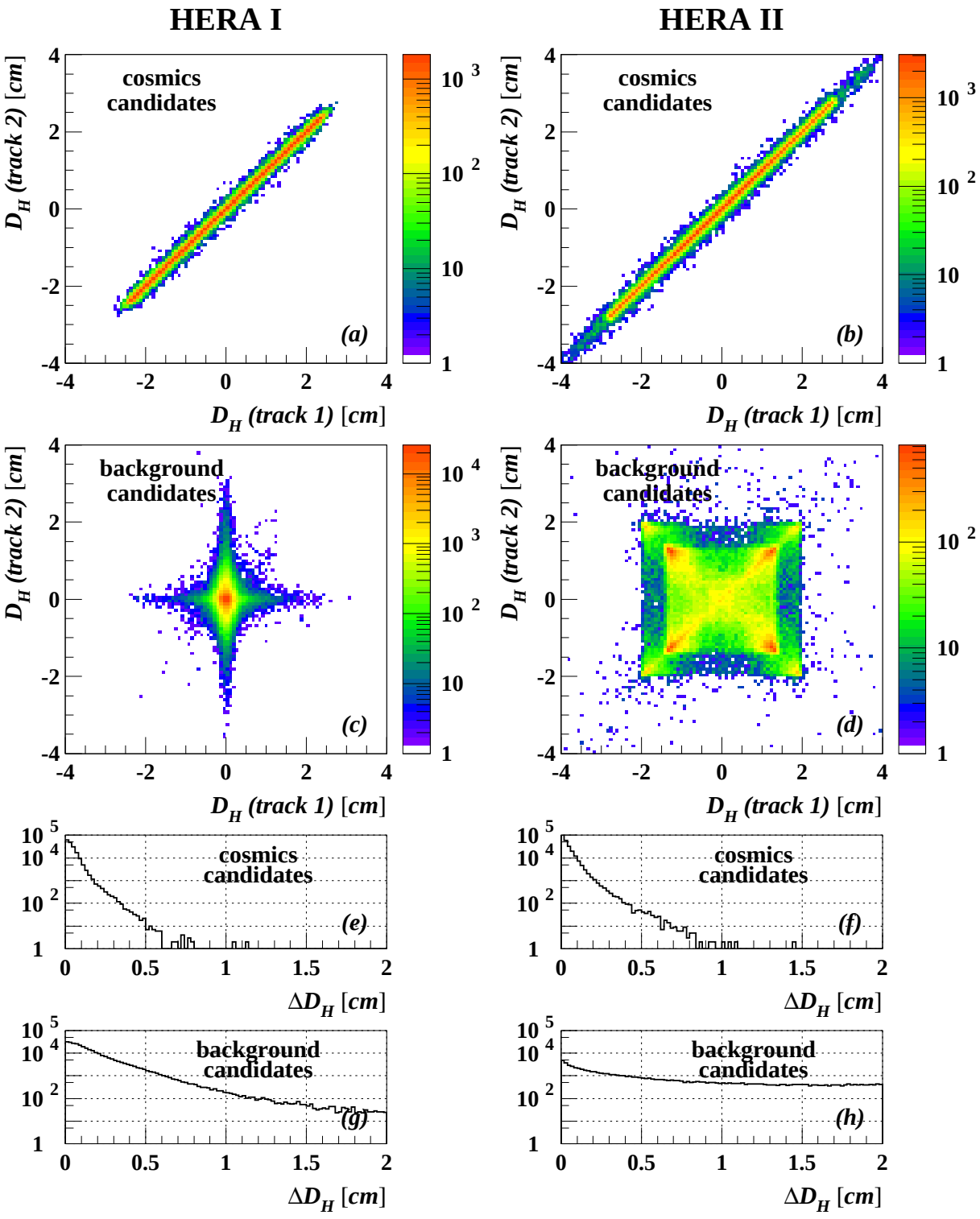

Figure B.8: Helix parameters D_H for the two tracks and their difference ΔD_H of cosmics candidates and expected background candidates, separated for HERA I and HERA II.

Appendix C

ZEUS software tools

For several issues software packages are designed and used by the whole ZEUS collaboration. In this appendix the most important ZEUS software tools for this dissertation will be introduced.

C.1 Calorimeter islands and ZUFOs

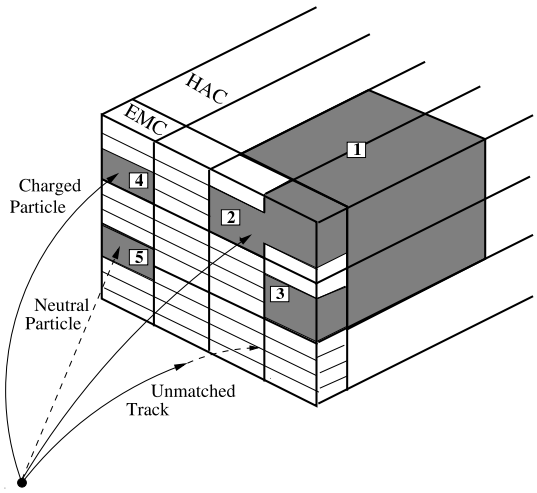

Figure C.1: Reconstruction of ZUFO's. Different ZUFO-types are shown.

Most of the showers in the calorimeter are spread out over more than one calorimeter cell. For the reconstruction of single events it is mandatory to combine the cell-signals into clusters, covering the full deposit of a primary particle (or jet). This is done by the islands algorithm [61, 62], which first combines adjacent cells separated for EMC, HAC1 and HAC2 sections into two-dimensional cell islands. In a second step, the cell islands are combined to 3-dimensional cone islands. At this level one can calculate the EMC-energy-fraction of an island, which is an important discriminator to distinguish between electron and hadron deposits in the calorimeter.

After some further corrections on backsplash [63] the cone islands are combined with CTD tracks to Zeus Unified Objects (ZUFOs)[1] [64]. A ZUFO can contain any number of tracks and islands (including zero, see Fig. C.1). Within this thesis only ZUFOs with exactly

[1] ZUFOs are also called Energy Flow Objects (EFOs).

one assigned track and one island will be used. For this type of ZUFOs one can attach calorimeter-related properties to tracks.

C.2 DIS Electron finders

The identification of the scattered electron in a deep inelastic scattering (DIS) event is mandatory for many analyses. The DIS-electrons are typically high-energetic ($> 10\,\text{GeV}$) and mostly scattered in the rear direction (well separated from other particles in the same event). Under such kinematic conditions the calorimeter-based electron identification is very efficient. Therefore the standard DIS-electron finders are based on the shower-shape identification.

ZEUS is using two different electron finders:

SINISTRA electron finder

The electron finder SINISTRA95 is a feed-forward neuronal network. [65] The energy deposits in the calorimeter-cells are obtained as a discrete representation of the shower profile, which are expanded in terms of rotationally invariant moments of two orthogonal function sets, representing the shower shape in the two planes perpendicular and longitudinal to the initial direction of the particle. These moments (after normalisation to their corresponding variance) and the total energy of the cluster are the 17 input variables of the neuronal network.

SINISTRA is optimised for DIS-electrons in the RCAL.

EM electron finder

The EM electron finder [66, 67] uses both calorimeter and tracking information (where available) and takes the geometrical organisation of the detector into account. Likelihoods for 4 calorimeter-related and 3 track-island-matching-related variables are combined in a global likelihood for the electron identification.

C.3 The conversion finder CONVERT2

The software package CONVERT2 [50] was written for HERA I data to identify electron-positron pairs emerging from photon conversions.

The idea of the conversion finder is based on the special topology of photon conversion pairs. As the photon is massless one expects the two decay products both to move in the same direction. As they are oppositely charged, their trajectories turn into different directions in the solenoidal magnetic field. Thus the photon conversion finder is searching for track pairs with opposite charge, which are parallel and close together at their point of closest approach.

CONVERT2 calculates a distance parameter D using the distance of closest approach Δxy of the two helices in the xy-plane and their opening polar angle $\Delta\theta$. Δxy is defined as the distance between the two helices in the xy-plane along the straight line connection between the two centres of the two helices (circles in the xy-plane). The parameter D is

the quadratic sum of these two values, weighted by their resolution:

$$D = \sqrt{\left(\frac{\Delta xy}{\sigma(\Delta xy)}\right)^2 + \left(\frac{\Delta\Theta}{\sigma(\Delta\Theta)}\right)^2} \quad . \tag{C.1}$$

This distance parameter D is the main discriminator in CONVERT2 to identify photon conversions. Furthermore, the distance in z D_z between the two helices at their point of closest approach is calculated and stored, but not used for the selection in the standard CONVERT2 applications. The point of closest approach is stored as well; it is the origin of the photon conversion.

The photon conversion finder was designed for two different cases: if photon conversion background has to be rejected from data samples, electrons from photon conversions have to be found with high efficiency. In this case soft selection cuts are applied to reject all candidates for photon conversions. The second possible application of the conversion finder is the selection of conversion samples with high purity. For this task the selection cuts are much harder.

It is necessary to mention, that CONVERT2 was written and tuned during HERA I. This implies, that the resolutions $\sigma(\Delta xy)$ and $\sigma(\Delta\theta)$ were determined using HERA I data only. As the running conditions for the CTD have changed for HERA II, it is likely that these parameters have changed as well. However, no update of CONVERT2 for HERA II data is available yet.

Appendix D

Function to describe the threshold effect

The probability density function for the measured signal height s should be a LANDAU distribution. The low value range of a LANDAU can be described very well with a Gaussian distribution $d(s)$. As the threshold effect only affects the lowest end of the distribution of signal heights, this replacement is very safe. In first order the width of $d(s)$ scales with the mean value $< d(s) >$. This condition is fulfilled by the following equations:

$$d(s) = \frac{1}{b} \cdot g\left(\frac{s}{b} - a\right) \tag{D.1}$$

$$g(x) = \frac{1}{\sqrt{2\pi}} \exp\left(-\frac{1}{2}x^2\right) \tag{D.2}$$

where b is the width of $d(s)$ and a is the mean value of $d(s)$ in units of b. Using

$$\int_{-\infty}^{\infty} y \cdot g(y)\, dy = 0 \quad \text{and} \quad \int_{-\infty}^{\infty} g(y)\, dy = 1 \quad , \tag{D.3}$$

one derives immediately

$$\begin{aligned} < d(s) > &= \frac{1}{b} \int_{-\infty}^{\infty} s \cdot g\left(\frac{s}{b} - a\right)\, ds \\ &= \int_{-\infty}^{\infty} (b(y+a))\, g(y)\, dy \\ &= b \int_{-\infty}^{\infty} y \cdot g(y)\, dy + ab \int_{-\infty}^{\infty} g(y)\, dy \\ &= 0 + ab \end{aligned} \tag{D.4}$$

Now we want to know the mean value of $d(s)$ under the assumption of a threshold c:

$$< d(s) > |_C = \int_c^{\infty} s \cdot d(s)\, ds = b \int_{c/b-a}^{\infty} y \cdot g(y)\, dy + ab \int_{c/b-a}^{\infty} g(y)\, dy \quad . \tag{D.5}$$

The first integral computes like

$$\int_{\tilde{c}}^{\infty} y \cdot g(y)\, dy \;=\; \int_{\tilde{c}}^{\infty} y \cdot \exp\left(-\frac{1}{2}y^2\right) dy \;=\; -\int_{-\tilde{c}^2/2}^{-\infty} \exp(z)\, dz \;=\; \exp\left(-\frac{\tilde{c}^2}{2}\right) \quad . \tag{D.6}$$

One expects the threshold to be far below the mean of $d(s)$, which means $c \ll ab$. In this case for the second integral one can use the approximation

$$\int_{c/b-a}^{\infty} g(y)\, dy \;=\; 1 - \int_{-\infty}^{c/b-a} g(y)\, dy \;\approx\; 1 \quad . \tag{D.7}$$

Using Eqns. D.6 and D.7, Eqn. D.5 simplifies to

$$< d(s) > |_C \;\approx\; b \cdot \exp\left(-\frac{1}{2}\left(\frac{c}{b} - a\right)^2\right) \;+\; ab \quad . \tag{D.8}$$

Furthermore, we employ

$$(c - ab)^2 \;=\; c^2 - 2abc + (ab)^2 \;\approx\; -2abc + (ab)^2$$

and Eqn. D.4 to end up with

$$\begin{aligned} < d(s) > |_C \;&\approx\; b \cdot \exp\left(\frac{ac}{b} - \frac{a^2}{2}\right) \;+\; ab \;=\; ab \cdot \left(1 \;+\; \frac{1}{a}\exp\left(-\frac{a^2}{2}\right)\exp\left(\frac{ac}{b}\right)\right) \\ &=\; < d(s) > \cdot \left(1 + \tilde{a} \cdot \exp\left(\frac{\tilde{b}}{< d(s) >}\right)\right) \quad , \end{aligned} \tag{D.9}$$

using the replacements

$$\begin{aligned} \tilde{a} \;&=\; \frac{1}{a}\exp\left(-\frac{a^2}{2}\right) \\ \tilde{b} \;&=\; a^2 c \quad . \end{aligned}$$

Appendix E

Remainder term treatment

Very often effects, happening on single wires, have to be calculated using global track variables. Especially for ψ' this is an important simplification. Instead of calculating corrections for each hit separately and afterwards calculating the (truncated) mean, the order is reversed: the correction is applied to the mean dE/dx of all hits of one track. If the correction depends on a variable, which varies between different hits (like ψ') it is calculated using the mean value of the parameter. As these operations are not distributive, an error is made by this approach. It is needed to estimate this error.

The following calculation always treats the true dE/dx like the mean value of many measurements. For better readability the 'mean brackets' are not written. For the same reasons, the truncation is skipped.

Let's think about the case, that the measurement of dE/dx depends on one variable ξ. The measured dE/dx_m is then given as the mean value of dE/dx for all hits, which means

$$\frac{dE}{dx}_m = \frac{1}{n}\sum_{i=1}^{n}\frac{dE}{dx}\cdot f(\xi_i) \quad . \tag{E.1}$$

$f(\xi_i)$ is the function which describes the dependence of dE/dx on ξ. As dE/dx is now equal for all hits, this can be rewritten as

$$\begin{aligned}
\frac{dE}{dx}_m &= \frac{dE}{dx}\cdot\frac{1}{n}\sum_{i=1}^{n} f(\xi_i) \\
&= \frac{dE}{dx}\cdot\frac{1}{n}\sum_{i=1}^{n}\left(f(\bar{\xi})+f(\xi_i)-f(\bar{\xi})\right) \\
&= \frac{dE}{dx}\cdot\left(f(\bar{\xi})+\frac{1}{n}\sum_{i=1}^{n}\left(f(\xi_i)-f(\bar{\xi})\right)\right) \\
&= \frac{dE}{dx}\cdot\left(f(\bar{\xi})+\mathcal{R}\right) \quad .
\end{aligned} \tag{E.2}$$

To estimate the size of the remainder term $\mathcal{R}$ we can use the Taylor series of $f(\xi_i)$:

$$f(\xi_i) = a + b \cdot \xi_i + c \cdot \xi_i^2 \tag{E.3}$$

$$\begin{aligned} \mathcal{R} &= \frac{1}{n} \sum_{i=1}^{n} \left(a + b\xi_i + c\xi_i^2 - a - b\bar{\xi} - c\bar{\xi}^2 \right) \\ &= \frac{1}{n} \left(b \sum_{i=1}^{n} (\xi_i - \bar{\xi}) \; + \; c \sum_{i=1}^{n} (\xi_i^2 - \bar{\xi}^2) \right) \\ &= c \cdot V(\xi) \quad . \end{aligned} \tag{E.4}$$

As a benefit of using mean values the lowest-two order terms disappear. The size of the error is given by the factor of the quadratic term in $f(\xi)$ and the variance of the ξ_i.

Appendix F

Remainder term calculation for $\overline{\psi'}$

It was shown, that for the drift-time effect correction the remainder term cannot be neglected. This appendix shows how it is calculated and used in the corrections.

Compared with Appendix E, in this special case Eqn. E.1 can be written as

$$s_m = \frac{1}{n}\sum_{i=1}^{n} s|_{\psi'=0} \cdot f(\psi') \quad , \quad \text{with} \tag{F.1}$$

$$\begin{array}{rcl} s & : & \text{signal, if there would be no effect from the remainder term} \\ s_m & : & \text{measured signal, including the effect of the remainder} \end{array}$$

The correction function $f(\psi')$ can be described by its Taylor series:

$$f(\psi') = \sum_{i=0}^{\infty} b_i \cdot (\psi')^i \tag{F.2}$$

where the parameters b_i depend on $s|_{\psi'=0}$.

For the two reference points in dE/dx, given by the pion and electron tuning sample, the parameters $b_{i\,j},\ j = 1, 2$ can be extracted as shown later.

Using the shortcuts

$$\begin{array}{rcll} e_j & : & \text{expected signal for tuning sample } j & \\ g_i & := & \dfrac{b_{i\,2} - b_{i\,1}}{e_2 - e_1} & \\ k & := & s|_{\psi'=0} \cdot \mathcal{R} & , \quad \text{effect of the remainder} \\ d_0 & := & s|_{\psi'=0} & \end{array}$$

one can write down the following relations:

$$\begin{array}{rcl} s & = & s_m - k \\ d_0 & = & b_{0\,1} - g_0 e_1 + g_0 s \\ k & = & (b_{2\,1} - g_2 e_1 + g_2 s) \cdot V(\psi') \cdot d_0 \quad . \end{array} \tag{F.3}$$

The latter two equations use the linear extrapolation of the factors in the Taylor series between the two tuning samples. Furthermore the last equation uses Eqn. E.4.

This leads to an equation to calculate k, using only b_{ij}, e_j, s_m and $V(\psi')$.

The last step in this calculation is to extract b_{ij} from the tuning samples. One is interested in the mean value of the derivatives in the range of ψ' covered by the track. This can be done by calculating the Taylor series of Eqn. 4.29 for variable expansion points and taking the mean evolution parameters by integrating them within the covered ψ' range.

Finally one transformation has to be handled properly: Eqn. 4.29 is a function of $\overline{\psi'}$ whereas Eqn. F.2 depends on ψ'. This has two consequences: One of them is, that in the profile histograms for extracting the fit parameters s_m has to be replaced by $s = s_m - k$. The other effect is given in the scale of the abszissa of these profiles. For most of the tracks ψ' of the innermost hits is close to 0 (this is at least true for primary-vertex tracks). For such tracks the scale between $\overline{\psi'}$ and ψ' is approximately a factor of 2. As one uses the second derivative of $f(\psi')$ in this calculation, this leads to an overestimation of the remainder by a factor of 4.

Appendix G

End-plate correction with the applied hit-weight function

In chapter 4.3.1.7 the calculation of the parameter A is only shown for a step function to describe the hit weights (Eqn. 4.14). This appendix shows, that a very similar calculation can be done for the really used weight function as shown in Figure 4.52:

$$f(\Delta z) = \begin{cases} 1 & : \quad \Delta z_{lim} \leq \Delta z \\ 1 - (1 - \frac{\Delta z}{\Delta z_{lim}}) \cdot c & : \quad \Delta z_{lim}/2 < \Delta z < \Delta z_{lim} \\ 1 - \frac{1}{2} \cdot c & : \quad \Delta z < \Delta z_{lim} \end{cases} \quad . \tag{G.1}$$

By integration of $f(\Delta z)$ one can rewrite A as

$$A = \frac{3}{8}\, \Delta z_{lim} \cdot c \quad .$$

Using the names

$$\begin{aligned} n_u &:= \text{number of unaffected hits} \\ n_a &:= \text{number of affected hits} \\ n_h &:= \text{number of all hits} \end{aligned}$$

equation 4.17 transforms into

$$\begin{aligned} f &:= \frac{n_u + \sum\limits_{\Delta z_i < \Delta z_{lim}} f(\Delta z_i)}{n_h} \\ &= 1 - c\frac{\sum\limits_{\Delta z_i < \Delta z_{lim}/2} \frac{1}{2} + \sum\limits_{\Delta z_{lim}/2 < \Delta z_i < \Delta z_{lim}} (1 - \frac{\Delta z_i}{\Delta z_{lim}})}{n_h} \\ &= 1 - \frac{A}{\Delta z_{lim}} \cdot \frac{8}{3}\frac{\sum\limits_{\Delta z_i < \Delta z_{lim}/2} \frac{1}{2} + \sum\limits_{\Delta z_{lim}/2 < \Delta z_i < \Delta z_{lim}} (1 - \frac{\Delta z_i}{\Delta z_{lim}})}{n_h} \quad . \end{aligned} \tag{G.2}$$

This is quite similar to Eqn. 4.17. The only change is

$$n_a \quad \rightsquigarrow \quad \frac{8}{3}\left(\sum_{\Delta z_i < \Delta z_{lim}/2} \frac{1}{2} + \sum_{\Delta z_{lim}/2 < \Delta z_i < \Delta z_{lim}} (1 - \frac{\Delta z_i}{\Delta z_{lim}}) \right) \quad . \tag{G.3}$$

If we define the weight of a hit according to the end plate effect to be the difference $(1 - f(\Delta z_i))$, both terms can be interpreted as the sum of these weights, normalized by c. In case of the step function, each of the affected hits has a normalised weight of 1 and the sum of these weights is simply the number of affected hits. Using f from Eqn. G.1, all hits with $\Delta z_i < \Delta z_{lim}/2$ have a normalised weight of 1/2 and hits with $\Delta z_{lim}/2 < \Delta z_i < \Delta z_{lim}$ have a weight $(1 - \frac{\Delta z_i}{\Delta z_{lim}})$.

In the limit of many equidistant hits it can also be shown, that both sides of Eqn. G.3 are identical: In each of the ranges $\Delta z_i < \Delta z_{lim}/2$ and $\Delta z_{lim}/2 < \Delta z_i < \Delta z_{lim}$ half of the affected hits can be found and necessarily

$$\begin{aligned} & \frac{8}{3}\left(\sum_{\Delta z_i < \Delta z_{lim}/2} \frac{1}{2} + \sum_{\Delta z_{lim}/2 < \Delta z_i < \Delta z_{lim}} (1 - \frac{\Delta z_i}{\Delta z_{lim}})\right) \\ = \; & \frac{8}{3}\left(\frac{1}{2} \cdot \frac{n_a}{2} + \frac{1}{4} \cdot \frac{n_a}{2}\right) \\ = \; & n_a \quad . \end{aligned}$$

Applying the replacement of Eqn. G.3 in Chapter 4.3.1.7 does not harm any of the calculations. Thus the parameter A can still be calculated with Eqn. G.3 and 4.20.

Appendix H

Uncertainty of the end-plate-effect correction

The end-plate-effect correction has features which require special methods to measure its uncertainty. This appendix describes why a 'traditional' error propagation cannot work for this correction and how the proper uncertainty calculation has to be done.

First one should focus on the propagation of the error $\sigma(\Delta z)$. The uncertainty of the reconstructed z-positions of single hits is a consequence of the uncertainty of the fitted track helix. If one varies the parameters of the helix within their errors, the z-positions of all hits vary simultaneously. Especially if one restricts to the outermost hits of the track (the only relevant hits for calculating the end-plate-effect correction) it is a very good approximation to assume, that a variation of the helix corresponds to simultaneous shifts of the z-position of all hits. This argumentation is also true for the distance Δz of the hits to the end-plate. Figure H.1 displays the dependence of the end-plate-effect correction factor f on the variation of the Δz-positions of the hits. As an example, a typical track passing through the end-plate in the middle of the 7^{th} superlayer is shown. The dependence has a sawtooth-shape. The error propagation of $\sigma(\Delta z)$ to an error σf can be calculated as the mean variation of f when varying Δz within its resolution of $\approx 2\,\text{cm}$ as shown in Fig. 4.51.

If one shifts the hits closer to the end-plate (decreasing variation of Δz), f increases. As soon as the outermost hit is shifted beyond the sensitive volume of the CTD, this hit is

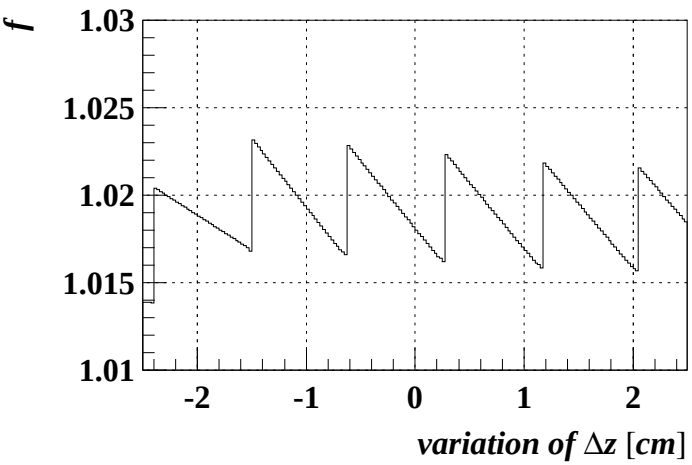

Figure H.1: Variation of the correction factor f for the end-plate-effect correction depending on the variation of the z-positions of the hits. A track passing through the end-plate in the middle of the 7^{th} superlayer was used for this plot.

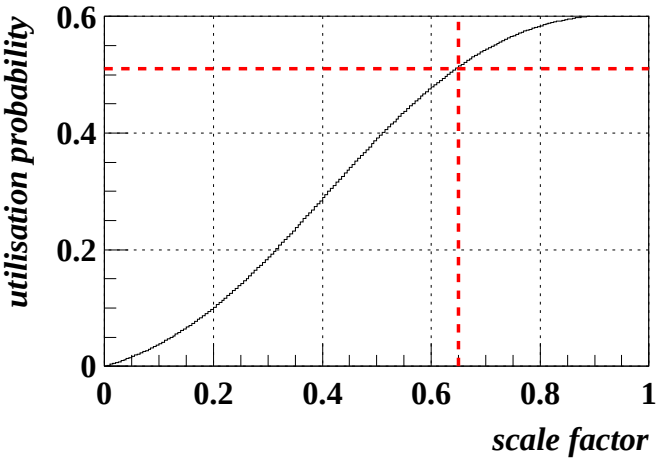

Figure H.2: The probability of a hit with reduced signal height (scale factor) to be used for the truncated mean value. The dashed lines indicate typical values for the end-plate-effect correction.

not taken into account anymore and therefore the correction factor plumps down. These oscillations happen at a scale which is much smaller than the typical resolution $\sigma(\Delta z)$. To measure the uncertainty of f with respect to the Δz-resolution, it is not sufficient to compute f for the two variations $\pm\sigma(\Delta z)$. Instead, one first has to compute the extreme values f_{max}, f_{min} of f just before and after a 'jump'. As between these jumps f rises almost linearly, a very good approximation of the uncertainty is given by

$$\sigma(f) = \frac{1}{\sqrt{12}} (f_{max} - f_{min}) \quad . \tag{H.1}$$

Another part of the uncertainty is caused by the selection of hits for the truncated mean calculation. This selection has a huge impact on the uncertainty, because the whole end-plate effect is caused by a small fraction of all hits of the track (only the ones close to the end-plate). If some of these hits are not used for the dE/dx calculation, the size of the correction changes significantly. Furthermore, the end-plate effect reduces the height of the signal and therefore increases the probability for affected hits to be one of the lowest 10% of all hits and therefore to be rejected by the truncation method. This kind of dependence is shown in Fig. H.2: The probability for a hit to be used by the truncated mean method is shown depending on the scale factor of this hit compared to the other hits of the same track. The lines in the plot indicate typical values for hits, affected by the end-plate effect. One can see, that roughly 1/2 of these hits are rejected by the truncated mean. This is still a very conservative assumption: As the end-plate-effect correction was calculated with tracks, which also suffer from this hit rejection, a big fraction of tracks used to extract the parameters for the end-plate-effect correction are in fact not end-plate-affected (their critical hits are rejected). Thus the end-plate effect is larger than suggested by the correction parameters.[1]

The 'real' size of the end-plate effect can be calculated. In order to do this one needs to know the number of hits within one track, which are affected by the end-plate. Figure H.3 shows the number of hits within the critical distance to the end-plate for each track. One can see, that if a track suffers from the end-plate effect (more than 0 critical hits), most probably 2 hits are within this range. The relation between the visible and the real size

[1] Besides the increased probability for a hit close to the end-plate to be rejected by the truncated mean calculation, there is in addition an increased probability for such a track to fall below the threshold limit. Thus the real probability for a hit close to the end-plate to be used for the dE/dx calculation is even lower.

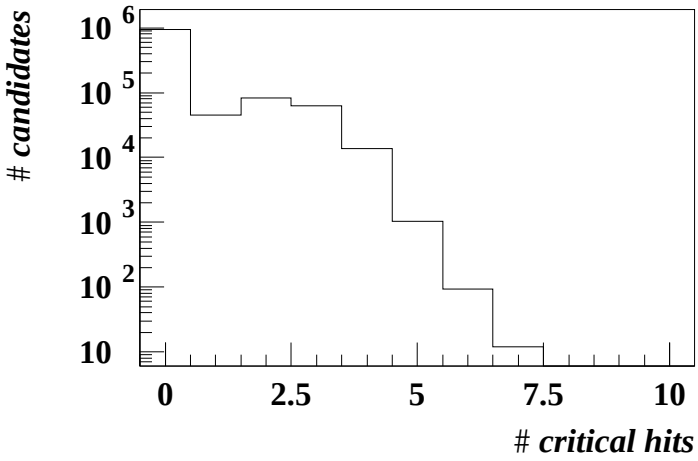

Figure H.3: The number of possible hits for the track within a critical distance to the end-plate.

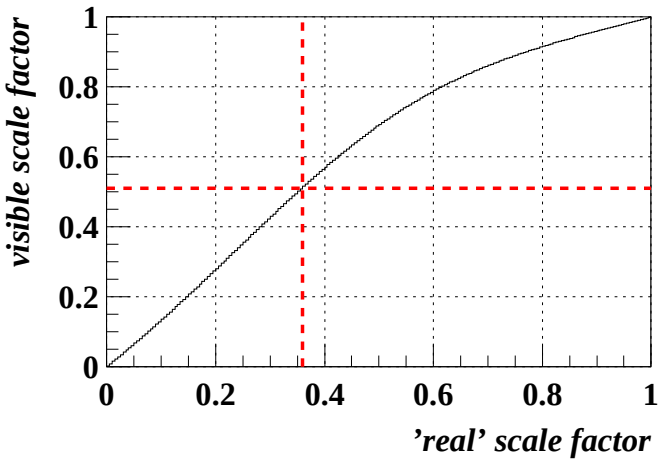

Figure H.4: The relation between the visible and the real scale factor for hits, which are maximum end-plate-affected. The calculation is done for tracks with 30 used hits. The dashed lines represent typical values.

of the end-plate effect for tracks with 30 used hits and 2 hits in the critical range close to the end-plate is shown in Fig. H.4. One finds a typical 'real' scale of about 40%.

Based on this number, one can calculate the variation of the end-plate-effect correction.

Appendix I

Projections in tetrahedron plots

The correlations between likelihood ratios of 4 different particle hypotheses can be visualised in a 3-dimensional scatter plot. The constraint on the sum of these likelihood ratios to be 1 causes all dots of this plot to be located within a tetrahedron. To show this plot on a 2-dimensional paper-sheet, the 4 surfaces of the tetrahedron are shown after projecting all entries from the inner volume onto these surfaces.

The projection can be carried out in different ways. This appendix describes the differences between a parallel projection and a point projection, using the pion data sample as an example.

A parallel projection means, that the value within the projection axis is ignored. An entry in one edge of a triangle means, that the corresponding hypothesis has the probability 1 (with respect to all four hypotheses). The major handicap of this kind of projection is, that the sum rule is broken (L_r for the projection axis is 'removed'). Therefore a probability of 0 does not anymore mean, that the entry ends up at an edge of a triangle. One way to construe this is to say, that the size of the projected triangle varies with L_r of the projection axis. If in the projection axis the probability is 1, the entry ends up in the centre of the triangle.

The point projection projects along straight lines through the corner opposite to the projection plane. This means the position, where an entry is shown in the projected triangle, represents how the probabilities between the shown three particle types are shared. One can also say, the fourth particle type is neglected; the normalisation of the likelihood ratios is restricted to the three shown particle types. This implies, that entries in the corner of the projected axis cannot be shown: A probability of 1 for the cancelled particle type implies, that all three remaining types have zero probability, therefore the denominator in the normalisation is zero. The benefit of this kind of projection is to preserve the sum rule, therefore entries with zero probability are always shown on the edge of the triangle. On the other hand in this projection a probability of 1 does not correspond to the whole four-particle-types system, but only to the three types which are shown in the triangle. If for example a particle has zero probability to be a kaon or a proton and nonzero probability for the pion and electron hypotheses, in the triangles which contain the pion and the electron hypothesis the entry will appear somewhere on the edge between these two particle types, whereas for example in the pion-kaon-proton triangle it will appear exactly in the pion corner (restricted to the pion-kaon-proton system this candidate is for sure a pion). The different appearances of the two projection types

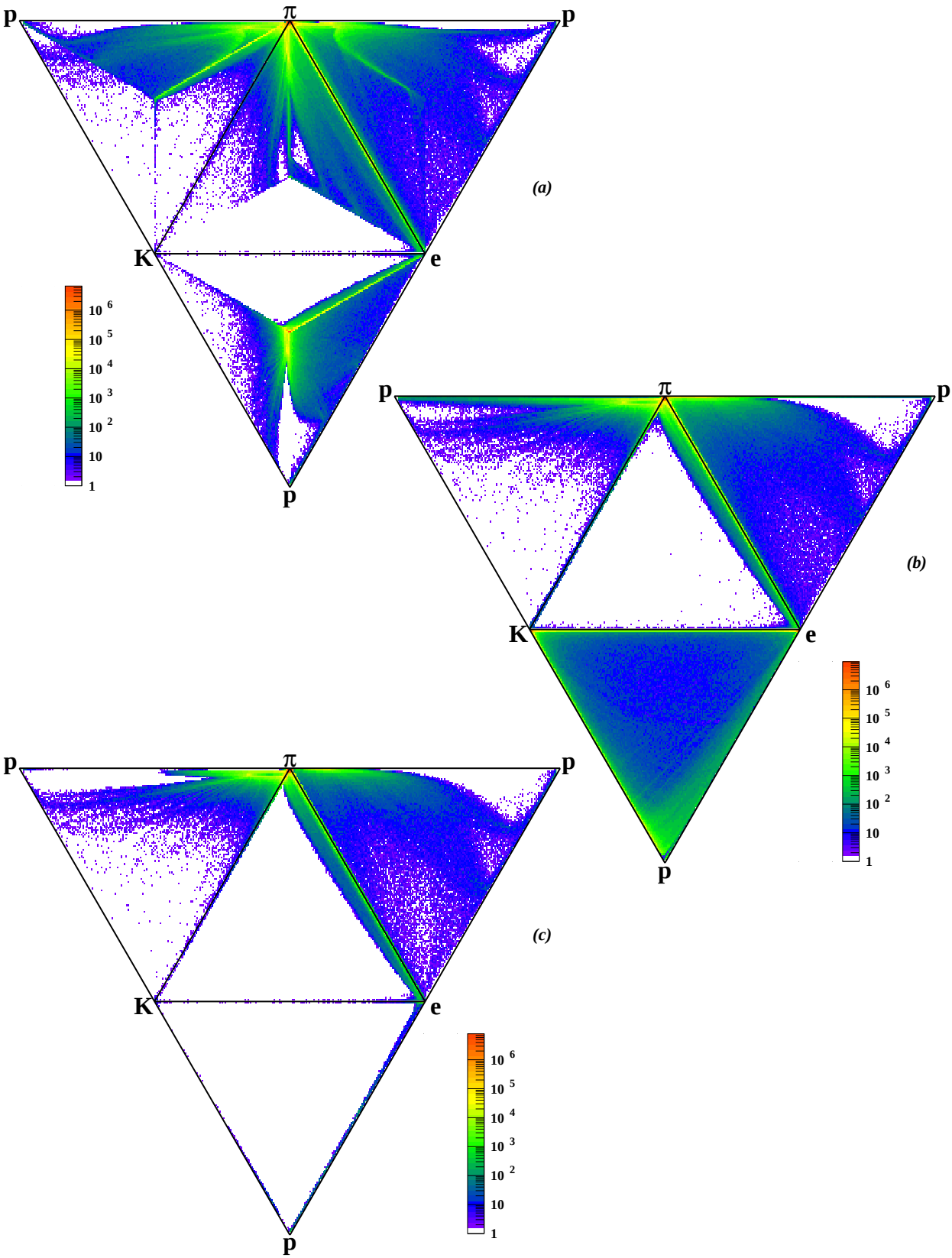

Figure I.1: Likelihood ratios of the pion sample projected to the surface of the accessible tetrahedron. (a) parallel projection, (b) point projection, (c) point projection with preselected tracks (not too low probability for pions).

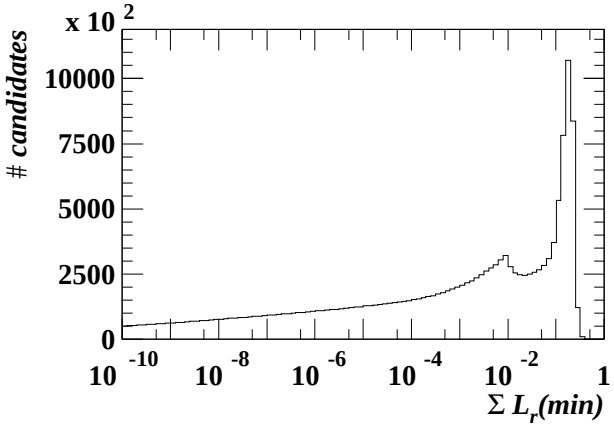

Figure I.2: Histogram of the sum of the likelihood ratios of the two most unlikely hypotheses (after corrections). This number represents the distance of the candidate to the closest surface of the tetrahedron.

can be seen in Fig. I.1. The parallel projection is shown in (a). The observed structures are caused by the projection method. For example each triangle seems to be split into three sub-triangles. The rates along the edges of these sub-triangles are very high. This happens, because in most cases there exist no more than two hypotheses with a probability significantly higher than 0. If one of these two hypotheses is the one in the projection axis, the entry will appear in the tetrahedron plot somewhere on the straight line between the centre of the triangle and the edge corresponding to the second hypothesis with high probability. Thus these lines are highly populated. This becomes most obvious in the K-p-e-triangle: as the shown sample are pions, most of the entries are in the centre of the triangle, but depending on the momentum it might be, that the Bethe-Bloch curve for pions approaches the one of another particle type. In this case, the entry in the plot can be found closer to the edge of that particle type. Another distinctive feature is the almost empty sub-triangle in the K-p-e- and the K-e-π-system between the K-e-line and the triangle centre. One can expect that most of the entries in the tetrahedron are close to one of its surfaces (usually the probability for at least one of the three particle types is almost 0). Based on this assumption the empty sub-triangles indicate, that there are almost no tracks on the corresponding surfaces.

The assumption, that most entries in the tetrahedron are located close to its surface, is verified in Fig. I.2, which shows the sum of $L_r(i)$ for the two particle types with the lowest probabilities. As the sum of all 5 $L_r(i)$'s is 1 by definition, this number is the distance of the entry to the triangle's surface (as this calculation uses all 5 hypotheses in fact this the distance to the surface of the 4-dimensional pentahedron including the muon-hypothesis). One finds that almost all entries are within the 5%-range to the closest surface.

In the point projection (Fig I.1 (b)) the structures caused by the projection method disappear. For example in the K-e-π-triangle one can see much better, that the probability for kaons in almost all cases is very small. Therefore this kind of projection is the preferred one. In the K-p-e-triangle the entries are spread over most of the area: for tracks with a pion-probability of almost 1, the way, how the remaining probability is split between kaon-, proton- and electron-hypothesis, is almost meaningless. In order not to be mislead by such entries, it is useful to select only such tracks for filling each triangle of the histogram, which have a reasonable probability to represent one of the three particle types in the triangle's edges (in other words, show only entries which are close to the visualised surface of the tetrahedron). This is granted by imposing two conditions for candidates to enter the plot.

- The sum of the three probabilities corresponding to the triangle under investigation

has to be larger than 95%. After this cut only entries close to the surface are shown in the corresponding triangle. One does not look 'through' the tetrahedron anymore to entries located close to the other 3 sides. According to Fig. I.2 almost all candidates are within a 5%-range to one of the surfaces, therefore almost no candidates will be removed from all 4 surfaces at the same time.

- One is not interested in the distribution of L_r between three hypotheses if one already knows, that the candidate under investigation is identified as belonging to one of the other remaining particle types. Such candidates should not be shown in the tetrahedron plot. Therefore it is requested, that the sum of $L_r(i)$ for the three hypotheses shown in a triangle has to be at least as big as the sum of the a-priori probabilities for the corresponding particle types.

A helpful side-effect of such a selection is the fact, that there is almost no difference left between parallel and point projection, because all entries shown at a surface are located very close to that surface before they are projected.

The result of this preselection is given in Fig. I.1 (c); as expected most of the entries in the K-p-e-triangle disappeared, the remaining ones are all located on or close to the edges of the triangle, mostly preferred in one of the corners.

In all three visualisations one observes, that most of the entries are very close to the pion-corner. This shows, that the majority of the pions are identified very well.

References

[1] A. Longhin, *Measurement of Beauty Production at HERA with a $D*+\mu$ Tag.* Ph.D. Thesis, Universita di Padova, Padova, Italy, Report DESY-THESIS-2004-050, 2003;
ZEUS Coll., S. Chekanov et al., Phys. Rev. **D 70**, 12008 (2004);
ZEUS Coll., S. Chekanov et al., Phys. Lett. **B 599**, 173 (2004);
O. Gutsche, *Measurement of Beauty Quark Cross Sections in Photoproduction with the ZEUS Experiment at the Electron-Proton Collider HERA.* Ph.D. Thesis, Hamburg University, Report DESY-THESIS-2005-010, 2005;
I. Bloch, *Measurement of Beauty Production from Dimuon Events at HERA / ZEUS.* Ph.D. Thesis, Hamburg University, Report DESY-THESIS-2005-034, 2005.

[2] ZEUS Coll., S. Chekanov et al., Eur. Phys. J. **C 38**, 29 (2004);
ZEUS Coll., S. Chekanov et al., Phys. Lett. **B 610**, 212 (2005).

[3] ZEUS Coll., S. Chekanov et al., Eur. Phys. J. **C 44**, 351 (2005).

[4] ZEUS Coll., S. Chekanov et al., Phys. Lett. **B 591**, 7 (2004).

[5] M. Wing, *The Study of Heavy Quark Production in High E_T Photoproduction at HERA Using the ZEUS Detector.* Ph.D. Thesis, University College London, London, Report RAL-TH-1999-011, 1999.

[6] O.M. Kind, *Production of Heavy Flavours with Associated Jets at HERA.* Ph.D. Thesis, Universität Bonn, Bonn, Germany, Report BONN-IR-07-04, 2007, available on `http://www-zeus.physik.uni-bonn.de/german/phd.html`.

[7] M. Jüngst, *Elektronidentifikation mit dem ZEUS-Detektor und Bestimmung des Beauty-Produktionsquerschnitts.* Diploma Thesis, Universität Bonn, Bonn, Germany, Report BONN-IB-05-15, 2005, available on `http://www-zeus.physik.uni-bonn.de/german/diploma.html`.

[8] E.A. Nuncio-Quiroz, *Beauty production at HERA in the semileptonic muon+electron channel and Next-to-Leading Order QCD Effects. In preparation.* Ph.D. Thesis, Universität Hamburg, Hamburg, Germany, 2007.

[9] M. Hausschild, *Particle Identification Techniques with dE/dx*, 2003, available on `http://hausch.home.cern.ch/hausch/MediPix/Talks/dEdx.pdf`.

[10] *HERA – A Proposal for a Large Electron Proton Colliding Beam Facility at DESY.* DESY Report HERA 81-10, Hamburg, Germany, 1981.

[11] U. Schneekloth, *The HERA Luminosity Upgrade.* DESY Report HERA 98-05, Hamburg, Germany, 1998.

[12] D. Bailey et al., *Study of beam-induced backgrounds in the ZEUS detector from 2002 HERA running* (unpublished). ZEUS Note 02-018, 2002;
D. Bailey et al., *Addendum – Study of beam-induced backgrounds in the ZEUS detector from 2002 HERA running* (unpublished). ZEUS Note 02-020, 2002;
D. Bailey et al., *Addendum – Study of beam-induced backgrounds in the ZEUS detector from 2002 HERA running* (unpublished). ZEUS Note 02-027, 2002.

[13] ZEUS Coll., U. Holm (ed.), *The ZEUS Detector*. Status Report (unpublished), DESY, 1993, available on `http://www-zeus.desy.de/bluebook/bluebook.html`.

[14] E. Hilger, *ZEUS Coordinate System* (unpublished). ZEUS-86-17, internal ZEUS note, 1986.

[15] A. Bamberger et al., Nucl. Inst. Meth. **A 382**, 419 (1996);
A. Bornheim, *Kalibration des Presamplers für die Elektron-Energiemessung im ZEUS-Detektor*. Diploma Thesis, Universität Bonn, Bonn, Germany, Report BONN-IB-95-24, 1995, available on `http://www-zeus.physik.uni-bonn.de/german/diploma.html`.

[16] A. Dwurazny et al., Nucl. Inst. Meth. **A 277**, 176 (1989);
ZEUS colaboration, *Proposal for a Hadron-Electron separator in the ZEUS Forward and Barrel Calorimeters* (unpublished). ZEUS-91-044, internal ZEUS Note, 1991.

[17] H. Bärwolff et al., Nucl. Inst. Meth. **A 283**, 467 (1989).

[18] B. Foster et al., Nucl. Inst. Meth. **A 338**, 254 (1994).

[19] C. Catterall, *Measurement of Charged Particles from the Hadronic Final State of Electron-Proton Deep Inelastic Scattering at the Centre of Mass Energy of* 296 *GeV*. Ph.D. Thesis, University of London, London, 1995.

[20] K. Long, D. H. Saxon and B. T. Payne, *ZEUS CTD Parameters issue 5 - revised* (unpublished). ZEUS-89-23, internal ZEUS note, 1989.

[21] M. Sutton, *Status of the ZEUS CTD Gas System*, available on `http://www-zeus.desy.de/components/ctd/WWW/gas/gasnow-bw.html`.

[22] J.A. Blissett et al., Nucl. Inst. Meth. **A 245**, 291 (1986).

[23] D.S. Bailey et al., Nucl. Inst. Meth. **A 396**, 320 (1997).

[24] S.M. Fisher, P. Palazzi, B. Rousseau and M. Ruggier, *ADAMO Users Guide – Version 3.3*. CERN ECP, available on `http://adamo.web.cern.ch/Adamo/guide/Document.html`.

[25] O. Deppe, *Measurement of $D^{\star\pm}$ Electroproduction at HERA*. Ph.D. Thesis, Hamburg University, Hamburg (Germany), Report DESY-THESIS-2000-006, 1999.

[26] L. Malter, Phys. Rev. **50**, 48 (1936).

[27] D. Bailey, R. Hall-Wilton, Comp. Phys. Comm. (2001).

[28] V. Chiochia et al., Nucl. Inst. Meth. **A 501**, 60 (2003);
C. Coldewey, for the ZEUS MVD group, Nucl. Inst. Meth. **A 453**, 149 (2000);
C. Coldewey, Nucl. Inst. Meth. **A 447**, 44 (2000);
R. Klanner, *Prepared for International Europhysics Conference on High- Energy Physics (EPS-HEP 99)*, 1999;
A. Garfagnini, Nucl. Inst. Meth. **A 435**, 34 (1999);
D. Dannheim et al., Nucl. Inst. Meth. **A 505**, 663 (2003).

[29] I. Bloch, private communication;
I. Giller, private communication;
R. Hori, private communication.

[30] J. Krüger, *The Uranium Scintillator Calorimeter for the ZEUS Detector at the Electron - Proton collider HERA: The Heart of ZEUS*. Habilitation Thesis, Universität Hamburg, Report DESY-F35-92-02, 1992.

[31] G.F. Hartner et al., *VCTRAK(3.07/04): Offline Output Information* (unpublished). ZEUS-97-064, internal ZEUS Note, 1997.

[32] G.F. Hartner, *VCTRAK Briefing: Program and Math* (unpublished). ZEUS-98-058, internal ZEUS Note, 1998.

[33] R. Hall-Wilton et al., *The CTD Tracking Resolution* (unpublished). ZEUS-99-024, internal ZEUS-note, 1999.

[34] W. Verkerke, *Measurement of Charm Production Deep Inelastic Scattering*. Thesis, University of Amsterdam, 1998.

[35] E. Rutherford, Phil. Mag. **21**, 669 (1911).

[36] N. Bohr, Phil. Mag. **25**, 10 (1913).

[37] H. Bethe, Ann. Phys. **5**, 325 (1930);
H. Bethe, Z. Phys. **76**, 293 (1932).

[38] Chr. Møller, Ann. Phys. **14**, 531 (1932).

[39] M. Born, Z. Phys. **38**, 803 (1926).

[40] F. Bloch, Ann. Phys. **16**, 285 (1933).

[41] S.M. Seltzer, M.J. Berger, Int. J. Appl. Radiation Isotope **33**, 1189 (1982).

[42] E. Fermi, Phys. Rev. **57**, 485 (1940).

[43] R.M. Sternheimer, Phys. Rev. **145**, 247 (1966);
R.M. Sternheimer, Phys. Rev. **164**, 349 (1967);
R.M. Sternheimer, Phys. Rev. B **26**, 6067 (1982).

[44] W.H. Barkas, M.J.Berger, *Tables of energy losses and ranges of heavy charged particles*. National Academy of Sciences - National Research Council, NAS-NRC Publication 1133, NASA-SP 3013, 1964.

[45] U. Fano, Ann. Rev. Nucl. Part. Sci. **13**, 1 (1963).

[46] W.W.M. Allison, J.H. Cobb, Ann. Rev. Nucl. Part. Sci. **30**, 253 (1980).

[47] W. Blum, L. Rolandi, *Particle Detection with Drift Chambers*. Springer, Berlin, 1993.

[48] L.D. Landau, *On the energy loss of fast particles by ionisation*, in *Collected Papers of L.D. Landau*, ed. D.ter Haar, p. 188. Pergamon, Oxford, 1965. Reprint of L.D. Landau, *On the energy loss of fast particles by ionisation* in J. Phys. U.S.S.R. 8, 201 (1944).

[49] M.S. Livingston, H.A. Bethe, Rev. Mod. Phys. **9**, 245 (1936).

[50] L. Köpke, R. van Woudenberg, *Photon Conversions in the ZEUS Detector* (unpublished). ZEUS-94-016, internal ZEUS-note, 1994.

[51] W. Verkerke, *Minutes of tracking meeting 8 May 1996*, 1996.

[52] M. Matoba, T. Hirose, T. Sakae, H. Kametani, H. Ijiri, T. Shintake, IEEE Trans. Nucl. Sci. **NS-32**, 541 (1985).

[53] D.G. Sideris, *Simulation of the avalanche regioon of an anode wire in the ZEUS CTD* (unpublished). ZEUS Note 95-076, 1995.

[54] S. Marawske, *Improvement of $< dE/dx >$ Measurements in the Central Tracking Detector of ZEUS at HERA*. Diploma Thesis, Universität Bonn, Bonn, Germany, Report BONN-IB-05-07, 2005, available on `http://www-zeus.physik.uni-bonn.de/german/diploma.html`.

[55] R. Zimmermann, *Kalibrierung und Charakterisierung der dE/dx-Information der Zentralen Driftkammer bei ZEUS*. Diplom Thesis, Universität Bonn, Bonn, Germany, 2007.

[56] K. Hebbel, *Measurement of Charm Production in Deep Inelastic ep Scattering at HERA*. Ph.D. Thesis, Hamburg University, Hamburg (Germany), Report DESY-THESIS-2000-016, 2000.

[57] Available on `http://www-zeus.desy.de/~tcbol/index`.

[58] U. Bassler and G. Bernardi, Nucl. Inst. Meth. **A 361**, 197 (1995).

[59] D. Bartsch, *Messung von Charm-Erzeugung in tief-inelastischer Positron-Proton-Streuung mit ZEUS an HERA*. Diploma Thesis, Universität Bonn, Bonn, Germany, Report BONN-IB-01-10, 2001, available on `http://www-zeus.physik.uni-bonn.de/german/diploma.html`.

[60] Particle Data Group, W.-M. Yao et al., J. Phys. **G 33**, 1 (2006).

[61] L.L. Wai, *Search for an $\mathcal{O}(100\,GeV)$ Mass Right-Handed Electron Neutrino at the HERA Electron-Proton Collider Using the ZEUS Detector*. Ph.D. Thesis, Columbia University, Nevis Laboratories, Irvington (USA), 1995.

[62] M. Grothe, *Untersuchungen zum Nachweis von Elektronen aus semileptonischen Zerfällen von Charm Quarks mit dem ZEUS-Detektor*. Diploma Thesis, Universität Bonn, Bonn, Germany, Report BONN-IB-94-23, 1994, available on `http://www-zeus.physik.uni-bonn.de/german/diploma.html`.

[63] J. Grosse-Knetter, *Energy Correction for Islands* (unpublished). ZEUS-97-039, internal ZEUS Note, 1997.

[64] N. Tuning, *ZUFOs: Hadronic Final State Reconstruction with Calorimeter, Tracking and Backsplash Correction* (unpublished). ZEUS-01-021, internal ZEUS Note, 2001.

[65] R. Sinkus and T. Voss, Nucl. Inst. Meth. **A 391**, 360 (1997).

[66] B. Straub, *The em Electron Finder* (unpublished), available on `http://www-zeus.desy.de/~straub/ZEUS_ONLY/doc/em.ps`.

[67] M. Własenko, private communication.